Novel Microelectrodes and Methods for Real-Time Electrochemical Detection of Neurotransmitters

Pumidech Puthongkham
Lampang, Thailand

Bachelor of Science in Chemistry, Chulalongkorn University, Thailand, 2014

A Dissertation presented to the Graduate Faculty
of the University of Virginia in Candidacy for the Degree of
Doctor of Philosophy

Department of Chemistry

University of Virginia
May 2020

Novel Microelectrodes and Methods for Real-Time Electrochemical Detection of Neurotransmitters

Pumidech Puthongkham
Lampang, Thailand

Bachelor of Science in Chemistry, Chulalongkorn University, Thailand, 2014

A Dissertation presented to the Graduate Faculty
of the University of Virginia in Candidacy for the Degree of
Doctor of Philosophy

Department of Chemistry

University of Virginia
May 2020

Committee members:
B. Jill Venton (advisor)
Ian Harrison
Brooks H. Pate
Andreas Gahlmann
Elizabeth J. Opila

Abstract

Fast-scan cyclic voltammetry (FSCV) with carbon-fiber microelectrodes (CFMEs) is one of the standard techniques for real-time detection of neurotransmitters *in vivo* with rapid dynamics. Although the current FSCV methods are sufficient for monitoring dopamine and some other electroactive neurotransmitters, FSCV can be further optimized to improve its analytical performance and expand the application to new molecules and new biological experiments. My dissertation examines three strategies to improve FSCV detection of neurotransmitters, including redox mechanism investigation, microelectrode modification, and automated data analysis.

Chapter 1 covers the theory and recent advances in FSCV detection of neurotransmitters, electrochemical properties of carbon nanomaterials, and signal and image processing for automated data analysis. In Chapter 2, the oxidation potential and mechanism of histamine at carbon electrodes was established to develop a better FSCV method. From electrochemical studies and surface characterization, histamine oxidation required 1.1 V and underwent one-electron, one-proton oxidation, generated polymer product, and fouled the electrode. The mechanism was utilized to explain the FSCV response of histamine. Nafion coating was then proposed to limit the electrode fouling from histamine electropolymerization to improve its FSCV detection.

Chapters 3 and 4 present two new carbon nanomaterials-modified CFMEs for dopamine detection. Carbon nanohorns (CNHs) improved the sensitivity of CFMEs for dopamine detection by increasing the electrode surface area and dopamine adsorption extent. Oxidative etching of the CNH-modified CFMEs further enhanced the adsorption and sensitivity. Nanodiamonds (NDs) size and functional groups were compared on their electrocatalytic properties and sensitivity. Carboxylated NDs improved the sensitivity by

increasing the surface oxide groups and density of states to enhanced dopamine adsorption and electron transfer kinetics. Both CNHs and NDs also exhibited antifouling properties against serotonin electrochemical fouling and tissue biofouling. Thus, CNHs and NDs are beneficial for improving sensitivity and decreasing electrode fouling.

In Chapter 5, a novel software for FSCV data analysis was proposed to automate the analysis of transient adenosine events. Here, the software utilized the structural similarity image analysis to identify adenosine from the color plot by comparing it with the adenosine references. Digital filtering was also implemented to detrend the background drift to better identify smaller events. The software successfully distinguished transient adenosine events against noise and chemical interferents. The structural similarity image analysis was also generalized to detect dopamine, including simultaneous events with dopamine and adenosine.

Overall, my dissertation demonstrates novel methods to improve the FSCV detection of neurotransmitters. Knowing the histamine redox mechanism leads to better method development. Integrating carbon nanomaterials on microelectrodes enhances their electrochemical properties and analytical performance. Automated software for adenosine transient detection improves the performance and consistency of the analysis. Better methods for real-time detection of neurotransmitters will lead to the understanding of our brain chemistry to devise a treatment for neurodegenerative diseases.

Table of Contents

List of Figures

List of Tables

Acknowledgments

My Ph.D. journey at the Department of Chemistry, University of Virginia would not have been completed without the tremendous support during these five years from my awesome advisor, Dr. Jill Venton. Dr. Venton is a model scientist who had constantly given me numerous opportunities to conceive many projects from my diverse interests in electrochemistry, nanomaterials, and programming. In the process, she had helped me improve my research design and statistics and had spent her significant amount of time and patience to edit my papers while sharpening my writing and presentation skills. I thank Dr. Venton for guiding me to be a better scientist, and I could not imagine having a better Ph.D. advisor than her. Also, I would like to express my gratitude to my dissertation committee members: Dr. Ian Harrison, Dr. Brooks Pate, Dr. Andreas Gahlmann, and Dr. Elizabeth Opila for their valuable ideas, comments, and suggestions.

I would like to thank everyone in the Venton lab for their support. Special thanks to Dr. Cheng Yang, my mentor, who had trained me since Day 1 and had given me many suggestions, both science-related and everyday life. He also helped me to get the carbon nanohorns sample. My special regards to Dr. Mallikarjunarao Ganesana and Dr. Mimi Shin for helping me edit papers and dissertations. I also thank them for their food insights and outstanding sense of humor. I thank Dr. Dana DiScenza, our lab manager, who also helped me edit papers and dissertations. I also thank my labmates who I am honored to work with to expand our electrochemistry horizon: Qun Cao, Yuanyu Chang, Zijun Shao, Yasmine Zubi, Samuel Wachamo, and Julia Lucktong. I thank Dr. Scott Lee who initiated the histamine mechanism project and collected initial data. I thank Dr. Ganesana, Dr. Ying Wang, Jason Borgus, and Yuanyu Chang, who provided their data for the adenosine program development and testing.

Also, I would like to thank our collaborators. Many scientists and staffs at the Center for Nanophase Materials Sciences, Oak Ridge National Laboratory had provided their material science insights and instrument training: Dr. Ilia Ivanov, Dr. Nick Lavrik, Dr. Dave Geohegan, Dr. Alex Puretzky, and Dale Hensley. I also thank the carbon nanopipette project collaborators from the City University of New York: Dr. Michael Mirkin, Dr. Keke Hu, and Rui Jia. I thank Dr. Julian Rocha from the Gahlmann lab, who helped me initiate the first lines of the adenosine program code.

Finally, I thank Thai students at the University of Virginia, our small but close-knit community, for providing moral support and listening to my vent. I am also grateful to have the continuous support from my teachers, my professors, and my friends from Thailand. Most importantly, I am grateful for my Mom and Dad. You guys believe in me choosing this journey. I hope I make you proud.

[Note: In the Spring 2020, the Novel Coronavirus (COVID-19) outbreak was getting serious to the point that social distancing was required, thus I had to defense my dissertation via video conference. I thank everyone again for help and support (emotionally!) during this hard time.]

"It is our choices… that show what we truly are, far more than our abilities."
Albus Dumbledore to Harry Potter
in Harry Potter and the Chamber of Secrets, J. K. Rowling

CHAPTER 1

Introduction

Chapter 1 was reprinted and modified in part from *Anal. Methods* **2019,** *11,* 247-261 and *Analyst* **2020,** *145,* 1087-1102 published by The Royal Society of Chemistry.

Electrochemistry is a subfield of chemistry that studies chemical processes that involve an electron transfer. The Faradaic current from a redox reaction is proportional to the concentration of an electroactive species. This quantitative relationship enables the use of electrochemical methods to analyze those species. Neurochemists have adopted fast-scan cyclic voltammetry (FSCV) to characterize and quantify a neurotransmitter *in vivo* with subsecond dynamics, coupled with carbon-fiber microelectrodes (CFMEs) to achieve micrometers resolution. In FSCV, the Faradaic current is measured to directly quantitate the changes in neurotransmitter concentration. Although the current FSCV methods have successfully enabled several major findings in neuroscience, their analytical performance must be improved to investigate new neurotransmitters and more complicated biological questions. This dissertation aims to use chemistry, material science, and data analysis to improve the FSCV methods for neurotransmitter detection.

1.1 Fast-Scan Cyclic Voltammetry for Neurotransmitter Detection

1.1.1 Principles of Fast-Scan Cyclic Voltammetry

FSCV is an electrochemical technique that has exquisite temporal resolution and sensitivity for measurement of rapid neurotransmitter dynamics *in vivo*.[1–3] FSCV was developed by Millar in 1979 and was later popularized by Wightman.[4–6] Theoretical treatment and instrumentation for FSCV at ultramicroelectrodes was proposed by Savéant and Amatore.[7–9] FSCV was modified from cyclic voltammetry (CV), which is a classical electrochemical technique employing potential sweep to study the redox mechanism of an electroactive species. Unlike the classical CV, where scan rates are in the order of tens to hundreds mV/s, FSCV is conducted with higher scan rate (100 V/s or faster).[2] Fig. 1.1A shows the typical applied potential waveform for the FSCV of dopamine ("the dopamine

waveform"). A holding potential of –0.4 V is applied to the working electrode to selectively preconcentrate cationic dopamine on the electrode surface. Then, a triangular waveform with a scan rate of 400 V/s is applied repeatedly to scan the electrode to a switching potential of +1.3 V and back to oxidize dopamine and reduce dopamine-o-quinone, respectively. The triangular waveform is applied at a repetition frequency of 10 Hz, so one CV is obtained every 100 ms and the cationic dopamine is adsorbed on the electrode surface during the holding potential period before the triangular waveform.

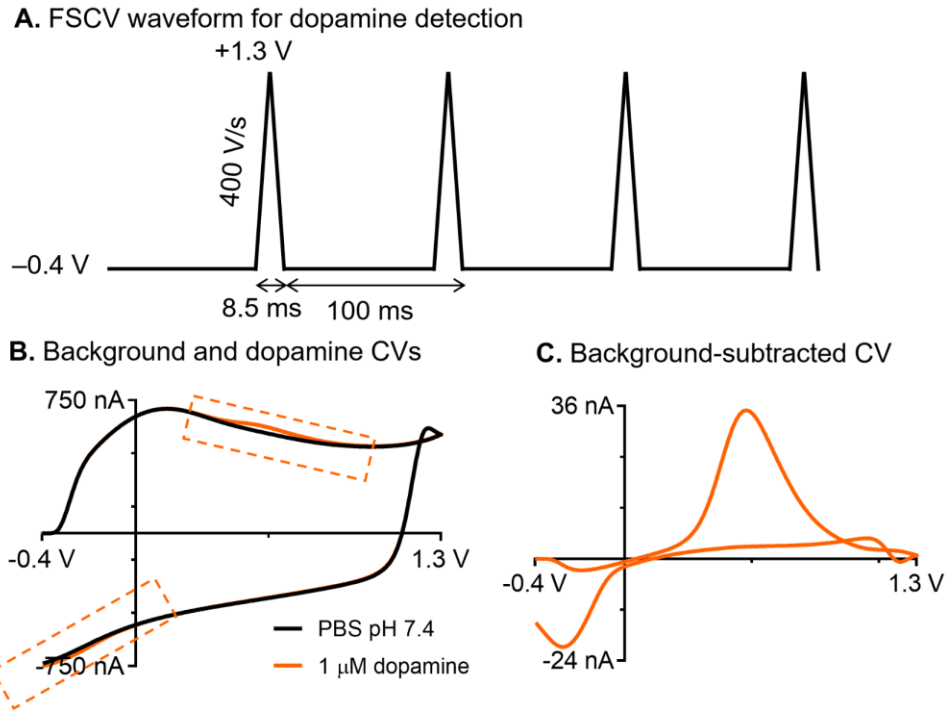

Fig. 1.1 FSCV of dopamine. (A) Applied potential waveform using –0.4 V holding potential, +1.3 V switching potential, 400 V/s scan rate, and 10 Hz repetition rate. (B) Cyclic voltammogram of PBS pH 7.4 (black) and 1 µM dopamine in the same buffer (orange). Dashed boxes emphasize the difference between them. (C) Background-subtracted cyclic voltammogram of 1 µM dopamine.

When no electroactive species is present, applying the triangular waveform results in charging current from electrical double layer at the electrode interface[10] and gives the

background cyclic voltammogram (Fig. 1.1B, black curve). The background charging current (i_{BG}) is proportional to the scan rate (v), electrode surface area (A), and specific capacitance (C_{d}) (Eq. 1.1).[10]

$$i_{\mathrm{BG}} = C_{\mathrm{d}} A v \qquad \text{(Eq. 1.1)}$$

Therefore, the electrode surface area can be calculated from the background current. Because of the high scan rate of FSCV, the background current is much larger than the Faradaic current. For instance, FSCV of 1 μM dopamine (Fig. 1.1B, orange curve) generates only 40 nA anodic current, which is hard to distinguish from the larger background voltammogram (about 600 nA, 15-fold larger). However, if the background voltammogram is stable, then it can be subtracted out from the overall cyclic voltammogram to produce a background-subtracted cyclic voltammogram (Fig. 1.1C), which has a unique shape depending on redox potential, electron transfer kinetics, and mass transport for each electroactive species. This background subtraction makes FSCV a differential technique that can detect a rapid change in concentration but not a basal level concentrations.[2]

The Faradaic current of an electroactive species in CV and FSCV depends on the process controlling the redox reaction. For species with adsorption-controlled redox such as dopamine and other cationic neurotransmitters,[11] the peak current (i_{p}) is proportional to the surface coverage (Γ^*) and scan rate (Eq. 1.2).[10]

$$i_{\mathrm{p}} = \frac{n^2 F^2}{4RT} v A \Gamma^* \qquad \text{(Eq. 1.2)}$$

Therefore, the peak current is also proportional to the concentration in the linear isotherm region, where the surface coverage is proportional to the concentration in the bulk solution. The cyclic voltammogram of adsorption-controlled redox reaction has a symmetrical peak

shape.[10] In contrast, anionic molecules such as ascorbic acid and 3,4-dihydroxyphenylacetic acid (DOPAC) are electrostatically repelled by the negative holding potential and thus are diffusion-controlled in FSCV.[12] The diffusion-controlled cyclic voltammograms are characterized by a duck-shape. The Faradaic current of diffusion-controlled redox reaction is proportional to the square root of scan rate and still proportional to the bulk concentration (C^*) of a species with diffusion coefficient D (Eq. 1.3 for the reversible diffusion-controlled reaction).[10]

$$i_{\mathrm{p}} = (2.69 \times 10^5) n^{3/2} A D^{1/2} C^* v^{1/2} \qquad \text{(Eq. 1.3)}$$

The dopamine waveform in Fig. 1.1A has 100-ms temporal resolution, sufficient for monitoring rapid neurotransmitter release.[1] Because ten cyclic voltammograms are obtained every second, an hour-long measurement will yield 36,000 voltammograms, which are hard to manually examine. To represent continuous FSCV data, individual cyclic voltammograms are stacked together as a three-dimensional current-potential-time plot, as illustrated in Fig. 1.2A, which shows the FSCV data from 5-s bolus injection from 1 µM dopamine followed by buffer washing. A simpler, two-dimensional false color plot, which is the bird's eye view of the 3D plot, is conventionally used to picture all data (Fig. 1.2B).[13] The false color plot allows better interpretation of multiple analytes, noise, and signal drift. For simple measurements where only one electroactive species is monitored, a current-time trace (stacked on the color plot in Fig. 1.2B) shows how the concentration changes over time. The response time of an electrode is usually evaluated from the rise time, which is the time from 10% to 90% of the peak current.[14,15]

The typical working electrode for FSCV measurements is a cylindrical or disk-shaped carbon-fiber microelectrode (CFME) made from a carbon fiber pulled in a glass capillary and sealed with epoxy (Fig. 1.3).[1,16] CFMEs have been widely used for FSCV

measurements, particularly *in vivo*, because their small size (7 µm diameter) allows implantation in specific brain regions. The small size provides low *RC* constant that gives fast signal equilibration, and carbon has biocompatibility that limits tissue damage compared to other materials such as metal.[17] The small surface area generates low currents, in the range of nA, so the Ohmic drop is negligible and only two electrodes (without auxiliary electrode) are required for the electrochemical cell.[2]

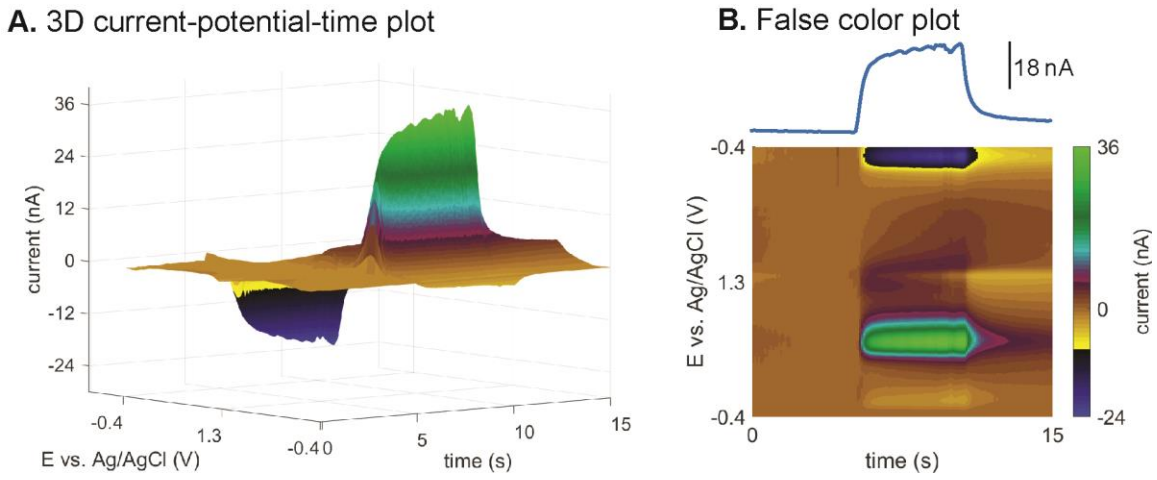

Fig. 1.2 FSCV data representation. (A) Three-dimensional current-potential-time plot and (B) conventional false color plot with anodic peak current-time trace (top) of 5-s bolus injection (black line) of 1 µM dopamine.

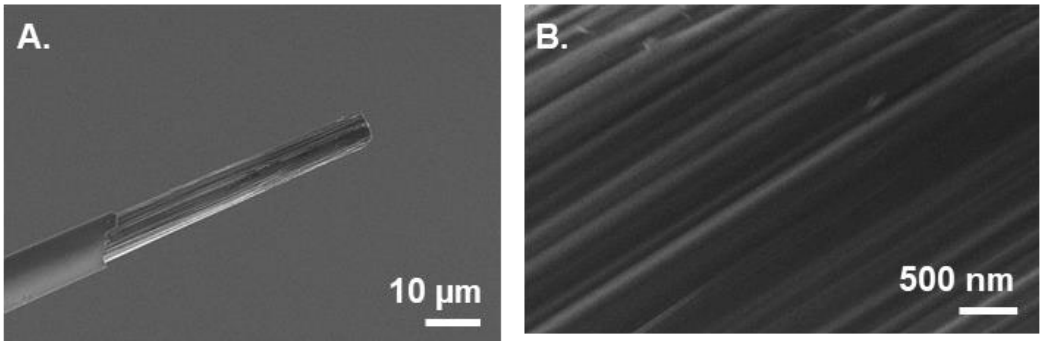

Fig. 1.3 SEM images of cylindrical CFME sealed in glass capillary at (A) 1000× and (B) 25000× magnification.

1.1.2 Compatibility with Monitoring Biological Neurotransmission

The human central nervous system is complex, consisting of several hundred trillion synapses and connections.[18] Thus, simpler model organisms such as rodents[19] and *Drosophila*[20] are often used to investigate the chemical neurotransmission instead. In general, electrochemistry is a versatile technique that has been widely used to detect electroactive neurotransmitters *in vivo* because it is fast and inexpensive, and the biological fluid is inherently buffered. However, nonelectroactive neurotransmitters such as acetylcholine and glutamate cannot be directly oxidized or reduced and require a mediator or biological recognition units such as enzymes and antibodies that specifically convert them to an electroactive product.[2]

FSCV is suitable for *in vivo* monitoring of chemical neurotransmission because it meets several requirements. First, the small size of CFMEs leads to micrometer-range spatial resolution with minimal tissue damage.[2] Thus, it is used to monitor discrete parts of brain and nervous systems such as different brain regions in rats and mice.[21] Second, FSCV is a highly sensitive technique that can measure low concentrations of neurotransmitter release with better limit of detections, such as dopamine releases from an electrical stimulation of rat brain in the range of 0.1–1 μM.[1] Third, FSCV provides high selectivity from the unique cyclic voltammograms for specific neurotransmitters. Thus, it is compatible for use in biological fluid, which consists of many compounds, including high-concentration interferents such as ascorbic acid and a group of catecholamines for dopamine detection.[2,22] Fourth, FSCV has 100-ms temporal resolution from the dopamine waveform, sufficient to monitor rapid release or phasic firing of neurotransmitter that usually occurs at 15-100 Hz.[1] This phasic firing of dopamine is important for the reward

system and drug addiction.[1,23] Last but not least, FSCV is robust enough for continuous measurements, ranging from few hours to several days for chronic implantation.[19]

FSCV has been the key analytical technique for several major findings in neuroscience. For example, subsecond release of dopamine in the midbrain promotes cocaine seeking behavior of rats.[23] The high sensitivity of FSCV revealed that rapid dopamine release during intracranial self-stimulation decays to smaller amounts of release, showing dopamine itself is not the reward signal.[24] In fact, many studies that have pinpointed the role of dopamine in reward rely on FSCV because of its rapid temporal response.[25–27] Moreover, FSCV has been expanded to investigate other compounds. Transient adenosine release modulates blood flow and phasic dopamine release in the caudate-putamen.[28–30] FSCV was used to discover multiple rates of serotonin uptake and histamine and serotonin co-secretion from mast cells.[31,32] Recently, FSCV has been extended to study the role of adenosine during stroke.[28,33] Thus, FSCV is a versatile technique for *in vivo* monitoring of neurotransmitters with rapid dynamics.

There are other electrochemical techniques used in neurotransmitter detection in addition to FSCV. Table 1.1 compares their figures of merit with FSCV. Amperometry holds a constant potential to oxidize or reduce an electroactive species. FSCV has a higher selectivity than amperometry, which cannot discriminate signals from molecules which can be oxidized or reduced at similar potentials such as dopamine and ascorbic acid. On the other hand, the sampling rate of amperometry is only limited by electronics, so its temporal resolution is better than FSCV.[34] Amperometry is still in use to quantify neurotransmitters in a vesicle during exocytosis.[35,36] Pulse voltammetry, including differential pulse voltammetry and square wave voltammetry, gives peak-shaped voltammograms computed from the difference between after and before the potential

pulse. These pulse techniques eliminate the background noise and enhance the sensitivity, and they resolve the Faradaic peaks from two electroactive species with more than 100 mV peak separation.[2] The Plaxco group demonstrated aptamer-based sensors for drug monitoring *in vivo* with 3-s temporal resolution.[37] However, common pulse voltammetry methods require up to a minute to scan one waveform to obtain a voltammogram, thus it lacks sufficient temporal resolution for measurement of rapid neurotransmitter release compared to FSCV.[2]

Table 1.1 Figures of merit of major electroanalytical techniques for neurotransmitter detection

Techniques	Sensitivity	Selectivity	Temporal resolution
Amperometry	Low (25-100 nM LOD dopamine but enough to count molecules)[38]	Low (all compounds that can be oxidized or reduced at the applied potential will give a signal.)	Highest (electronic sampling rate, $\leq$ 1 ms)[2]
Pulse Voltammetry	High (10 nM LOD dopamine)[38]	High (molecules with oxidation potential differs more than 100 mV is resolved.)[2]	Low (up to 1 min)
Fast-Scan Cyclic Voltammetry	High (10 nM LOD dopamine)[38]	Highest (CV shape identifies molecule, but similar species may have similar CV.)	High (triangular waveform frequency, 100 ms)

Neurochemists also utilize other analytical techniques. Microdialysis extracts biological fluid by pumping and collecting a perfusion fluid through a membrane in a probe to obtain a dialysate.[39] A separation technique, such as liquid chromatography and capillary electrophoresis, is usually coupled to the probe to separate and quantify the neurotransmitters in the dialysate.[36] Although microdialysis is the most widely used technique to gain rich chemical information, the sampling and separation are too slow and not sufficient to monitor the rapid neurotransmission.[36] Spectroscopy imaging visualizes the chemical information to the specific part of cell, tissue, or brain.[36] Recently, fluorescence imaging from genetically encoded G protein-coupled receptors were

developed to achieve millisecond temporal resolution,[40,41] but the technique may limit the depth of tissue that can be imaged.[42] Mass spectrometry is another technique used that gives mass spectra that provide chemical signature of each neurotransmitters. Many ionization methods have been developed to solve matrix effects and stability of neurotransmitter ions.[43] Mass spectrometry imaging has also been developed to combine the powerful chemical selectivity with the spatial data from the imaging. Nevertheless, sample preparation and quantitative calibration need to be optimized in the future.[36]

1.1.3 Analytical Challenges for Fast-Scan Cyclic Voltammetry

Although FSCV with CFMEs has been implemented to monitor rapid release of dopamine and other neurotransmitters for nearly four decades, improvements are still needed to explore new molecules and new biological experiments. FSCV, like other techniques, still has many analytical challenges that must be overcome:

- *Sensitivity:* Traditional FSCV has limit of detection for dopamine in the low nM range, but other neurochemicals may be present at even lower concentrations (such as neuropeptides).[42] Thus, improvements are needed in S/N ratios and to disambiguate small Faradaic signals from background drift and noise *in vivo*.[44,45]

- *Selectivity:* Many neurotransmitters have similar voltammograms because they have the same electroactive moiety (such as dopamine, epinephrine, norepinephrine, and DOPAC)[6] or similar peak potentials (such as H_2O_2, adenosine, and histamine).[46,47] Thus, new strategies to make selective electrodes are needed, as well as new data analysis strategies to distinguish signals from multiple analytes.[19,44,48]

- *Electrode fouling:* Biofouling limits the electrode surface area and electron transfer kinetics. It typically arises from adsorption of biomolecules or byproducts of

electrochemical oxidation from molecules such as serotonin.[49,50] Electrode fouling reduces the sensitivity, shifts the Faradaic peaks, and leads to signal instability over time, so new methods are needed to reduce fouling.[51]

- *Temporal resolution:* FSCV has traditionally been performed at 10 Hz because higher repetition rates reduce the signal.[11] More rapid measurements with high sensitivity might uncover even more rapid signals in the brain.

1.2 Electrochemistry of Common Neurotransmitters

A neurotransmitter that can be detected by FSCV must be electroactive, and its redox mechanism must be examined to understand its electrochemical response to develop an appropriate waveform, microelectrode, and data analysis algorithm. Fundamental studies using FSCV, more conventional electrochemical techniques such as CV and amperometry, and spectroscopic characterization should be performed to determine the redox potential and redox mechanism of an electroactive neurotransmitter.[52] This section introduces the oxidation mechanism and FSCV response of common neurotransmitters including dopamine, serotonin, and adenosine. Later, Chapter 2 of this dissertation will reveal the oxidation mechanism of neurotransmitter histamine, as its electrochemistry was less studied.

1.2.1 Dopamine

Dopamine is a catecholamine neurotransmitter which plays an important role in motor and cognitive functions and the reward system.[1] Dopamine electrochemistry is well-characterized, so it is normally used as the standard neurotransmitter to test new electrochemical sensors. The formal potential of dopamine is +0.2 V vs Ag/AgCl. Fig. 1.4

describes the mechanism of dopamine oxidation. At a potential higher than +0.2 V, the catechol moiety of dopamine is oxidized to quinone via two-electron, two-proton process.[2] Then, the quinone product can undergo cyclization via 1,4-Michael addition to leucodopaminechrome. In conventional CV, scanning to higher voltage drives the secondary oxidation, converting leucodopaminechrome to dopaminechrome, which undergoes rearrangement to 5,6-dihydroxyindole. The indole product can be polymerized with another dopamine intermediate to become polydopamine.[53,54] Nevertheless, all steps after the primary oxidation of dopamine are not usually observed *in vivo* because of the low dopamine concentration.[55]

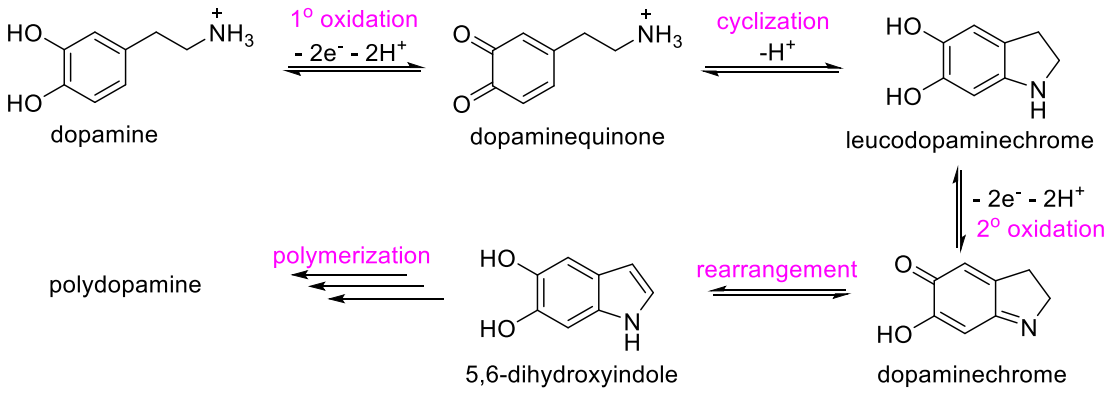

Fig. 1.4 Mechanism of dopamine oxidation[54,55]

In FSCV at CFMEs using the dopamine waveform at 400 V/s, the anodic peak of dopamine is observed at approximately +0.5 V (Fig. 1.1C), 0.3-V shifted from dopamine formal potential because the electron transfer process cannot catch up with the fast potential sweeping.[56] Subsequent reactions after the primary oxidation are not usually observed in FSCV at CFME because of the low concentration *in vivo* and high FSCV scan rate.[55] At this high scan rate, dopamine oxidation is adsorption-controlled, so the sensitivity of dopamine detection can be improved by increasing the adsorption coverage

of dopamine on the electrode, either by lowering the holding potential or increasing the switching potential.[14,57] Another approach to enhance sensitivity to dopamine is to modify or replace the CFME with an electrode material that adsorbs more dopamine. Chapter 1.3 will discuss more on the effect of chemical structure of carbon electrodes on their electrochemical performance toward dopamine detection.

1.2.2 Serotonin

Serotonin (5-hydroxytryptamine) is an indole-derivative neurotransmitter responsible for depression and anxiety and has been monitored by FSCV.[58,59] Serotonin oxidation involves a two-electron, one-proton process on the indole ring (Fig. 1.5) when a potential of +0.35 V or higher is applied.[2,60] The positively-charged oxidation product is very reactive and is immediately attacked by another serotonin molecule to produce a variety of serotonin dimer and polymer structures. This rapid polymerization causes the preceding oxidation to be irreversible, and it forms an insulating film and fouls the electrode surface (Fig. 1.6A) by decreasing the electrode surface area and limiting the electron transfer kinetics of the electrode.[50] The serotonin metabolite 5-hydroxyindole acetic acid (5-HIAA) also undergoes the same oxidation mechanism and cause electrode fouling.[58] Detection of serotonin and 5-HIAA *in vivo* thus suffers the sensitivity degradation due to the electrochemical fouling along the course of experiment.

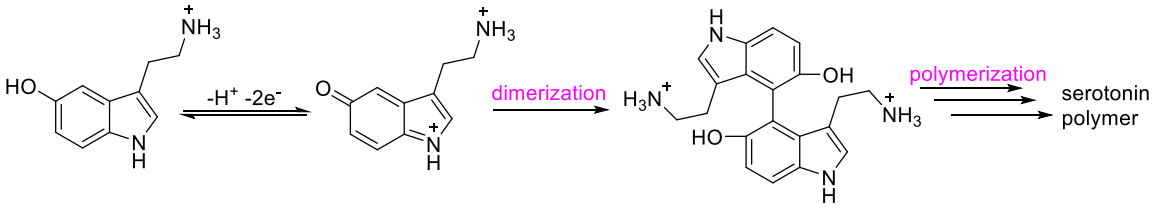

Fig. 1.5 Mechanism of serotonin oxidation. The scheme shows one possible structure of serotonin dimer.[60]

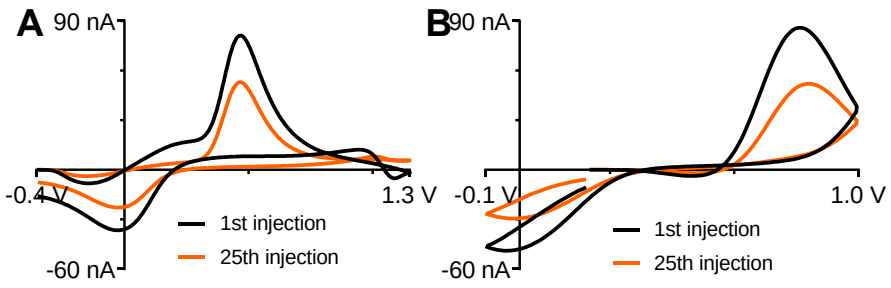

Fig. 1.6 FSCV of 1 µM serotonin using (A) the dopamine waveform (B) the Jackson waveform. Cyclic voltammograms obtained from 1st and 25th 3-s injection every 15 s. Electrode fouling are observed in both waveforms.

Many strategies have been designed to alleviate the electrochemical fouling of serotonin and 5-HIAA in FSCV detection. Jackson et al. proposed the N-shaped waveform to selectively monitor serotonin against dopamine and reduce the serotonin electrochemical fouling in FSCV,[50] and this waveform is still the predominant waveform for serotonin detection. The waveform holds at +0.2 V to limit serotonin byproduct adsorption, ramps quickly at 1000 V/s to 1.0 V to limit the fouling, but scans down to -0.1 V on the backward scan to allow the cathodic peak to be detected. Nevertheless, the fouling is still observable (Fig. 1.6B). The electrode materials were also optimized to limit the adsorption of the fouling species. Nafion-coated CFMEs were used with the N-shaped waveform to utilize the size-exclusion properties of Nafion to eliminate serotonin and 5-HIAA fouling in FSCV.[50,58] Chapters 3 and 4 of this dissertation will present another strategy, using carbon nanomaterials to enhance both antifouling properties and sensitivity of the CFMEs for serotonin.

1.2.3 Adenosine

Adenosine is a neuromodulator that regulates blood flow and is involved in ischemia and stroke.[61] The Venton lab pioneered using FSCV to detect the transient

release of adenosine *in vivo*.[28–30] Fig. 1.7 illustrates the mechanism of adenosine oxidation, which undergoes three two-electron, two-proton steps.[62,63] The primary and secondary oxidations are irreversible and occur at the purine ring to generate carbonyl groups at vacant positions, and the tertiary oxidation deprotonates all the purine nitrogen atoms. With conventional CV, the primary anodic peak is observed around +1.2 V,[64] so the high scan rate of FSCV will shift the peak to a more positive potential, hence the full peak cannot be observed using the dopamine waveform. The switching potential of the FSCV waveform must be extended to +1.45 V or +1.50 V to get the full peak.[30,61] For an *in vitro* experiment, adenosine has the primary anodic peak at +1.35 V on the backward scan because of the fast potential sweeping (Fig. 1.8). The secondary anodic peak then occurs at +1.0 V and is not present before the primary anodic peak. The tertiary oxidation peak is small or not observed in FSCV.[61] This multistep mechanism of adenosine oxidation results in the cyclic voltammogram shape changing during the same injection or the same adenosine transient release,[65] and the secondary anodic peak current lags about 0.1-0.3 s from the primary anodic current.

Because the voltammogram shape of adenosine is changing in the same event, it complicates the automated data analysis. Traditionally, chemometric techniques such as principal component analysis (PCA) and regression (PCR) are classical multivariate analyses that have been widely used in the FSCV field to extract the signal contribution from CVs of different analytes such as dopamine[66] from nonfaradaic and noise components.[19,67,68] However, building a training set and computing the principal components from the varied voltammogram shapes of adenosine is challenging. Chapter 1.4 of this dissertation will discuss an alternative approach to detect adenosine signals in FSCV color plots.

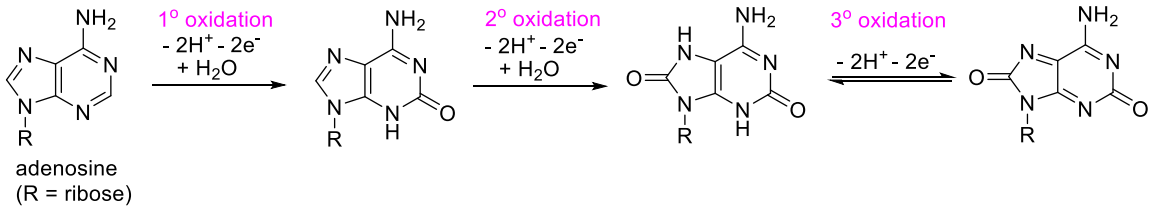

Fig. 1.7 Mechanism of adenosine oxidation.[62,63]

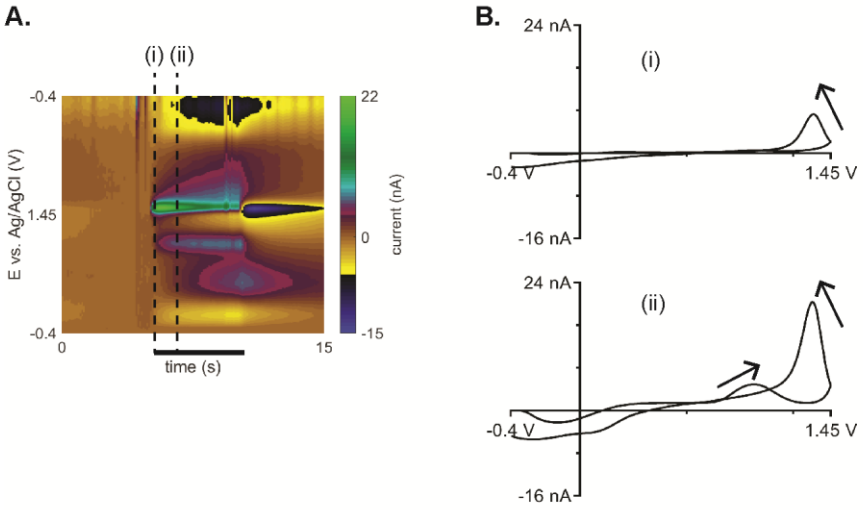

Fig. 1.8 FSCV of 1 µM adenosine. (A) False color plot of 5-s injection of the adenosine solution *in vitro*. (B) CVs at 0.1 s and 1.1 s injection illustrates the growth of secondary peak. Arrows indicate scan direction.

1.3 Carbon Nanomaterials for Microelectrode Development

1.3.1 Structure and Properties of Carbon Electrodes

Carbon is the best electrode material for *in vivo* detection of neurotransmitters because its chemical and surface structure facilitates rapid electron transfer kinetics for neurotransmitter redox reactions.[22,38,69] CFMEs have a similar chemical structure to other common carbon electrodes such as glassy carbon electrodes (GCEs) and screen-printed carbon electrodes (SPCEs); all mainly consist of graphitic carbons.[69] There are two types

of graphitic carbon planes when they are stacked: a basal plane parallel to the graphite sheet, and an edge plane at the edge of the graphite layers that is perpendicular to the graphite sheet (Fig. 1.9) and consists of defects.[70] While the basal planes have a conjugated system that increases the electrical conductivity, it is the edge planes that enhance the adsorption of cationic neurotransmitters and increase the density of electronic states to accelerate electron transfer kinetics.[69–72] The amount of defects is measured by Raman spectroscopy by a ratio of graphitic D peak area (around 1350 cm^{-1}) to the graphitic G peak area (1580 cm^{-1}). Higher D/G ratio indicates more defects and edge planes in the structure.[69] In addition, the structure of CFMEs also contains oxygen-containing functional groups that promote the electrostatic adsorption and sensitivity of cationic neurotransmitters.[69] The oxygen content of carbon electrode is measured by X-ray photoelectron spectroscopy or energy-dispersive X-ray spectroscopy.

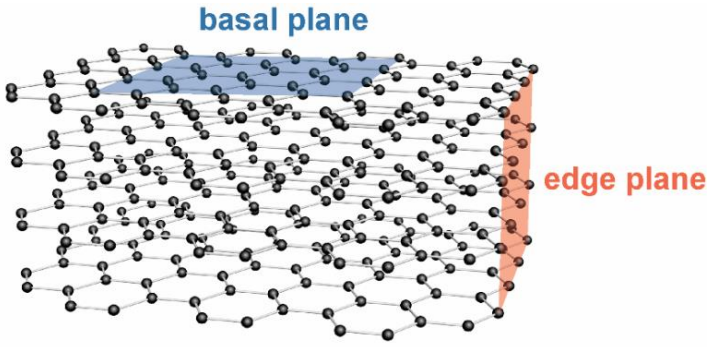

Fig. 1.9 Schematic diagram of edge and basal plane from a stack of graphene layers of graphitic carbon materials.

Most studies on electrode developments in FSCV concentrate on making defect-rich and surface oxide-rich electrodes to increase the adsorption of neurotransmitters and promote electrocatalytic effects to enhance sensitivity. Many strategies have been used to introduce surface groups on the carbon electrode surface, particularly surface oxide

groups which are known to adsorb dopamine. Chemical treatments can increase oxides, such as NaOH etching, or the carbon surface functionalized via diazonium ion reduction, thermal reactions, photochemical reactions, or click chemistry.[69] Electrochemical treatment, by using a waveform with an extended anodic limit, is also used to increase the oxygen content.[57] Flame etching also increased the CFME sensitivity for dopamine and other neurotransmitters by overoxidation mechanism.[73]

Although the chemical structure of CFMEs enhances their electrocatalytic properties and adsorption, CFMEs can also suffer signal degradation over time due to biofouling by biomolecules or electrochemical fouling due to adsorption of oxidative electropolymerization products.[50] Adsorption of these biomolecules and polymers decreases the electroactive surface area and limits the electron transfer kinetics; both phenomena deteriorate signal and sensitivity.[74] Moreover, calibration of CFMEs is particularly challenging as the electrode surface as well as sensing environment can also alter diffusion and adsorption of analytes to the electrode, leading to differences in electrode sensitivity *in vitro* and *in vivo.*[75] Therefore, significant efforts have been focused on developing antifouling electrode material that gives stable current response and improve its lifetime.

1.3.2 Structure and Properties of sp^2-Hybridized Carbon Nanomaterials

One popular strategy to improve the electrochemical properties of an electrochemical sensor is to incorporate carbon nanomaterials on the electrode surface. Carbon nanomaterials consist of a network of carbon atoms with a size of 1–100 nm in at least one dimension.[38,76] In general, carbon nanomaterials are advantageous because of their high specific surface area and low toxicity compared to other nanomaterials.[38,76]

There are many types of carbon nanomaterials, according to the bonding between carbon atoms in the nanomaterial structure. Due to the diverse family of carbon nanomaterials with unique physicochemical properties, the electrochemistry field has explored numerous carbon nanomaterial-modified electrodes for applications in analytical chemistry.[38]

Carbon nanomaterials are classified according to the hybridization of the carbons. The largest group is sp^2-hybridized carbon nanomaterials, including graphene, carbon nanotubes (CNTs), carbon nanospikes (CNSs), and carbon nanohorns (CNHs).[76] These nanomaterials have high electrical conductivity due to their extended conjugated systems. Graphene (Fig. 1.10A) is a sheet of sp^2 carbon connected in a two-dimensional hexagonal lattice and has metallic conductivity.[76,77] Graphene-modified CFMEs were utilized in mice hippocampal tissue to improve the current signals for CV detection of dopamine.[78] However, preparing a true, single-layer graphene is difficult, so some electrochemical sensors are usually built out of 3D forms of graphene to prevent graphene layer restacking.[79–81] Alternatively, graphene oxide (Fig. 1.10B) is often used to enhance the oxygen content and defect sites to improve adsorption capability, but the conductivity is usually decreased.[69,82]

Other sp^2-carbon nanomaterials are shaped by folding the graphene sheet. CNTs are a rolled graphene sheet in a tube morphology, as single-walled CNTs (Fig. 1.10C) or multi-walled CNTs, and are one of the most investigated nanomaterial for microelectrode fabrication.[22,83] CNT ends have a high density of edge planes that exhibit electrocatalytic properties and surface oxides that strongly enhance dopamine adsorption.[15,69] Hence, CNTs enhance the electrochemical signals for both adsorption-controlled species such as dopamine[15,84] in FSCV and diffusion-controlled species such as ascorbic acid.[38,85] On the other hand, CNSs are a form of graphene that have a spike morphology and are grown

on metal wires.[86] CNS microelectrodes have high surface roughness, are defect-rich and contain many oxides, and dopamine adsorption is enhanced in FSCV detection.[86,87] CNHs (Fig. 1.10D) are graphene sheets rolled in a conical structure, which leads to enhanced electric field and adsorption strength at the tip.[88–90] Each individual CNH cone also spontaneously aggregates as a dahlia-like morphology, increasing porosity and adsorption.[90,91] Therefore, CNHs are a promising nanomaterial to improve dopamine detection at CFME.

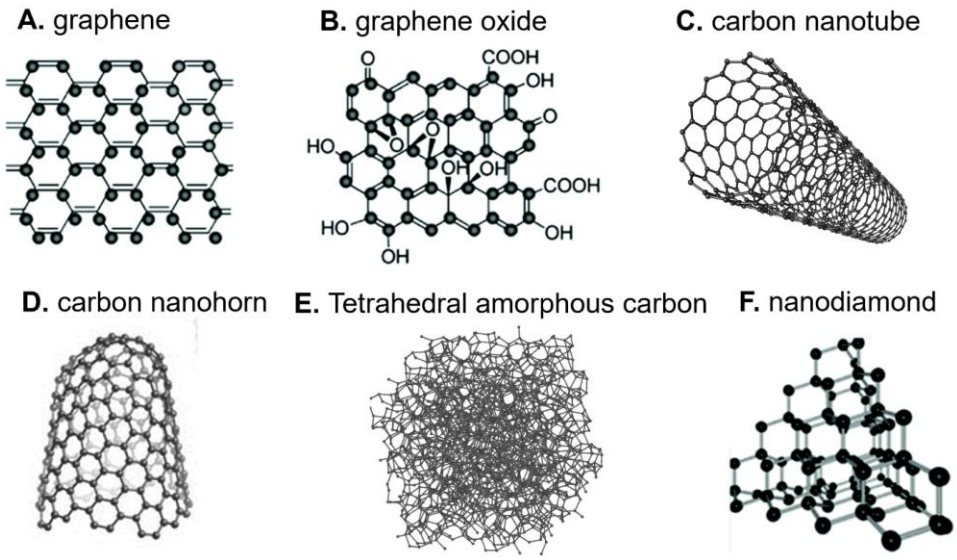

Fig. 1.10 Structure of example carbon nanomaterials: (A) graphene, (B) graphene oxide, (C) single-walled carbon nanotube, (D) carbon nanohorn, (E) tetrahedral amorphous carbon, and (F) nanodiamond.[92]

1.3.3 Structure and Properties of sp^3-Hybridized Carbon Nanomaterials

Another class of carbon nanomaterials is sp^3-hybridized carbon nanomaterials, which have less conductivity than sp^2-carbon nanomaterials.[76,93] Tetrahedral carbons exist in many forms. Tetrahedral amorphous carbon (taC, Fig. 1.10E) is an amorphous sp^3-hybridized carbon structure without crystallinity. A taC thin film electrode was

fabricated and had a wide potential window (-1.6 to +1.7 V vs Ag/AgCl). The oxygen content on taC surface correlated with faradaic current of electroactive species,[94] and the material was responsive to dopamine.[95] Carbon quantum dots, or carbon dots, are spherical nanoparticles consisting of sp^3-carbon amorphous networks.[76] They are a promising nanomaterial for neurotransmitter detection because of their high surface area and high oxygen content. Carbon electrodes modified by carbon dots had improved sensitivity and electrocatalytic properties toward dopamine detection.[96,97]

Diamond is a crystalline tetrahedral network of carbon atoms and is an electrical insulator, but its chemical derivatives and nanoallotropes have been explored on their electrochemical properties.[98,99] Boron-doped diamonds (BDDs) are not a nanomaterial but a classic material that has been widely investigated because of their combined stability, wide potential window, and enhanced electrochemical activity.[48,98] Due to their limited surface functional groups, BDD electrodes also alleviate electrochemical fouling and biofouling, but they do not promote dopamine adsorption.[48,100–103] Nanodiamond (ND, Fig. 1.10F), a nanoparticle diamond synthesized via detonation of explosive organic compounds,[104] has sp^3-hybridized carbon core with defects including sp^2 carbons and functional groups on its surface.[105] A thin film of ND has better electron transfer kinetics and lower overpotential than BDD for several redox probes,[106] ND particles on the electrode surface also improve cell viability, demonstrating the potential of the electrode to be used long-term without damaging the cells.[107] Therefore, ND has the potential to be an electrode material that enhances dopamine adsorption and sensitivity while exhibiting antifouling properties from its diamond core structure.

1.3.4 Preparation of Carbon Nanomaterial Microelectrodes

There are many methods to fabricate carbon nanomaterial electrodes. Some electrodes are fabricated by putting carbon nanomaterials on the standard electrodes such as GCEs, SPCEs, and CFMEs. Other modified electrodes are prepared by having only carbon nanomaterials as the active electrode material on the conductive but not electrochemically active substrate such as bare metal wires.

The simplest methods for preparing carbon nanomaterial electrodes are dip coating and drop casting. The carbon nanomaterials are dissolved or dispersed in an appropriate solvent, usually with a surfactant. Then, the electrode is dipped in the dispersion for a period of time for the dip coating method, or the dispersion is dropped on the electrode surface to evaporate the solvent for the drop casting method.[38] For instance, graphene oxide synthesized via the Hummers method was drop-casted on GCE to increase dopamine anodic current.[108] CNT-modified CFMEs have been prepared by dip coating to enhance FSCV detection.[109,110] NDs were sprayed and drop-casted on conducting Si substrate to improve the electrocatalytic effect and limit of detection for dopamine detection.[107] Dip coating and drop casting methods are simple and can be done in any basic laboratory. However, dissolving carbon nanomaterials in a solvent might lead to aggregation such as graphene restacking, which limits the conductivity and electrocatalytic effect. Reproducibility is also an issue because there are many variables in the procedures, thus the optimization must be done carefully.

Electrodeposition and electrophoretic deposition are another group of techniques that improve reproducibility of the electrode fabrication. In both techniques, an electrical potential is applied to an electrode in a carbon nanomaterials dispersion. The electrostatic attraction or electrochemical reaction of carbon nanomaterials deposits them on the

electrode surface. CNTs, graphene, graphene oxide, and reduced graphene oxide were prepared on GCEs and CFMEs by electrodeposition to enhance dopamine detection.[82,111,112] CNT-modified CFME was prepared by electrophoretic deposition for *in vivo* ascorbic acid detection.[113] These electrochemical methods are advantageous because most deposition variables can be controlled by a potentiostat, and the orientation of depositing material is more controllable than dip coating and drop casting techniques. Co-deposition of carbon nanomaterials with other materials such as conducting polymers[82] and metal nanoparticles[114] is also possible with electrodeposition. Nevertheless, some aggregation in the electrodeposition solution might be possible. Supporting electrolyte is also required for these electrochemical methods, and the high ionic strength of the solution may destabilize and precipitate the nanomaterials.[115]

Direct growth by chemical vapor deposition (CVD) and direct laser writing (DLW) are emerging techniques with the progress in nanofabrication technology to prepare carbon nanomaterial electrodes. Graphene flat electrodes have been prepared from CVD on a metal substrate for electrochemical measurement of dopamine and ferrocene methanol.[116,117] 3D graphene was fabricated on an indium tin oxide planar substrate by CO_2 DLW of spin-coated polyimide, and had good electrochemical activity toward surface sensitive probes.[79] CNTs and CNSs have been directly grown on a metal wire by CVD to enhance dopamine FSCV detection.[84,86] For CNSs, direct current plasma-enhanced CVD is the only method for their fabrication on a conductive substrate.[87] The taC film was prepared by direct current magnetron sputtering and cathodic vacuum arc.[107,118] Carbon nanomaterial electrodes produced by direct growth is advantageous because the amount, spatial orientation, and defects density can be controlled by the growing condition, which leads to the homogeneous surface and high reproducibility. However, the procedures

also require a cleanroom and special instruments, which might not be possible for some laboratories. Some nanomaterial growth also requires a catalyst, which may contaminate the electrochemical response and increases the cell toxicity.[84,119] In addition, direct growth of some carbon nanomaterials on a small substrate, such as CNHs and NDs, is impossible at this time.

Finally, carbon nanomaterials can be spun to get fiber or yarn electrodes, which have been fabricated by several methods. CNT yarns or threads were prepared from spinning and pulling out CNT bundles grown on an array.[120,121] CNT yarn microelectrodes exhibited high sensitivity, high antifouling properties, and high temporal resolution toward FSCV detection of dopamine due to their electrocatalytic properties and surface roughness.[122–124] Alternatively, CNT fibers made from suspending CNTs in a surfactant solution then wet spun in a polymer solution such as polyethyleneimine and poly(vinyl alcohol) enhanced sensitivity and antifouling properties for FSCV detection of dopamine.[125,126] Graphene nanocomposite fiber was also prepared from electrospinning of a graphene dispersion in polyaniline and polystyrene mixtures to enhance surface area and electrocatalytic effects.[127] Hence, carbon nanomaterial fiber fabrication is another versatile method to produce a microelectrode, but the nanomaterials must be suspended in a polymer matrix, which affects their electrochemical properties.

Carbon nanomaterials can further be functionalized or pretreated similar to the plain carbon electrodes before or after electrode modification to enhance their electrochemical properties. Acid pretreatment increased oxygen groups and improved electrocatalytic properties, and electrophilic addition incorporated specific functional groups to optimize the selectivity.[76] Surface treatments also change the oxide functionalization; for example, oxygen plasma etching or laser treatment of CNT yarns

increased the oxygen content.[124,128] Too much functionalization on the sp^2-hybridized carbon nanomaterials disrupts the conjugation and decreases the conductivity of the electrode.[129] Therefore, the extent of functionalization and orientation of groups should be carefully controlled.

Chapters 3–4 of this dissertation will present how manipulating the carbon structure of the microelectrode by CNHs and NDs influences the adsorption and sensitivity of dopamine detection. The effect of carbon nanomaterials surface functionalization will be studied, and the modified electrodes will be investigated on the sensitivity, selectivity, and antifouling properties for FSCV detection of neurotransmitters.

1.4 Data Analysis for Fast-Scan Cyclic Voltammetry

1.4.1 Digital Filtering for Data Preprocessing

FSCV data from continuous measurements usually contain noise and background drift, which convolute and hide the neurotransmitter Faradaic signals. Data preprocessing is the first step after data collection to clean the data for actual analysis, reduce the noise, and improve the S/N ratio.[130] Signal processing techniques such as digital filtering and deconvolution have been widely applied in analytical chemistry because they are available in many data analysis software and programming languages.[131] Signal filtering has an advantage over other chemometric methods such as principal component analysis because it does not require any training set.

Some digital filters for data preprocessing are in the frequency domain, and each filter is characterized by frequency function and cutoff frequency (f_c), with an amplitude of -3 dB, half-powered of an original signal. High-pass filters pass the rapid signal fluctuations, which are usually of neurotransmitters, but not the background drift, which is

low frequency (Fig. 1.11A). DeWaele et al. proposed a zero-phase high-pass Butterworth filter to remove background drift in FSCV data.[44] The filter was successful in eliminating the low-frequency baseline drift from continuous FSCV data for 24 hours measurement *in vitro* and 5 hours measurement *in vivo*, and all characteristics of the dopamine Faradaic peak were preserved. On the other hand, low-pass filters eliminate high-frequency electrical glitches and smooth the signal (Fig. 1.11B).[131,132] The Heien group demonstrated noise removal using a low-pass Butterworth filter.[132] Frequency-domain filters in general cause passband ripples before and after the peaks and affect amplitude reading, so there is a trade-off between data cleaning and the amplitude loss.

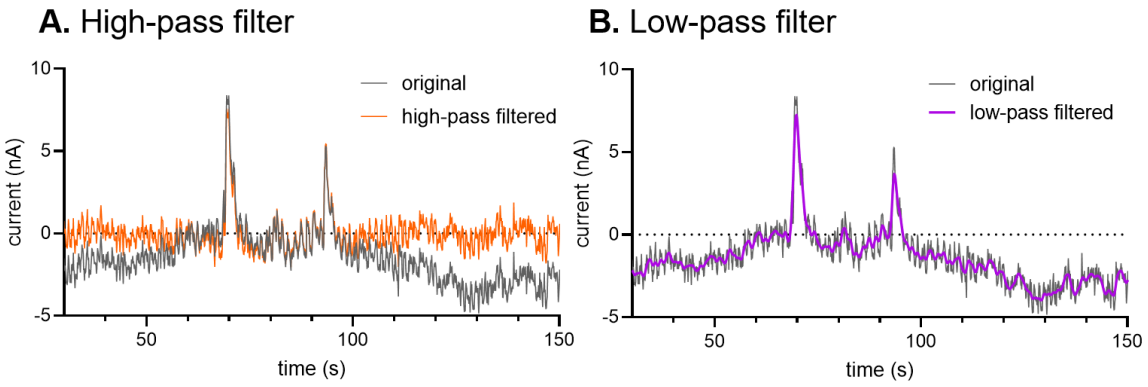

Fig. 1.11 Frequency-domain filtered data. (A) high-pass filter (f_c = 0.03 Hz) and (B) low-pass filter (f_c = 0.5 Hz). The second-order Butterworth design is used in both filters.

There are also time-domain filters, which are widely used to smooth the signal. For instance, moving average filter (Fig. 1.12A) replaces the data point by the average value of the data in the window with a specified width. A window width of 15 replaces the data point with the average between the seven adjacent points before, the data point itself, and seven adjacent points after.[133] A moving average filter is easy to implement, but the smoothing generally leads to amplitude reduction for a very sharp peak, thus sometimes

the weight coefficients are used to calculate the weighted moving average instead. Savitzky and Golay proposed the alternative method to smooth the data using least square polynomial fitting.[133] The data points in the window are fitted to the high-order polynomial by least square regression instead (Fig. 1.12B). The fitted polynomial better represents the data than the moving average and is still able to eliminate the spiked noise or outlier, but a wider window might be required. The Savitzky-Golay filter has been widely used in signal processing in many fields and is an alternative method to smooth the data in addition to the low-pass filter while preserving the peak amplitude.

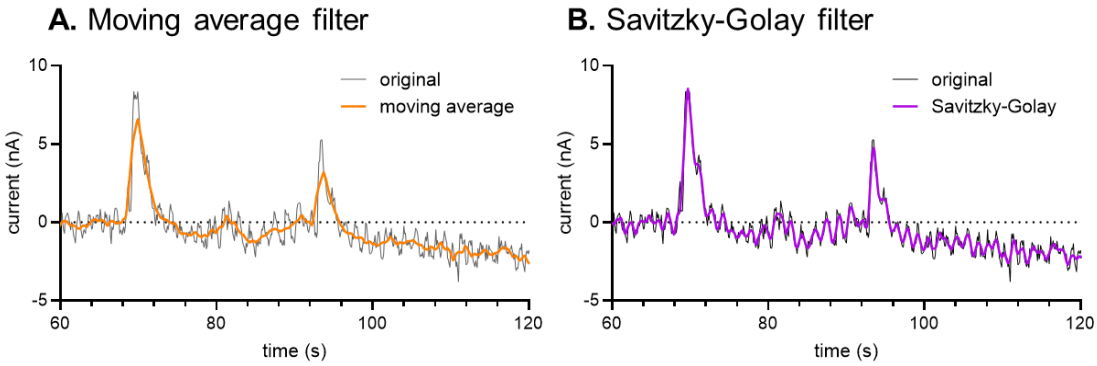

Fig. 1.12 Time-domain filtered data (a) moving average filter and (b) Savitzky-Golay filter with window size = 15.

1.4.2 Principal Component Analysis and Regression for Signal Decomposition

Principal component analysis (PCA) and principal component regression (PCR) are multivariable techniques widely used to extract the signal contribution from different analytes such as dopamine[66] from nonfaradaic and noise components in FSCV data.[19,67,68] PCA uses a linear algebra technique to decompose the cyclic voltammogram from a training set into principal components (PCs), which are linear combinations of data points. The first PC must span across the voltammogram in the direction that yields the maximum

variance, then the next PC direction is orthogonal to the first PC.[68] Ideally, each PC should represent each chemical component. For example, one PC may represent the Faradaic current from electroactive species, and another PC may represent the pH changes. After that, the regression equations are constructed between the concentration changes and the scores, and the equations are used for the experimental data.[68] Training sets can be collected *in vitro* from different electrodes for a range of neurotransmitter concentrations and *in vivo* from different animals and concatenated as a standard library for future experiments and animals to reduce variability and analysis time.[19] Different origins between the training set and experimental data also allow statistical independence.[19]

PCR offers several advantages. It discriminates the faradaic contribution from neurotransmitters against the random signal change.[134] The residual analysis also helps to detect other interferents.[68] However, the training set substantially affect the quality of PCR analysis. PCR theory and a recent critique of application in FSCV by the Wightman group[68] suggests that the training set should be collected from known signals in the same animals. The discrepancy of the experimental condition between the training sets in the library and the experimental data led to poor signal resolution and inaccurate quantification of the neurotransmitter concentration.[68] Moreover, PCR is not effective to analyze a compound which its cyclic voltammogram shape changes within the same event such as adenosine because the shape changing limits the quality of the decomposed PCs. Hence, an alternative method which is compatible with shape changing is preferred.

1.4.3 Alternative Methods for Fast-Scan Cyclic Voltammetry Data Analysis

Mathematical techniques were combined with waveform manipulation to predict the noise and nonfaradaic signal to remove it from the main electrochemical signal.

Monovalent and divalent cations electrostatically interact with the surface-oxide group on the CFMEs, so the Wightman group studied the effect of local changes in those ions on the background charging current.[135] Then, they proposed to apply an 80-120 mV constant-potential pulse before the dopamine waveform to estimate the impulse response caused by nonfaradaic processes, and deconvoluted that response to obtain cleaner color plots. The Sombers group adapted paired-pulse voltammetry by applying a double triangular waveform by using smaller first (-0.4 to +0.8 V) and larger second triangular waveform (-0.4 to +1.4 V).[45,136] The smaller cyclic voltammogram from the first triangular waveform was used to predict the background drift in the larger voltammogram by using partial least square regression (PLSR). The procedure was successful in removing the pH shift and background drift and detect dopamine and H_2O_2 *in vivo*.

Some analytes are detected by using the empirical rule from its current-potential-time characteristic. Spontaneous transient adenosine events have been characterized *in vivo* in different rat brain regions, but the events are random in nature so their analysis is challenging.[21,137] The Venton group developed an automated software to identify and characterize transient adenosine events from the FSCV data.[65] The program scanned for the possible events from the peaks in current-time trace at primary and secondary anodic peak potentials. Several rules were applied to verify whether it is an adenosine transient, including a minimum signal-to-noise ratio, required time delay, and set peak current ratio between primary and secondary peak of the event. Nevertheless, the program utilizes only two current-time traces, and electrical noise around two anodic peaks can still cause spurious false positives or false negatives.

Alternatively, FSCV color plots can be analyzed by image processing and analysis tools because the color plot is designed to visualize the Faradaic signals, drift, and noises

in the continuous data.[13] Detection of a neurotransmitter signal in the color plot is then abstracted to the object recognition problem. There are many algorithms available for object recognition to compare the color plot from experimental data to the known signal of a neurotransmitter. For example, the mean-squared error (MSE) method is widely used to compare the pixel intensity of the same location in both sample and reference image, but slight shift of the whole image deteriorates the score.[138] Therefore, a different object recognition algorithm should be implemented to analyze FSCV data because of the possibility in signal drift and chemical interference. Chapter 5 of this dissertation will present a novel software that uses an alternative image analysis technique to automate the automated the detection and analysis of adenosine transient events from FSCV data.

1.5 Overview of the Dissertation

For nearly four decades, FSCV with CFME has been used to monitor rapid neurotransmission of many electroactive neurotransmitters. Still, many improvements are required to improve the analytical performance of FSCV to investigate more complicated biological questions. This dissertation aims to develop an improved method for FSCV detection of neurotransmitters by the three independent strategies (Fig. 1.13).

The first strategy is to study the redox mechanism of a neurotransmitter at carbon electrodes to understand its FSCV response to develop a better detection method. Histamine is a neurotransmitter that regulates sleep-wake cycle and involves in the immune response.[139] Although histamine has been studied on its rapid mode of neurotransmission using FSCV,[31,140] there are disagreements between histamine FSCV methods and histamine oxidation potential. In Chapter 2, electrochemical and surface characterization techniques are combined to determine the required potential and

mechanism of histamine oxidation at carbon electrodes. Histamine oxidation is shown to foul the electrode. Because histamine fouling deteriorates its FSCV signal, Nafion coating will be applied as a method to reduce the fouling. This chapter illustrates that knowing redox mechanism of neurotransmitter leads to the better FSCV detection method.

The second strategy is to fabricate a carbon nanomaterial electrode to enhance its electrochemical properties toward neurotransmitter detection. Chapter 3 describes the fabrication of CNH-modified CFME by electrodeposition. CNHs enhance the adsorption of dopamine and other cationic neurotransmitters because of the defect-rich structure of CNHs, the enhanced electric field at the CNH tips, and the porosity from the CNHs dahlia-like aggregation.[89] Oxidative etching of the CNH-modified CFME further enhances the dopamine adsorption. Next, Chapter 4 explores the electrochemical properties of ND-modified CFMEs prepared by drop casting. CFMEs modified by NDs with different sizes and surface functional groups are compared, and the 15-nm carboxylated ND-modified CFME performs the best. The optimized electrodes have an improved sensitivity for dopamine detection and antifouling properties due to the surface oxide groups and hydrophilicity.[141] These two chapters demonstrate the structure-properties relationship of the carbon nanomaterials structure to improve the FSCV detection.

The third strategy is to devise new software to automate the analysis of FSCV data to improve accuracy, precision, and consistency in recognizing neurotransmitter signal. Chapter 5 presents the application of structural similarity (SSIM) index,[138] an image analysis technique which mimics the human visual system by comparing the whole structure of the sample and reference images instead of the pixel-by-pixel method in MSE. The SSIM index was implemented to detect adenosine transient event from an FSCV color plot by comparing it to the adenosine reference color plots. Combining with digital filters

to correct the background drift, the SSIM index is successful in detecting small adenosine transient events with an improved accuracy and precision. Its versatility is also demonstrated by modifying the software to detect co-released dopamine in adenosine data. This chapter shows the novel application of image analysis techniques to enhance electrochemical detection of neurotransmitters.

Overall, this dissertation utilizes the knowledge and tools from electrochemistry, carbon nanomaterials, and data analysis to advance the real-time electrochemical detection of neurotransmitters. Chapter 6 also the future directions of the FSCV and electrochemistry field from the recent advances in micro/nanoelectrode fabrication and machine learning for data analysis.

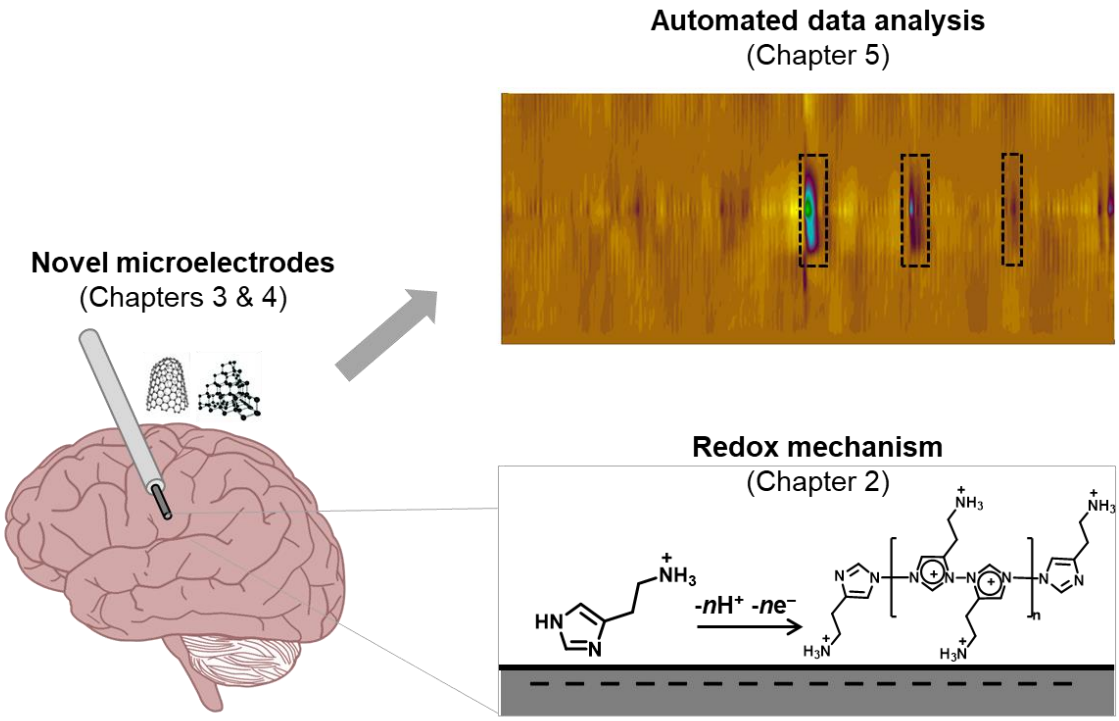

Fig. 1.13 Three approaches for FSCV method development: investigation of redox mechanism, development of carbon nanomaterial microelectrodes, and implementation of automated data analysis.

1.6 References

(1) Venton, B. J.; Wightman, R. M. Psychoanalytical Electrochemistry: Dopamine and Behavior. *Anal. Chem.* **2003**, *75* (19), 414A-421A.

(2) Robinson, D. L.; Hermans, A.; Seipel, A. T.; Wightman, R. M. Monitoring Rapid Chemical Communication in the Brain. *Chem. Rev.* **2008**, *108*, 2554–2584.

(3) Roberts, J. G.; Sombers, L. A. Fast-Scan Cyclic Voltammetry: Chemical Sensing in the Brain and Beyond. *Anal. Chem.* **2018**, *90* (1), 490–504.

(4) Armstrong-James, M.; Millar, J. Carbon Fibre Microelectrodes. *J. Neurosci. Methods* **1979**, *1* (3), 279–287.

(5) Armstrong-James, M.; Millar, J.; Kruk, L. Quantification of Noradrenaline Iontophoresis. *Nature* **1980**, *288*, 181–183.

(6) Baur, J. E.; Kristensen, E. W.; May, L. J.; Wiedemann, D. J.; Wightman, R. M. Fast-Scan Voltammetry of Biogenic Amines. *Anal. Chem.* **1988**, *60* (13), 1268–1272.

(7) Amatore, C.; Maisonhaute, E.; Simonneau, G. Ultrafast Cyclic Voltammetry: Performing in the Few Megavolts per Second Range without Ohmic Drop. *Electrochem. Commun.* **2000**, *2* (2), 81–84.

(8) Andrieux, C. P.; Garreau, D.; Hapiot, P.; Pinson, J.; Savéant, J. M. Fast Sweep Cyclic Voltammetry at Ultra-Microelectrodes. Evaluation of the Method for Fast Electron-Transfer Kinetic Measurements. *J. Electroanal. Chem.* **1988**, *243* (2), 321–335.

(9) Garreau, D.; Hapiot, P.; Savéant, J. M. Instrumentation for Fast Voltammetry at Ultramicroelectrodes. Stability and Bandpass Limitations. *J. Electroanal. Chem.* **1989**, *272* (1–2), 1–16.

(10) Bard, A. J.; Faulkner, L. R. *Electrochemical Methods: Fundamentals and Applications*, 2nd ed.; John Wiley and Sons: New York, 2001.

(11) Bath, B. D.; Michael, D. J.; Trafton, B. J.; Joseph, J. D.; Runnels, P. L.; Wightman, R. M. Subsecond Adsorption and Desorption of Dopamine at Carbon-Fiber Microelectrodes. *Anal. Chem.* **2000**, *72* (24), 5994–6002.

(12) Huffman, M. L.; Venton, B. J. Electrochemical Properties of Different Carbon-Fiber Microelectrodes Using Fast-Scan Cyclic Voltammetry. *Electroanalysis* **2008**, *20* (22), 2422–2428.

(13) Michael, D.; Travis, E. R.; Wightman, R. M. Color Images for Fast-Scan CV Measurements in Biological Systems. *Anal. Chem.* **1998**, *70* (17), 586A-592A.

(14) Heien, M. L. A. V; Phillips, P. E. M.; Stuber, G. D.; Seipel, A. T.; Wightman, R. M. Overoxidation of Carbon-Fiber Microelectrodes Enhances Dopamine Adsorption and Increases Sensitivity. *Analyst* **2003**, *128*, 1413–1419.

(15) Xiao, N.; Venton, B. J. Rapid, Sensitive Detection of Neurotransmitters at Microelectrodes Modified with Self-Assembled SWCNT Forests. *Anal. Chem.* **2012**, *84*, 7816–7822.

(16) Huffman, M. L.; Venton, B. J. Carbon-Fiber Microelectrodes for in Vivo Applications. *Analyst* **2009**, *134*, 18–24.

(17) Garris, P. A.; Wightman, R. M. Different Kinetics Govern Dopaminergic Transmission in the Amygdala, Prefrontal Cortex, and Striatum: An in Vivo Voltammetric Study. *J. Neurosci.* **1994**, *14* (1), 442–450.

(18) Silbereis, J. C.; Pochareddy, S.; Zhu, Y.; Li, M.; Sestan, N. The Cellular and Molecular Landscapes of the Developing Human Central Nervous System. *Neuron* **2016**, *89* (2), 248.

(19) Rodeberg, N. T.; Sandberg, S. G.; Johnson, J. A.; Phillips, P. E. M.; Wightman, R. M. Hitchhiker's Guide to Voltammetry: Acute and Chronic Electrodes for in Vivo Fast-Scan Cyclic Voltammetry. *ACS Chem. Neurosci.* **2017**, *8*, 221–234.

(20) Shin, M.; Copeland, J. M.; Venton, B. J. Drosophila as a Model System for Neurotransmitter Measurements. *ACS Chem. Neurosci.* **2018**, *9* (8), 1872–1883.

(21) Lee, S. T.; Venton, B. J. Regional Variations of Spontaneous, Transient Adenosine Release in Brain Slices. *ACS Chem. Neurosci.* **2018**, *9* (3), 505–513.

(22) Jacobs, C. B.; Peairs, M. J.; Venton, B. J. Review: Carbon Nanotube Based Electrochemical Sensors for Biomolecules. *Anal. Chim. Acta* **2010**, *662* (2), 105–127.

(23) Phillips, P. E. M.; Stuber, G. D.; Helen, M. L. A. V; Wightman, R. M.; Carelli, R. M. Subsecond Dopamine Release Promotes Cocaine Seeking. *Nature* **2003**, *422* (6932), 614–618.

(24) Rodeberg, N. T.; Johnson, J. A.; Bucher, E. S.; Wightman, R. M. Dopamine Dynamics during Continuous Intracranial Self-Stimulation: Effect of Waveform on Fast-Scan Cyclic Voltammetry Data. *ACS Chem. Neurosci.* **2016**, *7* (11), 1508–1518.

(25) Wenzel, J. M.; Oleson, E. B.; Gove, W. N.; Cole, A. B.; Gyawali, U.; Dantrassy, H. M.; Bluett, R. J.; Dryanovski, D. I.; Stuber, G. D.; Deisseroth, K.; et al. Phasic Dopamine Signals in the Nucleus Accumbens That Cause Active Avoidance Require Endocannabinoid Mobilization in the Midbrain. *Curr. Biol.* **2018**, *28* (9), 1392-1404.e5.

(26) Willuhn, I.; Burgeno, L. M.; Groblewski, P. A.; Phillips, P. E. M. Excessive Cocaine Use Results from Decreased Phasic Dopamine Signaling in the Striatum. *Nat. Neurosci.* **2014**, *17* (5), 704–709.

(27) Schindler, A. G.; Soden, M. E.; Zweifel, L. S.; Clark, J. J. Reversal of Alcohol-Induced Dysregulation in Dopamine Network Dynamics May Rescue Maladaptive Decision-Making. *J. Neurosci.* **2016**, *36* (13), 3698–3708.

(28) Wang, Y.; Venton, B. J. Correlation of Transient Adenosine Release and Oxygen Changes in the Caudate-Putamen. *J. Neurochem.* **2017**, *140* (1), 13–23.

(29) Ross, A. E.; Venton, B. J. Adenosine Transiently Modulates Stimulated Dopamine Release in the Caudate-Putamen via A1 Receptors. *J. Neurochem.* **2015**, *132* (1), 51–60.

(30) Nguyen, M. D.; Venton, B. J. Fast-Scan Cyclic Voltammetry for the Characterization of Rapid Adenosine Release. *Comput. Struct. Biotechnol. J.* **2015**, *13*, 47–54.

(31) Pihel, K.; Hsieh, S.; Jorgenson, J. W.; Wightman, R. M. Electrochemical Detection of Histamine and 5-Hydroxytryptamine at Isolated Mast Cells. *Anal. Chem.* **1995**, *67* (24), 4514–4521.

(32) Travis, E. R.; Wang, Y. M.; Michael, D. J.; Caron, M. G.; Wightman, R. M. Differential Quantal Release of Histamine and 5-Hydroxytryptamine from Mast Cells of Vesicular Monoamine Transporter 2 Knockout Mice. *Proc. Natl. Acad. Sci. U. S. A.* **2000**, *97* (1), 162–167.

(33) Ganesana, M.; Venton, B. J. Early Changes in Transient Adenosine during Cerebral Ischemia and Reperfusion Injury. *PLoS One* **2018**, *13* (5), e0196932.

(34) Zhang, B.; Heien, M. L. A. V.; Santillo, M. F.; Mellander, L.; Ewing, A. G. Temporal Resolution in Electrochemical Imaging on Single PC12 Cells Using Amperometry and Voltammetry at Microelectrode Arrays. *Anal. Chem.* **2011**, *83* (2), 571–577.

(35) Li, X.; Majdi, S.; Dunevall, J.; Fathali, H.; Ewing, A. G. Quantitative Measurement of Transmitters in Individual Vesicles in the Cytoplasm of Single Cells with Nanotip Electrodes. *Angew. Chem., Int. Ed.* **2015**, *54* (41), 11978–11982.

(36) Ganesana, M.; Lee, S. T.; Wang, Y.; Venton, B. J. Analytical Techniques in Neuroscience: Recent Advances in Imaging, Separation, and Electrochemical Methods. *Anal. Chem.* **2017**, *89* (1), 314–341.

(37) Arroyo-Currás, N.; Somerson, J.; Vieira, P. A.; Ploense, K. L.; Kippin, T. E.; Plaxco, K. W. Real-Time Measurement of Small Molecules Directly in Awake, Ambulatory Animals. *Proc. Natl. Acad. Sci. U. S. A.* **2017**, *114* (4), 645–650.

(38) Yang, C.; Denno, M. E.; Pyakurel, P.; Venton, B. J. Recent Trends in Carbon Nanomaterial-Based Electrochemical Sensors for Biomolecules: A Review. *Anal. Chim. Acta* **2015**, *887*, 17–37.

(39) Kennedy, R. T. Emerging Trends in in Vivo Neurochemical Monitoring by Microdialysis. *Curr. Opin. Chem. Biol.* **2013**, *17* (5), 860–867.

(40) Sun, F.; Zeng, J.; Jing, M.; Zhou, J.; Feng, J.; Owen, S. F.; Luo, Y.; Li, F.; Wang, H.; Yamaguchi, T.; et al. A Genetically Encoded Fluorescent Sensor Enables Rapid and Specific Detection of Dopamine in Flies, Fish, and Mice. *Cell* **2018**, *174* (2), 481–496.

(41) Patriarchi, T.; Cho, J. R.; Merten, K.; Howe, M. W.; Marley, A.; Xiong, W. H.; Folk, R. W.; Broussard, G. J.; Liang, R.; Jang, M. J.; et al. Ultrafast Neuronal Imaging of Dopamine Dynamics with Designed Genetically Encoded Sensors. *Science* **2018**, *360*, eaat4422.

(42) Shin, M.; Wang, Y.; Borgus, J. R.; Venton, B. J. Electrochemistry at the Synapse. *Annu. Rev. Anal. Chem.* **2019**, *12* (1), 297–321.

(43) Spengler, B. Mass Spectrometry Imaging of Biomolecular Information. *Anal. Chem.* **2015**, *87* (1), 64–82.

(44) DeWaele, M.; Oh, Y.; Park, C.; Kang, Y. M.; Shin, H.; Blaha, C.; Bennet, K. E.; Kim, I. Y.; Lee, K. H.; Jang, D. P. Baseline Drift Detrending Techniques for Fast Scan Cyclic Voltammetry. *Analyst* **2017**, *142*, 4317–4321.

(45) Meunier, C. J.; McCarty, G. S.; Sombers, L. A. Drift Subtraction for FSCV Using Double-Waveform Partial-Least-Squares Regression. *Anal. Chem.* **2019**, *91*, 7319–7327.

(46) Wilson, L. R.; Panda, S.; Schmidt, A. C.; Sombers, L. A. Selective and Mechanically Robust Sensors for Electrochemical Measurements of Real-Time Hydrogen Peroxide Dynamics in Vivo. *Anal. Chem.* **2018**, *90* (1), 888–895.

(47) Ross, A. E.; Venton, B. J. Sawhorse Waveform Voltammetry for Selective Detection of Adenosine, ATP, and Hydrogen Peroxide. *Anal. Chem.* **2014**, *86* (15), 7486–7493.

(48) Bennet, K. E.; Tomshine, J. R.; Min, H.-K.; Manciu, F. S.; Marsh, M. P.; Paek, S. B.; Settell, M. L.; Nicolai, E. N.; Blaha, C. D.; Kouzani, A. Z.; et al. A Diamond-Based Electrode for Detection of Neurochemicals in the Human Brain. *Front. Hum. Neurosci.* **2016**, *10* (March), 1–12.

(49) Liu, X.; Xiao, T.; Wu, F.; Shen, M.-Y.; Zhang, M.; Yu, H.; Mao, L. Ultrathin Cell-Membrane-Mimic Phosphorylcholine Polymer Film Coating Enables Large Improvements for In Vivo Electrochemical Detection. *Angew. Chem., Int. Ed.* **2017**, *56* (39), 11802–11806.

(50) Jackson, B. P.; Dietz, S. M.; Wightman, R. M. Fast-Scan Cyclic Voltammetry of 5-Hydroxytryptamine. *Anal. Chem.* **1995**, *67* (6), 1115–1120.

(51) Harreither, W.; Trouillon, R.; Poulin, P.; Neri, W.; Ewing, A. G.; Safina, G. Cysteine Residues Reduce the Severity of Dopamine Electrochemical Fouling. *Electrochim. Acta* **2016**, *210*, 622–629.

(52) Lim, G. N.; Ross, A. E. Purine Functional Group Type and Placement Modulate the Interaction with Carbon-Fiber Microelectrodes. *ACS Sens.* **2019**, *4*, 479–487.

(53) Li, S.; Wang, H.; Young, M.; Xu, F.; Cheng, G.; Cong, H. Properties of Electropolymerized

Dopamine and Its Analogues. *Langmuir* **2018**, *35*, 1119–1125.

(54) Liu, Y.; Ai, K.; Lu, L. Polydopamine and Its Derivative Materials: Synthesis and Promising Applications in Energy, Environmental, and Biomedical Fields. *Chem. Rev.* **2014**, *114* (9), 5057–5115.

(55) Yang, C.; Hu, K.; Wang, D.; Zubi, Y.; Lee, S. T.; Puthongkham, P.; Mirkin, M. V.; Venton, B. J. Cavity Carbon-Nanopipette Electrodes for Dopamine Detection. *Anal. Chem.* **2019**, *91*, 4618–4624.

(56) Venton, B. J.; Cao, Q. Fundamentals of Fast-Scan Cyclic Voltammetry for Dopamine Detection. *Analyst* **2020**, *145*, 1158–1168.

(57) Takmakov, P.; Zachek, M. K.; Keithley, R. B.; Walsh, P. L.; Donley, C.; McCarty, G. S.; Wightman, R. M. Carbon Microelectrodes with a Renewable Surface. *Anal. Chem.* **2010**, *82* (5), 2020–2028.

(58) Hashemi, P.; Dankoski, E. C.; Petrovic, J.; Keithley, R. B.; Wightman, R. M. Voltammetric Detection of 5-Hydroxytryptamine Release in the Rat Brain. *Anal. Chem.* **2009**, *81* (22), 9462–9471.

(59) Borue, X.; Cooper, S.; Hirsh, J.; Condron, B.; Venton, B. J. Quantitative Evaluation of Serotonin Release and Clearance in Drosophila. *J. Neurosci. Methods* **2009**, *179* (2), 300–308.

(60) Wrona, M. Z.; Dryhurst, G. Electrochemical Oxidation of 5-Hydroxytryptamine in Aqueous Solution at Physiological PH. *Bioorg. Chem.* **1990**, *18* (3), 291–317.

(61) Swamy, B. E. K.; Venton, B. J. Subsecond Detection of Physiological Adenosine Concentrations Using Fast-Scan Cyclic Voltammetry. *Anal. Chem.* **2007**, *79* (2), 744–750.

(62) Dryhurst, G.; Elving, P. J. Electrochemical Oxidation of Adenine: Reaction Products and Mechanisms. *J. Electrochem. Soc.* **1968**, *115* (10), 1014.

(63) Xu, Y.; Venton, B. J. Rapid Determination of Adenosine Deaminase Kinetics Using Fast-Scan Cyclic Voltammetry. *Phys. Chem. Chem. Phys.* **2010**, *12* (34), 10027–10032.

(64) Goyal, R. N.; Sangal, A. Electrochemical Investigations of Adenosine at Solid Electrodes. *J. Electroanal. Chem.* **2002**, *521* (1–2), 72–80.

(65) Borman, R. P.; Wang, Y.; Nguyen, M. D.; Ganesana, M.; Lee, S. T.; Venton, B. J. Automated Algorithm for Detection of Transient Adenosine Release. *ACS Chem. Neurosci.* **2017**, *8* (2), 386–393.

(66) Heien, M. L. A. V.; Johnson, M. A.; Wightman, R. M. Resolving Neurotransmitters Detected by Fast-Scan Cyclic Voltammetry. *Anal. Chem.* **2004**, *76* (19), 5697–5704.

(67) Hermans, A.; Keithley, R. B.; Kita, J. M.; Sombers, L. A.; Wightman, R. M. Dopamine Detection with Fast-Scan Cyclic Voltammetry Used with Analog Background Subtraction. *Anal. Chem.* **2008**, *80* (11), 4040–4048.

(68) Johnson, J. A.; Rodeberg, N. T.; Wightman, R. M. Failure of Standard Training Sets in the Analysis of Fast-Scan Cyclic Voltammetry Data. *ACS Chem. Neurosci.* **2016**, *7* (3), 349–359.

(69) McCreery, R. L. Advanced Carbon Electrode Materials for Molecular Electrochemistry. *Chem. Rev.* **2008**, *108* (7), 2646–2687.

(70) Banks, C. E.; Compton, R. G. New Electrodes for Old: From Carbon Nanotubes to Edge Plane Pyrolytic Graphite. *Analyst* **2006**, *131* (1), 15–21.

(71) Banks, C. E.; Moore, R. R.; Davies, T. J.; Compton, R. G. Investigation of Modified Basal Plane Pyrolytic Graphite Electrodes: Definitive Evidence for the Electrocatalytic Properties of the Ends of Carbon Nanotubes. *Chem. Commun.* **2004**, *16*, 1804–1805.

(72) Yuan, W.; Zhou, Y.; Li, Y.; Li, C.; Peng, H.; Zhang, J.; Liu, Z.; Dai, L.; Shi, G. The Edge- and Basal-Plane-Specific Electrochemistry of a Single-Layer Graphene Sheet. *Sci. Rep.* **2013**, *3* (Cvd), 2248.

(73) Strand, A. M.; Venton, B. J. Flame Etching Enhances the Sensitivity of Carbon-Fiber Microelectrodes. *Anal. Chem.* **2008**, *80* (10), 3708–3715.

(74) Peltola, E.; Sainio, S.; Holt, K. B.; Palomäki, T.; Koskinen, J.; Laurila, T. Electrochemical Fouling of Dopamine and Recovery of Carbon Electrodes. *Anal. Chem.* **2018**, *90*, 1408–1416.

(75) Schuweiler, D. R.; Howard, C. D.; Ramsson, E. S.; Garris, P. A. Improving in Situ Electrode Calibration with Principal Component Regression for Fast-Scan Cyclic Voltammetry. *Anal. Chem.* **2018**, *90*, 13434–13442.

(76) Georgakilas, V.; Perman, J. A.; Tucek, J.; Zboril, R. Broad Family of Carbon Nanoallotropes: Classification, Chemistry, and Applications of Fullerenes, Carbon Dots, Nanotubes, Graphene, Nanodiamonds, and Combined Superstructures. *Chem. Rev.* **2015**, *115* (11), 4744–4822.

(77) Novoselov, K. S.; Geim, A. K.; Morozov, S. V; Jiang, D.; Zhang, Y.; Dubonos, S. V.; Grigorieva, I. V; Firsov, A. A. Electric Field Effect in Atomically Thin Carbon Films. *Science* **2004**, *306* (5696), 666–669.

(78) Zhu, M.; Zeng, C.; Ye, J. Graphene-Modified Carbon Fiber Microelectrode for the Detection of Dopamine in Mice Hippocampus Tissue. *Electroanalysis* **2011**, *23* (4), 907–914.

(79) Hong, Q.; Yang, L.; Ge, L.; Liu, Z.; Li, F. Direct-Laser-Writing of Three-Dimensional Porous Graphene Frameworks on Indium-Tin Oxide for Sensitive Electrochemical Biosensing. *Analyst* **2018**, *143* (14), 3327–3334.

(80) Manzanares Palenzuela, C. L.; Novotný, F.; Krupička, P.; Sofer, Z.; Pumera, M. 3D-Printed Graphene/Polylactic Acid Electrodes Promise High Sensitivity in Electroanalysis. *Anal. Chem.* **2018**, *90* (9), 5753–5757.

(81) Wu, Y.; Zhu, J.; Huang, L. A Review of Three-Dimensional Graphene-Based Materials: Synthesis and Applications to Energy Conversion/Storage and Environment. *Carbon* **2019**, *143*, 610–640.

(82) Taylor, I. M.; Robbins, E. M.; Catt, K. A.; Cody, P. A.; Happe, C. L.; Cui, X. T. Enhanced Dopamine Detection Sensitivity by PEDOT/Graphene Oxide Coating on in Vivo Carbon Fiber Electrodes. *Biosens. Bioelectron.* **2017**, *89*, 400–410.

(83) Iijima, S. Helical Microtubules of Graphitic Carbon. *Nature* **1991**, *354*, 56–58.

(84) Yang, C.; Jacobs, C. B.; Nguyen, M. D.; Ganesana, M.; Zestos, A. G.; Ivanov, I. N.; Puretzky, A. A.; Rouleau, C. M.; Geohegan, D. B.; Venton, B. J. Carbon Nanotubes Grown on Metal Microelectrodes for the Detection of Dopamine. *Anal. Chem.* **2016**, *88*, 645–652.

(85) Xiang, L.; Yu, P.; Hao, J.; Zhang, M.; Zhu, L.; Dai, L.; Mao, L. Vertically Aligned Carbon Nanotube-Sheathed Carbon Fibers as Pristine Microelectrodes for Selective Monitoring of Ascorbate in Vivo. *Anal. Chem.* **2014**, *86* (8), 3909–3914.

(86) Zestos, A. G.; Yang, C.; Jacobs, C. B.; Hensley, D.; Venton, B. J. Carbon Nanospikes Grown on Metal Wires as Microelectrode Sensors for Dopamine. *Analyst* **2015**, *140*, 7283–7292.

(87) Cao, Q.; Hensley, D. K.; Lavrik, N. V; Venton, B. J. Carbon Nanospikes Have Better Electrochemical Properties than Carbon Nanotubes Due to Greater Surface Roughness and Defect Sites. *Carbon* **2019**, *155*, 250–257.

(88) Azami, T.; Kasuya, D.; Yoshitake, T.; Kubo, Y.; Yudasaka, M.; Ichihashi, T.; Iijima, S.

Production of Small Single-Wall Carbon Nanohorns by CO2 Laser Ablation of Graphite in Ne-Gas Atmosphere. *Carbon* **2007**, *45* (6), 1364–1367.

(89) Berber, S.; Kwon, Y.-K.; Tománek, D. Electronic and Structural Properties of Carbon Nanohorns. *Phys. Rev. B* **2000**, *62* (4), R2291–R2294.

(90) Karousis, N.; Suarez-Martinez, I.; Ewels, C. P.; Tagmatarchis, N. Structure, Properties, Functionalization, and Applications of Carbon Nanohorns. *Chem. Rev.* **2016**, *116* (8), 4850–4883.

(91) Yang, C. M.; Noguchi, H.; Murata, K.; Yudasaka, M.; Hashimoto, A.; Iijima, S.; Kaneko, K. Highly Ultramicroporous Single-Walled Carbon Nanohorn Assemblies. *Adv. Mater.* **2005**, *17*, 866–870.

(92) Yan, Q. L.; Gozin, M.; Zhao, F. Q.; Cohen, A.; Pang, S. P. Highly Energetic Compositions Based on Functionalized Carbon Nanomaterials. *Nanoscale* **2016**, *8* (9), 4799–4851.

(93) Siddiqui, S.; Dutta, G.; Tan, C.; Arumugam, P. U. Nanocrystalline Diamond Electrodes: Enabling Electrochemical Microsensing Applications with High Reliability and Stability. *IEEE Nanotechnol. Mag.* **2016**, *10* (3), 12–20.

(94) Laurila, T.; Rautiainen, A.; Sintonen, S.; Jiang, H.; Kaivosoja, E.; Koskinen, J. Diamond-like Carbon (DLC) Thin Film Bioelectrodes: Effect of Thermal Post-Treatments and the Use of Ti Adhesion Layer. *Mater. Sci. Eng., C* **2014**, *34* (1), 446–454.

(95) Laurila, T.; Protopopova, V.; Rhode, S.; Sainio, S.; Palomäki, T.; Moram, M.; Feliu, J. M.; Koskinen, J. New Electrochemically Improved Tetrahedral Amorphous Carbon Films for Biological Applications. *Diam. Relat. Mater.* **2014**, *49*, 62–71.

(96) Fang, J.; Xie, Z.; Wallace, G.; Wang, X. Co-Deposition of Carbon Dots and Reduced Graphene Oxide Nanosheets on Carbon-Fiber Microelectrode Surface for Selective Detection of Dopamine. *Appl. Surf. Sci.* **2017**, *412*, 131–137.

(97) Devi, N. R.; Kumar, T. H. V.; Sundramoorthy, A. K. Electrochemically Exfoliated Carbon Quantum Dots Modified Electrodes for Detection of Dopamine Neurotransmitter. *J. Electrochem. Soc.* **2018**, *165* (12), G3112–G3119.

(98) Yang, N.; Foord, J. S.; Jiang, X. Diamond Electrochemistry at the Nanoscale: A Review. *Carbon* **2016**, *99*, 90–110.

(99) Holt, K. B. Undoped Diamond Nanoparticles: Origins of Surface Redox Chemistry. *Phys. Chem. Chem. Phys.* **2010**, *12*, 2048.

(100) Patel, B. A.; Bian, X.; Quaiserová-Mocko, V.; Galligan, J. J.; Swain, G. M. In Vitro Continuous Amperometric Monitoring of 5-Hydroxytryptamine Release from Enterochromaffin Cells of the Guinea Pig Ileum. *Analyst* **2007**, *132* (1), 41–47.

(101) Patel, A. N.; Unwin, P. R.; MacPherson, J. V. Investigation of Film Formation Properties during Electrochemical Oxidation of Serotonin (5-HT) at Polycrystalline Boron Doped Diamond. *Phys. Chem. Chem. Phys.* **2013**, *15* (41), 18085–18092.

(102) Park, J.; Quaiserová-Mocko, V.; Pecková, K.; Galligan, J. J.; Fink, G. D.; Swain, G. M. Fabrication, Characterization, and Application of a Diamond Microelectrode for Electrochemical Measurement of Norepinephrine Release from the Sympathetic Nervous System. *Diam. Relat. Mater.* **2006**, *15* (4–8), 761–772.

(103) Chang, A. Y.; Dutta, G.; Siddiqui, S.; Arumugam, P. U. Surface Fouling of Ultrananocrystalline Diamond Microelectrodes during Dopamine Detection: Improving Lifetime via Electrochemical Cycling. *ACS Chem. Neurosci.* **2018**, *10*, 313–322.

(104) Mochalin, V. N.; Shenderova, O.; Ho, D.; Gogotsi, Y. The Properties and Applications of Nanodiamonds. *Nat. Nanotechnol.* **2011**, *7* (1), 11–23.

(105) Holt, K. B.; Ziegler, C.; Caruana, D. J.; Zang, J.; Millán-Barrios, E. J.; Hu, J.; Foord, J. S. Redox Properties of Undoped 5 Nm Diamond Nanoparticles. *Phys. Chem. Chem. Phys.* **2008**, *10* (2), 303–310.

(106) Hian, L. C.; Grehan, K. J.; Compton, R. G.; Foord, J. S.; Marken, F. Influence of Thin Film Properties on the Electrochemical Performance of Diamond Electrodes. *Diam. Relat. Mater.* **2003**, *12* (3–7), 590–595.

(107) Peltola, E.; Wester, N.; Holt, K. B.; Johansson, L. S.; Koskinen, J.; Myllymäki, V.; Laurila, T. Nanodiamonds on Tetrahedral Amorphous Carbon Significantly Enhance Dopamine Detection and Cell Viability. *Biosens. Bioelectron.* **2017**, *88*, 273–282.

(108) Wang, Y.; Li, Y.; Tang, L.; Lu, J.; Li, J. Application of Graphene-Modified Electrode for Selective Detection of Dopamine. *Electrochem. Commun.* **2009**, *11* (4), 889–892.

(109) Hočevar, S. B.; Wang, J.; Deo, R. P.; Musameh, M.; Ogorevc, B. Carbon Nanotube Modified Microelectrode for Enhanced Voltammetric Detection of Dopamine in the Presence of Ascorbate. *Electroanalysis* **2005**, *17* (5–6), 417–422.

(110) Ross, A. E.; Venton, B. J. Nafion-CNT Coated Carbon-Fiber Microelectrodes for Enhanced Detection of Adenosine. *Analyst* **2012**, *137* (13), 3045–3051.

(111) Chen, L.; Tang, Y.; Wang, K.; Liu, C.; Luo, S. Direct Electrodeposition of Reduced Graphene Oxide on Glassy Carbon Electrode and Its Electrochemical Application. *Electrochem. Commun.* **2011**, *13*, 133–137.

(112) Zhang, Y.; Ji, Y.; Wang, Z.; Liu, S.; Zhang, T. Electrodeposition Synthesis of Reduced Graphene Oxide-Carbon Nanotube Hybrids on Indium Tin Oxide Electrode for Simultaneous Electrochemical Detection of Ascorbic Acid, Dopamine and Uric Acid. *RSC Adv.* **2015**, *5*, 106307–106314.

(113) Xiao, T.; Jiang, Y.; Ji, W.; Mao, L. Controllable and Reproducible Sheath of Carbon Fibers with Single-Walled Carbon Nanotubes through Electrophoretic Deposition for in Vivo Electrochemical Measurements. *Anal. Chem.* **2018**, *90* (7), 4840–4846.

(114) Liu, G. T.; Chen, H. F.; Lin, G. M.; Ye, P. ping; Wang, X. P.; Jiao, Y. Z.; Guo, X. Y.; Wen, Y.; Yang, H. F. One-Step Electrodeposition of Graphene Loaded Nickel Oxides Nanoparticles for Acetaminophen Detection. *Biosens. Bioelectron.* **2014**, *56*, 26–32.

(115) Desai, C.; Chen, K.; Mitra, S. Aggregation Behavior of Nanodiamonds and Their Functionalized Analogs in an Aqueous Environment. *Environ. Sci. Process. Impacts* **2014**, *16* (3), 518–523.

(116) Li, W.; Tan, C.; Lowe, M. A.; Abruña, H. D.; Ralph, D. C. Electrochemistry of Individual Monolayer Graphene Sheets. *ACS Nano* **2011**, *5* (3), 2264–2270.

(117) Wu, T.; Alharbi, A.; Kiani, R.; Shahrjerdi, D. Quantitative Principles for Precise Engineering of Sensitivity in Graphene Electrochemical Sensors. *Adv. Mater.* **2018**, *1805752*, 1–12.

(118) Palomäki, T.; Chumillas, S.; Sainio, S.; Protopopova, V.; Kauppila, M.; Koskinen, J.; Climent, V.; Feliu, J. M.; Laurila, T. Electrochemical Reactions of Catechol, Methylcatechol and Dopamine at Tetrahedral Amorphous Carbon (Ta-C) Thin Film Electrodes. *Diam. Relat. Mater.* **2015**, *59*, 30–39.

(119) Schrand, A. M.; Dai, L.; Schlager, J. J.; Hussain, S. M.; Osawa, E. Differential Biocompatibility of Carbon Nanotubes and Nanodiamonds. *Diam. Relat. Mater.* **2007**, *16* (12), 2118–2123.

(120) Jiang, K.; Li, Q.; Fan, S. Spinning Continuous Carbon Nanotube Yarns. *Nature* **2002**, *49* (1999), 5246–5252.

(121) Li, W.; Jayasinghe, C.; Shanov, V.; Schulz, M. Spinning Carbon Nanotube Nanothread

under a Scanning Electron Microscope. *Materials (Basel).* **2011**, *4* (9), 1519–1527.

(122) Schmidt, A. C.; Wang, X.; Zhu, Y.; Sombers, L. A. Carbon Nanotube Yarn Electrodes for Enhanced Detection of Neurotransmitter Dynamics in Live Brain Tissue. *ACS Nano* **2013**, *7* (9), 7864–7873.

(123) Jacobs, C. B.; Ivanov, I. N.; Nguyen, M. D.; Zestos, A. G.; Venton, B. J. High Temporal Resolution Measurements of Dopamine with Carbon Nanotube Yarn Microelectrodes. *Anal. Chem.* **2014**, *86* (12), 5721–5727.

(124) Yang, C.; Trikantzopoulos, E.; Nguyen, M. D.; Jacobs, C. B.; Wang, Y.; Mahjouri-Samani, M.; Ivanov, I. N.; Venton, B. J. Laser Treated Carbon Nanotube Yarn Microelectrodes for Rapid and Sensitive Detection of Dopamine in Vivo. *ACS Sens.* **2016**, *1* (5), 508–515.

(125) Zestos, A. G.; Jacobs, C. B.; Trikantzopoulos, E.; Ross, A. E.; Venton, B. J. Polyethylenimine Carbon Nanotube Fiber Electrodes for Enhanced Detection of Neurotransmitters. *Anal. Chem.* **2014**, *86* (17), 8568–8575.

(126) Zestos, A. G.; Venton, B. J. Communication—Carbon Nanotube Fiber Microelectrodes for High Temporal Measurements of Dopamine. *J. Electrochem. Soc.* **2018**, *165* (12), G3071–G3073.

(127) Promphet, N.; Rattanarat, P.; Rangkupan, R.; Chailapakul, O.; Rodthongkum, N. An Electrochemical Sensor Based on Graphene/Polyaniline/Polystyrene Nanoporous Fibers Modified Electrode for Simultaneous Determination of Lead and Cadmium. *Sens. Actuators, B* **2015**, *207* (PartA), 526–534.

(128) Yang, C.; Wang, Y.; Jacobs, C. B.; Ivanov, I.; Venton, B. J. O2 Plasma Etching and Anti-Static Gun Surface Modifications for CNT Yarn Microelectrode Improve Sensitivity and Anti-Fouling Properties. *Anal. Chem.* **2017**, 5605–5611.

(129) Kaplan, A.; Yuan, Z.; Benck, J. D.; Govind Rajan, A.; Chu, X. S.; Wang, Q. H.; Strano, M. S. Current and Future Directions in Electron Transfer Chemistry of Graphene. *Chem. Soc. Rev.* **2017**, *46* (15), 4530–4571.

(130) Brereton, R. G. *Chemometrics for Pattern Recognition*; John Wiley and Sons: West Sussex, 2010.

(131) Bucher, E. S.; Brooks, K.; Verber, M. D.; Keithley, R. B.; Owesson-White, C.; Carroll, S.; Takmakov, P.; McKinney, C. J.; Wightman, R. M. Flexible Software Platform for Fast-Scan Cyclic Voltammetry Data Acquisition and Analysis. *Anal. Chem.* **2013**, *85* (21), 10344–10353.

(132) Atcherley, C. W.; Vreeland, R. F.; Monroe, E. B.; Sanchez-Gomez, E.; Heien, M. L. A. V. Rethinking Data Collection and Signal Processing. 2. Preserving the Temporal Fidelity of Electrochemical Measurements. *Anal. Chem.* **2013**, *85* (16), 7654–7658.

(133) Savitzky, A.; Golay, M. J. E. Smoothing and Differentiation of Data by Simplified Least Squares Procedures. *Anal. Chem.* **1964**, *36* (8), 1627–1639.

(134) Keithley, R. B.; Heien, M. L. A. V.; Wightman, R. M. Multivariate Concentration Determination Using Principal Component Regression with Residual Analysis. *TrAC, Trends Anal. Chem.* **2009**, *28* (9), 1127–1136.

(135) Johnson, J. A.; Hobbs, C. N.; Wightman, R. M. Removal of Differential Capacitive Interferences in Fast-Scan Cyclic Voltammetry. *Anal. Chem.* **2017**, *89* (11), 6166–6174.

(136) Meunier, C. J.; Mitchell, E. C.; Roberts, J. G.; Toups, J. V.; McCarty, G. S.; Sombers, L. A. Electrochemical Selectivity Achieved Using a Double Voltammetric Waveform and Partial Least Squares Regression: Differentiating Endogenous Hydrogen Peroxide Fluctuations from Shifts in PH. *Anal. Chem.* **2018**, *90* (3), 1767–1776.

(137) Nguyen, M. D.; Lee, S. T.; Ross, A. E.; Ryals, M.; Choudhry, V. I.; Venton, B. J. Characterization of Spontaneous, Transient Adenosine Release in the Caudate-Putamen and Prefrontal Cortex. *PLoS One* **2014**, *9* (1), e87165.

(138) Wang, Z.; Bovik, A. C.; Sheikh, H. R.; Simoncelli, E. P. Image Quality Assessment: From Error Visibility to Structural Similarity. *IEEE Trans. Image Process.* **2004**, *13* (4), 600–612.

(139) Haas, H. L.; Sergeeva, O. A.; Selbach, O. Histamine in the Nervous System. *Physiol. Rev.* **2008**, *88*, 1183–1241.

(140) Samaranayake, S.; Abdalla, A.; Robke, R.; Wood, K. M.; Zeqja, A.; Hashemi, P. In Vivo Histamine Voltammetry in the Mouse Premammillary Nucleus. *Analyst* **2015**, *140* (11), 3759–3765.

(141) Mochalin, V. N.; Shenderova, O.; Ho, D.; Gogotsi, Y. The Properties and Applications of Nanodiamonds. *Nat. Nanotechnol.* **2012**, *7*, 11–23.

CHAPTER 2

Mechanism of Histamine Oxidation and Electropolymerization at Carbon Electrodes

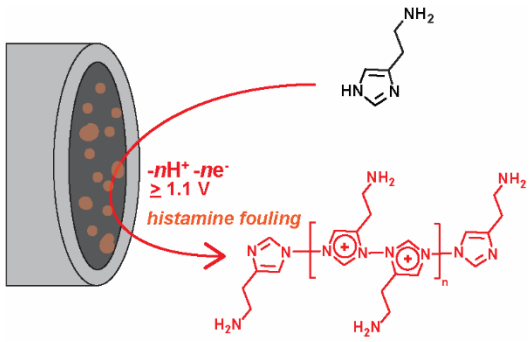

Chapter 2 was reprinted from *Anal. Chem.* **2019,** *91,* 8366-8373.

Abstract

Histamine plays an important role in neuromodulation and the biological immune response. Although many electrochemical methods have been developed for histamine detection, the mechanism of its redox reaction has not been directly investigated. Here, we studied the mechanism of histamine oxidation at carbon electrodes and used that mechanistic information to design better fast-scan cyclic voltammetry (FSCV) methods for histamine. Using amperometry, cyclic voltammetry (CV), and X-ray photoelectron spectroscopy (XPS), we demonstrate that histamine oxidation requires a potential of at least +1.1 V vs Ag/AgCl. We propose that histamine undergoes one-electron oxidation on an imidazole nitrogen that produces a radical. The radical species dimerize and continue to undergo oxidation, leading to electropolymerization, which fouls the electrode. CV shows a peak at 1.3 V that is pH dependent, consistent with a one-proton, one-electron oxidation reaction. This mechanism is confirmed using 1- and 3-methylhistamine, which do not electropolymerize, compared to N^{α}-methylhistamine, which does. XPS also revealed a nitrogen-containing product adsorbed on the electrode surface after histamine oxidation. For FSCV detection of histamine at carbon-fiber microelectrodes, histamine oxidation was adsorption-controlled, and the anodic peak was observed at +1.2 V on the backward scan because of the rapid scan rate. However, the oxidation fouled the electrode and convoluted the FSCV temporal response; therefore, we implemented Nafion coating to alleviate the electrode fouling and preserve the time response of FSCV. Knowing the mechanism of histamine oxidation will facilitate design of better electrochemical methods for real-time monitoring of histamine.

2.1 Introduction

Histamine is known for its role in immune responses as an inflammatory agent causing allergic reactions.[1,2] It also functions as a neurotransmitter and neuromodulator, regulating the sleep cycle.[1] Many methods have been developed for histamine analysis, including microdialysis coupled to liquid chromatography (LC) with fluorescence detection, which measures histamine over long time frames.[3] For single cell content analysis, capillary LC with amperometric detection was used to detect histamine content in single mast cells.[2] Histamine was quantified in the ventral nerve cord of fruit flies using capillary electrophoresis with fast-scan cyclic voltammetry (FSCV) detection.[4] FSCV is also used to measure real-time release of histamine. Wightman's group used FSCV to demonstrate that histamine and serotonin are coreleased from vesicles in mast cells,[5,6] and FSCV was also used *in vivo* to study histamine and serotonin corelease in the brain.[7] Despite the fact that there are many papers using electrochemistry to detect histamine, there is no literature proposing a mechanism of histamine oxidation. Understanding the mechanism of oxidation is important to help design electrochemical methods to detect histamine and interpret electrochemical data.

While the redox mechanism of histamine oxidation has not been thoroughly investigated, there is one study on the oxidation of imidazole in organic solvents. Histamine (2-(1*H*-imidazol-4-yl)ethanamine) is an imidazole derivative, so its mechanism of oxidation might be similar. Imidazole oxidation occurred at 1.5 V vs Ag/Ag^+, and the mechanism was the generation of a radical cation on a ring nitrogen, which subsequently dimerized and underwent electropolymerization.[8] Similarly, most studies that have detected histamine in aqueous solution at carbon electrodes have reported high oxidation potentials. The histamine anodic peak is at 1.2 V vs saturated calomel electrode (SCE)

at glassy carbon electrodes (GCE), 1.4 V vs SCE at boron-doped diamond electrodes, and 1.1 V vs SCE at carbon-fiber microelectrodes (CFME).[2,9] These high oxidation potentials are almost out of the potential window for carbon electrodes and make histamine difficult to study in aqueous solutions. The FSCV community has developed several waveforms to monitor histamine dynamics *in vivo*. The Wightman group used a +0.1 V holding potential and +1.4 V switching potential with an 800 V/s scan rate and found a strong histamine primary anodic peak around +1.3 V vs SCE and broad secondary anodic peak at +0.9 V vs SCE.[2] Because of the fast scan rate, the time required for the histamine electron transfer process cannot catch up with the potential ramping,[10] and the primary peak is located on the backward scan. The Lee group used a waveform from –0.4 to +1.4 V vs Ag/AgCl at a scan rate of 400 V/s, and both primary and secondary anodic peaks were at the same positions as those in Wightman's work.[11] However, the Hashemi lab recently developed an FSCV waveform that only scans to 1.1 V, and they claim the histamine faradaic peak is at 0.3 V vs Ag/AgCl and that previous reports of peaks at 1.3 V vs Ag/AgCl correspond to histamine adsorption.[12] Therefore, there is controversy in the FSCV field over the potential of histamine oxidation, which needs more mechanistic insight.

In this work, we use amperometry, cyclic voltammetry (CV), X-ray photoelectron spectroscopy (XPS), and FSCV to propose a mechanism of histamine oxidation and electropolymerization at carbon electrodes. Using amperometry, we show that histamine is not oxidized until 1.1 V. CV with a 50 mV/s scan rate shows a peak at 1.3 V that is pH dependent, consistent with a one-proton, one-electron oxidation reaction. CV of histamine derivatives with methyl groups on the nitrogens confirm that histamine electropolymerizes after oxidation, forming dimers with the nitrogens on the imidazole rings, and this causes

electrode fouling. XPS reveals a large increase in surface nitrogen content after histamine oxidation, consistent with electropolymerization of histamine that fouls the surface. With FSCV, potentials over 1.1 V are necessary to observe faradaic oxidation of histamine, but fouling is observed, particularly with a 1.45 V switching potential. However, Nafion coating alleviates fouling and provides better current vs time traces for histamine detection.[13] This improved understanding of the mechanism of histamine oxidation, and particularly its electropolymerization, will help in future development of electrochemical methods to detect histamine in biological systems.

2.2 Experimental Section

2.2.1 Chemicals

Histamine dihydrochloride, 1-methylhistamine dihydrochloride, 3-methylhistamine dihydrochloride, and N^{α}-methylhistamine dihydrochloride were purchased from Millipore Sigma (Burlington, MA). A stock solution of each chemical was prepared in 0.1 M $HClO_4$. Final working solutions were prepared by diluting the stock solution in a phosphate buffered saline (PBS) (131.25 mM NaCl, 3.00 mM KCl, 10 mM NaH_2PO_4, 1.2 mM $MgCl_2$, 2.0 mM Na_2SO_4, and 1.2 mM $CaCl_2$ with pH adjusted to 7.4) or 0.1 M phosphate buffer to the desired concentration. In some cases, high-concentration solutions were prepared by directly dissolving the chemicals in the buffer and adjusting the pH and volume of the solution appropriately.

2.2.2 Microelectrode Preparation

A cylindrical CFME was prepared as described elsewhere.[14] Briefly, a 7 µm diameter T-650 carbon fiber (Cytec Engineering Materials, West Patterson, NJ) was pulled

into a 1.28 mm inner diameter × 0.68 mm outer diameter glass capillary (A-M Systems, Sequim, WA) by an aspirating pump. The capillary was then pulled by a vertical puller (Narishige, Tokyo, Japan) to get two electrodes. The fiber was cut to a length of 100 µm. The electrode was epoxied by dipping in a solution of 14% *m*-phenylenediamine hardener (Acros Organics, Morris Plains, NH) in Epon Resin 828 (Miller-Stephenson, Danbury, CT) at 80^{o}C for 30 s to seal the fiber with the glass capillary. The electrode was then left at room temperature overnight, cured at 100^{o}C for 2 h, and 150^{o}C for overnight.

Nafion-modified CFMEs (Nafion/CFMEs) were prepared by applying a pulsed chronoamperometry waveform between 0.0 V for 1 s and 1.0 V for 1 s for 60 cycles in a 5% Nafion in methanol solution (LQ-1105-MeOH, Ion Power, New Castle, DE) to CFME working electrode vs Ag/AgCl reference electrode and Pt counter electrode. The modified electrode was baked at 70^{o}C for 10 min and left at room temperature overnight before use.

2.2.3 Electrochemical Instrumentation

Amperometry and CV measurements were taken on a potentiostat (Gamry Instruments, Warminster, PA) using a 3-mm diameter glassy carbon working electrode (GCE), Ag/AgCl reference electrode, and Pt counter electrode (CH Instruments, Austin, TX). GCE was polished with 1.0 µm and then 0.3 µm alumina polishing powder before use. Amperometry was performed by applying a constant potential in a stirred solution. CV measurements were performed in a stagnant solution with a scan rate of 50 mV/s if not specified.

FSCV experiments were performed using a two-electrode system, including CFME or Nafion/CFME working electrode backfilled with 1 M KCl and a Ag/AgCl reference

electrode. All electrodes were connected to a ChemClamp potentiostat and headstage (Dagan, Minneapolis, MN). The FSCV waveform, unless stated otherwise, was applied to a CFME with a holding potential of –0.4 V, a switching potential of +1.3 or +1.45 V, a scan rate of 400 V/s, and a repetition rate of 10 Hz. The buffer and test solutions were flowed by the electrode in a flow cell at a 2 mL/min by a syringe pump (Harvard Apparatus, Holliston, MA). The flow-injection system consists of a six-port loop injector with an air actuator (VIVI Valco Instruments, Houston, TX). The data were collected with HDCV Analysis software (Department of Chemistry, University of North Carolina at Chapel Hill).

2.2.4 XPS

Characterization of histamine oxidation product was performed by applying a repeated CV waveform to a screen-printed carbon electrode (SPCE) (Pine Instrument, Grove City, PA) in a histamine solution. SPCEs were characterized by using an X-ray photoelectron spectrometer (Physical Electronics, Chanhassen, MN) at the UVa Nanoscale Materials Characterization Facility to obtain elemental composition and electronic states information. The Al Kα monochromatic X-ray source (1486.6 eV) was used with a pass energy of 224 eV for elemental composition and 55 eV for electronic state information. The XPS spectra were analyzed with MultiPak software which came with the instrument. All spectra were corrected for the charging effect by shifting the C 1s peak to the binding energy of 284.8 eV.

2.2.5 Statistics

All values in this work are the mean ± standard deviation (SD) for *n* number of measurements, except for the XPS experiment from which the average values from two

electrodes are reported. Statistics were performed in GraphPad Prism 7.0 (GraphPad Software, La Jolla, CA), and significance was defined at $p < 0.05$.

2.3 Results and Discussion

2.3.1 Amperometry of Histamine

To determine the required potential for histamine oxidation at carbon electrodes, amperometry was performed at a GCE. GCE has a similar graphitic structure[15] to a CFME but has a larger surface area, which makes the measurements easier. Three different applied potentials are plotted: 0.9 V (Fig. 2.1A), 1.1 V (Fig. 2.1B), and 1.3 V (Fig. 2.1C). For each experiment, in a stirred solution, PBS was injected twice and then histamine was injected to raise the concentration 50 μM twice. PBS injections did not change the measured current at any potential. For histamine injections, the current did not increase at the applied potential of 0.9 V; thus, histamine cannot be oxidized at a potential lower than 0.9 V. At 1.1 V, histamine increased the current noticeably above the baseline. However, the second injection increased the current less than the first injection, and the current slowly fell back to the baseline despite histamine being present and constant stirring. The current increase was larger at an applied potential of 1.3 V, but the decrease was also more dramatic and the histamine faradaic current was much higher for the first injection than the second injection.

On the basis of these amperometry experiments, we conclude that histamine oxidation occurs around 1.1 V and is not observed before 0.9 V. We also hypothesize that oxidation of histamine fouls the electrode surface because the signal for histamine decreases, and there is a lower current from the second histamine injection compared to the first injection. Imidazole undergoes an oxidation and then polymerizes,[8] and histamine

could similarly undergo oxidation and polymerize to form the polymer that adheres to the electrode surface. To confirm the mechanism and fouling hypothesis, cyclic voltammetry and electrode surface characterization were performed.

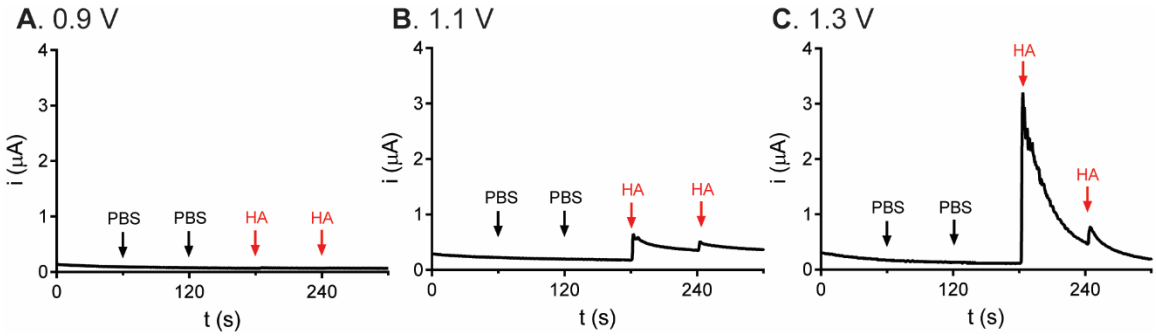

Fig. 2.1 Amperograms of PBS and histamine (HA) at GCE held at different constant potentials vs Ag/AgCl. (A) 0.9, (B) 1.1, and (C) 1.3 V. To a stirred solution of PBS pH 7.4, PBS was injected twice as a control, followed by two injections of 10 mM histamine to raise the concentration by 50 μM in the whole solution. Data were collected by Scott Lee.

2.3.2 CV of Histamine at GCE

To obtain more information about histamine oxidation at carbon electrodes, CV was performed at a GCE with a voltage triangular waveform of –0.5 to +1.5 V at 50 mV/s for 5 cycles (Fig. 2.2A). Histamine oxidation was studied at a high concentration (50 mM) to distinguish its anodic peak at physiological pH (7.4). In the first CV cycle, the histamine anodic current started to rise at 0.96 V vs Ag/AgCl and peaked with a current ($i_{p,a}$) of 87 μA at a peak potential (E_{pa}) of 1.33 V on the forward scan. Cathodic currents were not detected, indicating the reaction is not reversible. The $i_{p,a}$ was higher than background current (21 μA at 1.5 V, Fig. 2.3A). No anodic peak was detected before 1.0 V, consistent with the amperometry data that found no faradaic processes before that potential. In subsequent cycles, the anodic peak dramatically diminished, and CV of the last cycle was

almost identical to the background CV. Hence, the oxidation of histamine in PBS occurs after 1.0 V and is irreversible, and the oxidation product fouls the electrode.

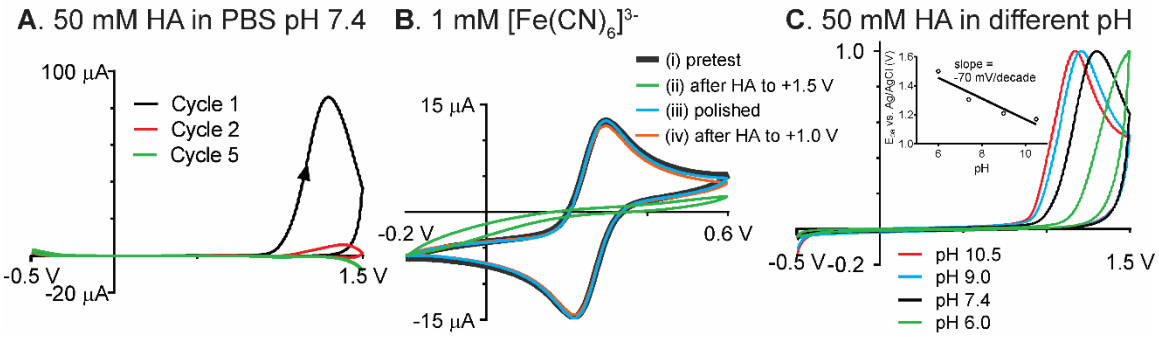

Fig. 2.2 (A) Background-subtracted cyclic voltammogram of 50 mM histamine in PBS pH 7.4 at GCE. Scan rate 50 mV/s. (B) Cyclic voltammogram of 1 mM $[Fe(CN)_6]^{3-}$ in 1 M KCl at GCE performed (i) at a fresh electrode, (ii) after GCE was scanned in 50 mM histamine from -0.5 to +1.5 V, (iii) electrode polished after (ii), and (iv) after electrode scanned in 50 mM histamine from -0.5 to +1.0 V. Scan rate 100 mV/s. Polymerization of histamine at waveform to 1.5 V prevents histamine detection, but electrode can be regenerated by polishing. Scanning to 1.0 V does not produce polymerization or fouling. (C) Cyclic voltammogram of 50 mM histamine in phosphate buffer at different pH. Inset illustrates the pH-dependence of anodic peak potential. Scan rate 50 mV/s.

The existence and fouling of the histamine oxidation product on the GCE was also confirmed by performing CV of 1 mM $[Fe(CN)_6]^{3-}$, a standard inner sphere redox probe, on GCE before and after histamine oxidation (Fig. 2.2B). A fresh GCE gave the quasi-reversible CV with equal anodic and cathodic currents (i) higher than background (Fig. 2.3B). However, after histamine was oxidized, no ferricyanide CV was observed (ii, Fig. 2.2B) because the histamine oxidation product fouled the electrode and prevented ferricyanide redox at the GCE surface. The electrode was polished to renew the surface, and the reversible ferricyanide CV returned with identical anodic and cathodic currents (iii). To prove that histamine was not oxidized at lower potentials, CV was applied between –0.5 and +1.0 V in 50 mM histamine solution, and the ferricyanide CV resembled that of

the freshly polished GCE because histamine was not polymerized (iv). This result supports the previous findings that no faradaic oxidation of histamine occurs in this potential range.

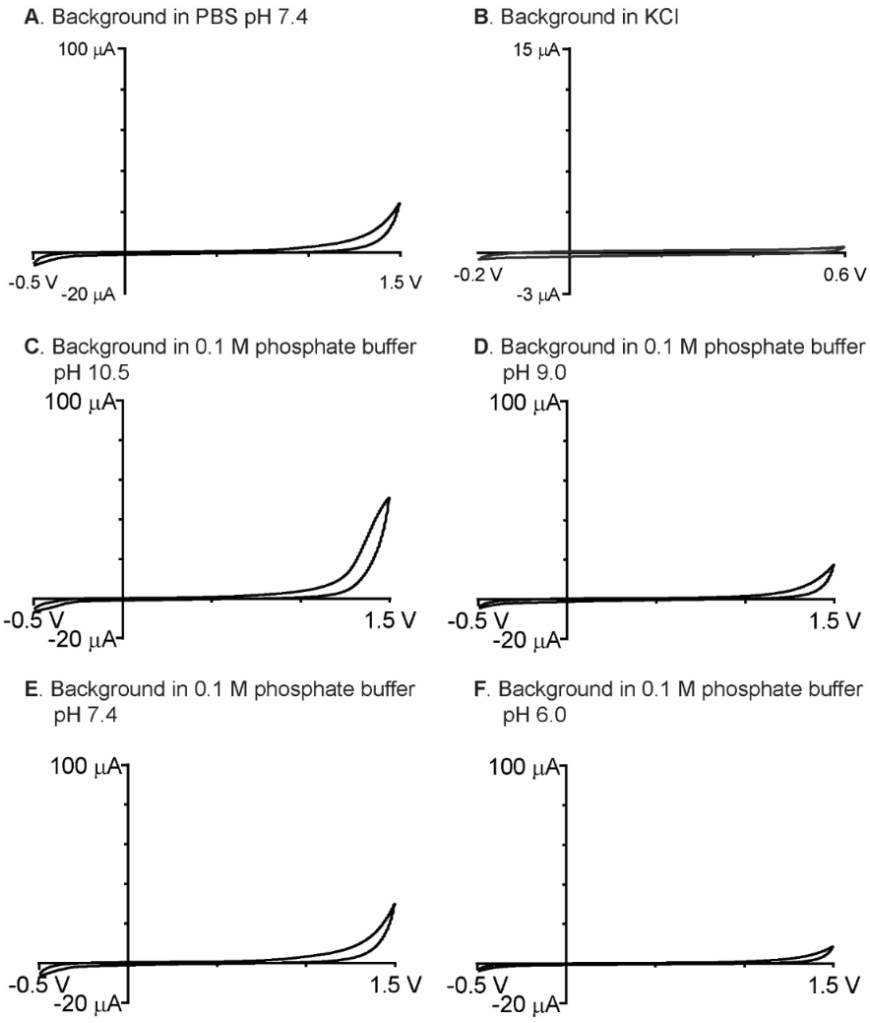

Fig. 2.3 Background CV of GCE in (A) PBS pH 7.4. Scan rate 50 mV/s, (B) 1 M KCl. Scan rate 100 mV/s, (C) 0.1 M phosphate buffer pH 10.5, (D) 0.1 M phosphate buffer pH 9.0, (E) 0.1 M phosphate buffer pH 7.4, and (F) 0.1 M phosphate buffer pH 6.0. Scan rate 50 mV/s.

The effect of pH on histamine oxidation at GCE was also investigated using CV in a 0.1 M phosphate buffer prepared at different pH values (Fig. 2.2C). Lower pH shifted the peaks positively, and the full anodic peak of histamine cannot be observed with

scanning limits of 1.5 V when the pH was lower than 6. The electrode fouling caused by histamine oxidation was also slower at lower pH (Fig. 2.4A-B). In contrast, the histamine peak shifted negatively when the pH increased (Fig. 2.4C). Since pH affected the oxidation of histamine, its oxidation mechanism involves a proton transfer step from the oxidation intermediate. The slope between E_{pa} and pH is –70 ± 17 mV/decade (Fig. 2.2C inset), indicating the ratio of transferred electron to proton to be approximately 1 despite nonideal Nernstian behavior because of its irreversible oxidation. This pH dependence means that for *in vivo* measurements, shifts in pH during biological experiments would also change the histamine oxidation current, but these changes are expected to be small because the brain is well-buffered, and pH shifts are generally only 0.05 units.[16]

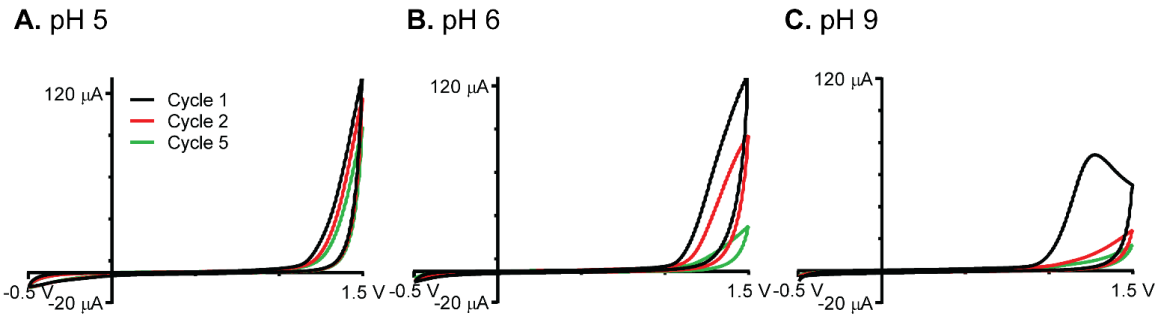

Fig. 2.4 Cyclic voltammogram for 5 cycles of 50 mM histamine in phosphate buffer at (A) pH 5.0, (B) pH 6.0, and (C) pH 9.0. Scan rate 50 mV/s.

From the data, we propose the mechanism of the electrochemical oxidation of histamine (Fig. 2.5) based on the proposed mechanism of imidazole oxidation.[8] Histamine undergoes one-electron oxidation to become a radical cation with a positive charge on an imidazole nitrogen. The radical stabilizes itself by dimerization with another histamine radical, and electron delocalization allows the dimer to lose two imidazole nitrogen protons. The number of protons and electrons is consistent with the pH data because it

is a one-proton and one-electron loss per histamine. Also, the loss of a proton causes the whole reaction to be more difficult at lower pH, as we observed. The proposed mechanism shows a loss of one proton per histamine molecule, so higher pH drives the equilibrium to the product formation. The dimer then goes through electropolymerization, a series of one-electron oxidations and dimerizations to form a "polyhistamine" polymer. This polyhistamine adsorbs on the carbon electrode surface and fouls the electrode.

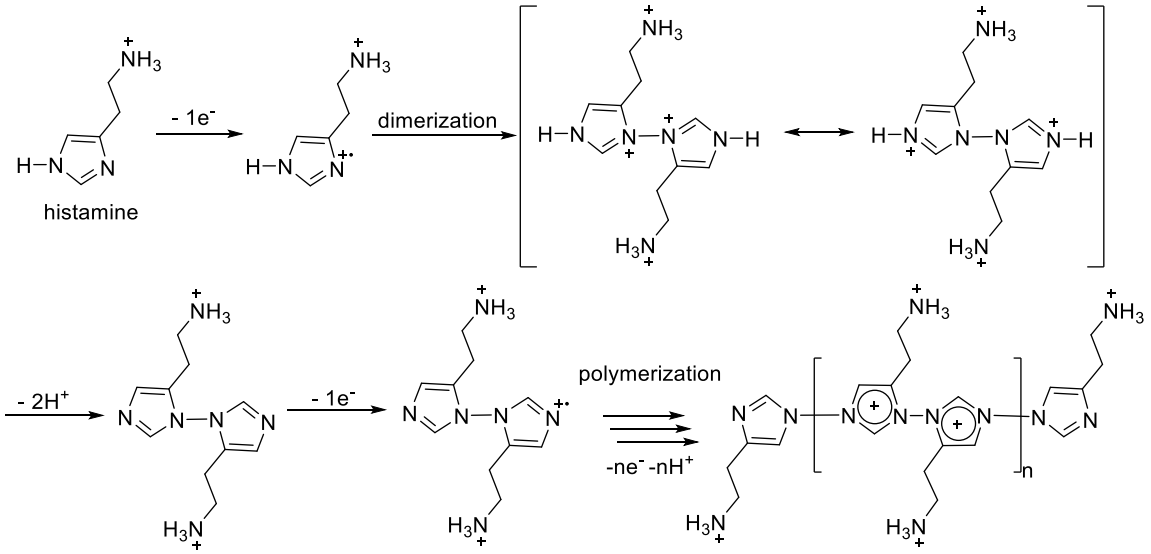

Fig. 2.5 Mechanism of the oxidative electropolymerization of histamine.

2.3.3 CV of Histamine Derivatives at GCE

To further verify the proposed mechanism of histamine electropolymerization, several derivatives of histamine were examined. Because the proposed electropolymerization of histamine needs chain elongation at positions 1 and 3 of the imidazole ring, any functionalization on these positions should inhibit polymerization and electrode fouling. Three derivatives were tested: 1-methylhistamine (1-MeHA), 3-methylhistamine (3-MeHA), and N^{α}-methylhistamine (N^{α}-MeHA). CV was performed by scanning the potential between –0.5 and +1.5 V for 10 cycles to examine electrode fouling.

For 2 mM histamine at pH 7.4, fouling is observed and the CVs from cycle 1 to cycle 10 decrease by about 75 % in current (Fig. 2.6A). Here, a lower concentration was used so the fouling was slower than that for 50 mM histamine in Fig. 2.2A. The anodic peaks in the CVs of 2 mM 1-MeHA (Fig. 2.6B) and 3-MeHA (Fig. 2.6C) have similar features and did not decrease from cycle 1 to 10. Thus, 1-MeHA and 3-MeHA undergo one-electron oxidation and likely form a dimer, but the methyl group on position 1 or 3 prevents polymerization (Fig. 2.7A). The final oxidation product of these two derivatives should be just their dimer, and this dimer did not cause electrode fouling. The anodic peak of both compounds also shifted positively compared to histamine because the dimer product might be unstable or the methyl group causes the oxidation to be more difficult. In contrast, the CV current from N^{α}-MeHA (Fig. 2.6D) progressively declined from cycle 1 to 10, indicating electrode fouling. The amine aliphatic chain is not involved in the reaction; therefore, methyl substitution at that position still allows the oxidative electropolymerization of N^{α}-MeHA to occur, as illustrated in Fig. 2.7B. However, the methyl group on the amine aliphatic chain could cause steric hindrance and may either slow the electropolymerization process or shrink the polymer size, so the current decrease and electrode fouling from N^{α}-MeHA electropolymerization is slower than that of histamine.

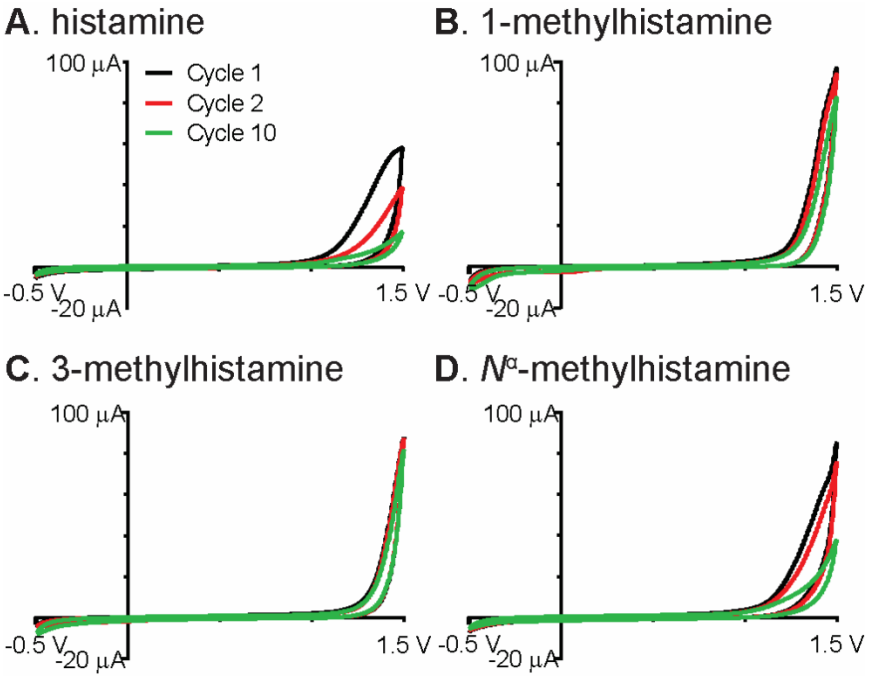

Fig. 2.6 Cyclic voltammogram of 2 mM (A) histamine, (B) 1-MeHA, (C) 3-MeHA, and (D) *N*$^{\alpha}$-MeHA in PBS pH 7.4 at GCE. Scan rate 50 mV/s, repeated for 10 cycles.

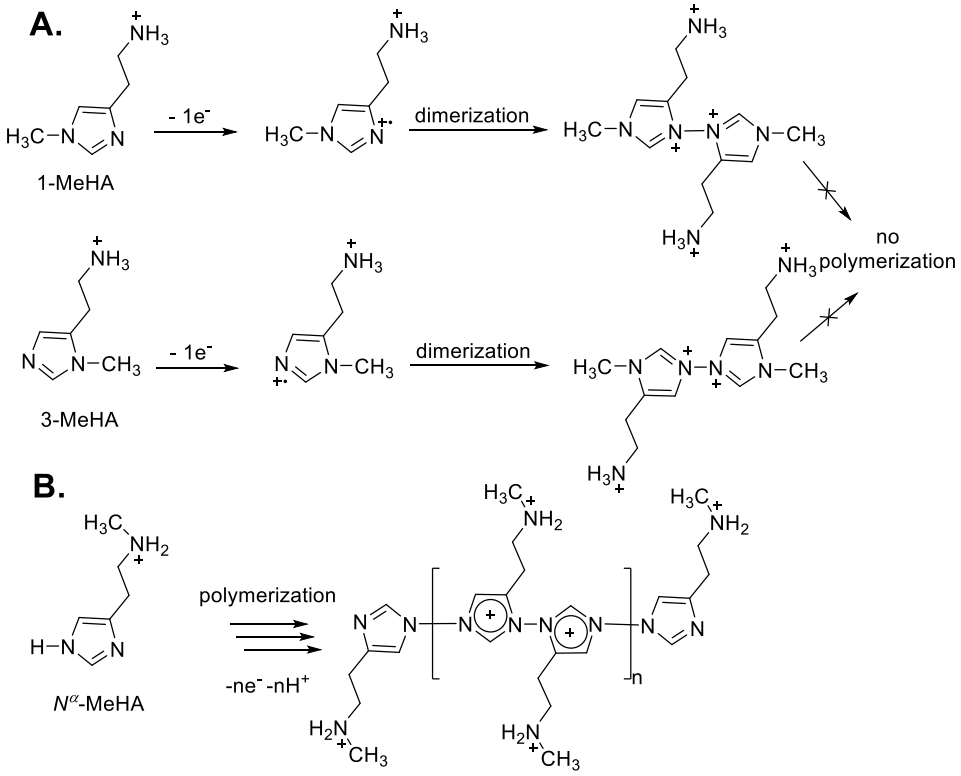

Fig. 2.7 Mechanism of (A) electrochemical oxidation of 1-MeHA and 3-MeHA, and (B) oxidative electropolymerization of *N*$^{\alpha}$-MeHA.

2.3.4 XPS Confirms Histamine Polymerization.

To test the proposed polymerization, we also performed XPS to measure surface elemental composition and electronic states of each element. Screen-printed carbon electrodes (SPCEs) were used as the working electrode instead of GCEs because they are flat and easily analyzed using XPS. Four samples of SPCE were characterized: new SPCE, SPCE scanned in PBS from -0.5 to +1.5 V, SPCE scanned in 50 mM histamine from -0.5 to +1.0 V, and SPCE scanned in 50 mM histamine from -0.5 to +1.5 V. Table 2.1 summarizes the elemental composition and nitrogen peak position of each SPCE (Fig. 2.8 plots the actual XPS spectra with peaks fittings). The nitrogen composition of new SPCE, SPCE scanned in histamine to +1.0 V, and SPCE scanned in PBS were low, not

above 2-3%. This nitrogen on the SPCE, which had the binding energy of 399.8 eV, may be due to impurities on the electrode, and the electrode exposed to histamine may have a little physisorption of histamine on the SPCE surface, but it is not much. In contrast, the nitrogen content of SPCE scanned in histamine to +1.5 V is 15.5%. Moreover, the overall nitrogen peak shape changed, and there was a new subpeak at 400.9 eV in addition to the original 399.8 eV peak (Fig. 2.8D). The nitrogen binding energy of 400.9 eV is consistent with a nitrogen in an aromatic ring-like imidazole.[17] This higher nitrogen content and new peak position indicates the existence of nitrogen-containing polymer on the SPCE surface after histamine oxidation, which is consistent with the proposed mechanism that histamine undergoes electropolymerization. This nitrogen peak only occurs when the electrode is scanned to higher potentials in histamine and not when it is scanned to +1.0 V or when histamine is not present.

Table 2.1 XPS spectral information

Samples	**Atomic elemental composition[a]**			**N position (eV)**
	%C	**%O**	**%N**	
New SPCE	67.9	16.5	2.4	399.8
SPCE in PBS to +1.5 V	62.1	21.9	nd	N/A
SPCE in histamine to +1.0 V	66.3	17.2	3.1	399.9
SPCE in histamine to +1.5 V	51.4	22.6	15.5	399.8, 400.9

[a]nd = not detected. Values shown are average values from two samples. Other atoms might be present, so atomic compositions do not add to 100%.
[b]N positions are corrected by shifting the C 1s peak to 284.8 eV.

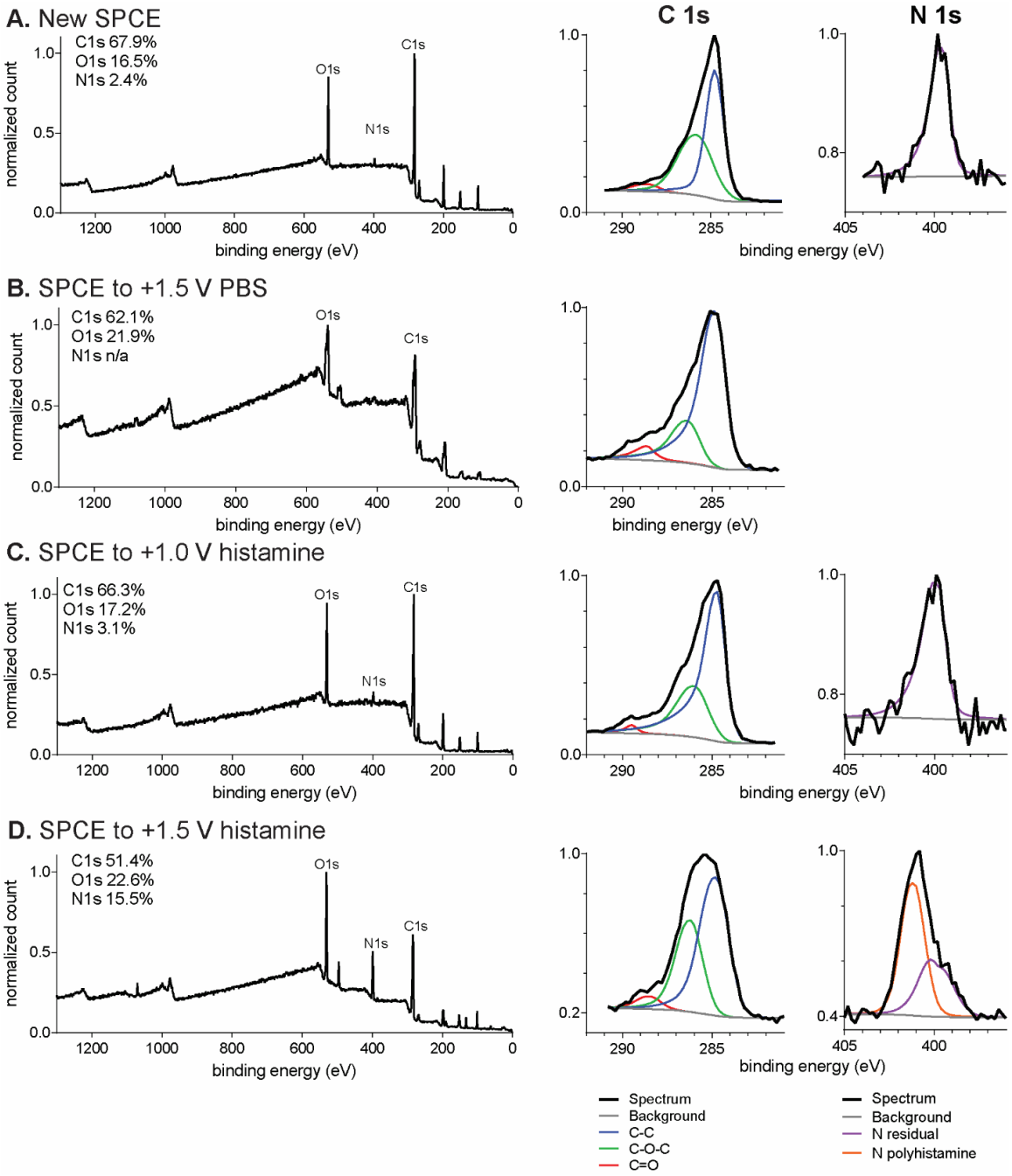

Fig. 2.8 XPS Spectra and C 1s and N 1s peaks fitting of (A) New SPCE, (B) SPCE scanned in PBS from -0.5 V to +1.5 V for 20 cycles, (C) SPCE scanned in 50 mM histamine from -0.5 V to +1.0 V for 20 cycles, (D) SPCE scanned in 50 mM histamine from -0.5 V to +1.5 V for 20 cycles.

2.3.5 FSCV of Histamine at CFMEs

For real-time measurements of neurotransmitters, FSCV is predominantly used,[18,19] so we investigated the detection of histamine using FSCV. FSCV parameters were investigated to understand how they influence the oxidation current for histamine. First, the switching potential was varied. For lower switching potentials of 0.5, 0.9, and 1.0 V (Fig. 2.9A), the current dips below baseline on the forward scan at negative potentials and then there was a weak, broad peak of only 3 nA around 0.4 V on the forward scan. The small peak is not likely a faradaic peak because it occurs almost a volt lower than the faradaic peaks in slow scan CV or amperometry. Instead, this peak is a background current change that arises when the background capacitance changes from histamine adsorption. The log-log plot of this peak current at 0.4 V vs scan rate has a slope close to 1 (Fig. 2.10), indicating adsorptive capacitance change. Similarly, adsorption of dopamine to a carbon electrode can cause small, broad nonfaradaic peaks in background-subtracted CVs.[20] The 1.0 V scan has a small peak on the back scan near the switching potential, which is likely still an adsorption peak (given the slow scan and XPS results).

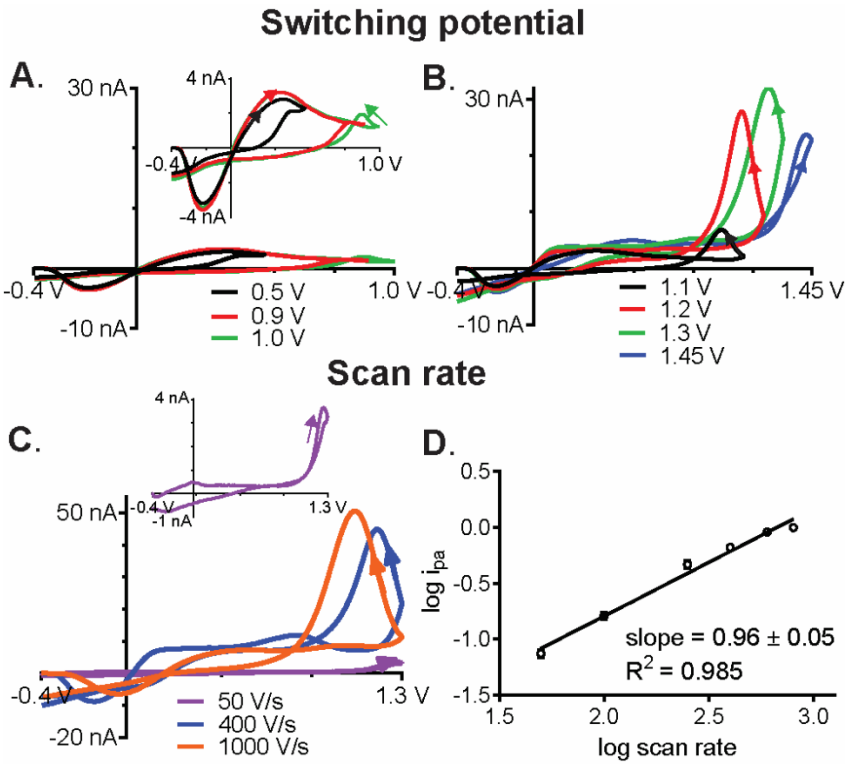

Fig. 2.9 FSCV of 1 µM histamine at CFME using different waveform parameters. (A-B) CV from different switching potential at a holding potential of -0.4 V and scan rate of 400 V/s. The inset of panel A shows the enlarged CV from 0.5, 0.9, and 1.0 V switching potential. (C) CV from different scan rate using -0.4 V holding potential and 1.3 V switching potential, and (D) log-log plot between normalized anodic peak current (i_{pa}) and scan rate (n = 4). The inset of panel C shows the enlarged CV from the 50 V/s scan rate. Arrows mark direction of scan.

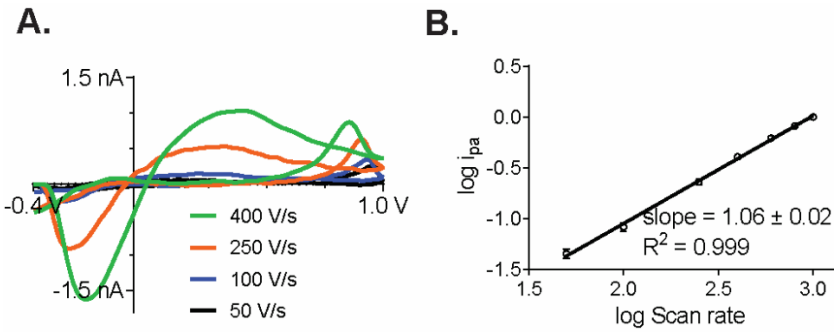

Fig. 2.10 FSCV scan rate experiment using 1.0 V switching potential. (A) CV from different scan rate using -0.4 V holding potential and 1.0 V switching potential. (B) log-log plot between normalized 0.4 V peak current (i_{pa}) and scan rate (n = 4).

Faradaic peaks are better observed with higher switching potentials (Fig. 2.9B). The peak current increased with switching potential from 7 nA at 1.1 V, to 22 nA at 1.2 V, to 30 nA at 1.3 V. Lower currents were expected for the lower holding potentials of 1.1 and 1.2 V because the CV of histamine at slower scan rates (Fig. 2.2A) had a peak maximum at 1.3 V. With a switching potential of 1.45 V, the anodic peak is near the switching potential on the forward scan, but the current is lower than with 1.3 V switching potential. While more oxidation is expected to occur at higher potentials because more time is spent above the E^0, the fouling from electropolymerization likely happens immediately and decreases the current.

To investigate scan rate dependence, we varied the FSCV scan rate from 50 to 1000 V/s. A scan rate of 50 V/s resulted in the E_{pa} of 1.26 V on the forward scan (Fig. 2.9C), but a higher scan rate shifted the peak to the backward scan: 1.19 V for 400 V/s and 1.07 V for 1000 V/s because of the time for electron transfer. The log-log plot of normalized histamine anodic peak current (i_{pa}) vs scan rate (Fig. 2.9D) had a slope of 0.96 ± 0.05 (n = 4), which is close to 1 and indicates adsorption-controlled oxidation of histamine at CFMEs. Histamine has a pK_a of the aliphatic amine group of 9.11,[21] so it is cationic at physiological pH. The negatively charged oxygen surface functional groups of CFMEs adsorb the cationic histamine by electrostatic interactions before electron transfer. However, the response is linear only to 800 V/s and not 1000 V/s because the time of the scan is too fast to fully complete the oxidation at that fast scan rate.

Our results show that it is necessary to scan to higher switching potentials (1.3 V or above) to fully detect faradaic peaks for histamine. These results are consistent with early FSCV literature, which observed a histamine peak above 1.1 V on the back scan when higher switching potentials were used (vs Ag/AgCl or SCE).[2,9,11] However, this work

and mechanism is in contrast to the waveform developed by the Hashemi group,[12] which scans only to 1.1 V (vs Ag/AgCl) and reports that the broad FSCV peak at 0.3 V is the faradaic process. All of the mechanistic data from amperometry, slow scan CV, XPS, and fast scan CV point to no faradaic reactions occurring before 1.0 V. Thus, the small peaks observed at 0.3 V are broad and likely background changes due to adsorption. Waveform manipulation alone will not be able to shift the peak significantly unless there is an electrocatalyst on the electrode surface. One advantage of not using a high switching potential is that there will not be fouling due to electropolymerization, but this is also indicative that no faradaic reaction takes place.

2.3.6 Histamine Fouling with FSCV

FSCV is also a good technique to study the effect of fouling on the electrode surface because many scans are collected over time. Fig. 2.11A shows cyclic voltammograms and false color plots of 1 µM histamine FSCV with a switching potential of 1.3 V. Histamine was continuously flowed by the electrode surface for 5 s, and the CV changes significantly during that time. Initially (0.5 s after histamine exposure), there was an anodic peak of 24 nA around +1.21 V ("primary anodic peak", labeled "1°" in Fig. 5) on the backward scan. At 1.0 s, the primary anodic peak reached a maximum current about 32 nA. When histamine had been present for 5.0 s, the primary peak shifted later, to +1.15 V on the backward scan, and the anodic current decreased to 24 nA. The peak current decreased because of the electrode fouling from polyhistamine, and the peak potential shifted because of the sluggish electron transfer kinetics after the fouling.

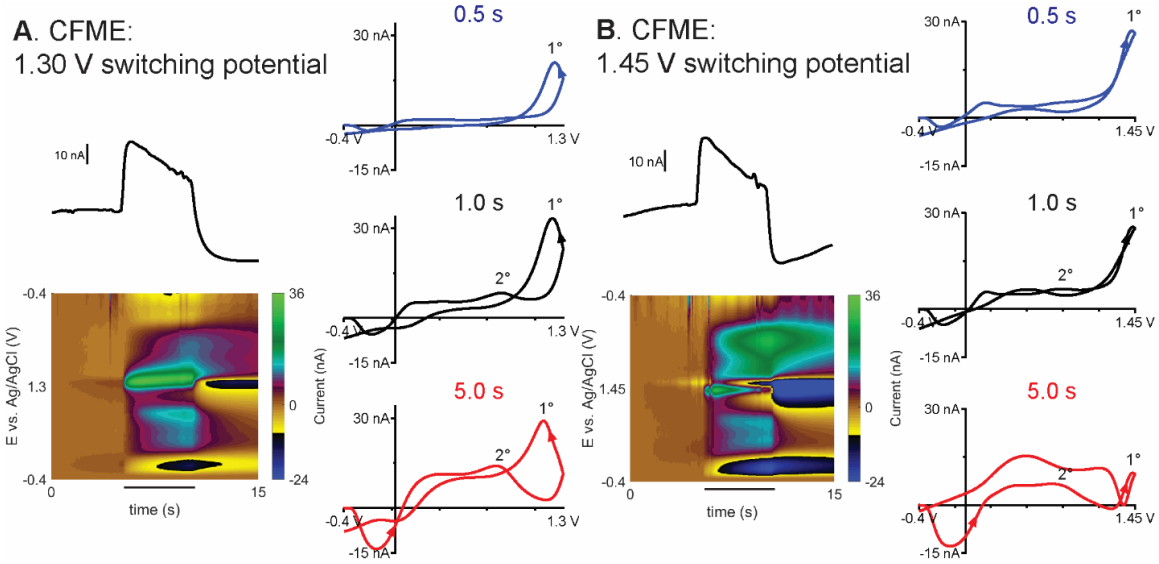

Fig. 2.11 FSCV of 1 µM histamine at CFME. Current-time trace, false color plot, CVs at 0.5, 1.0, and 5.0 s injection from different FSCV switching potential: (A) 1.30 and (B) 1.45 V. Black lines under the color plots indicate histamine was flowing by the electrode. 1º and 2º indicates primary and secondary anodic peak, respectively. More detailed peak labeling can be found in Fig. 2.12.

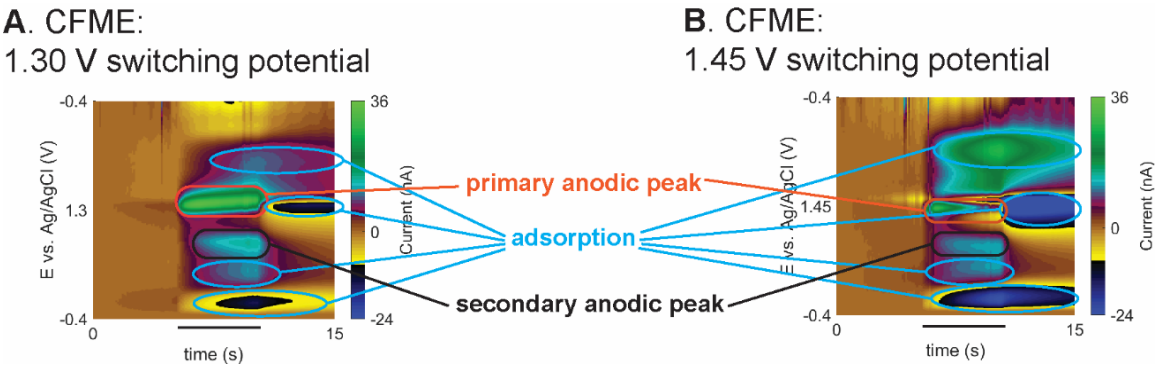

Fig. 2.12 Labelled false color plots from FSCV of 1 µM histamine at CFME in Fig. 2.11 (A) 1.30 V switching potential and (B) 1.45 V switching potential.

During the histamine injection, there was also a small secondary peak ("secondary anodic peak", labeled "2°" in Fig. 2.11) of 8 nA that appeared at +0.80 V on the forward scan in later CVs but was not present in the first CVs. This secondary peak grew to 11 nA after 5 s of histamine. The 0.8 V secondary peak on the front scan may be due to

oxidation of imidazole rings in the polymer coating as the oxidation potential is lower for an adsorbed species because it is on the electrode surface. The extended conjugated system in the adsorbed polyhistamine may also stabilize the radical cation generated from polyhistamine oxidation and decrease the oxidation potential.

In addition to the faradaic peaks, at later times there were other small, broader peaks near –0.17 V and 0.4 V on the forward scan and 0.5 V on the backward scan. Fig. 2.12 labels these peaks on a color plot. These currents are likely due to background subtraction errors due to capacitance changes when the polymer adsorbed. The extra peaks grow in over time and are present after histamine is washed out of the flow cell, indicating that they are due to a polymer build up on the surface.

FSCV of 1 µM histamine was also performed using a switching potential of 1.45 V (Fig. 2.11B), which is the waveform used to detect high oxidation potential analytes such as adenosine.[22–24] Initially, the primary anodic peak was located on the forward scan at 1.42 V and had a current of 25 nA. However, after 5 s of histamine exposure, the peak had diminished greatly, losing about 75% of the signal (8 nA). Interestingly, the peak did not shift in voltage, which may be due to the CFME etching at high potentials, which renews the carbon surface.[25] Histamine FSCV using 1.45 V switching potential also had the secondary anodic peak (0.8 V forward scan) and small broad adsorption peaks (labeled in Fig. 2.12). Many of these small peaks are likely due to changes in the background current from adsorption of the polymer. *In vivo*, pH changes also cause broad peaks due to background subtraction errors[16] and data processing techniques such as principal component regression (PCR) can be implemented to separate the contribution from pH shift.[26]

Although the advantage of using FSCV for real-time measurement is to obtain the molecular fingerprint from the CV, FSCV data are usually analyzed by monitoring the peak current from one potential in the CV over time. The ideal shape of a current vs time trace is square because flow injection is used to expose the electrode to a square bolus of histamine. However, the current vs time trace in Fig. 2.11 shows the peak current at the oxidation potential decreases when histamine is present and even appears to drop below baseline after it is washed out. These errors are caused by histamine fouling, which changes the background charging current. These current vs time traces are not be amenable to kinetic modeling, and the fouling would need to be deconvoluted, so we explored methods to alleviate the electrode fouling.

2.3.7 Nafion Prevents Electrode Fouling from Histamine Electropolymerization

Electropolymerization of histamine causes electrode fouling, and the current vs time responses are not square but convoluted by the fouling peaks (Fig. 2.11A and Fig. 2.11B). Nafion is a negatively-charged perfluorosulfonate polymer used to eliminate interferences and prevent electrode fouling via electrostatic repulsion and size exclusion.[27–29] Nafion/CFMEs were prepared by electrodeposition[30] of Nafion from a solution in methanol (the chronoamperogram from electrodeposition is shown in Fig. 2.13). At Nafion-coated electrodes, the CV and anodic current for histamine stayed the same throughout the injection for the 1.3 V switching potential, and the peak position stayed at 1.18 V on the back scan (Fig. 2.14A). The color plot also shows some small, broad currents at other peaks, similar to bare CFMEs, but the current-time trace is much more square and more faithful to the time course of the histamine change. Nafion prevents electrode fouling because a polymer is already present on the surface; thus, the histamine

polymer cannot build up on the surface. There are also electrostatic and size exclusion effects of Nafion to prevent fouling as well.[29] The histamine anodic current was smaller with Nation coating than that of the bare CFME, likely because Nafion coating restricted histamine diffusion to the electrode surface or the inhibition of polyhistamine formation decreased the current for electron transfer.

After Nafion, with a 1.45 V switching potential, the color plot is much cleaner than that with a 1.3 V potential and the current vs time curve is more square (Fig. 2.14B). The false color plot, CVs, and current-time trace illustrate less electrode fouling, similar to when 1.3 V switching potential was used. Currents obtained with the 1.45 V switching potential and Nafion are larger than with the 1.3 V potential, which would increase electrode sensitivity. Overall, Nafion coating prevents electrode fouling caused by the polymer buildup from histamine oxidation. Nafion should be considered for future studies examining histamine *in vivo* to prevent electrode fouling by histamine polymerization.

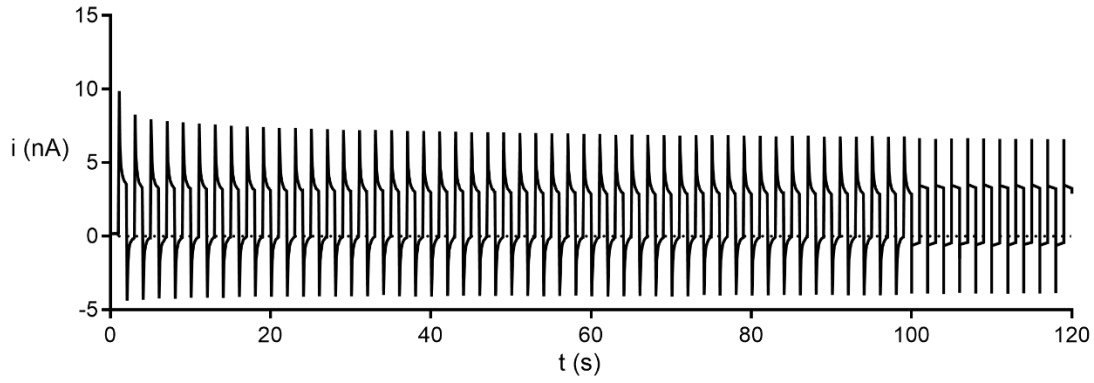

Fig. 2.13 Chronoamperogram from Nafion electrodeposition. A pulsed waveform between 0.0 V to 1 s and 1.0 V for 1 s for 60 cycles was applied to the CFME.

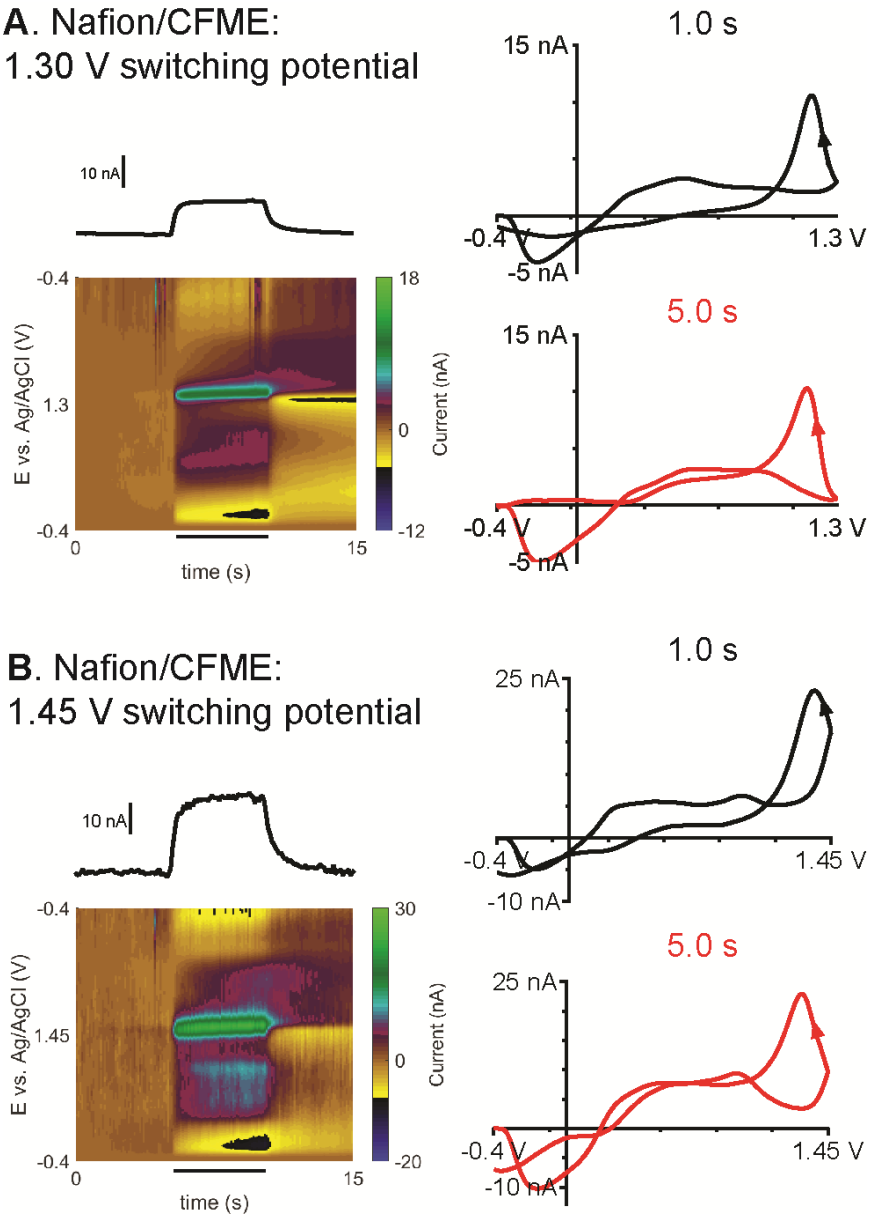

Fig. 2.14 FSCV of 1 µM histamine at Nafion/CFME. Current-time trace, false color plot, CVs at 1.0 s and 5.0 s injection from different FSCV switching potential: (A) 1.30 and (B) 1.45 V. Black lines under the color plots indicate histamine was flowing by the electrode.

2.4 Conclusions

Histamine undergoes oxidative electropolymerization with a required oxidation potential of at least 1.1 V at carbon electrodes, including GCE, SPCE, and CFME. The polymer product fouls the electrode, reducing the sensitivity for histamine. FSCV of histamine had an anodic peak at 1.2 V on the backward scan and secondary peaks due to histamine polymer being oxidized on the surface. Nafion coating helps eliminate the electrode fouling observed with FSCV. Future research can utilize the fundamental understanding of histamine electrochemistry presented here to develop better electrochemical sensors and methods for real-time monitoring of histamine.

2.5 References

(1) Haas, H. L.; Sergeeva, O. A.; Selbach, O. Histamine in the Nervous System. *Physiol. Rev.* **2008**, *88*, 1183–1241.

(2) Pihel, K.; Hsieh, S.; Jorgenson, J. W.; Wightman, R. M. Electrochemical Detection of Histamine and 5-Hydroxytryptamine at Isolated Mast Cells. *Anal. Chem.* **1995**, *67* (24), 4514–4521.

(3) Flik, G.; Folgering, J. H. A.; Cremers, T. I. H. F.; Westerink, B. H. C.; Dremencov, E. Interaction Between Brain Histamine and Serotonin, Norepinephrine, and Dopamine Systems: In Vivo Microdialysis and Electrophysiology Study. *J. Mol. Neurosci.* **2015**, *56* (2), 320–328.

(4) Denno, M. E.; Privman, E.; Borman, R. P.; Wolin, D. C.; Venton, B. J. Quantification of Histamine and Carcinine in Drosophila Melanogaster Tissues. *ACS Chem. Neurosci.* **2016**, *7* (3), 407–414.

(5) Pihel, K.; Hsieh, S.; Jorgenson, J. W.; Wightman, R. M. Quantal Corelease of Histamine and 5-Hydroxytryptamine from Mast Cells and the Effects of Prior Incubation. *Biochemistry* **1998**, *37* (4), 1046–1052.

(6) Travis, E. R.; Wang, Y. M.; Michael, D. J.; Caron, M. G.; Wightman, R. M. Differential Quantal Release of Histamine and 5-Hydroxytryptamine from Mast Cells of Vesicular Monoamine Transporter 2 Knockout Mice. *Proc. Natl. Acad. Sci. U. S. A.* **2000**, *97* (1), 162–167.

(7) Hashemi, P.; Dankoski, E. C.; Wood, K. M.; Ambrose, R. E.; Wightman, R. M. In Vivo Electrochemical Evidence for Simultaneous 5-HT and Histamine Release in the Rat Substantia Nigra Pars Reticulata Following Medial Forebrain Bundle Stimulation. *J. Neurochem.* **2011**, *118* (5), 749–759.

(8) Wang, H. L.; O'Malley, R. M.; Fernandez, J. E. Electrochemical and Chemical Polymerization of Imidazole and Some of Its Derivatives. *Macromolecules* **1994**, *27* (4), 893–901.

(9) Sarada, B. V.; Rao, T. N.; Tryk, D. A.; Fujishima, A. Electrochemical Oxidation of Histamine and Serotonin at Highly Boron- Doped Diamond Electrodes. *Anal. Chem.* **2000**, *72* (7), 1632–1638.

(10) Stamford, J. A. Effect of Electrocatalytic and Nucleophilic Reactions on Fast Voltammetric Measurements of Dopamine at Carbon Fiber Microelectrodes. *Anal. Chem.* **1986**, *58* (6), 1033–1036.

(11) Chang, S. Y.; Jay, T.; Muñoz, J.; Kim, I.; Lee, K. H. Wireless Fast-Scan Cyclic Voltammetry Measurement of Histamine Using WINCS - A Proof-of-Principle Study. *Analyst* **2012**, *137* (9), 2158–2165.

(12) Samaranayake, S.; Abdalla, A.; Robke, R.; Wood, K. M.; Zeqja, A.; Hashemi, P. In Vivo Histamine Voltammetry in the Mouse Premammillary Nucleus. *Analyst* **2015**, *140* (11), 3759–3765.

(13) Qi, L.; Thomas, E.; White, S. H.; Smith, S. K.; Lee, C. A.; Wilson, L. R.; Sombers, L. A. Unmasking the Effects of L-DOPA on Rapid Dopamine Signaling with an Improved Approach for Nafion Coating Carbon-Fiber Microelectrodes. *Anal. Chem.* **2016**, *88* (16), 8129–8136.

(14) Huffman, M. L.; Venton, B. J. Electrochemical Properties of Different Carbon-Fiber Microelectrodes Using Fast-Scan Cyclic Voltammetry. *Electroanalysis* **2008**, *20* (22), 2422–2428.

(15) McCreery, R. L. Advanced Carbon Electrode Materials for Molecular Electrochemistry. *Chem. Rev.* **2008**, *108* (7), 2646–2687.

(16) Venton, B. J.; Michael, D. J.; Wightman, R. M. Correlation of Local Changes in Extracellular Oxygen and PH That Accompany Dopaminergic Terminal Activity in the Rat Caudate-Putamen. *J. Neurochem.* **2003**, *84* (2), 373–381.

(17) Al-Hinai, M.; Hassanien, R.; Watson, S. M. D.; Wright, N. G.; Houlton, A.; Horrocks, B. R. Metal-Conductive Polymer Hybrid Nanostructures: Preparation and Electrical Properties of Palladium–Polyimidazole Nanowires. *Nanotechnology* **2016**, *27* (9), 095704.

(18) Venton, B. J.; Wightman, R. M. Psychoanalytical Electrochemistry: Dopamine and Behavior. *Anal. Chem.* **2003**, *75* (19), 414A-421A.

(19) Ganesana, M.; Lee, S. T.; Wang, Y.; Venton, B. J. Analytical Techniques in Neuroscience: Recent Advances in Imaging, Separation, and Electrochemical Methods. *Anal. Chem.* **2017**, *89* (1), 314–341.

(20) Bath, B. D.; Michael, D. J.; Trafton, B. J.; Joseph, J. D.; Runnels, P. L.; Wightman, R. M. Subsecond Adsorption and Desorption of Dopamine at Carbon-Fiber Microelectrodes. *Anal. Chem.* **2000**, *72* (24), 5994–6002.

(21) Altun, Y.; Köseoğlu, F. Stability of Copper(II), Nickel(II) and Zinc(II) Binary and Ternary Complexes of Histidine, Histamine and Glycine in Aqueous Solution. *J. Solution Chem.* **2005**, *34* (2), 213–231.

(22) Swamy, B. E. K.; Venton, B. J. Subsecond Detection of Physiological Adenosine Concentrations Using Fast-Scan Cyclic Voltammetry. *Anal. Chem.* **2007**, *79* (2), 744–750.

(23) Nguyen, M. D.; Lee, S. T.; Ross, A. E.; Ryals, M.; Choudhry, V. I.; Venton, B. J. Characterization of Spontaneous, Transient Adenosine Release in the Caudate-Putamen and Prefrontal Cortex. *PLoS One* **2014**, *9* (1), e87165.

(24) Ganesana, M.; Venton, B. J. Early Changes in Transient Adenosine during Cerebral Ischemia and Reperfusion Injury. *PLoS One* **2018**, *13* (5), e0196932.

(25) Takmakov, P.; Zachek, M. K.; Keithley, R. B.; Walsh, P. L.; Donley, C.; McCarty, G. S.;

Wightman, R. M. Carbon Microelectrodes with a Renewable Surface. *Anal. Chem.* **2010**, *82* (5), 2020–2028.

(26) Keithley, R. B.; Mark Wightman, R.; Heien, M. L. Multivariate Concentration Determination Using Principal Component Regression with Residual Analysis. *TrAC, Trends Anal. Chem.* **2009**, *28* (9), 1127–1136.

(27) Mauritz, K. A.; Moore, R. B. State of Understanding of Nafion. *Chem. Rev.* **2004**, *104* (10), 4535–4585.

(28) Vreeland, R. F.; Atcherley, C. W.; Russell, W. S.; Xie, J. Y.; Lu, D.; Laude, N. D.; Porreca, F.; Heien, M. L. Biocompatible PEDOT:Nafion Composite Electrode Coatings for Selective Detection of Neurotransmitters in Vivo. *Anal. Chem.* **2015**, *87* (5), 2600–2607.

(29) Cao, Q.; Puthongkham, P.; Venton, B. J. Review: New Insights into Optimizing Chemical and 3D Surface Structures of Carbon Electrodes for Neurotransmitter Detection. *Anal. Methods* **2019**, *11* (3), 247–261.

(30) Hashemi, P.; Dankoski, E. C.; Petrovic, J.; Keithley, R. B.; Wightman, R. M. Voltammetric Detection of 5-Hydroxytryptamine Release in the Rat Brain. *Anal. Chem.* **2009**, *81* (22), 9462–9471.

CHAPTER 3

Carbon Nanohorn-Modified Carbon-Fiber Microelectrodes for Dopamine Detection

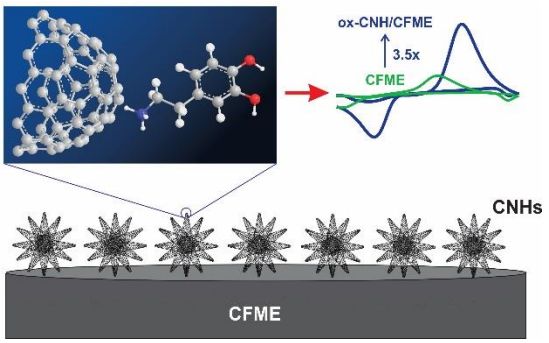

Chapter 3 was reprinted from *Electroanalysis* **2018,** *30,* 1073-1081 with the permission from Wiley.

Abstract

Carbon nanohorns (CNHs), closed cone-shaped cages of sp^2-hybridized carbons, are a promising nanomaterial to improve carbon-fiber microelectrode (CFME) dues to their high specific surface area and edge planes, but few studies have tested their electrochemical properties. Here, we tested the dopamine detection at electrodeposited CNHs on CFME (CNH/CFME). The optimized concentration of CNHs in the deposition solution is 0.5 mg/mL, and the optimized electrodeposition waveform is 10 cycles of triangular waveform scanned from –1.0 V and +1.0 V at 50 mV/s. Using fast-scan cyclic voltammetry, the optimized CNH/CFME enhances dopamine peak current to 2.3 ± 0.2 times that of the CFME. To further increase the current, CNH/CFMEs were oxidized in NaOH (ox-CNH/CFME), which creates more defects and surface oxide groups to adsorb dopamine. The oxidative etching further increases the peak current to 3.5 ± 0.2 times of the CFME, and ox-CNH/CFME had a limit of detection of 6 ± 2 nM. The dopamine anodic current at ox-CNH/CFME was stable for 8 h of continuous scanning. The ox-CNH/CFME enhanced the anodic peak current for other cationic neurotransmitters including epinephrine, norepinephrine, and serotonin, but less enhancement was found for ascorbic acid, showing higher selectivity for cationic molecules. CNHs also decreased tissue biofouling at CFME. Thus, electrodeposited CNHs are a promising new method for increasing the surface area and current of CFMEs for dopamine detection.

3.1 Introduction

The carbon nanohorn (CNH) is a cone-shaped cage of graphene consisting of mainly sp^2-hybridized carbons. Each individual cone has a diameter of 2–5 nm and a length of 40–50 nm, and has a 5 pentagon-shaped closed cap.[1,2] CNH cones can form dahlia-like aggregates, like petals sticking out from a center, with an overall diameter of 100 nm.[2] The small sizes, combined with conjugated π-bonds, result in high specific surface area and high electronic conductivity.[2] CNHs have similar properties to the ends of carbon nanotubes (CNTs); thus, they can be easily opened and oxidized to provide edge-plane carbon sites and oxide-containing functional groups.[2–4] In addition, the conical structure causes high porosity, ring strain, and high electric field at the cone tip, which is significant for high adsorption capability, electron transfer kinetics, and chemical reactivity.[1,2,5] One key feature distinguishing CNHs from other carbon nanomaterials is high purity because CNHs can be synthesized via laser ablation of graphite at room temperature without any metal catalyst.[2,6] Because of these unique properties, CNHs have been used in various applications including gas adsorptions,[7] drug carriers,[8] and electrochemical energy devices.[9] However, there have been relatively few reports of using CNHs for electrochemical sensors.

Many carbon nanomaterials have been used to modify and improve the performance of electrochemical sensors, particularly to coat glassy carbon or carbon-fiber microelectrodes (CFMEs) to improve sensitivity.[10,11] Graphene itself has a large specific surface area, high conductivity, and good electrocatalytic properties,[10,12] and has been drop-casted, as reduced graphene oxide, onto glassy carbon electrodes to enhance the signal for dopamine.[13] Another popular nanomaterial is the CNT, which is a rolled graphene sheet existing as a hollow tube.[10,12] When the end of the tube is opened, it

generates defect sites or edge plane sites, which promote electron transfer, causing electrocatalytic effects and enhancing adsorption of cationic neurotransmitters such as dopamine and epinephrine.[10,14,15] CNTs can be made into electrodes in a variety of ways: they can be dip-coated or drop-casted onto an electrode,[16–19] grown on a substrate to make an electrode,[20,21] or spun as a fiber[22–24] or yarn[25–27] which is then fabricated into a microelectrode. CNT electrodes work best with the ends aligned and directly exposed to the solution, leading to the theory that the greatest electroactive sites are on the exposed ends.[20,21] CNHs have only been sparsely used as electrochemical sensors, but the hypothesis is that they would provide good electrochemical enhancement because their properties are similar to those of CNT ends.[1,2,7] The cone-shaped CNH ends can be oxidized and opened and the dahlia-like aggregates expose the ends like petals, leading to strong adsorption of cationic molecules.[2,3,11,14] CNHs have been used to fabricate electrodes; for example, drop-casting CNHs improved the limit of detection (LOD) of screen-printed electrode.[28] A CNH-modified glassy carbon electrode resolved dopamine, uric acid, and ascorbic acid peaks[29] and resolved dihydroxybenzene isomer peaks.[30] However, smaller CNH-modified electrodes that are suitable for *in vivo* measurements of neurotransmitters have not been fabricated, and drop-casting is not an effective method for coating cylindrical microelectrodes.[10] Thus, new methods for depositing CNHs must also be developed.

The purpose of this study was to optimize fabrication of CNH-modified microelectrodes and explore their properties for the fast-scan cyclic voltammetric (FSCV) determination of dopamine. Here, we develop electrodeposition as a simple procedure to prepare the carbon nanohorn-modified carbon-fiber microelectrode (CNH/CFME) from a CNH dispersion. Parameters for electrodeposition were optimized and electrodeposition

deposits more CNHs than dip-coating alone. CNHs increase the Faradaic current of dopamine redox reaction, and oxidative etching of CNH/CFME (ox-CNH/CFME) increased the current for dopamine even more because it opens the CNH tips. Overall, CNHs are a promising nanomaterial for use in electrochemical neurotransmitter sensors and can easily be electrodeposited to improve dopamine detection.

3.2 Experimental Section

3.2.1 Chemicals

Dopamine, epinephrine, norepinephrine, serotonin, and ascorbic acid were purchased from Acros Organics (Morris Plains, NJ). A 10 mM stock solution of each analyte was prepared in 0.1 M $HClO_4$. The final working solutions were daily prepared by diluting the stock solution in a phosphate buffer saline (PBS) (131.25 mM NaCl, 3.00 mM KCl, 10 mM NaH_2PO_4, 1.2 mM $MgCl_2$, 2.0 mM Na_2SO_4, and 1.2 mM $CaCl_2$ with pH adjusted to 7.4) to the desired concentration.

3.2.2 Preparation of CNH/CFME and ox-CNH/CFME

Prior to the electrode modification, a cylindrical CFME was prepared by the same procedure as the previous work.[31] Briefly, a T-650 carbon fiber (7-μm diameter, Cytec Engineering Materials, West Patterson, NJ) was pulled into a glass capillary (1.28 mm inner diameter × 0.68 mm outer diameter, A-M Systems, Sequim, WA) by an aspirating pump. Then, the capillary was pulled by an electrode puller (model PE-21, Narishige, Tokyo, Japan) to get two electrodes. The extended fiber was cut to a length of 100 μm. After that, each electrode was epoxied by dipping in an 80°C-solution of Epon Resin 828 (Miller-Stephenson, Danbury, CT) and 14% *m*-phenylenediamine hardener (Acros

Organics, Morris Plains, NH) for 30 s to seal the fiber with the glass capillary. Finally, the epoxied electrode was left overnight at room temperature, cured in an oven at 100^{o}C for 2 h, and 150^{o}C overnight. An electrical connection between the fiber and a connecting wire was made by filling 1 M KCl in the capillary before using.

To prepare the modified electrodes, single-walled CNHs synthesized at Oak Ridge National Laboratory (ORNL), Oak Ridge, TN (Transmission electron microscopy (TEM) image of CNHs is shown in Fig. 3.1A) were dispersed in water with 0.1 M NaCl and 0.01 M sodium dodecyl sulfate (SDS) and homogenized with an ultrasonic tissue homogenizer (model 150VT, Biologics, Manassas, VA) for 10 min. The TEM images of CNHs were obtained using an FEI Titan 80-300 TEM (FEI Company, Hillsboro, OR) at the Nanoscale Materials Characterization Facility, Department of Materials Science and Engineering, University of Virginia. Samples were prepared by drop-casting of either CNH dispersion or oxidized CNH dispersion on the carbon type-B, 200-mesh, copper TEM grid (Ted Pella, Redding, CA). The acceleration voltage is 300 kV. After that, the electrodeposition was performed in a batch electrochemical cell containing Ag/AgCl reference electrode, Pt counter electrode, and CFME working electrode in the CNH dispersion. Using a potentiostat (Gamry Instruments, Warminster, PA), a repeated cyclic voltammetric waveform between –1.0 to +1.0 V at a scan rate of 50 mV/s for 5–25 cycles was applied to the CFME to obtain the CNH/CFME. Finally, the oxidative etching was done by applying a constant potential of +1.5 V for 1–4 min to the CNH/CFME to obtain the ox-CNH/CFME. All modified electrodes were left overnight before they were tested.

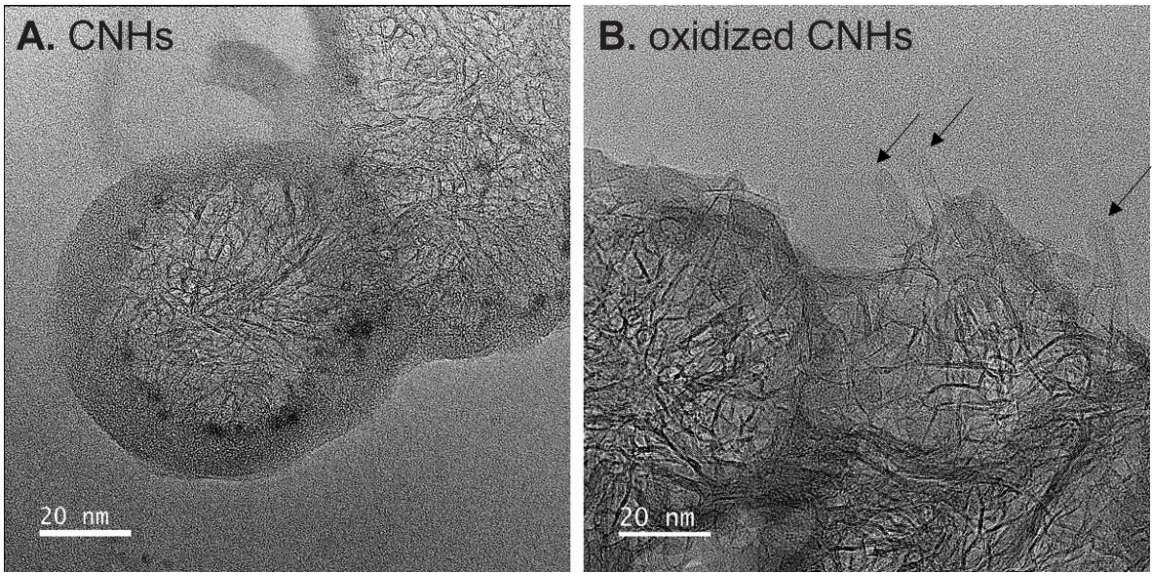

Fig. 3.1 TEM images of (A) CNHs and (B) oxidized CNHs. The CNHs form dahlia like structures, but more loose, open-ended CNHs are present for the oxidized CNHs (example arrows) compared to the not oxidized CNHs. TEM images were collected by Helge Heinrich, Nanoscale Materials Characterization Facility, Department of Materials Science and Engineering, University of Virginia.

3.2.3 Surface Characterization

Scanning electron microscopy (SEM) images were taken using Quanta 650 (FEI Company, Hillsboro, OR) at the Nanoscale Materials Characterization Facility, Department of Materials Science and Engineering, University of Virginia. The secondary electron detector images were recorded with an accelerating voltage of 2 kV and a working distance of approximately 10 mm. Raman spectra were obtained from a Renishaw 100 confocal micro-Raman system (Renishaw, Hoffman Estates, IL) at ORNL, using 532-nm laser.

3.2.4 FSCV Instrumentation

FSCV experiments were performed with a ChemClamp potentiostat and headstage (Dagan, Minneapolis, MN). The triangular waveform with a holding potential

of –0.4 V, a switching potential of +1.3 V, a scan rate of 400 V/s, and a repetition rate of 10 Hz was applied to a working microelectrode versus Ag/AgCl reference electrode. The buffer and test solutions were injected through the flow cell at 2 mL/min by a syringe pump (Harvard Apparatus, Holliston, MA) and a flow-injection system consisting of a six-port loop injector with an air actuator (VIVI Valco Instruments, Houston, TX). The data were collected with HDCV Analysis software (Department of Chemistry, University of North Carolina at Chapel Hill).

3.2.5 Statistics

All values are given as the mean ± standard error of the mean (SEM) for *n* number of electrodes. All statistical tests were performed in GraphPad Prism 7.0 (GraphPad Software, La Jolla, CA), and significance was defined at $p < 0.05$.

3.3 Results and Discussion

The goal of this study is to investigate the extent to which CNHs and oxidative etching improve FSCV electrochemical detection of dopamine. CNHs were prepared as a conductive, homogeneous dispersion in order to be compatible with the electrodeposition technique and to prevent inter-dahlia agglomeration of CNHs.[32] The solvent contained 0.1 M NaCl as a supporting electrolyte and 0.01 M SDS as a surfactant to disperse CNHs. Fig. 3.1A shows a TEM image of the CNH dahlias. Electrodeposition was performed by using CV waveform which can attract CNH particles from the dispersion onto the CFME surface by electrostatic interaction.[33] Each dahlia CNHs particle is surrounded by SDS molecules as a negatively charged micelle. The positively scanned

CV waveform attracts the negative micelles to bring and attach CNHs on the CFME surface; then the SDS molecules are dissolved back into the aqueous solution.

3.3.1 Surface and Electrochemical Characterization of CNH/CFME

CFMEs were initially subjected to the electrodeposition from a 0.5 mg/mL CNH dispersion with a slow-scan CV waveform (–1.0 V to +1.0 V, 50 mV/s, 10 cycles). The SEM images in Fig. 3.3A show distributed spherical particles on the carbon fiber which are not present on an unmodified CFME (Fig. 3.2). From Fig. 3.3B, which is the enlarged image of CNH/CFME, these CNHs are between 80–120 nm, which is consistent with the reported diameter of the dahlia-aggregated CNHs.[2] This spherical shape and size is also similar to other reported literature on the CNH-modified electrodes[34,35] and CNH assemblies.[36] Therefore, these SEM images confirm that CV electrodeposition technique is an appropriate technique to prepare CNH/CFME. CNH particles did not completely cover the carbon-fiber surface, even when the CNH concentration or electrodeposition cycles were increased. Instead, using higher CNH concentrations led to agglomeration of the dahlia-CNHs, and resulted in thicker, but uneven coatings which are undesirable for our electroanalytical application.[10]

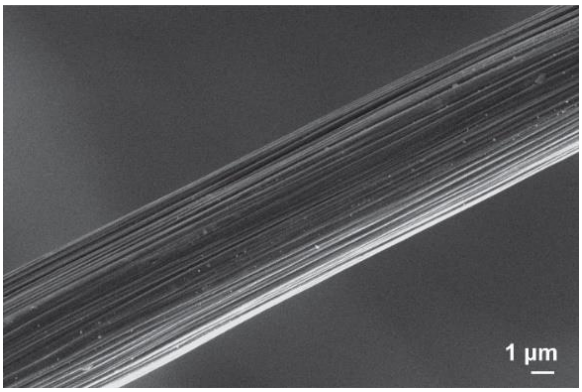

Fig. 3.2 SEM image of an unmodified CFME.

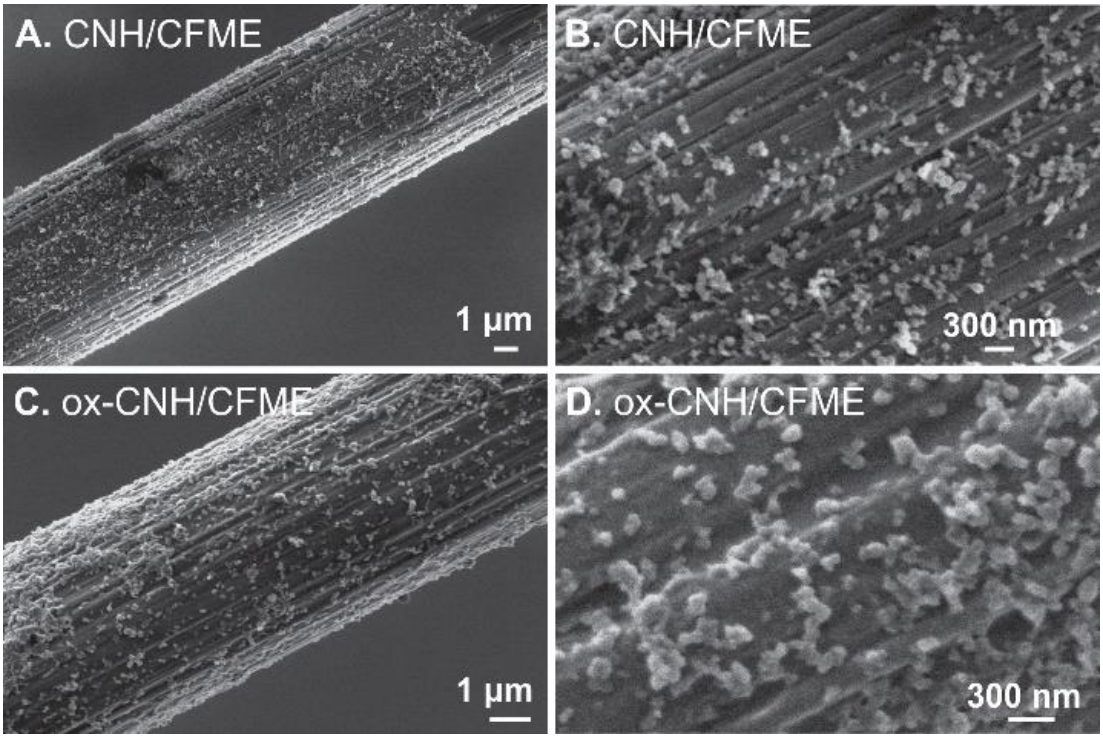

Fig. 3.3 SEM images show the electrodeposited CNHs on the CFME surface. (A-B) CNH/CFME prepared from electrodeposition of 0.5 mg/mL CNH using 10 cycles of CV scanned between –1.0 V to +1.0 V at a scan rate of 50 mV/s. (C-D) ox-CNH/CFME prepared from the oxidative etching of CNH/CFME in 1 M NaOH at a constant potential of +1.5 V vs. Ag/AgCl for 1.5 min.

Fig. 3.4 shows FSCV detection of 1 µM dopamine before and after electrodeposition of CNHs. From the representative cyclic voltammogram (Fig. 3.4A), CNHs enhanced the dopamine anodic peak current from 20 nA to about 50 nA, an increase of 2.5-fold. The cathodic current also increased by the same magnitude. The background current, or charging current, is proportional to the electrode surface area and specific capacitance of the electrode material.[37] From Fig. 3.4B, the background current increased from about 500 nA to 750 nA, about 1.5-fold, at this particular electrode. The magnitude of background current increase is less than that of the peak current. The other features of the CV, including ΔE_p, and ratio of anodic to cathodic peak did not obviously change, which implies that there is no electrocatalytic effect of CNHs.

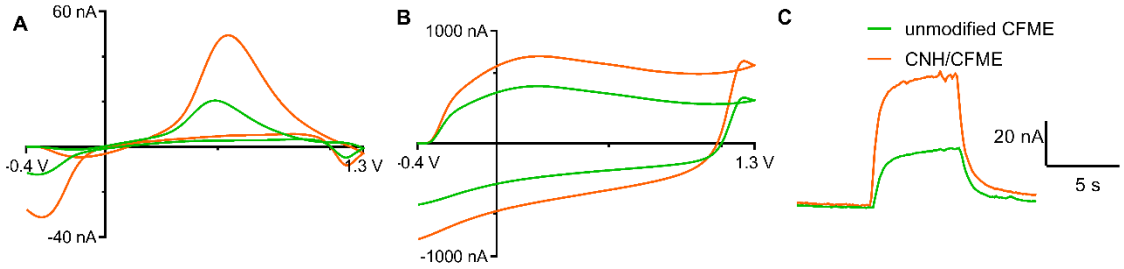

Fig. 3.4 Example data before and after CNH deposition. FSCV response from unmodified CFME (green line) and CNH/CFME (orange line) prepared from the electrodeposition of 0.5 mg/mL CNH using 10 cycles of CV scanned between –1.0 V to +1.0 V at a scan rate of 50 mV/s. (A) background-subtracted CV of 1 µM dopamine, (B) background current in PBS pH 7.4, and (C) current vs. time trace of bolus injection of 1 µM dopamine.

3.3.2 Optimization of CNH Electrodeposition

We optimized the CNH electrodeposition process by varying the concentration of CNHs in the dispersion and the number of electrodeposition cycles. In Fig. 3.5A, electrodeposition was performed in CNH dispersions at concentrations from 0.1 to 1.5 mg/mL and there was a significant main effect of CNH concentration on the anodic peak current for 1 µM dopamine (one-way ANOVA, $p < 0.001$, n = 4-6). The control here is blank electrodeposition, where the electrodeposition waveform was applied to the CFME in the solvent without CNHs. All CNH concentrations above 0.1 mg/mL significantly increased the anodic peak current of 1 µM dopamine compared to control (Bonferonni post-test, n = 4–6). The anodic peak current increased with increasing CNH concentration from 0.1 to 0.5 mg/mL, but then plateaued or even decreased slightly after that. The background current also significantly increased with CNH concentration (one-way ANOVA, $p < 0.05$, n = 4-6, Fig. 3.6A), thus the cause of the plateau is likely a thicker, multilayer CNH deposition with higher concentrations. Here, our result indicates 0.5 mg/mL as the optimum concentration of CNH and this was used in all further experiments.

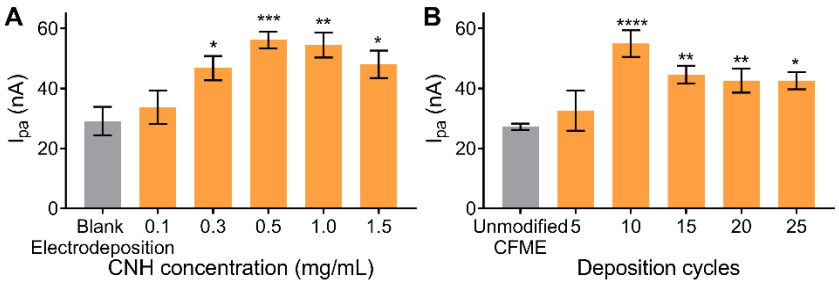

Fig. 3.5 Optimization of CNH deposition parameters. Average 1 µM dopamine anodic peak currents for CNH/CFME preparation. (A) Effect of CNH concentration while using 10 cycles of electrodeposition waveform. Blank electrodeposition was used as a control; the electrodeposition waveform was applied to a CFME in the solvent without CNHs. (B) Effect of number of deposition cycles while using 0.5 mg/mL CNH dispersion. Unmodified CFME was used as a control. (n = 4–6, error bars represent SEM, one-way ANOVA with Bonferroni post-test compared to the control (gray bars). *p < 0.05, **p < 0.01, ***p < 0.001, ****p < 0.0001)

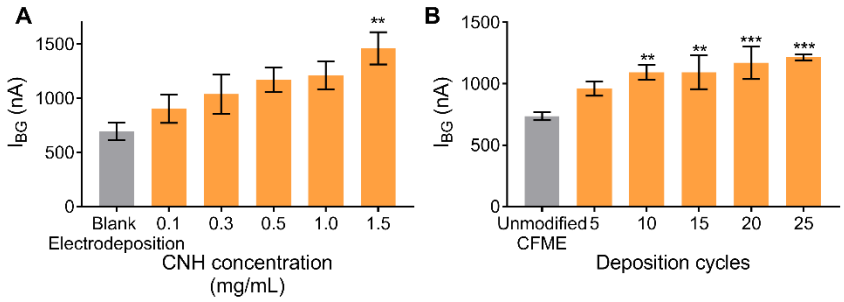

Fig. 3.6 Background currents obtained in PBS pH 7.4 for optimization of CNH deposition parameters. (A) Effect of CNH concentration while using 10 cycles of electrodeposition waveform. Blank electrodeposition was used as a control; the electrodeposition waveform was applied to a CFME in the solvent without CNHs. (B) Effect of number of deposition cycles while using 0.5 mg/mL CNH dispersion. Unmodified CFME was used as a control. (n = 4–6, error bars represent SEM, one-way ANOVA with Bonferonni post-test compared to the control (gray bars), *p < 0.05, **p < 0.01, ***p < 0.001)

Fig. 3.5B shows the effect of number of deposition cycles, from 5 cycles to 25 cycles. The control is an unmodified CFME. There is a significant main effect of number of deposition cycles (one-way ANOVA, p < 0.0001, n = 4-6). Increasing from 5 to 10 cycles enhances the anodic peak current of the CNH/CFME because using higher number of deposition cycles provides more time for negatively-charged CNHs to be electrodeposited

on the CFME. However, the response plateaus after 10 cycles, despite the fact that the background keeps increasing (Fig. 3.6B), likely because the thicker coating layer would not all be accessible for electrochemical reactions. CVs are noisier when CNH/CFMEs are prepared with higher number of electrodeposition cycles or CNH concentrations. This noise may come from the agglomeration of CNH particles on the electrode surface or in the dispersion and noise is proportional to background current and electrode surface area. [38] Therefore, the optimized number of electrodeposition cycles is 10 cycles.

In addition, a dip coating control was performed by dipping the CFME in the 0.5 mg/mL without applying a potential. Immersing the CFME in CNH dispersion for 800 s (the same length of time as 10 cycles of electrodeposition) caused no effect as the anodic peak currents for dopamine before (26 ± 4 nA) and after dip coating (27 ± 4 nA) were not significantly different (paired *t*-test, $p = 0.898$, $n = 5$). Thus, electrodeposition is crucial to coat the CNHs on the carbon-fiber surface.

The optimized CNH/CFME was electrochemically characterized and average data from five electrodes is shown in Table 3.1. CNH/CFME has a 2.3 ± 0.2 times higher anodic peak current than CFME and a 1.5 ± 0.1 times higher background current. The LOD was found by determining the concentration of dopamine giving signal-to-noise ratio (S/N) of 3. Because CNH/CFME gives higher noise than CFME due to greater surface area, the LOD (11 ± 1 nM) is only slightly smaller and not significantly different than that of CFME (15 ± 1 nM) (unpaired *t*-test, $p = 0.095$, $n = 4$). Other electrochemical parameters, including anodic-cathodic peak separation (ΔE_p), anodic-cathodic peak current ratio (i_{pa}/i_{pc}), and rise time are not different between CNH/CFME and unmodified CFME. The LOD of CNH/CFME is compared with previous literature in Table 3.2. Our electrode has better LOD than previous CNH-modified screen-printed[28] and glassy carbon electrodes[29]

because of less agglomeration from electrodeposition compared to drop-casting. The LOD is also better than other CNT or graphene-modified electrodes prepared from other techniques.[16,39,40]

Table 3.1 Average electrochemical response to 1 µM dopamine and limit of detection for dopamine at unmodified CFME, CNH/CFME, and ox-CNH/CFME (n = 5).

Electrode	Peak current enhancement[a]	Background enhancement	ΔE_p (mV)	i_{pa}/i_{pc}	rise time[b] (s)	LOD (nM)
CFME	1 (defined)	1 (defined)	832 ± 2	1.65 ± 0.05	1.1 ± 0.1	15 ± 1
CNH/CFME	2.3 ± 0.2	1.5 ± 0.1	835 ± 2	1.68 ± 0.05	1.1 ± 0.2	11 ± 1
ox-CNH/CFME	3.5 ± 0.1	1.6 ± 0.3	825 ± 10	1.63 ± 0.05	1.1 ± 0.1	6 ± 2

[a] ratio of the anodic peak current obtained from modified electrode to that obtained from unmodified CFME.
[b] time from 10% to 90% of the peak current

Table 3.2 LOD for dopamine detection compared at several carbon nanohorn-electrochemical sensors.

Electrode material	Technique[a]	LOD	Ref.
CNH/CFME	FSCV	15 nM	This work
ox-CNH/CFME	FSCV	6 nM	This work
CNH/glassy carbon electrode	LSV	60 nM	[29]
CNH/screen-printed carbon electrode	DPV	100 nM	[28]
oxidized CNH/ screen-printed carbon electrode	DPV	400 nM	[28]

[a] FSCV = fast-scan cyclic voltammetry, LSV = linear seep voltammetry, DPV = differential pulse voltammetry

CNHs form a dahlia-like aggregate on the carbon-fiber surface. Each dahlia particle has a spherical shape with rough, porous surface, which provide interstitial surface area to adsorb dopamine on the electrode surface.[1,7] The sparse, monolayer of CNHs on the carbon-fiber surface is similar to that of CNTs grown on metal electrode.[21] This morphology provides a more accessible surface area for electroactive species, and leads

to increases in redox current. Because the dopamine redox reaction at carbon-based microelectrode is adsorption-controlled,[41] the peak current increase should be proportional to the surface area increase, which can be estimated from the background charging current, assuming the carbon nanohorns and fibers have the same capacitance.[37] As shown in Fig. 3.4 and Table 3.1, CNH/CFMEs have a higher increase in Faradaic current than background current. Thus, CNHs enhance the specific adsorption of dopamine on the CNH/CFME surface in addition to increasing the surface area. Previous computer simulation and adsorption modeling suggest that CNHs have a high electric field at their cone tips, which also have defect sites containing surface oxide groups.[1,2,7] Hence, the CNH tips, which point radially outward from the aggregate center, enhance the dopamine adsorption. However, CNHs do not show electrocatalytic effect for dopamine redox reaction at CNH/CFME and thus peak potentials are not changed.

3.3.3 Surface Characterization and Optimization of Oxidative Etching

The CNH/CFME was further modified to improve the sensitivity toward dopamine detection by oxidative etching. This process generates defects in carbon microstructure and increases the amount of surface oxides.[21,42] The procedure was adapted from a study which oxidatively etched a vertically-aligned CNT-sheathed CFME for neurotransmitter detection.[43] The optimized CNH/CFME was oxidized by applying a constant potential of +1.5 V vs. Ag/AgCl in 1 M NaOH. Fig. 3.3C-D shows the SEM images of ox-CNH/CFME. No difference is observed in the morphology of the carbon-fiber or deposited CNHs between CNH/CFME and ox-CNH/CFME, which is expected because the oxidative etching should be on a smaller scale. Raman spectra were compared (Fig. 3.7) before and after etching to evaluate the intensity ratio of the D (defect) band around 1350 cm^{-1}

and the G (graphitic) band around 1580 cm^{-1}. The D/G ratio indicates proportion of the sp^3-hybridized carbons compared to that of sp^2-hybridized carbons.[12,21] The D/G ratio of ox-CNH/CFME (3.1 ± 0.1) is significantly higher than that ratio of CNH/CFME (2.7 ± 0.1) (unpaired *t*-test, $p < 0.05$, $n = 4$), so the ox-CNH/CFME has more defect sites or edge planes than CNH/CFME and can lead to increased dopamine adsorption.[11,14]

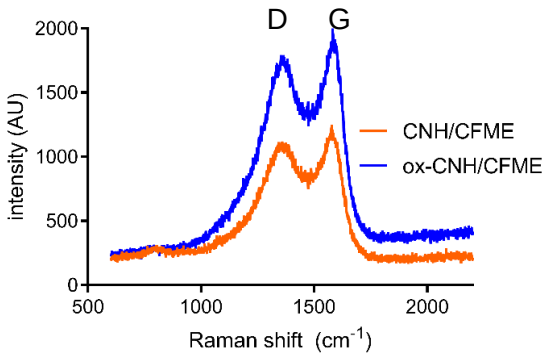

Fig. 3.7 Raman spectra of CNH/CFME prepared from the electrodeposition of 0.5 mg/mL CNH using 10 cycles of CV scanned between –1.0 V to +1.0 V at a scan rate of 50 mV/s and ox-CNH/CFME prepared from the oxidative etching of CNH/CFME in 1 M NaOH at a constant potential of +1.5 V vs. Ag/AgCl for 90 s.

Fig. 3.8 shows the electrochemical response of ox-CNH/CFME compared to that of CNH/CFME. In Fig. 3.8A, the anodic peak current of 1 µM dopamine at ox-CNH/CFME is increased from 50 nA to 75 nA, or about 1.5 times that of the CNH/CFME. The cathodic peak current also increases by the same magnitude. The peaks are shifted about 200 mV in the positive direction after oxidation. The background current of the ox-CNH/CFME is almost unchanged, from 960 nA to 980 nA after etching (Fig. 3.8B), and the background peaks are also positively shifted. The time response trace for ox-CNH/CFME and CNH/CFME to an injection of dopamine are not different from each other, showing that a fast time response is maintained after oxidation (Fig. 3.8C). As a control, unmodified CFMEs were also applied the +1.5 V constant potential for 90 s in 1 M NaOH. The anodic peak current for dopamine after the oxidation (34 ± 3 nA) is not significantly changed from

the unmodified CFME (30 ± 2 nA) (paired *t*-test, p = 0.071, n = 5), indicating that the current increase of ox-CNH/CFME is due to oxidation of the CNHs.

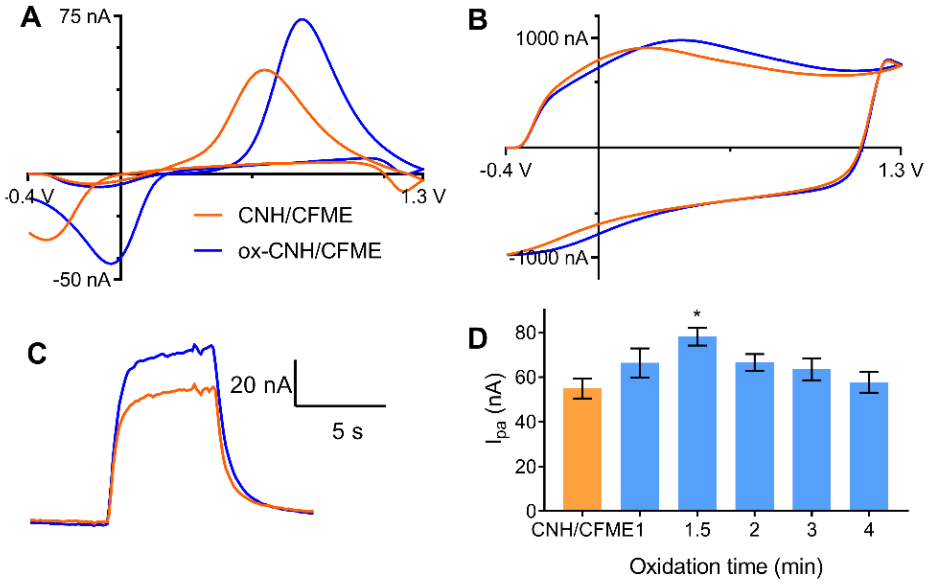

Fig. 3.8 Oxidized CNH electrodes. (A-C). FSCV response of ox-CNH/CFME (blue line) prepared from 1.5-min oxidative etching of the optimized CNH/CFME (orange line). (A) background-subtracted CV of 1 µM dopamine, (B) background current in PBS pH 7.4, and (C) current vs. time trace in response to a bolus of 1 µM dopamine. (D) Optimization of oxidative etching time, response is anodic current for 1 µM dopamine. (n = 4–6, error bars represent SEM, one-way ANOVA with Bonferroni post-test compared to CNH/CFME (an orange bar), *p < 0.05)

Fig. 3.8D shows the effect of varying the oxidative etching time from 1 to 4 min on the anodic peak current of 1 µM dopamine. There is a significant main effect of oxidation time on the anodic current (one-way ANOVA, p < 0.05, n = 4-6). The peak current of 1 µM dopamine at ox-CNH/CFME was maximal at 1.5 min and significantly higher than the non-oxidized CNH/CFME (Bonferonni post-test, p < 0.05, n = 4–6). The background current of ox-CNH/CFME is not affected by the oxidation time (Fig. 3.9) (one-way ANOVA, p = 0.891, n = 4-6), implying there are no changes in electrode surface area from oxidative etching.

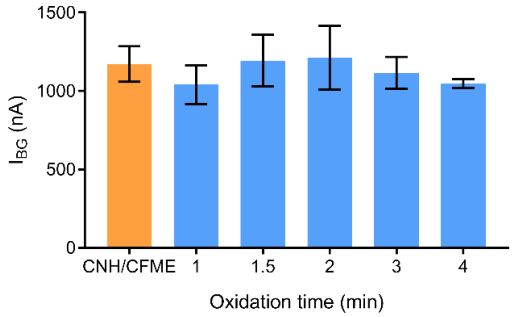

Fig. 3.9 Background currents obtained in PBS pH 7.4 for optimization of the oxidative etching of the optimized CNH/CFME. (n = 4–6, error bars represent SEM, one-way ANOVA with Bonferroni post-test compared to CNH/CFME (an orange bar))

The average electrochemical characterization data from the optimized ox-CNH/CFME with 1 µM dopamine are shown in Table 3.1. The dopamine peak current is increased from CNH/CFME by 1.5 times, or a total of 3.5 ± 0.2 times compared to unmodified CFME. The background current enhancement is 1.6 ± 0.3 times of the unmodified CFME, as the oxidation does not affect the background current significantly. The ΔE_p and i_{pa}/i_{pc} ratio of ox-CNH/CFME are also unchanged after the oxidative etching. The dopamine LOD for ox-CNH/CFME is 6 ± 2 nM, which is significantly improved from the CNH/CFME (unpaired *t*-test, $p < 0.01$, $n = 5$) while maintaining the same rise time (unpaired *t*-test, $p = 0.831$, $n = 5$).

The oxidation of CNHs has been performed by various methods including O_2,[4] H_2O_2,[3] or HNO_3.[36] These studies found the oxidation process opening the tips of each CNH creates sp^3-hybridized carbons and surface oxide groups.[3,4,36] The CNH tips have ring strain caused by pentagon nonplanar structure, so they are easier oxidized than the cone wall.[1] The oxidized CNHs, as shown in the TEM image in Fig. 3.1B, had looser and more opened dahlia-aggregated structure than the pristine CNHs. Our results indicate the increasing of D/G ratio of ox-CNH/CFME from that of CNH/CFME from Raman

spectroscopy, so the edge planes and surface oxide groups are created while the same surface area is maintained because of the unchanged background current. The increased oxide groups without a change in background improves the S/N ratio and the LOD, making the ox-CNH/CFME a better probe for FSCV detection of dopamine. The whole CV of the dopamine obtained from ox-CNH/CFME is positively shifted in potential from that of CNH/CFME by 200 mV (Fig. 3.8A). Because the etching process introduces oxide groups, which are negatively charged at pH 7.4, more positive charge is required to overcome the surface charge. This shifting is similar to a previous study on oxygen-plasma etched CNT yarn microelectrodes that also had shifted CVs.[27]

3.3.4 Analytical Performance of the ox-CNH/CFME

The electrochemical properties of ox-CNH/CFME were studied and analytical figures of merit obtained for dopamine. Fig. 3.10A-B illustrate the relationship between anodic peak current of dopamine with varied scan rate from 50 to 1000 V/s at the ox-CNH/CFME. The linearity of the peak current with scan rate (R^2 = 0.998) and not square root of scan rate (R^2 = 0.982) indicates that the dopamine redox reaction at ox-CNH/CFME is adsorption-controlled.[37] The result indicates the important role of ox-CNH/CFME surface, i.e. surface oxide groups, in dopamine adsorption.[11]

Fig. 3.10C shows the concentration dependence of dopamine anodic peak current at ox-CNH/CFME. The electrode was tested with 50 nM to 100 µM dopamine in PBS pH 7.4. The peak current was linear with dopamine concentration up to 5 µM (R^2 = 0.987), or two orders of magnitudes from 50 nM, as shown in Fig. 3.10D. At higher concentration, the peak current deviates from linearity because all the surface sites are occupied and the dopamine redox reaction could become diffusion-controlled, as supported by the shape of

CV of 100 μM dopamine (Fig. 3.10E). The CV of adsorption-controlled electron transfer has symmetrical peak shapes because the process is similar to the thin-layer electrochemical cell condition, while the CV peak of diffusion-controlled process is unsymmetrical, and has the more traditional “duck-like” shape.[37] This saturation is similar to the previous work,[41] which found that redox reaction at CFMES is diffusion-controlled at higher dopamine concentrations. In addition, the CV of 50 nM is shown (Fig. 3.10E) to demonstrate the potential of the ox-CNH/CFME to detect dopamine at a very low concentration near the LOD.

In biological experiments, neurotransmitters are usually monitored for several hours. To investigate the stability and reproducibility of ox-CNH/CFME in dopamine detection, the FSCV waveform was continuously applied to the electrode, and the anodic peak current of dopamine was measured every 2 h for 8 h. Fig. 3.10F shows that the peak current does not dramatically change throughout the experiment. The relative standard deviation (RSD) of the peak current at the same electrode is 7.4 $\pm$ 1.0% (n = 3). These results confirm good stability of the ox-CNH/CFME and indicate that the deposited CNH on the carbon-fiber surface does not fall off the electrode, even when it is scanned for a long period of time.

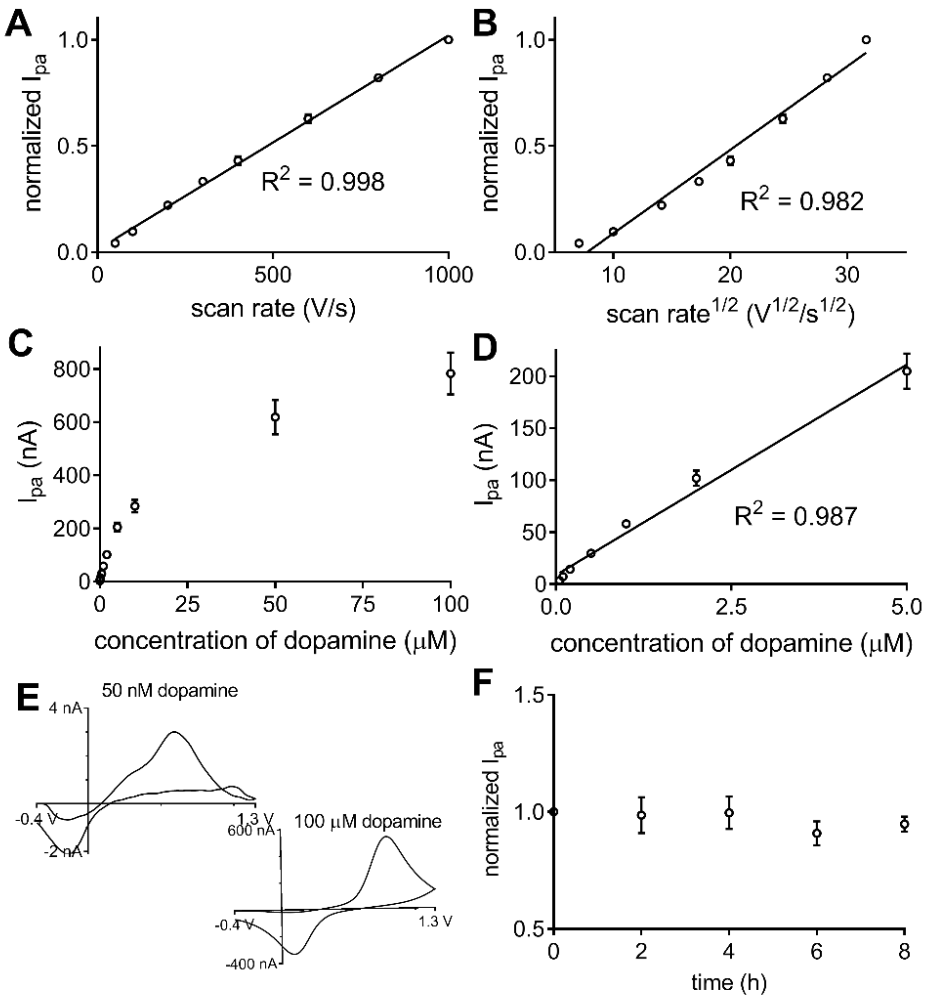

Fig. 3.10 Analytical performance of ox-CNH/CFME. (A-B) Scan rate dependence. Anodic peak current of 1 µM dopamine is plotted vs (A) scan rate or (B) square root of scan rate *(n* = 4*)*. The plot is more linear vs scan rate indicating adsorption-controlled kinetics. (C-D) Concentration dependence. (C) Plot of anodic peak current vs. dopamine concentration from 50 nM to 100 µM (*n* = 4). (D) The current is linear from 50 nM to 5 µM *(n* = 4*)*. (E) Example CVs of 50 nM and 100 µM dopamine in PBS pH 7.4. (F) Stability. Peak current was stable when dopamine was measured every 2 h for 8 h *(n* = 3*)*. FSCV waveform was continuously applied. Error bars represent SEM.

We also examined the FSCV response from ox-CNH/CFME toward other neurochemicals including epinephrine, norepinephrine, serotonin, and ascorbic acid (Fig. 3.11). In general, the whole CV of all neurochemicals (Fig. 3.11A-D) shifts positively from

CV obtained at the unmodified CFME, similar to that of dopamine (Fig. 3.11A), due to the surface charge. The cationic neurotransmitters epinephrine, norepinephrine, and serotonin had similar peak current enhancements (2.8 ± 0.1 times for epinephrine (Fig. 3.11A), 2.1 ± 0.2 times for norepinephrine (Fig. 3.11B), and 2.2 ± 0.2 times for serotonin (Fig. 3.11C). Ascorbic acid is an anion with a high concentration in biological matrixthat can interfere electrochemical analysis.[44] Fig. 3.11D shows that the current enhancement of ascorbic acid (1.4 ± 0.1 times) is significantly less than that of dopamine (unpaired *t*-test, $p < 0.0001$, $n = 4$) because of the electrostatic repulsion between negatively-charged ascorbic acid and surface oxide groups on ox-CNH/CFME. The current enhancement of ascorbic acid is likely only caused by electrode surface area increase. These differences in the current enhancements show the enhanced selectivity of ox-CNH/CFME towards cations.

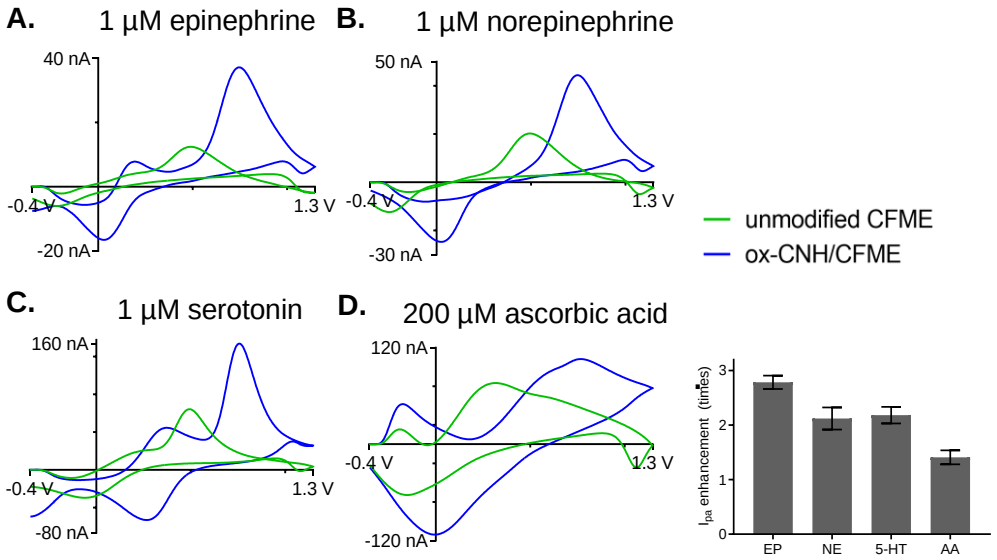

Fig. 3.11 Response to other neurochemicals. Response of ox-CNH/CFME (blue line) compared with unmodified CFME (green line). (A) 1 µM epinephrine (EP), (B) 1 µM norepinephrine (NE), (C) 1 µM serotonin (5-HT), and (D) 200 µM ascorbic acid (AA) in PBS pH 7.4. (E) anodic peak current enhancement at ox-CNH/CFME (compared to unmodified CFME ($n = 4$)). Error bars represent SEM.

A smaller peak was observed at about +0.4 V in the CV of epinephrine and serotonin ox-CNH/CFME. This peak corresponds to a cyclization of their quinone form via 1,4-Michael addition yielding leucoaminochromes.[45,46] The peak is observed at ox-CNH/CFME but not CFME because the quinone form, which is the oxidation products of those catecholamines, are adsorbed in the interstitial pore and tips of CNHs. Therefore, the products have longer time at the electrode surface and can undergo another electron transfer causing such cyclization. However, dopamine and norepinephrine have lower cyclization rate constant,[47] so their cyclization peaks were not observed.

One concern for possible use of microelectrodes *in vivo* is the fouling of the surface from proteins or from oxidation products of compounds, such as serotonin which can polymerize after oxidation.[48] The resistance of ox-CNH/CFME toward biofouling was determined by comparing the anodic peak current of 1 μM dopamine from the electrode before and after placing the electrode in the brain slice tissue (prepared by Scott Lee) for 2 h. The current after fouling (39 ± 5 nA) significantly decreases from original current (64 ± 3 nA) (paired *t*-test, $p < 0.005$, $n = 4$). However, the decrease is only about 40%, which is less than the decrease observed at unmodified CFMEs, where the dopamine anodic current decreased by 70%.[49] The background current at ox-CNH/CFME before (1080 ± 240 nA) and after biofouling (960 ± 140 nA) is not significantly different (paired *t*-test, $p = 0.500$, $n = 4$), consistent with our previous studies of oxygen plasma etched-CNT yarn microelectrode.[27] Edge planes and surface oxide groups from CNHs and oxidative etching increase the hydrophilicity of the electrode surface, which decreases the irreversible protein adsorption generally caused by hydrophobic interactions.[50] Higher hydrophilicity also increases wetting at the electrode surface, which helps to maintain the reproducibility

of the response and for CNHs to stay on the CFME surface. Future studies can test the performance of these CNH electrodes *in vivo*, but the resistance to biofouling will help maintain the signal enhancements in tissue.

3.4 Conclusions

We have optimized electrodeposition of carbon nanohorns to enhance the signal for dopamine using FSCV. The signal is further improved by oxidative etching that introduces more defect sites and surface oxide groups to enhance dopamine adsorption. Overall, the current for dopamine improves 3.5-time higher than unmodified CFME and the LOD is 6 nM, while the rapid time response is maintained, and the measurements are stable for 8 h, longer than a typical biological experiment. In addition, ox-CNH/CFME increased the signal from other cationic neurotransmitters including epinephrine, norepinephrine, and serotonin but not the anionic interferent ascorbic acid, demonstrating improved selectivity. Oxidized CNHs also improved the biofouling resistance of the microelectrode. Overall, CNHs are a promising nanomaterial to enhance sensitivity and selectivity for cationic neurotransmitters.

3.5 References

(1) Berber, S.; Kwon, Y.-K.; Tománek, D. Electronic and Structural Properties of Carbon Nanohorns. *Phys. Rev. B* **2000**, *62* (4), R2291–R2294.

(2) Karousis, N.; Suarez-Martinez, I.; Ewels, C. P.; Tagmatarchis, N. Structure, Properties, Functionalization, and Applications of Carbon Nanohorns. *Chem. Rev.* **2016**, *116* (8), 4850–4883.

(3) Xu, J.; Zhang, M.; Nakamura, M.; Iijima, S.; Yudasaka, M. Double Oxidation with Oxygen and Hydrogen Peroxide for Hole-Forming in Single Wall Carbon Nanohorns. *Appl. Phys. A Mater. Sci. Process.* **2010**, *100*, 379–383.

(4) Yang, C. M.; Kim, Y. J.; Miyawaki, J.; Kim, Y. A.; Yudasaka, M.; Iijima, S.; Kaneko, K. Effect of the Size and Position of Ion-Accessible Nanoholes on the Specific Capacitance of Single-Walled Carbon Nanohorns for Supercapacitor Applications. *J. Phys. Chem. C* **2015**, *119* (6), 2935–2940.

(5) Wang, X.; Lou, M.; Yuan, X.; Dong, W.; Dong, C.; Bi, H.; Huang, F. Nitrogen and Oxygen Dual-Doped Carbon Nanohorn for Electrochemical Capacitors. *Carbon* **2017**, *118*, 511–516.

(6) Iijima, S.; Yudasaka, M. Nano-Aggregates of Single-Walled Graphitic Carbon Nano-Horns. *Chem. Phys. Lett.* **1999**, *309*, 165–170.

(7) Russell, B. A.; Migone, A. D.; Petucci, J.; Calbi, M. M. Ethane Adsorption on Aggregates of Dahlia-like Nanohorns : Experiments and Computer Simulations. *Phys. Chem. Chem. Phys.* **2016**, *18*, 15436–15446.

(8) Ajima, K.; Murakami, T.; Mizoguchi, Y.; Tsuchida, K.; Ichihashi, T.; Iijima, S.; Yudasaka, M. Enhancement of in Vivo Anticancer Effects of Cisplatin by Incorporation inside Single-Wall Carbon Nanohorns. *ACS Nano* **2008**, *2* (10), 2057–2064.

(9) Zhang, Z.; Han, S.; Wang, C.; Li, J.; Xu, G. Single-Walled Carbon Nanohorns for Energy Applications. *Nanomaterials* **2015**, *5*, 1732–1755.

(10) Yang, C.; Denno, M. E.; Pyakurel, P.; Venton, B. J. Recent Trends in Carbon Nanomaterial-Based Electrochemical Sensors for Biomolecules: A Review. *Anal. Chim. Acta* **2015**, *887*, 17–37.

(11) McCreery, R. L. Advanced Carbon Electrode Materials for Molecular Electrochemistry. *Chem. Rev.* **2008**, *108* (7), 2646–2687.

(12) Georgakilas, V.; Perman, J. A.; Tucek, J.; Zboril, R. Broad Family of Carbon Nanoallotropes: Classification, Chemistry, and Applications of Fullerenes, Carbon Dots, Nanotubes, Graphene, Nanodiamonds, and Combined Superstructures. *Chem. Rev.* **2015**, *115* (11), 4744–4822.

(13) Yang, L.; Liu, D.; Huang, J.; You, T. Simultaneous Determination of Dopamine, Ascorbic Acid and Uric Acid at Electrochemically Reduced Graphene Oxide Modified Electrode. *Sens. Actuators, B* **2014**, *193*, 166–172.

(14) Banks, C. E.; Compton, R. G. New Electrodes for Old: From Carbon Nanotubes to Edge Plane Pyrolytic Graphite. *Analyst* **2006**, *131* (1), 15–21.

(15) E, S. P.; Miller, T. S.; Macpherson, J. V.; Unwin, P. R. Controlled Functionalisation of Single-Walled Carbon Nanotube Network Electrodes for the Enhanced Voltammetric Detection of Dopamine. *Phys. Chem. Chem. Phys.* **2015**, *17* (39), 26394–26402.

(16) Jacobs, C. B.; Vickrey, T. L.; Venton, B. J. Functional Groups Modulate the Sensitivity and Electron Transfer Kinetics of Neurochemicals at Carbon Nanotube Modified Microelectrodes. *Analyst* **2011**, *136*, 3557–3565.

(17) Swamy, B. E. K.; Venton, B. J. Carbon Nanotube-Modified Microelectrodes for Simultaneous Detection of Dopamine and Serotonin in Vivo. *Analyst* **2007**, *132* (9), 876–884.

(18) Ross, A. E.; Venton, B. J. Nafion-CNT Coated Carbon-Fiber Microelectrodes for Enhanced Detection of Adenosine. *Analyst* **2012**, *137* (13), 3045–3051.

(19) Peairs, M. J.; Ross, A. E.; Venton, B. J. Comparison of Nafion- and Overoxidized Polypyrrole-Carbon Nanotube Electrodes for Neurotransmitter Detection. *Anal. Methods* **2011**, *3* (10), 2379–2386.

(20) Xiao, N.; Venton, B. J. Rapid, Sensitive Detection of Neurotransmitters at Microelectrodes Modified with Self-Assembled SWCNT Forests. *Anal. Chem.* **2012**, *84*, 7816–7822.

(21) Yang, C.; Jacobs, C. B.; Nguyen, M. D.; Ganesana, M.; Zestos, A. G.; Ivanov, I. N.; Puretzky, A. A.; Rouleau, C. M.; Geohegan, D. B.; Venton, B. J. Carbon Nanotubes Grown on Metal Microelectrodes for the Detection of Dopamine. *Anal. Chem.* **2016**, *88*, 645–652.

(22) Harreither, W.; Trouillon, R.; Poulin, P.; Neri, W.; Ewing, A. G.; Safina, G. Carbon Nanotube Fiber Microelectrodes Show a Higher Resistance to Dopamine Fouling. *Anal. Chem.* **2013**, *85* (15), 7447–7453.

(23) Zestos, A. G.; Nguyen, M. D.; Poe, B. L.; Jacobs, C. B.; Venton, B. J. Epoxy Insulated Carbon Fiber and Carbon Nanotube Fiber Microelectrodes. *Sens. Actuators, B* **2013**, *182*, 652–658.

(24) Yang, C.; Trikantzopoulos, E.; Jacobs, C. B.; Venton, B. J. Evaluation of Carbon Nanotube Fiber Microelectrodes for Neurotransmitter Detection: Correlation of Electrochemical Performance and Surface Properties. *Anal. Chim. Acta* **2017**, *965*, 1–8.

(25) Jacobs, C. B.; Ivanov, I. N.; Nguyen, M. D.; Zestos, A. G.; Venton, B. J. High Temporal Resolution Measurements of Dopamine with Carbon Nanotube Yarn Microelectrodes. *Anal. Chem.* **2014**, *86*, 5721–5727.

(26) Yang, C.; Trikantzopoulos, E.; Nguyen, M. D.; Jacobs, C. B.; Wang, Y.; Mahjouri-Samani, M.; Ivanov, I. N.; Venton, B. J. Laser Treated Carbon Nanotube Yarn Microelectrodes for Rapid and Sensitive Detection of Dopamine in Vivo. *ACS Sens.* **2016**, 508–515.

(27) Yang, C.; Wang, Y.; Jacobs, C. B.; Ivanov, I.; Venton, B. J. O2 Plasma Etching and Anti-Static Gun Surface Modifications for CNT Yarn Microelectrode Improve Sensitivity and Anti-Fouling Properties. *Anal. Chem.* **2017**, 5605–5611.

(28) Valentini, F.; Ciambella, E.; Boaretto, A.; Rizzitelli, G.; Carbone, M.; Conte, V.; Cataldo, F.; Russo, V.; Casari, C. S.; Chillura-Martino, D. F.; et al. Sensor Properties of Pristine and Functionalized Carbon Nanohorns. *Electroanalysis* **2016**, *28* (10), 2489–2499.

(29) Zhu, S.; Li, H.; Niu, W.; Xu, G. Simultaneous Electrochemical Determination of Uric Acid, Dopamine, and Ascorbic Acid at Single-Walled Carbon Nanohorn Modified Glassy Carbon Electrode. *Biosens. Bioelectron.* **2009**, *25*, 940–943.

(30) Zhu, S.; Gao, W.; Zhang, L.; Zhao, J.; Xu, G. Simultaneous Voltammetric Determination of Dihydroxybenzene Isomers at Single-Walled Carbon Nanohorn Modified Glassy Carbon Electrode. *Sens. Actuators, B* **2014**, *198*, 388–394.

(31) Huffman, M. L.; Venton, B. J. Electrochemical Properties of Different Carbon-Fiber Microelectrodes Using Fast-Scan Cyclic Voltammetry. *Electroanalysis* **2008**, *20* (22), 2422–2428.

(32) Zhang, Y.; Ji, Y.; Wang, Z.; Liu, S.; Zhang, T. Electrodeposition Synthesis of Reduced Graphene Oxide-Carbon Nanotube Hybrids on Indium Tin Oxide Electrode for Simultaneous Electrochemical Detection of Ascorbic Acid, Dopamine and Uric Acid. *RSC Adv.* **2015**, *5*, 106307–106314.

(33) Oakes, L.; Westover, A.; Mahjouri-Samani, M.; Chatterjee, S.; Puretzky, A. A.; Rouleau, C.; Geohegan, D. B.; Pint, C. L. Uniform, Homogenous Coatings of Carbon Nanohorns on Arbitrary Substrates from Common Solvents. *ACS Appl. Mater. Interfaces* **2013**, *5*, 13153–13160.

(34) Zhang, L.; Lei, J.; Zhang, J.; Ding, L.; Ju, H. Amperometric Detection of Hypoxanthine and Xanthine by Enzymatic Amplification Using a Gold Nanoparticles–Carbon Nanohorn Hybrid as the Carrier. *Analyst* **2012**, *137* (13), 3126–3131.

(35) Zhu, S.; Zhao, X.; Chen, G.; Wang, H.; Xu, G.; You, J. Electrochemical Behavior and Voltammetric Determination of Dihydronicotinamide Adenine Dinucleotide Using a Glassy Carbon Electrode Modified with Single-Walled Carbon Nanohorns. *Ionics* **2015**, *21*, 2911–2917.

(36) Yang, C. M.; Noguchi, H.; Murata, K.; Yudasaka, M.; Hashimoto, A.; Iijima, S.; Kaneko, K. Highly Ultramicroporous Single-Walled Carbon Nanohorn Assemblies. *Adv. Mater.* **2005**,

17, 866–870.

(37) Bard, A. J.; Faulkner, L. R. *Electrochemical Methods: Fundamentals and Applications*, 2nd ed.; John Wiley and Sons: New York, 2001.

(38) Morgan, D. M.; Weber, S. G. Noise and Signal-to-Noise Ratio in Electrochemical Detectors. *Anal. Chem.* **1984**, *56* (13), 2560–2567.

(39) Rodthongkum, N.; Ruecha, N.; Rangkupan, R.; Vachet, R. W.; Chailapakul, O. Graphene-Loaded Nanofiber-Modified Electrodes for the Ultrasensitive Determination of Dopamine. *Anal. Chim. Acta* **2013**, *804*, 84–91.

(40) Ding, X.; Bai, J.; Xu, T.; Li, C.; Zhang, H.-M.; Qu, L. A Novel Nitrogen-Doped Graphene Fiber Microelectrode with Ultrahigh Sensitivity for the Detection of Dopamine. *Electrochem. Commun.* **2016**, *72*, 122–125.

(41) Bath, B. D.; Michael, D. J.; Trafton, B. J.; Joseph, J. D.; Runnels, P. L.; Wightman, R. M. Subsecond Adsorption and Desorption of Dopamine at Carbon-Fiber Microelectrodes. *Anal. Chem.* **2000**, *72* (24), 5994–6002.

(42) Takmakov, P.; Zachek, M. K.; Keithley, R. B.; Walsh, P. L.; Donley, C.; McCarty, G. S.; Wightman, R. M. Carbon Microelectrodes with a Renewable Surface. *Anal. Chem.* **2010**, *82* (5), 2020–2028.

(43) Xiang, L.; Yu, P.; Hao, J.; Zhang, M.; Zhu, L.; Dai, L.; Mao, L. Vertically Aligned Carbon Nanotube-Sheathed Carbon Fibers as Pristine Microelectrodes for Selective Monitoring of Ascorbate in Vivo. *Anal. Chem.* **2014**, *86* (8), 3909–3914.

(44) Robinson, D. L.; Venton, B. J.; Heien, M. L. A. V; Wightman, R. M. Detecting Subsecond Dopamine Release with Fast-Scan Cyclic Voltammetry in Vivo. *Clin. Chem.* **2003**, *49* (10), 1763–1773.

(45) Palomäki, T.; Chumillas, S.; Sainio, S.; Protopopova, V.; Kauppila, M.; Koskinen, J.; Climent, V.; Feliu, J. M.; Laurila, T. Electrochemical Reactions of Catechol, Methylcatechol and Dopamine at Tetrahedral Amorphous Carbon (Ta-C) Thin Film Electrodes. *Diam. Relat. Mater.* **2015**, *59*, 30–39.

(46) Chen, S. M.; Chen, J. Y.; Vasantha, V. S. Electrochemical Preparation of Epinephrine/Nafion Chemically Modified Electrodes and Their Electrocatalytic Oxidation of Ascorbic Acid and Dopamine. *Electrochim. Acta* **2006**, *52* (2), 455–465.

(47) Hu, M.; Fritsch, I. Application of Electrochemical Redox Cycling: Toward Differentiation of Dopamine and Norepinephrine. *Anal. Chem.* **2016**, *88* (11), 5574–5578.

(48) Harreither, W.; Trouillon, R.; Poulin, P.; Neri, W.; Ewing, A. G.; Safina, G. Cysteine Residues Reduce the Severity of Dopamine Electrochemical Fouling. *Electrochim. Acta* **2016**, *210*, 622–629.

(49) Singh, Y. S.; Sawarynski, L. E.; Dabiri, P. D.; Choi, W. R.; Andrews, A. M. Head-to-Head Comparisons of Carbon Fiber Microelectrode Coatings for Sensitive and Selective Neurotransmitter Detection by Voltammetry. *Anal. Chem.* **2011**, *83* (17), 6658–6666.

(50) Downard, A. J.; Roddick, A. D. Protein Adsorption at Glassy Carbon Electrodes: The Effect of Covalently Bound Surface Groups. *Electroanalysis* **1995**, *7* (4), 376–378.

CHAPTER 4

Nanodiamond Coating Improves the Sensitivity and Antifouling Properties of Carbon-Fiber Microelectrodes

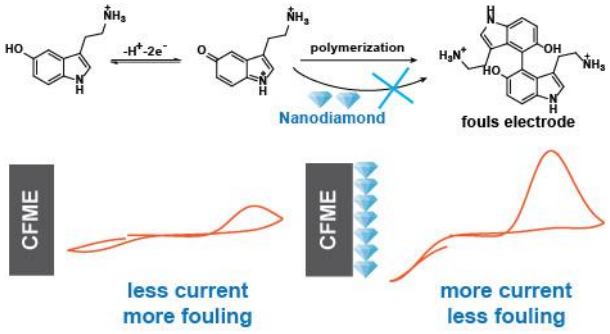

Chapter 4 was reprinted from *ACS Sens.* **2019,** *4,* 2403-2411.

Abstract

Nanodiamonds (NDs) are carbon nanomaterials with a core diamond crystalline structure and crystal defects, such as graphitic carbon and heteroatoms, on their surface. For electrochemistry, NDs are promising to increase active sites and decrease fouling, but NDs have not been studied for neurotransmitter electrochemistry. Here, we optimized ND coatings on microelectrodes and found that ND increases the sensitivity for neurotransmitters with fast-scan cyclic voltammetry detection and decreases electrochemical and biofouling. Different sizes and functionalizations of NDs were tested, and ND suspensions were drop-casted onto carbon-fiber microelectrodes (CFMEs). The 5-nm ND-H and 5 nm ND-COOH formed thick coatings, while the 15 and 60 nm ND-COOH formed more sparse coatings. With electrochemical impedance spectroscopy, 5 nm ND-H and 5 nm ND-COOH had high charge-transfer resistance, while 15 and 60 nm ND-COOH had low charge-transfer resistance. The 15-nm ND-COOH was optimal, with the best electrocatalytic properties and current for dopamine. Sensitivity was enhanced 2.1 ± 0.2 times and the limit of detection for dopamine improved to 3 ± 1 nM. ND coating increased current for other cations such as serotonin, norepinephrine, and epinephrine, but not for the anion ascorbic acid. Moreover, NDs decreased electrochemical fouling from serotonin and 5-hydroxyindoleacetic acid, and they also decreased biofouling in brain slice tissue by 50%. The current at biofouled ND-coated electrodes is similar to the signal of pristine, unfouled CFMEs. The carboxylated ND-modified CFMEs are beneficial for neurotransmitter detection because of easy fabrication, improved limit of detection, and antifouling properties.

4.1 Introduction

Nanodiamonds (NDs) or diamond nanoparticles are a carbon nanomaterial which has a diamond crystalline core structure made up from sp^3-hybridized carbon atoms, with heteroatoms and defects at their surface.[1–3] NDs can be synthesized via several methods, but the most common method is the detonation of trinitrotoluene and hexogen explosives in controlled, oxygen-deficient, high pressure, and high temperature environment;[4,5] hence, this ND is called "detonation ND." NDs have particle diameters from 1 to 500 nm as synthesized,[5–8] but they can aggregate to form larger particles.[9] Although the same sp^3 core structure causes bulk diamond to be a perfect electrical insulator, NDs are electrically conductive.[6,10] The contrasting electrical behaviors between NDs and bulk diamond are due to the surface defects and terminal groups of NDs which contain sp^2-hybridized carbons such as C=C, C=O, and COOH.[10] When NDs are coated on commonly used electrodes such as gold or glassy carbon, NDs act as an electrocatalyst for redox reactions of electroactive species including $[Fe(CN)_6]^{3-/4-}$, $[Ru(NH_3)_6]^{3+/2+}$, and nitrite ion.[10–12] Holt proposed that the energy levels of oxide groups increase the density of state of NDs, facilitating electrical conductivity and electrocatalysis.[13] The small size of NDs leads to high specific surface area and also enhances the electrochemical activity.[14–17] However, ND has not been widely used as an electrode material and has not been examined in biological applications, such as for neurotransmitter detection.

The neurochemistry community typically utilizes carbon-fiber microelectrodes (CFMEs) as the standard electrochemical sensor for real-time *in vivo* detection of neurotransmitters.[2,18–22] Many carbon nanomaterials including graphene,[23,24] carbon nanotubes (CNTs),[25–28] and carbon nanohorns[29] have been coated or grown on CFMEs to enhance surface area, electrocatalytic properties, and dopamine adsorption by adding

edge plane carbons.[2,20,30,31] These properties enhance the faradaic current and signal-to-noise ratio, improving analytical performance for dopamine detection. Carbon nanomaterials that have high number of defects and oxygen-containing surface functional group that increase hydrophilicity also exhibit antifouling properties against biofouling and electrochemical fouling.[2,31,32] Biofouling typically occurs when proteins adhere to the electrode surface via electrostatic or hydrophobic interactions, decreasing sensitivity by decreasing the electroactive area.[2,33] Electrochemical fouling from redox reactions of other electroactive species such as serotonin (5-HT) and 5-hydroxyindoleacetic acid (5-HIAA) also diminishes the electrode sensitivity.[34–37] Boron-doped diamond (BDD) electrodes are popularly used to limit biofouling and electrochemical fouling because they have fewer surface functional groups that adsorb fouling products.[35,38–44] For example, BDD-coated Pt wires are used to measure serotonin in the harsh conditions of the gut because of their antifouling properties.[40] However, BDD does not promote dopamine adsorption and gives less electrochemical activity, especially toward surface-sensitive probes. NDs prevent dopamine electrochemical fouling[45] and suppress the lithium dendrite growth in rechargeable batteries.[8] NDs also have improved biocompatibility compared to nanotube-based materials,[46] and promote cell viability because their synthesis does not require metal catalysts, which are sometimes present in CNT and cause cell toxicity.[14] These potential antifouling properties, combined with their electrocatalytic and adsorption properties, make NDs a promising electrode material for biological applications.

In this paper, we develop ND-modified CFMEs (ND/CFMEs) and explore their properties for neurochemical detection using fast-scan cyclic voltammetry (FSCV). NDs are produced in various sizes and surface terminal groups, such as hydrogen-terminated

or carboxyl-terminated,[4] which may affect their surface properties.[1,13,47] We optimized a simple drop-casting technique to deposit NDs from aqueous dispersions on the CFME surface and compared 5 nm H-terminated and COOH-functionalized NDs as well as 15 and 60 nm COOH-functionalized NDs. Larger, carboxylated (15-60 nm) particles were optimal as they enhanced the dopamine faradaic current, improved the limit of detection (LOD) for dopamine, and had electrocatalytic properties. ND coatings were antifouling, as the current decayed much less after implantation in brain tissue than CFMEs. ND/CFMEs also resisted electrochemical fouling by serotonin and 5-HIAA. Overall, increased sensitivity and decreased chemical and biofouling make ND-modified electrodes promising for in tissue neurotransmitter sensing.

4.2 Experimental Section

4.2.1 Chemicals

Dopamine, epinephrine, norepinephrine, serotonin, 5-HIAA, ascorbic acid, and potassium ferricyanide were purchased from Acros Organics (Morris Plains, NJ). A 10 mM stock solution of each neurotransmitter was prepared in 0.1 M $HClO_4$. The final working solutions were prepared by diluting the stock solution in a phosphate-buffered saline (PBS) (131.25 mM NaCl, 3.00 mM KCl, 10 mM NaH_2PO_4, 1.2 mM $MgCl_2$, 2.0 mM Na_2SO_4, and 1.2 mM $CaCl_2$ with pH adjusted to 7.4) to the desired concentration.

4.2.2 Preparation of ND/CFMEs

Before preparing the modified electrodes, a cylindrical CFME was fabricated by the same procedure as previous work.[48] A T-650 carbon fiber (7-µm diameter, Cytec Engineering Materials, West Patterson, NJ) was pulled into a glass capillary (1.28 mm

inner diameter × 0.68 mm outer diameter, A-M Systems, Sequim, WA) by an aspirating pump. Then, the capillary was pulled by an electrode puller (model PE-21, Narishige, Tokyo, Japan) to get two electrodes. The extended fiber was cut to a length of about 100 µm. After that, each electrode was epoxied by dipping in an 80°C-solution of 14% *m*-phenylenediamine hardener (Acros Organics, Morris Plains, NH) in Epon Resin 828 epoxy (Miller-Stephenson, Danbury, CT) for 30 s to seal the fiber with the glass capillary. The electrode was then dipped in acetone for 5 s. Finally, the epoxied electrode was cured overnight at room temperature, cured in an oven at 100°C for 2 h, and 150°C overnight. and the electrode capillary was back filled with 1 M KCl for electrical connection.

The 1% ND dispersions in water were purchased from Adámas Technologies (Raleigh, NC) and were bath sonicated for 15 min before use. Different NDs were compared: 5-nm hydrogen-terminated ND (ND-H 5), 5-nm carboxylated ND (ND-COOH 5), 15-nm carboxylated ND (ND-COOH 15), and 60-nm carboxylated ND (ND-COOH 60). ND-H and ND-COOH were reported the zeta potential at pH 7 to be +30 mV and –45 mV, respectively.[49] All NDs were characterized by transmission electron microscopy (TEM), X-ray photoelectron spectroscopy (XPS), and Raman spectroscopy before used (Fig. 4.1-4.3). To prepare the ND/CFMEs, 25 µL of the nanodiamond dispersion in water (equivalent to 0.25 mg of ND per drop) was dropped to cover the CFME tip on a glass slide on a hot plate, which accelerated solvent evaporation. The process was repeated to optimize the amount of NDs on CFME via the number of ND drops. Note that only some of the ND drop was deposited on the carbon fiber, and some was left on the glass slide. All ND/CFMEs were dried overnight at room temperature before characterization.

4.2.3 Surface Characterization

Scanning electron microscopy (SEM) images of the electrodes were taken with Quanta 650 (FEI Company, Hillsboro, OR), at the Nanoscale Materials Characterization Facility, UVa Department of Materials Science and Engineering. The secondary electron images were recorded with an acceleration voltage of 2 kV and a working distance of approximately 10 mm.

Transmission electron microscopy (TEM) images were obtained by using FEI Titan 80-300 TEM (FEI Company, Hillsboro, OR) at the UVa NMCF. ND dispersions were drop-casted on the carbon type-B, 200-mesh, copper TEM grid (Ted Pella, Redding, CA). The acceleration voltage is 300 kV.

X-ray photoelectron spectroscopy (XPS) of NDs were performed at PHI Versaprobe III XPS (Physical Electronics, Chanhassen, MN) at the UVa NMCF. The Al Ka monochromatic X-ray source (1486.6 eV) was used with a pass energy of 224 eV for elemental composition analysis and 55 eV for electronic state information. ND dispersions were drop-casted on the silicon wafer. The spectra were analyzed with MultiPak software which came with the instrument. All spectra were corrected for the charging effect by shifting the C 1s sp^3 peak to the binding energy of 284.8 eV.

Raman spectra were collected from Renishaw 100 confocal micro-Raman system (Renishaw, Hoffman Estates, IL) at the Center for Nanophase Materials Sciences (CNMS), Oak Ridge National Laboratory (ORNL), using 532-nm laser.

A. ND-H 5 nm

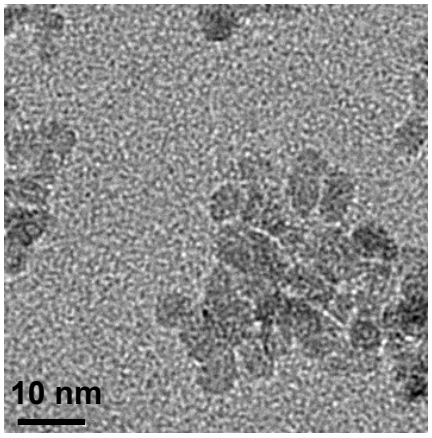

B. ND-COOH 5 nm

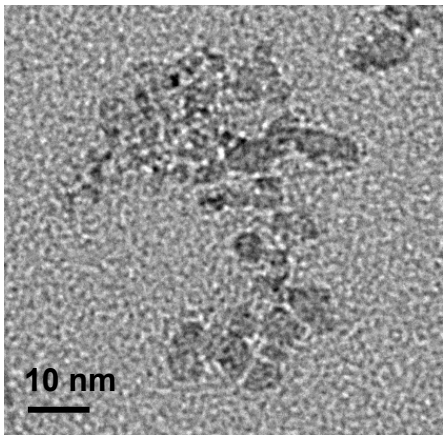

C. ND-COOH 15 nm

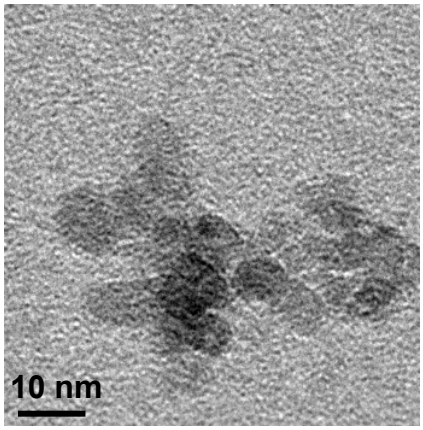

D. ND-COOH 60 nm

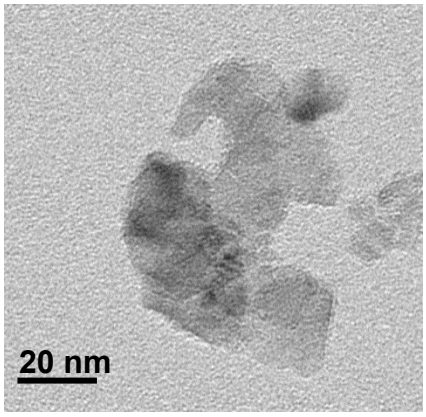

E. High magnification ND-COOH 15 nm

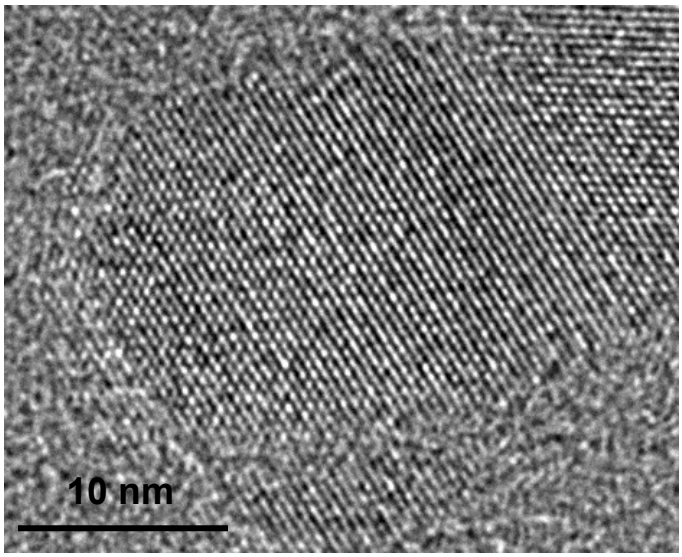

Fig. 4.1 TEM image of different NDs. (A) ND-H 5 nm, (B) ND-COOH 5 nm, (C) ND-COOH 15 nm, and (D) ND-COOH 60 nm. (E) Diamond crystalline lattice structure and sp^2 layer of ND-COOH 15 nm.

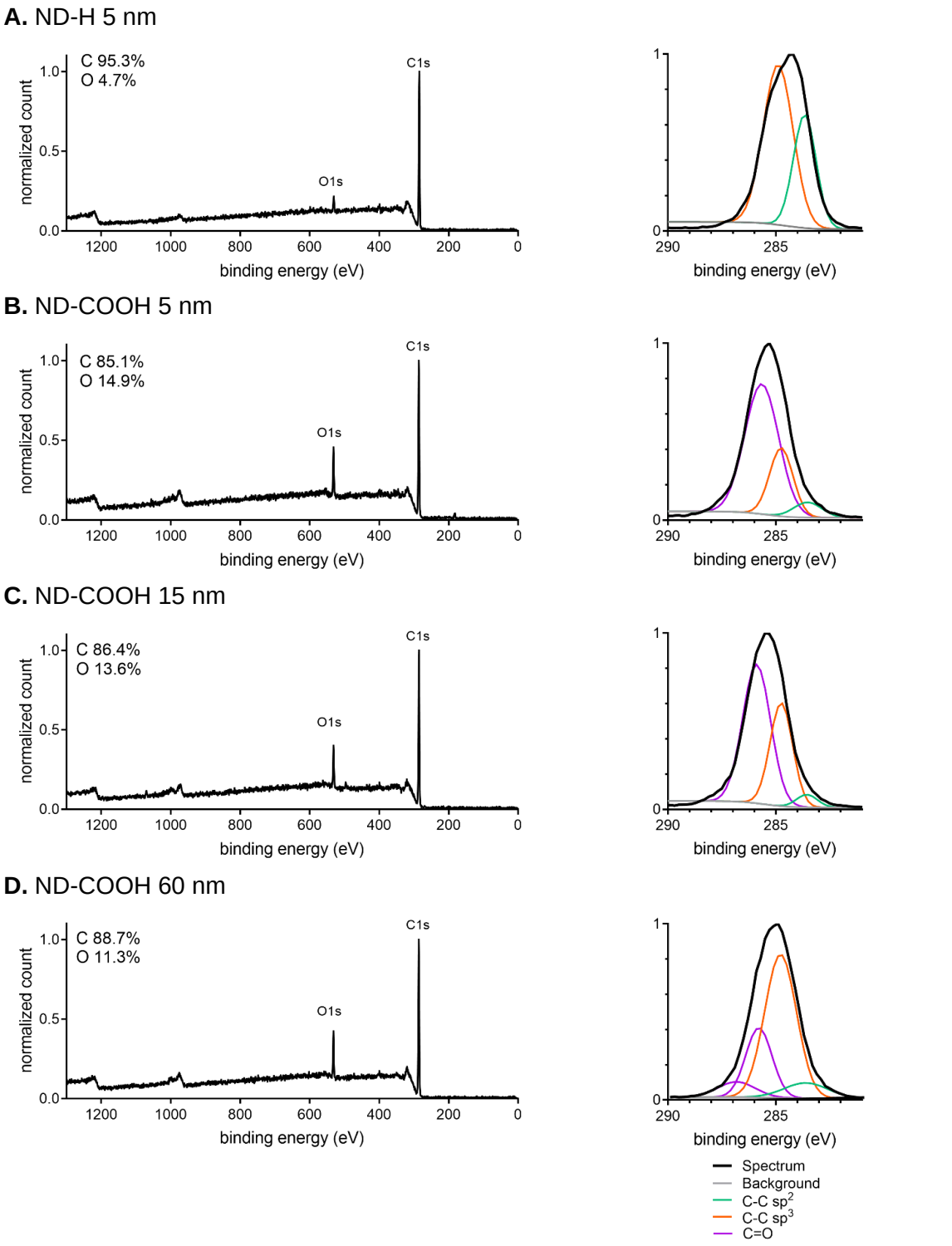

Fig. 4.2 XPS spectra and C1s peak fitting of (A) ND-H 5 nm, (B) ND-COOH 5 nm, (C) ND-COOH 15 nm, and ND-COOH 60 nm. Carboxylated NDs had higher oxygen percentage and C-O/C=O/COOH peak area than hydrogenated NDs.

Table 4.1 XPS spectral information of NDs

Samples	Atomic elemental composition[a]		Deconvoluted C 1s peaks area[b]		
	%C	%O	%sp^2 C-C	%sp^3 C-C	%C-O/ C=O/COOH
New SPCE	95.1	4.9	38.4	61.6	nd
SPCE in PBS to +1.5 V	85.9	14.1	8.5	29.4	62.1
SPCE in histamine to +1.0 V	87.3	12.7	5.7	43.5	50.8
SPCE in histamine to +1.5 V	88.9	11.1	10.3	58.7	31.0

[a]Values shown are average values from two samples. No other atoms were detectable.
[b]nd = Not detected.

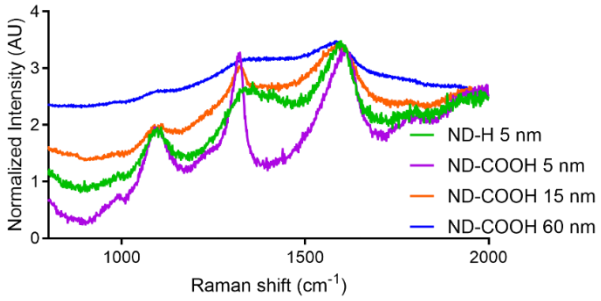

Fig. 4.3 Raman spectra of different NDs. The broad peak around 1090-1100 cm^{-1} is caused by nanodiamond surface plasmon,[50] and the peak around 1325 cm^{-1} is the diamond band.[1] The broad peak at 1590-1600 cm^{-1} is a feature of surface graphitic sp^2 structure (shifted "G band").[1] The spectra should have a graphitic "D band" at 1350-1360 cm^{-1} as well because of the oxidized sp^2 edge plane defects,[3] but it may be convoluted with the larger diamond band at the similar wavenumber. The broad spectra feature is due to the photoluminescence properties of NDs.

4.2.4 Electrochemical Instrumentation

FSCV experiments were conducted using a two-electrode system: CFME or ND/CFME working electrode vs Ag/AgCl reference electrode. The electrodes were connected to a ChemClamp potentiostat and headstage (Dagan, Minneapolis, MN). Unless stated otherwise, the standard FSCV waveform with a holding potential of –0.4 V, switching potential of +1.3 V, scan rate of 400 V/s, and repetition rate of 10 Hz was applied to the electrode. The PBS buffer and test solutions were injected through the flow cell by

an automated syringe pump (Harvard Apparatus, Holliston, MA) at a flow rate of 2 mL/min. The FSCV data were collected with HDCV Analysis software (Department of Chemistry, University of North Carolina at Chapel Hill). Electrochemical impedance spectroscopy (EIS) was performed at Gamry Reference 600 (Gamry Instruments, Warminster, PA) in a 10 mM $[Fe(CN)_6]^{3-}$ in 1 M KCl using CFME or ND/CFME working electrode, Ag/AgCl reference electrode, and Pt counter electrode. The DC applied potential was +0.24 V, the observed formal potential of $[Fe(CN)_6]^{3-}$, and the AC potential amplitude of 10 mV was applied on the formal potential of $[Fe(CN)_6]^{3-}$ with an initial and final frequency of 1 MHz and 1 Hz, respectively. The Nyquist plots were normalized by the electrode surface area.

4.2.5 Statistics

All reported values are given as the mean ± standard error of the mean (SEM) for *n* number of electrodes. All statistical analyses were performed in GraphPad Prism 8 (GraphPad Software, La Jolla, CA). Statistical significance was defined at $p < 0.05$.

4.3 Results and Discussion

4.3.1 Physical Characterization of ND/CFMEs

In this work, we examined four types of NDs: 5 nm ND particles with H termination (ND-H 5), 5 nm ND particles with carboxyl termination (ND-COOH 5),15 nm ND particles with carboxyl termination (ND-COOH 15), and 60 nm particles with carboxyl termination (ND-COOH 60). TEM images of NDs show the particle sizes, the core diamond crystalline structure, and the surface sp^2 carbons layer (Fig. 4.1). XPS spectra demonstrate that all ND-COOHs had higher oxygen composition and oxygen-contained carbons than ND-Hs (Fig. 4.2), and Raman spectra exhibit diamond band with graphitic features (Fig. 4.3).[1,50,51]

Microelectrodes were coated by repeated drop casting of 25 µL drops of a 1% aqueous ND dispersion onto a CFME. Fig. 4.4 shows the SEM images of 10 drop coatings of ND-H 5/CFME (Fig. 4.4A), ND-COOH 5/CFME (Fig. 4.4B), ND-COOH 15/CFME (Fig. 4.4C), and ND-COOH 60/CFME (Fig. 4.4D). The images illustrate deposited ND particles on the carbon fiber surface, as the unmodified carbon fiber is smooth (SEM image of CFME is shown in Fig. 4.5). The coatings for the 5 nm particles are denser than the coatings for the larger ND particles, which are more sparse. ND-H 5/CFME had small deposited particles, many in the range of tens of nm. The ND-COOH 5/CFME had a thicker coating consisting mainly of NDs smaller than 10 nm, and the SEM image is noisy because of the charging effects from the insulating, thicker coating. ND-COOH 15/CFME had a sparse coating of ND-COOHs, with larger particles in the tens to hundreds of nm, similar to the particles on the ND-COOH 60/CFME. The ND particle size from drop-casting was larger than the synthesized size because of aggregation of NDs in the dispersion.[9] Future research can investigate direct growth or deposition of ND particles on a conductive substrate to obtain more homogeneous, non-aggregated coatings.

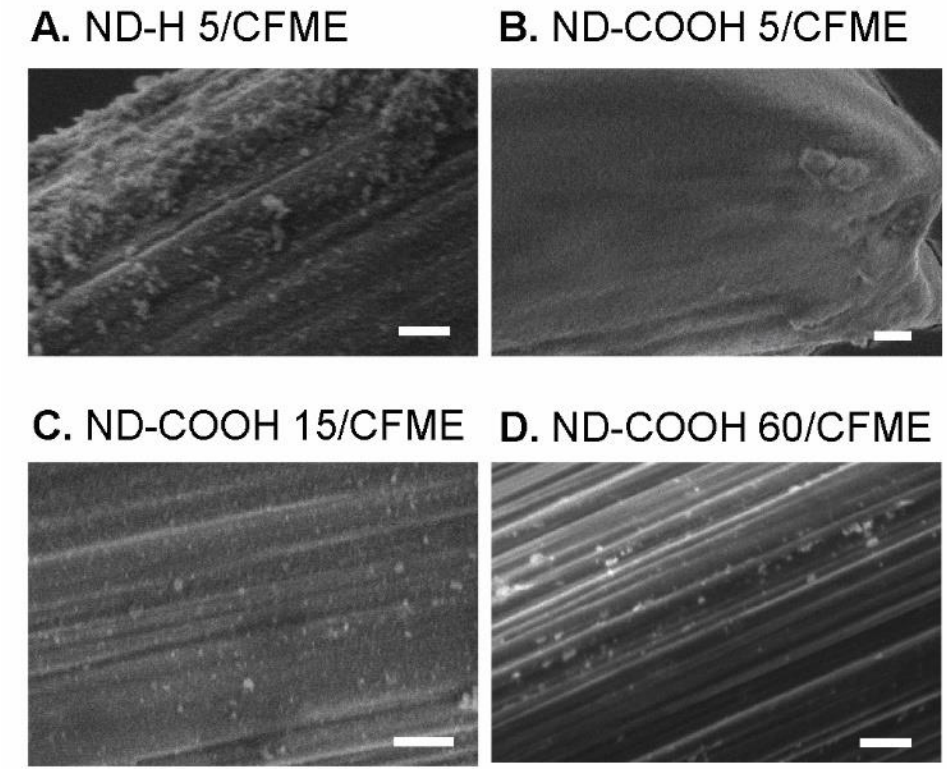

Fig. 4.4 Physical characterization of ND/CFMEs. SEM images of (A) ND-H 5/CFME, (B) ND-COOH 5/CFME, (C) ND-COOH 15/CFME, and (D) ND-COOH 60/CFME. The modified electrodes were prepared from drop casting for 10 drops. Scale bar: 500 nm.

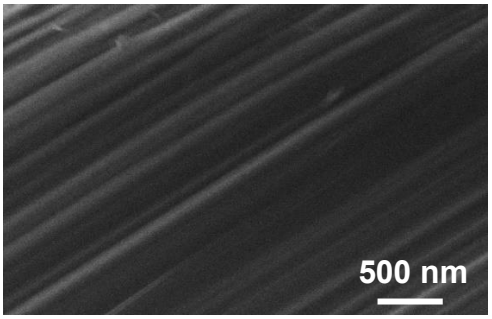

Fig. 4.5 SEM image of an unmodified CFME.

4.3.2 Electrocatalytic Properties of ND/CFMEs

We explored the electrocatalytic properties of all four types of NDs toward surface-sensitive redox probes. Fig. 4.6 shows the Nyquist plot from EIS of 10 mM $[Fe(CN)_6]^{3-}$. The EIS spectra did not resemble a perfect semicircle in the high frequency range and a line of unity slope in the low frequency range because diffusion profiles at microelectrodes are different from those of larger electrodes.[52] The size of the "semicircle" was qualitatively compared and fit to Randles equivalent circuit modified with non-linear resistance for microelectrodes[53] (Fig. 4.7) to investigate charge-transfer resistance (R_{ct}). The semicircle features of ND/CFMEs were all smaller than CFMEs, indicating a lower R_{ct}. The order of R_{ct} was ND-COOH 15 (0.30 ± 0.05 Ω cm^2) ≤ ND-COOH 60 (0.32 ± 0.03 Ω cm^2) < ND-COOH 5 (0.33 ± 0.01 Ω cm^2) < ND-H 5 (0.54 ± 0.08 Ω cm^2) ≤ CFME (2.7 ± 0.3 Ω cm^2) (n = 4). There was a big difference between the hydrogenated and carboxylated 5 nm particles with carboxylated particles better for electron transfer to ferricyanide. Interestingly, the more sparsely coated 15 and 60 nm ND particles had smaller R_{ct} values than 5-nm ND-COOH. This result was counterintuitive because usually smaller nanoparticles display better electrocatalytic enhancement.[54] The SEM image of larger ND-COOHs showed sparse coatings, which effectively adds active sites but does not destroy conductivity. However, the thick, film-like coatings of the smaller particles will worsen the charge transfer kinetics if the coating is resistant to electron transfer due to the sp^3 insulating nature of NDs, compared to graphitic carbon in the CFME.[30]

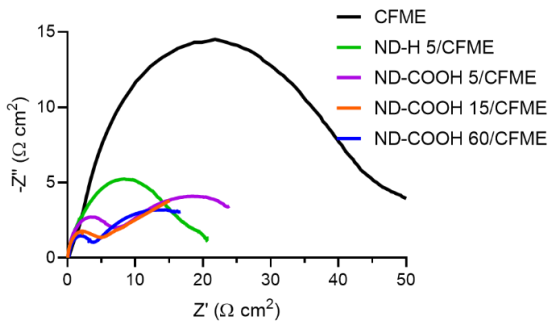

Fig. 4.6 Nyquist plot from EIS of 10 mM $[Fe(CN)_6]^{3-}$ in 1 M KCl using unmodified CFME (black), ND-H 5/CFME (green), ND-COOH 5/CFME (purple), ND-COOH 15/CFME (orange), and ND-COOH 60/CFME (blue). Both impedance axes were normalized by the electrode surface area.

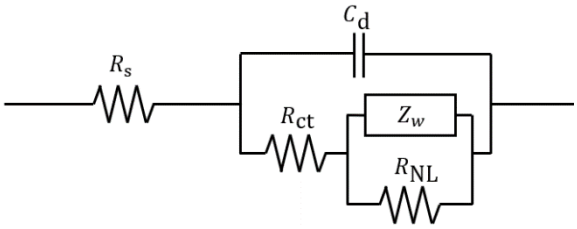

Fig. 4.7 Randles equivalent circuit with non-linear resistance accounting for spherical diffusion at microelectrode for EIS fitting. R_s: solution resistance, R_{ct}: charge-transfer resistance, Z_w: Warburg impedance, C_d: double-layer capacitance, R_{NL}: non-linear resistance.

Table 4.2 Parameters from EIS spectra fitting using the circuit in Fig. 4.7 (n = 4)

Samples	**R_{ct} (kΩ)**	**C_d (nF)**	**R_s (kΩ)**	**W (MΩs$^{1/2}$)**	**R_{NL} (kΩ)**
CFME	60 ± 6	0.45 ± 0.04	4.6 ± 0.9	3.7 ± 1.2	600 ± 60
ND-H 5/CFME	13 ± 2	0.36 ± 0.01	4.4 ± 0.2	12 ± 8	2200 ± 700
ND-COOH 5/CFME	9.5 ± 0.4	0.40 ± 0.02	4.1 ± 0.3	4.2 ± 0.6	600 ± 100
ND-COOH 15/CFME	6 ± 1	0.20 ± 0.02	3.6 ± 0.3	6.4 ± 0.3	860 ± 200
ND-COOH 60/CFME	7.8 ± 0.7	0.45 ± 0.07	4.4 ± 0.2	1.6 ± 0.3	420 ± 30

4.3.3 FSCV of Dopamine at CFMEs

All ND/CFMEs were investigated for their FSCV responses (Fig. 4.8). Example background charging currents are shown in Fig. 4.8A-E and they are all about the same size, around 700 nA. The average background currents (Fig. 4.8F) were not significantly different from each other (p = 0.1839, one-way ANOVA with Bonferroni post-test, n = 4-6). The background current is proportional to specific capacitance of the electrode material and electroactive surface area.[55] Although the sp^2 surface groups can increase the capacitance of BDD,[56,57] the 15 and 60 nm ND particles do not fully coat the surface, so they might not add much material for charging. The 5 nm particles actually show slightly decreased capacitance despite the fact they formed thicker coatings, implying the sp^3 hybridized ND exhibits a slightly lower capacitance that CFMEs.

The background-subtracted CVs of 1 μM dopamine were also compared (Fig. 4.8A-E). The example CVs show that dopamine current for the two 5 nm ND samples are slightly lower than CFMEs, while the current for the 15 and 60 nm ND are twice as large as CFMEs. There was a significant main effect of the ND type on the peak current (Fig. 4.8G, $p < 0.0001$, one-way ANOVA with Bonferroni post-test, n = 4-6). Bonferroni post-tests indicate ND-COOH 15 and ND-COOH 60 significantly increased the dopamine peak current ($p < 0.001$ and $p < 0.01$, respectively) while ND-H 5 and ND-COOH 5 did not change the current ($p = 0.0808$ and $p = 0.9517$, respectively). The highest dopamine peak current was obtained at the ND-COOH 15/CFME treated with 10 rounds of drop-casting; the peak current was enhanced by 1.9 ± 0.1 times. Fig. 4.9A shows optimization of the number of drops for drop casting and 10 drops were used for all further experiments.

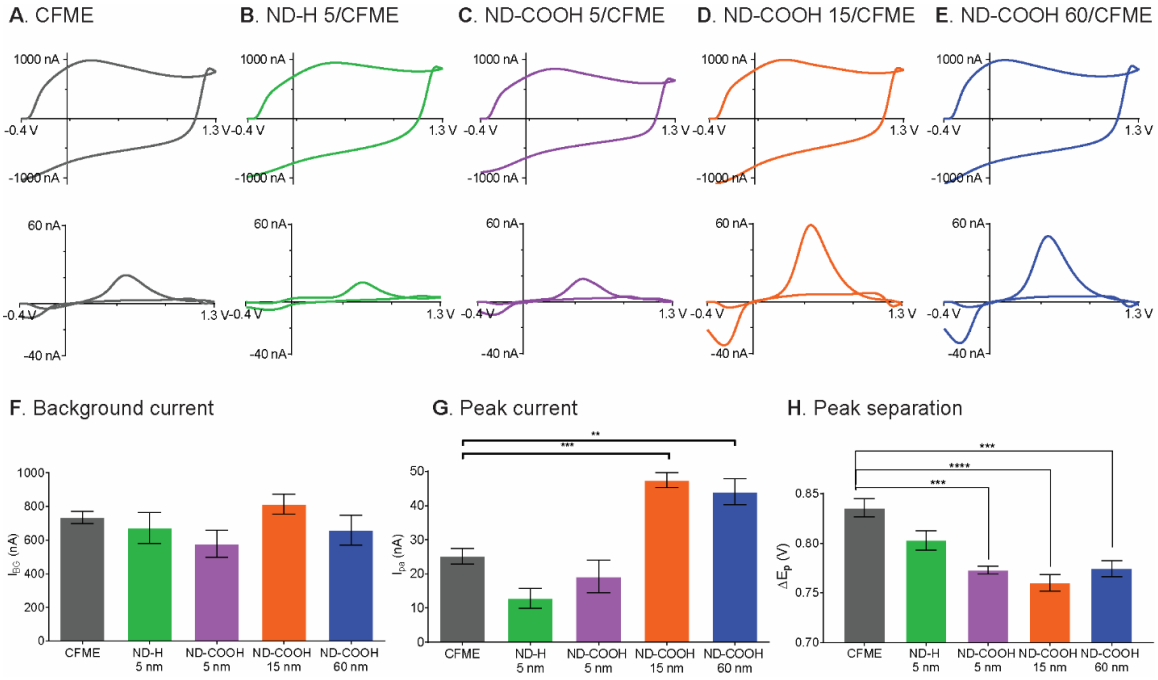

Fig. 4.8 FSCV responses: 1 µM dopamine (upper) and background current (lower) of (A) CFME, (B) ND-H 5/CFME, (C) ND-COOH 5/CFME, (D) ND-COOH 15/CFME, and (E) ND-COOH 60/CFME in PBS pH 7.4. The modified electrode was prepared from 10 drop castings. The average data includes (F) background current, (G), 1 µM dopamine peak current, and (H) peak separation. (**p < 0.01, ***p < 0.001, ****p < 0.0001, one-way ANOVA with Bonferroni post-test, n = 4-6 electrodes).

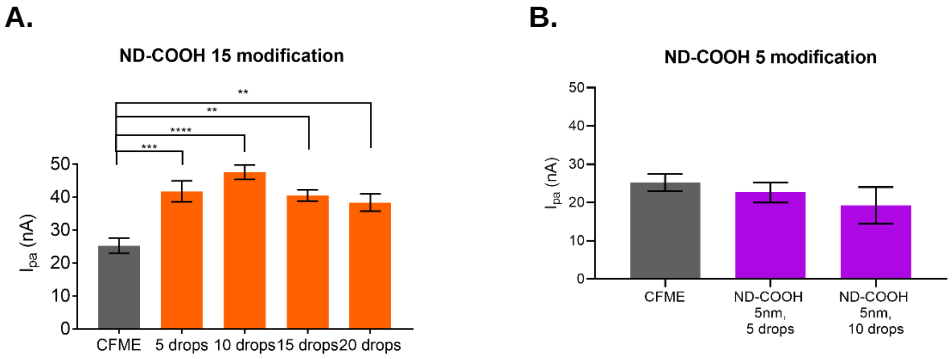

Fig. 4.9 Optimization of ND amount from drop casting. The unmodified CFMEs were drop casted by a different number of drops of (A) ND-COOH 15 and (B) ND-COOH 5. Average anodic peak current of 1 µM dopamine. (n = 4–6, one-way ANOVA with Bonferroni post-test compared to the unmodified CFME (black bar). **p < 0.01, ***p < 0.001)

Another interesting feature of the dopamine CV is the separation between anodic and cathodic peak (ΔE_p), as smaller ΔE_p values are correlated with faster electron transfer kinetics. Fig. 4.8H shows that there was a significant main effect of the ND type on the ΔE_p ($p < 0.0001$, one-way ANOVA with Bonferroni post-test, n = 4-6). Bonferroni post-tests indicated that all three ND-COOHs significantly decreased the ΔE_p ($p < 0.001$ for ND-COOH 5, $p < 0.0001$ for ND-COOH 15, and $p < 0.001$ for ND-COOH 60). However, ND-H 5 did not significantly affect the ΔE_p ($p = 0.0970$). Because smaller peak separation indicates better electrocatalytic properties,[55] ND-COOH catalyzed dopamine redox reaction at CFME but ND-H did not, consistent with the EIS experiment, which found higher R_{ct} values for ND-H than ND-COOH. The half-wave potentials ($E_{1/2}$) for dopamine oxidation at each electrode are 0.39 ± 0.02 V for CFME, 0.38 ± 0.02 V for ND-H 5, 0.35 ± 0.02 V for ND-COOH 5, 0.34 ± 0.01 V for ND-COOH 15, and 0.35 ± 0.01 V for ND-COOH 60. Hence, $E_{1/2}$ indicates the same trend of electrocatalytic effect to ΔE_p.

The optimized ND-COOH 15/CFME was further tested to look at adsorption dependence by varying the scan rate from 50 to 1000 V/s. The log-log plot of normalized dopamine anodic peak current vs scan rate (Fig. 4.10A) had a slope of 1.09 ± 0.04 (n = 3) which is close to 1. The slight deviation might be due to the heterogeneous coating on CFME. The slope indicates that anodic current was proportional to the scan rate, so the dopamine oxidation at ND-COOH 15/CFMEs is adsorption-controlled due to the electrostatic interaction.[55] The dopamine anodic current is lower and the oxidation is less adsorption-controlled at pH 2.4 (Fig. 4.11), where all carboxylic groups on the CFME and ND-COOH are protonated, so the electrostatic interactions are weaker.

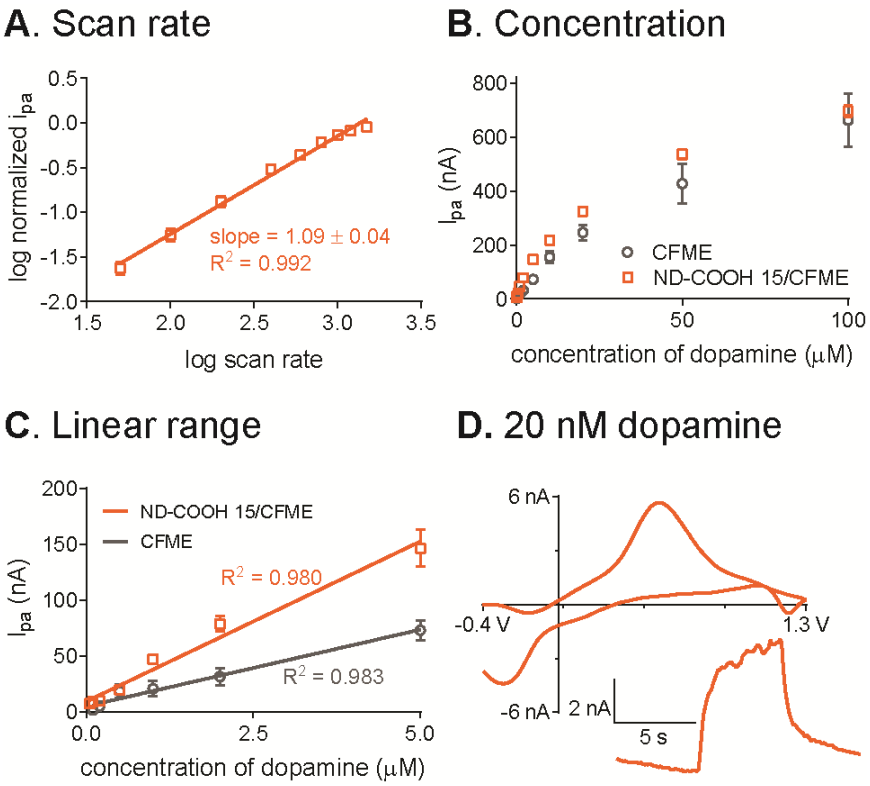

Fig. 4.10 Analytical performance of ND-COOH 15/CFME for dopamine detection. (A) log-log relationship between anodic peak current of 1 µM dopamine and scan rate (*n* = 3). (B) Concentration dependence from the anodic peak current of 20 nM to 100 µM dopamine in PBS pH 7.4 (*n* = 4), compared to unmodified CFME. (C) Linear range at both electrodes. (D) Example CV of 20 nM dopamine in PBS pH 7.4 with current-time trace inset for 5-s bolus injection.

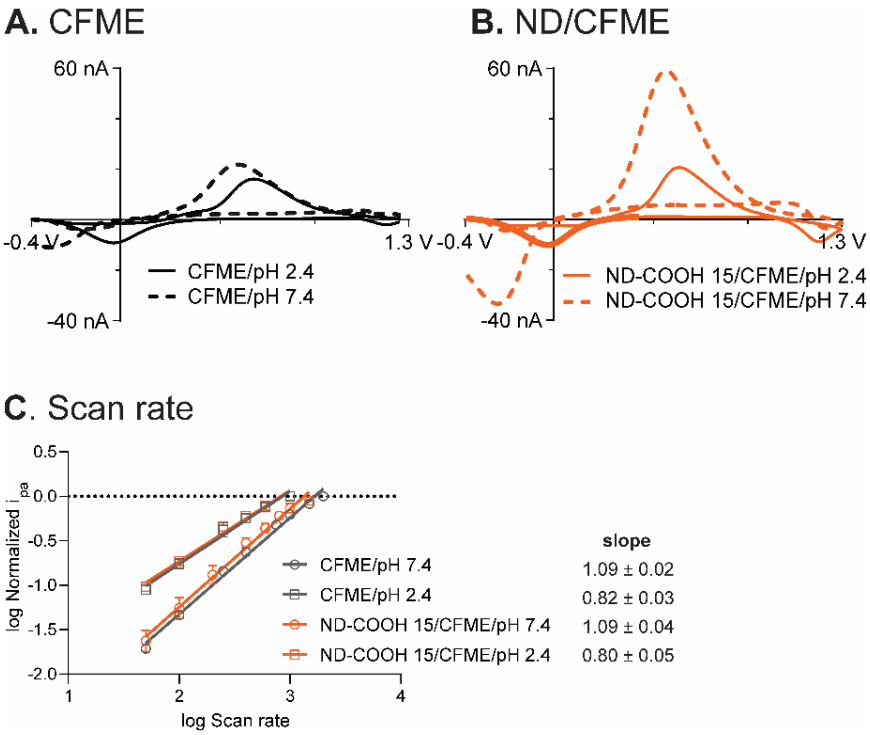

Fig. 4.11 Effect of pH on FSCV of dopamine at (A) CFME and (B) ND-COOH 15/CFME. pH 2.4 gave lower signals than pH 7.4. (C) log-log plot of normalized peak current vs scan rate and its slope (n = 4). Dopamine oxidation was less adsorption-controlled and more diffusion-controlled at pH 2.4 than pH 7.4.

4.3.4 Both Size and Functional Groups of NDs Affect Electrochemistry

The FSCV and EIS data revealed that carboxylated NDs had better electrocatalytic properties and peak currents than hydrogen-terminated NDs. For electrocatalytic properties, we consider the density of electronic states (DOS), and C=C and C=O ND surface groups can fill the bandgap, increasing the DOS and accelerating electron transfer kinetics.[13] In contrast, ND-H 5 lacks functional groups to increase the DOS and electrocatalytic effects were not observed.[13] Surface oxide groups such as hydroxyl, carbonyl, and carboxyl groups also enhance adsorption of dopamine (pK_a 8.9)[58] carbon electrodes, leading to higher peak oxidation currents.[13,59] Indeed, the 15 and 60 nm ND-

COOH electrodes exhibited increased anodic peak currents for dopamine FSCV as they added adsorption sites for dopamine.[60] On the other hand, hydrogenation of ND reduced adsorption by reducing active surface groups and the dopamine currents were slightly lower than at CFMEs, which are naturally partially oxygen-terminated. Hydrogenated NDs also exhibited less electrocatalytic properties, showing that the oxygen groups also facilitate electron transfer of surface sensitive species, as has been previously shown by Holt et al. as well.[10] Therefore, ND-COOH is a better electrode material for neurotransmitter detection than ND-H, a finding consistent with previous studies finding surface functional groups of NDs affect their physical and electrochemical properties.[8,10,13,14,45]

ND particle size affected the dopamine sensitivity for the COOH functionalized particles. The unanticipated result is that ND-COOH 5 did not increase the dopamine peak current, unusual because smaller nanoparticles have more concentrated surface functional groups and thus often exhibit higher current enhancement.[54] The SEM image of ND-COOH 5/CFME (Fig. 4.4B) showed a thick, film-like morphology coating on the carbon fiber surface, which could lead to slower mass transport to the electrode and lower dopamine peak current. Active adsorption sites that are too close together will not lead to larger current if the dopamine cannot access all of them. The ND-COOH 15 and ND-COOH 60 had similar currents and similar morphologies, with occasional particles adhered to the fiber surface, but not a full monolayer of coverage. While typically denser coverage might be better, the ND might also impede charge transfer and the smaller ND particles had higher R_{ct}, so the more sparse coatings of the 15 and 60 nm particles were more ideal.

4.3.5 Analytical Performance of ND Electrodes

ND-COOH 15/CFMEs were used to characterize the analytical performance of ND electrodes compared to bare CFMEs. Fig. 4.10B shows that current was linear with concentration from 20 nM to 5 µM (Fig. 4.10C) with R^2 = 0.980 for ND-COOH 15/CFME and R^2 = 0.983 for CFME. The sensitivity for dopamine detection was calculated from the slope of the calibration curve and ND-COOH 15/CFME were twice as sensitive, with a sensitivity of 29 ± 2 nA/µM compared to 14 ± 1 nA/µM for CFME (p < 0.01, unpaired t-test, n = 4). At higher concentrations, the adsorption sites were all occupied, and the response becomes more diffusion-controlled, as detailed in previous studies.[60]

The LOD of ND/CFMEs was calculated from the signal-to-noise (S/N) ratio obtained from peak current of 100 nM dopamine, and LOD was defined at S/N = 3. From Table 4.3, the LOD of ND-COOH 15/CFME is 2.6 ± 1.0 nM, which is significantly better than the unmodified CFME (p < 0.05, unpaired t-test, n = 4). Noise is proportional to background current and because the faradaic current increased, but the background did not, the S/N ratio and LOD improved.[61] The FSCV of 20 nM dopamine (Fig. 4.10D) shows how ND electrodes can detect very low concentrations of dopamine with the usual dopamine CV shape, and a current-time trace with a signal much larger than the baseline noise. Table 4.3 also shows that the rise times (defined as time from 10% to 90% of the maximum current) were not changed for ND electrodes (p = 0.628, unpaired t-test, n = 4). The ND/CFMEs electrodes were stable when FSCV waveform was continuously applied to the electrode for 4 h, and the 1 µM dopamine peak current was measured every hour (Fig. 4.12). The normalized peak current remained the same with the relative standard deviation of 3.4 ± 0.6% (n = 4), so the ND particles were attached well to the CFME surface.

Table 4.3 Analytical characterization of ND electrodes

Samples	Sensitivity (nA/mM)	LOD (nM)	ΔE_p (mV)	rise time (s)
CFME	14 ± 1	7 ± 1	835 ± 9	1.9 ± 0.1
ND-COOH 15/CFME	29 ± 2**	3 ± 1*	760 ± 8***	1.9 ± 0.1

*p < 0.05, **p < 0.01, ***p < 0.001 by unpaired t-test. n=4-5

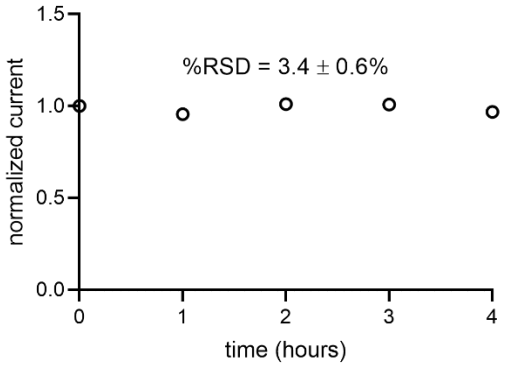

Fig. 4.12 Normalized peak current of 1 µM dopamine measured at the ND-COOH 15/CFME every 1 h for 4 h (n = 4). FSCV waveform was continuously applied to the electrode.

4.3.6 Response to Other Neurochemicals

The ND-COOH 15/CFME was also investigated for detection of other neurochemicals, including epinephrine, norepinephrine, serotonin, and ascorbic acid (Fig. 4.13). The oxidation currents were larger at the ND-coated electrodes for the cations epinephrine, norepinephrine, and serotonin than for the anion ascorbic acid. For epinephrine, there was an additional anodic peak around 0.0 V, which corresponds to the oxidative cyclization making leucoaminochrome.[62] The cyclization kinetics of epinephrine is faster than that of dopamine and norepinephrine, where the cyclization peak is not observed.[63] Serotonin is an important neurotransmitter for regulation of mood[34] and has an oxidation peak at 0.6 V, similar to dopamine, but a reduction peak at 0 V, which is more positive than dopamine. The peak current enhancements for cationic neurotransmitters

were similar to dopamine: 1.5 ± 0.1 times increase for epinephrine (Fig. 4.13A), 1.7 ± 0.2 times for norepinephrine (Fig. 4.13B), and 1.7 ± 0.3 times for serotonin (Fig. 4.13C) (n = 4). In contrast, ascorbic acid, in the form of anionic ascorbate at physiological pH, exhibited no current enhancement at ND-COOH 15/CFME: 1.0 ± 0.1 times (n = 4) (Fig. 4.13D). The carboxylate and surface oxide groups of ND-COOHs selectively adsorbed cationic molecules and repelled anionic molecules. Also, NDs did not increase electrode surface area, thus the peak current of ascorbic acid was not increased. Therefore, ND-COOHs provided selectivity toward cationic neurotransmitter detection and limited the anionic interferents from high concentration of anionic ascorbate *in vivo*.[64]

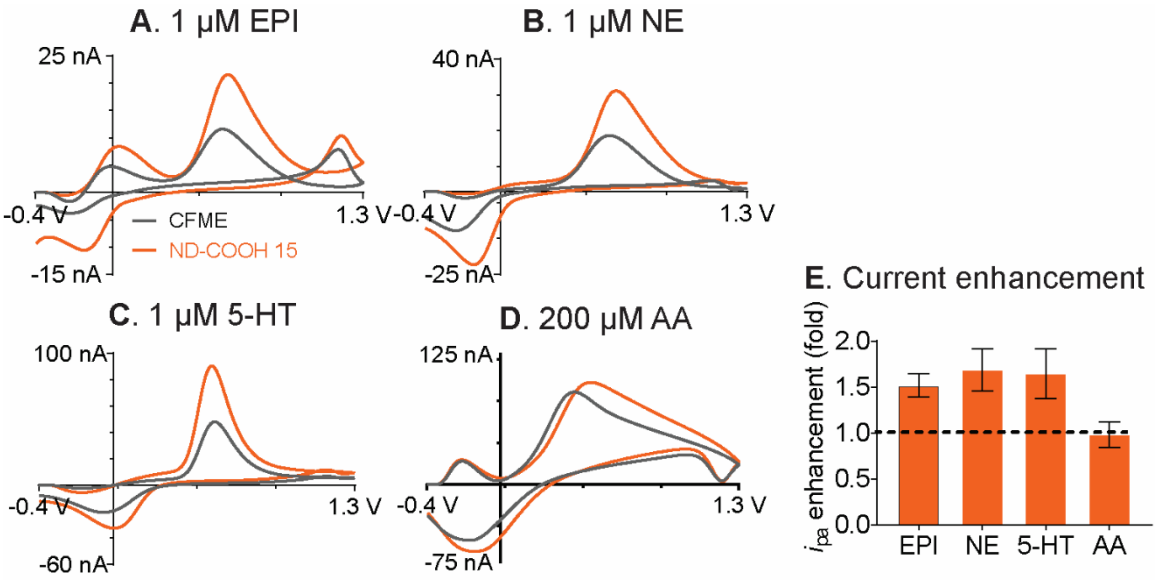

Fig. 4.13 Response to other neurochemicals for unmodified CFME (black) and ND-COOH 15/CFME (orange) in PBS, pH 7.4. (A) 1 µM epinephrine (EPI), (B) 1 µM norepinephrine (NE), (C) 1 µM serotonin (5-HT), (D) 200 µM ascorbic acid (AA), and (E) anodic peak current enhancement (n = 4).

4.3.7 Antifouling Properties

Electrode fouling is a major concern in biological experiments as the response can decrease because of either the production of electroactive species that polymerizes on the electrode or adhesion of large biomolecules in biological environments.[32] ND-modified electrodes have previously been shown to resist some forms of fouling[35,38–44] so we evaluated the ND-COOH 15/CFME for antifouling properties. First, electrochemical fouling of serotonin was tested by repeatedly exposing the electrode to serotonin, as serotonin produces a radical species after oxidation that can polymerize and reduce the electroactive surface area.[35] FSCV was performed with the Jackson waveform, specific for serotonin (0.2 V holding potential, ramped up to +1.0 V, back to -0.1 V, then to 0.2 V at a scan rate of 1000 V/s), which has fast scan rates to "outrun" the polymerization and reduce the fouling.[34] Fig. 4.14A-B compare the CVs of serotonin from 1st and 25th repeated exposure to serotonin. At the CFME, the anodic peak current decreased by almost half, from 90 nA to 50 nA, but the ND-COOH 15/CFME decreased by only a quarter, from 150 to 110 nA. The peak current from 25th injection of serotonin at ND-COOH 15/CFME (i.e. after fouling) was higher than the peak current from 1st injection of serotonin at the unmodified CFME. Fig. 4.14C shows the normalized currents over the repeated injections, which show less fouling and less decay at ND-COOH 15/CFMEs (one-way ANOVA, $p < 0.0001$). The normalized current from 25th injection at ND-COOH 15/CFME (73 ± 1%) was significantly higher than CFME (54 ± 2%, $p < 0.0001$, one-way ANOVA, $n = 5$). We also tested electrodes coated with fewer drops of ND, and they alleviated fouling, but to a lesser extent, suggesting that fouling is related to surface coverage of ND (Fig. 4.15).

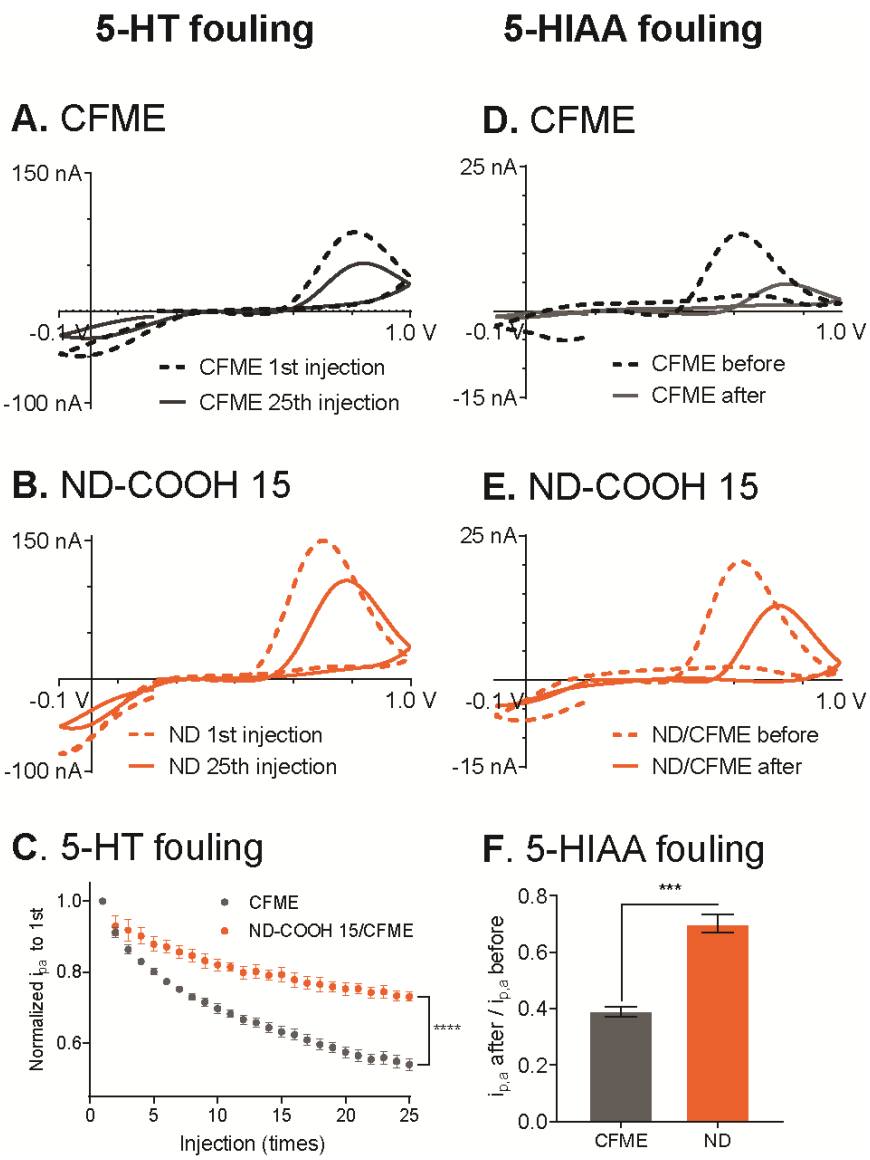

Fig. 4.14 Electrochemical fouling by serotonin (5-HT) and 5-HIAA. CV of 1 µM serotonin from 1st (dashed) and 25th (solid) 3-s injection at (A) CFME and (B) ND-COOH 15/CFME. (C) Normalized peak current for repeated injections of 5-HT. The currents are significantly different by the 25th injection (****$p < 0.0001$, one-way ANOVA, $n = 5$). (D) CFME and (E) ND-COOH 15/CFME CVs of 1 µM 5-HIAA before (dashed) and after (solid) electrodes were bathed in 1 µM 5-HIAA solution with the continuous waveform application for 1 hour. (F) 1 µM 5-HIAA normalized peak current after 1 hour of 5-HIAA fouling (***$p < 0.001$, unpaired t-test, $n = 4$). All electrochemical fouling experiment were performed using the Jackson serotonin waveform in PBS pH 7.4.

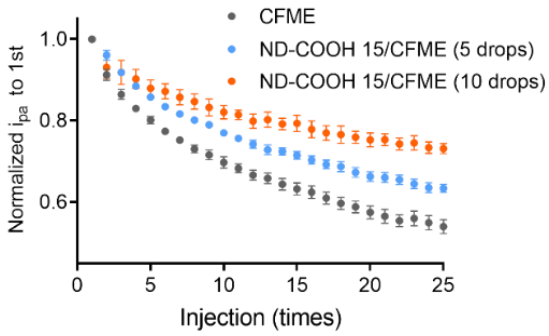

Fig. 4.15 Electrochemical fouling by serotonin. Normalized peak current for repeated injection of serotonin at CFME and ND-COOH 15/CFME prepared by 5 and 10 drop casting. (n = 5).

Electrochemical fouling was also tested for 5-HIAA, the serotonin metabolite found at high concentrations *in vivo*, which severely fouls the electrode via electropolymerization.[34] Despite the similar structure and oxidation between serotonin and 5-HIAA, the peak current of 5-HIAA was much lower because of the electrostatic repulsion between negative functional groups and anionic nature of 5-HIAA at pH 7.4. The electrode was tested for response to 5-HIAA, then bathed in the 1 µM 5-HIAA solution for 1 h with the Jackson waveform applied, and then the response to an injection of 1 µM 5-HIAA tested again. At CFMEs, the 5-HIAA anodic peak current decreased from 14 nA to 4 nA (Fig. 4.14D), while at ND electrodes, the decrease after 5-HIAA was only from 20 nA to 14 nA (Fig. 4.14E). As with serotonin, the current of the ND electrode after 5-HIAA fouling was similar to the bare CFME before fouling, proving that the ND modified electrode has bigger signals, even after fouling. Fig. 4.14F shows the average data, where the ND-COOH 15/CFME had 70 ± 3% of the original signal after fouling while the CFME had only 39 ± 2% (p < 0.001, unpaired t-test, n = 4). Therefore, ND-COOHs decreased electrochemical fouling from serotonin and 5-HIAA by about half.

Finally, the ND-COOH 15/CFME was investigated for their biofouling in rat brain slices, a popular *ex vivo* sample for neuroscience experiments.[65,66] Electrode fouling in

biological samples is caused by not only electropolymerization of neurochemicals but also adsorption of proteins or other biomolecules.[2,20] To evaluate the fouling, the electrodes were inserted in brain slice tissue, and the standard FSCV waveform was applied to the electrode continuously for 1 h. CVs of 1 µM dopamine CV were compared before and after being inserted to the brain. At CFMEs, the ΔE_p for dopamine is larger (about 150 mV) after the biofouling, which demonstrates sluggish kinetics caused by protein adsorption (Fig. 4.16A). The peak current also decreased from 28 nA to 5 nA at the CFME. In contrast, the ND-COOH 15/CFME had a smaller increase in ΔE_p (only about 30 mV), and the peak current decreased less, from 44 nA to 26 nA (Fig. 4.16B). On average, Fig. 4.16C shows that the normalized dopamine peak current after brain slice fouling for ND-CCOH 15/CFME (64 ± 5%) was significantly higher than CFME (24 ± 4%) ($p < 0.001$, unpaired *t*-test, $n = 4$). Again, the dopamine peak current at the partially fouled ND-COOH 15/CFME was approximately the same as that from the unfouled CFME.

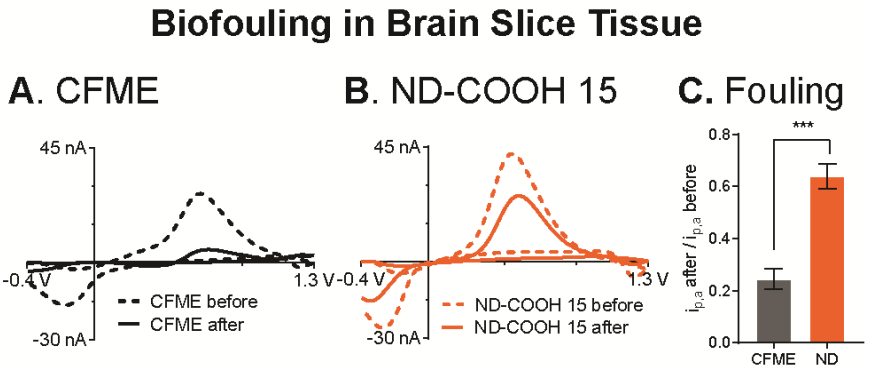

Fig. 4.16 Biofouling in brain slice tissue. CV of 1 µM dopamine in PBS pH 7.4 obtained before (dashed) and after (thick) the electrodes were implanted in the brain slice tissue for 1 hour with the dopamine waveform applied. (A) CFME and (B) ND-COOH 15/CFME. (C) Normalized peak current of 1 µM dopamine after to before brain slice implantation (***$p < 0.001$, unpaired *t*-test, $n = 4$).

These experiments demonstrate that ND-modified CFMEs exhibit antifouling properties and signals after electrochemical or tissue fouling were greater than bare CFMEs that had no fouling. A recent study found that CNT yarns prevent biofouling by proteins but not by serotonin electropolymerization, but this study shows that ND is beneficial for reducing fouling by both serotonin and proteins.[67] The antifouling properties for proteins are due to the surface being more hydrophilic. Contact angle measurements were performed on a flat, screen-printed carbon electrode (SPCE) for ND-COOH 15 and ND-H 5 drop casting (Fig. 4.17) and there was a significant main effect of the ND type on the contact angle ($p < 0.0001$, one-way ANOVA with Bonferroni post-test, $n = 4$). The contact angle of ND-COOH 15 (30 ± 4^{o}) was significantly lower than bare SPCE (69 ± 2^{o}, $p < 0.0001$), but the contact angle of ND-H 5 (58 ± 4^{o}) was not significantly different than bare SPCE ($p = 0.064$). Hence, NDs with carboxylic acid functionalization reduced severe fouling of CFMEs because they increased electrode surface hydrophilicity[4,6,45] and minimized the adsorption of hydrophobic biomolecules and polymers generated from electropolymerization of serotonin and 5-HIAA.

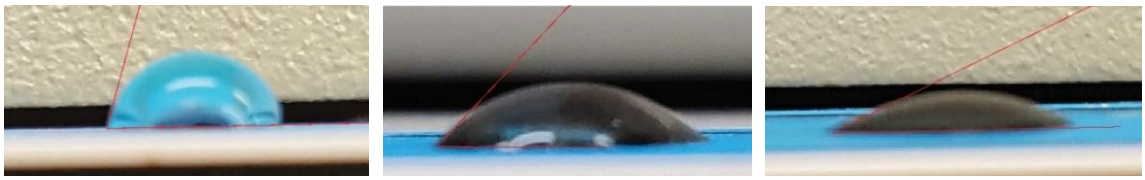

Fig. 4.17 Contact angle measurement of water drop on (A) SPCE (69 ± 2^{o}), (B) ND-H 5/SPCE (58 ± 4^{o}), and (C) ND-COOH 15/SPCE (30 ± 4^{o}) ($n = 4$).

ND/CFMEs are advantageous because they have some of the same antifouling properties of BDD,[35,40,44,68] but they also have better sensitivity for dopamine with FSCV detection.[39] Indeed, other polymer-based strategies for combatting fouling also suffer from

reducing the overall sensitivity of the electrode.[69,70] Hence, this work establishes NDs as a candidate electrode coating that actually increases the signal as well as inhibits fouling. Peltola et al also show that NDs enhance the biocompatibility of the electrode,[14] so these advantages of NDs may facilitate the long-term *in vivo* monitoring of neurotransmitters. More surface functional groups, such as zwitterionic groups, could be also tested to better inhibit biofouling.[2] Future research could explore the direct fabrication of NDs[71,72] on CFME or other microelectrodes to obtain more complete surface coverage of the larger particles, to enhance sensitivity and antifouling properties.

4.4 Conclusions

In summary, we optimized a simple drop-casting fabrication of NDs on CFMEs. The surface functional groups and size affected the electrochemical properties of the modified electrodes, with 15 or 60 nm COOH functionalized particles giving the best properties. The ND/CFMEs exhibited electrocatalytic properties toward surface-sensitive redox species and low charge transfer resistance. ND modification was beneficial for FSCV detection of dopamine as it doubled the dopamine faradaic current without changing the background current, improving the LOD to 3 nM. The modified electrodes also increased the selectivity from cationic neurotransmitters and against anionic interferents such as AA. ND coating also alleviated electrochemical fouling and biofouling, and the signals after fouling were larger or the same as CFMEs that had not been fouled. Overall, NDs are a promising nanomaterial to reduce electrode fouling while maintaining enhanced electrochemical signal.

4.5 References

(1) Mochalin, V. N.; Shenderova, O.; Ho, D.; Gogotsi, Y. The Properties and Applications of Nanodiamonds. *Nat. Nanotechnol.* **2012**, *7*, 11–23.

(2) Cao, Q.; Puthongkham, P.; Venton, B. J. Review: New Insights into Optimizing Chemical and 3D Surface Structures of Carbon Electrodes for Neurotransmitter Detection. *Anal. Methods* **2019**, *11* (3), 247–261.

(3) Georgakilas, V.; Perman, J. A.; Tucek, J.; Zboril, R. Broad Family of Carbon Nanoallotropes: Classification, Chemistry, and Applications of Fullerenes, Carbon Dots, Nanotubes, Graphene, Nanodiamonds, and Combined Superstructures. *Chem. Rev.* **2015**, *115* (11), 4744–4822.

(4) Dolmatov, V. Y. Detonation Synthesis Ultradispersed Diamonds: Properties and Applications. *Russ. Chem. Rev.* **2001**, *70*, 607–626.

(5) Iakoubovskii, K.; Baidakova, M. V.; Wouters, B. H.; Stesmans, A.; Adriaenssens, G. J.; Vul', A. Y.; Grobet, P. J. Structure and Defects of Detonation Synthesis Nanodiamond. *Diam. Relat. Mater.* **2000**, *9* (3), 861–865.

(6) Schrand, A. M.; Hens, S. A. C.; Shenderova, O. A. Nanodiamond Particles: Properties and Perspectives for Bioapplications. *Crit. Rev. Solid State Mater. Sci.* **2009**, *34* (1–2), 18–74.

(7) Mchedlov-Petrossyan, N. O.; Kamneva, N. N.; Marynin, A. I.; Kryshtal, A. P.; Ōsawa, E. Colloidal Properties and Behaviors of 3 Nm Primary Particles of Detonation Nanodiamonds in Aqueous Media. *Phys. Chem. Chem. Phys.* **2015**, *17* (24), 16186–16203.

(8) Cheng, X.-B.; Zhao, M.-Q.; Chen, C.; Pentecost, A.; Maleski, K.; Mathis, T.; Zhang, X.-Q.; Zhang, Q.; Jiang, J.; Gogotsi, Y. Nanodiamonds Suppress the Growth of Lithium Dendrites. *Nat. Commun.* **2017**, *8* (1), 336.

(9) Krüger, A.; Kataoka, F.; Ozawa, M.; Fujino, T.; Suzuki, Y.; Aleksenskii, A. E.; Vul', A. Y.; Osawa, E. Unusually Tight Aggregation in Detonation Nanodiamond: Identification and Disintegration. *Carbon* **2005**, *43* (8), 1722–1730.

(10) Holt, K. B.; Ziegler, C.; Caruana, D. J.; Zang, J.; Millán-Barrios, E. J.; Hu, J.; Foord, J. S. Redox Properties of Undoped 5 Nm Diamond Nanoparticles. *Phys. Chem. Chem. Phys.* **2008**, *10* (2), 303–310.

(11) Holt, K. B.; Caruana, D. J.; Millán-Barrios, E. J. Electrochemistry of Undoped Diamond Nanoparticles: Accessing Surface Redox States. *J. Am. Chem. Soc.* **2009**, *131* (32), 11272–11273.

(12) Chen, L. H.; Zang, J. B.; Wang, Y. H.; Bian, L. Y. Electrochemical Oxidation of Nitrite on Nanodiamond Powder Electrode. *Electrochim. Acta* **2008**, *53* (8), 3442–3445.

(13) Holt, K. B. Undoped Diamond Nanoparticles: Origins of Surface Redox Chemistry. *Phys. Chem. Chem. Phys.* **2010**, *12*, 2048.

(14) Peltola, E.; Wester, N.; Holt, K. B.; Johansson, L. S.; Koskinen, J.; Myllymäki, V.; Laurila, T. Nanodiamonds on Tetrahedral Amorphous Carbon Significantly Enhance Dopamine Detection and Cell Viability. *Biosens. Bioelectron.* **2017**, *88*, 273–282.

(15) Dai, W.; Li, M.; Gao, S.; Li, H.; Li, C.; Xu, S.; Wu, X.; Yang, B. Fabrication of Nickel/Nanodiamond/Boron-Doped Diamond Electrode for Non-Enzymatic Glucose Biosensor. *Electrochim. Acta* **2016**, *187*, 413–421.

(16) Chen, T. W.; Palanisamy, S.; Chen, S. M.; Velusamy, V.; Liu, Y. H.; Tseng, T. W.; Yu, M. C.; Lee, S. Y.; Chang, W. H.; Liu, X. Sensitive and Low-Potential Electrochemical Detection of Hydroquinone Using a Nanodiamond Modified Glassy Carbon Electrode. *Int. J. Electrochem. Sci.* **2017**, *12* (9), 8021–8032.

(17) Simioni, N. B.; Silva, T. A.; Oliveira, G. G.; Fatibello-filho, O. A Nanodiamond-Based Electrochemical Sensor for the Determination of Pyrazinamide Antibiotic. *Sens. Actuators, B* **2017**, *250*, 315–323.

(18) Huffman, M. L.; Venton, B. J. Carbon-Fiber Microelectrodes for in Vivo Applications. *Analyst* **2009**, *134*, 18–24.

(19) Shin, M.; Copeland, J. M.; Venton, B. J. Drosophila as a Model System for Neurotransmitter Measurements. *ACS Chem. Neurosci.* **2018**, *9* (8), 1872–1883.

(20) Ganesana, M.; Lee, S. T.; Wang, Y.; Venton, B. J. Analytical Techniques in Neuroscience: Recent Advances in Imaging, Separation, and Electrochemical Methods. *Anal. Chem.* **2017**, *89* (1), 314–341.

(21) Roberts, J. G.; Sombers, L. A. Fast-Scan Cyclic Voltammetry: Chemical Sensing in the Brain and Beyond. *Anal. Chem.* **2018**, *90* (1), 490–504.

(22) Hersey, M.; Berger, S. N.; Holmes, J.; West, A.; Hashemi, P. Recent Developments in Carbon Sensors for At-Source Electroanalysis. *Anal. Chem.* **2019**, *91* (1), 27–43.

(23) Taylor, I. M.; Robbins, E. M.; Catt, K. A.; Cody, P. A.; Happe, C. L.; Cui, X. T. Enhanced Dopamine Detection Sensitivity by PEDOT/Graphene Oxide Coating on in Vivo Carbon Fiber Electrodes. *Biosens. Bioelectron.* **2017**, *89*, 400–410.

(24) Zestos, A. G.; Yang, C.; Jacobs, C. B.; Hensley, D.; Venton, B. J. Carbon Nanospikes Grown on Metal Wires as Microelectrode Sensors for Dopamine. *Analyst* **2015**, *140*, 7283–7292.

(25) Xiao, N.; Venton, B. J. Rapid, Sensitive Detection of Neurotransmitters at Microelectrodes Modified with Self-Assembled SWCNT Forests. *Anal. Chem.* **2012**, *84*, 7816–7822.

(26) Ross, A. E.; Venton, B. J. Nafion-CNT Coated Carbon-Fiber Microelectrodes for Enhanced Detection of Adenosine. *Analyst* **2012**, *137* (13), 3045–3051.

(27) Yang, C.; Jacobs, C. B.; Nguyen, M. D.; Ganesana, M.; Zestos, A. G.; Ivanov, I. N.; Puretzky, A. A.; Rouleau, C. M.; Geohegan, D. B.; Venton, B. J. Carbon Nanotubes Grown on Metal Microelectrodes for the Detection of Dopamine. *Anal. Chem.* **2016**, *88*, 645–652.

(28) Swamy, B. E. K.; Venton, B. J. Carbon Nanotube-Modified Microelectrodes for Simultaneous Detection of Dopamine and Serotonin in Vivo. *Analyst* **2007**, *132* (9), 876–884.

(29) Puthongkham, P.; Yang, C.; Venton, B. J. Carbon Nanohorn-Modified Carbon Fiber Microelectrodes for Dopamine Detection. *Electroanalysis* **2018**, *30*, 1073–1081.

(30) McCreery, R. L. Advanced Carbon Electrode Materials for Molecular Electrochemistry. *Chem. Rev.* **2008**, *108* (7), 2646–2687.

(31) Yang, C.; Denno, M. E.; Pyakurel, P.; Venton, B. J. Recent Trends in Carbon Nanomaterial-Based Electrochemical Sensors for Biomolecules: A Review. *Anal. Chim. Acta* **2015**, *887*, 17–37.

(32) Yang, C.; Wang, Y.; Jacobs, C. B.; Ivanov, I.; Venton, B. J. O2 Plasma Etching and Anti-Static Gun Surface Modifications for CNT Yarn Microelectrode Improve Sensitivity and Anti-Fouling Properties. *Anal. Chem.* **2017**, 5605–5611.

(33) Xiao, T.; Wu, F.; Hao, J.; Zhang, M.; Yu, P.; Mao, L. In Vivo Analysis with Electrochemical Sensors and Biosensors. *Anal. Chem.* **2016**, *89*, 300–313.

(34) Hashemi, P.; Dankoski, E. C.; Petrovic, J.; Keithley, R. B.; Wightman, R. M. Voltammetric Detection of 5-Hydroxytryptamine Release in the Rat Brain. *Anal. Chem.* **2009**, *81* (22), 9462–9471.

(35) Patel, A. N.; Unwin, P. R.; MacPherson, J. V. Investigation of Film Formation Properties

during Electrochemical Oxidation of Serotonin (5-HT) at Polycrystalline Boron Doped Diamond. *Phys. Chem. Chem. Phys.* **2013**, *15* (41), 18085–18092.

(36) Fang, H.; Pajski, M. L.; Ross, A. E.; Venton, B. J. Quantitation of Dopamine, Serotonin and Adenosine Content in a Tissue Punch from a Brain Slice Using Capillary Electrophoresis with Fast-Scan Cyclic Voltammetry Detection. *Anal. Methods* **2013**, *5* (11), 2704–2711.

(37) Zestos, A. G.; Jacobs, C. B.; Trikantzopoulos, E.; Ross, A. E.; Venton, B. J. Polyethylenimine Carbon Nanotube Fiber Electrodes for Enhanced Detection of Neurotransmitters. *Anal. Chem.* **2014**, *86* (17), 8568–8575.

(38) Sarada, B. V.; Rao, T. N.; Tryk, D. A.; Fujishima, A. Electrochemical Oxidation of Histamine and Serotonin at Highly Boron- Doped Diamond Electrodes. *Anal. Chem.* **2000**, *72* (7), 1632–1638.

(39) Bennet, K. E.; Tomshine, J. R.; Min, H.-K.; Manciu, F. S.; Marsh, M. P.; Paek, S. B.; Settell, M. L.; Nicolai, E. N.; Blaha, C. D.; Kouzani, A. Z.; et al. A Diamond-Based Electrode for Detection of Neurochemicals in the Human Brain. *Front. Hum. Neurosci.* **2016**, *10*, 1–12.

(40) Patel, B. A.; Bian, X.; Quaiserová-Mocko, V.; Galligan, J. J.; Swain, G. M. In Vitro Continuous Amperometric Monitoring of 5-Hydroxytryptamine Release from Enterochromaffin Cells of the Guinea Pig Ileum. *Analyst* **2007**, *132* (1), 41–47.

(41) Granger, M. C.; Witek, M.; Xu, J.; Wang, J.; Hupert, M.; Hanks, A.; Koppang, M. D.; Butler, J. E.; Lucazeau, G.; Mermoux, M.; et al. Standard Electrochemical Behavior of High-Quality, Boron-Doped Polycrystalline Diamond Thin-Film Electrodes. *Anal. Chem.* **2000**, *72* (16), 3793–3804.

(42) Siddiqui, S.; Dutta, G.; Tan, C.; Arumugam, P. U. Nanocrystalline Diamond Electrodes: Enabling Electrochemical Microsensing Applications with High Reliability and Stability. *IEEE Nanotechnol. Mag.* **2016**, *10* (3), 12–20.

(43) Park, J.; Quaiserová-Mocko, V.; Pecková, K.; Galligan, J. J.; Fink, G. D.; Swain, G. M. Fabrication, Characterization, and Application of a Diamond Microelectrode for Electrochemical Measurement of Norepinephrine Release from the Sympathetic Nervous System. *Diam. Relat. Mater.* **2006**, *15* (4–8), 761–772.

(44) Chang, A. Y.; Dutta, G.; Siddiqui, S.; Arumugam, P. U. Surface Fouling of Ultrananocrystalline Diamond Microelectrodes during Dopamine Detection: Improving Lifetime via Electrochemical Cycling. *ACS Chem. Neurosci.* **2018**, *10*, 313–322.

(45) Peltola, E.; Sainio, S.; Holt, K. B.; Palomäki, T.; Koskinen, J.; Laurila, T. Electrochemical Fouling of Dopamine and Recovery of Carbon Electrodes. *Anal. Chem.* **2018**, *90*, 1408–1416.

(46) Schrand, A. M.; Dai, L.; Schlager, J. J.; Hussain, S. M.; Osawa, E. Differential Biocompatibility of Carbon Nanotubes and Nanodiamonds. *Diam. Relat. Mater.* **2007**, *16* (12), 2118–2123.

(47) Zang, J.; Wang, Y.; Bian, L.; Zhang, J.; Meng, F.; Zhao, Y.; Ren, S.; Qu, X. Surface Modification and Electrochemical Behaviour of Undoped Nanodiamonds. *Electrochim. Acta* **2012**, *72*, 68–73.

(48) Huffman, M. L.; Venton, B. J. Electrochemical Properties of Different Carbon-Fiber Microelectrodes Using Fast-Scan Cyclic Voltammetry. *Electroanalysis* **2008**, *20* (22), 2422–2428.

(49) Nunn, N.; Shenderova, O. Toward a Golden Standard in Single Digit Detonation Nanodiamond. *Phys. Status Solidi Appl. Mater. Sci.* **2016**, *213* (8), 2138–2145.

(50) Prawer, S.; Nugent, K. W.; Jamieson, D. N.; Orwa, J. O.; Bursill, L. A.; Peng, J. L. The Raman Spectrum of Nanocrystalline Diamond. *Chem. Phys. Lett.* **2000**, *332*, 93–97.

(51) Korepanov, V. I.; Hamaguchi, H. o.; Osawa, E.; Ermolenkov, V.; Lednev, I. K.; Etzold, B. J. M.; Levinson, O.; Zousman, B.; Epperla, C. P.; Chang, H. C. Carbon Structure in Nanodiamonds Elucidated from Raman Spectroscopy. *Carbon* **2017**, *121*, 322–329.

(52) Gabrielli, C.; Keddam, M.; Portail, N.; Rousseau, P.; Takenouti, H.; Vivier, V. Electrochemical Impedance Spectroscopy Investigations of a Microelectrode Behavior in a Thin-Layer Cell: Experimental and Theoretical Studies. *J. Phys. Chem. B* **2006**, *110* (41), 20478–20485.

(53) Park, H.; Takmakov, P.; Lee, H. Electrochemical Evaluations of Fractal Microelectrodes for Energy Efficient Neurostimulation. *Sci. Rep.* **2018**, *8* (1), 1–11.

(54) Varley, T. S.; Hirani, M.; Harrison, G.; Holt, K. B. Nanodiamond Surface Redox Chemistry: Influence of Physicochemical Properties on Catalytic Processes. *Faraday Discuss.* **2014**, *172* (0), 349–364.

(55) Bard, A. J.; Faulkner, L. R. *Electrochemical Methods: Fundamentals and Applications*, 2nd ed.; John Wiley and Sons: New York, 2001.

(56) Takagi, K.; Natsui, K.; Watanabe, T.; Einaga, Y. Increasing the Electric Double-Layer Capacitance in Boron-Doped Diamond Electrodes. *ChemElectroChem* **2019**, 1683–1687.

(57) Watanabe, T.; Shimizu, T. K.; Tateyama, Y.; Kim, Y.; Kawai, M.; Einaga, Y. Giant Electric Double-Layer Capacitance of Heavily Boron-Doped Diamond Electrode. *Diam. Relat. Mater.* **2010**, *19* (7–9), 772–777.

(58) Lv, X.; Hu, B.; Wang, Z.; Peng, J.; Weng, J. Two-Electron Oxidation of Dopamine Controlled by Surface Modification of Few-Layer Graphene. *Electrochim. Acta* **2015**, *180*, 43–52.

(59) Mochalin, V.; Osswald, S.; Gogotsi, Y. Contribution of Functional Groups to the Raman Spectrum of Nanodiamond Powders. *Chem. Mater.* **2009**, *128*, 273–279.

(60) Bath, B. D.; Michael, D. J.; Trafton, B. J.; Joseph, J. D.; Runnels, P. L.; Wightman, R. M. Subsecond Adsorption and Desorption of Dopamine at Carbon-Fiber Microelectrodes. *Anal. Chem.* **2000**, *72* (24), 5994–6002.

(61) Morgan, D. M.; Weber, S. G. Noise and Signal-to-Noise Ratio in Electrochemical Detectors. *Anal. Chem.* **1984**, *56* (13), 2560–2567.

(62) Chen, S. M.; Chen, J. Y.; Vasantha, V. S. Electrochemical Preparation of Epinephrine/Nafion Chemically Modified Electrodes and Their Electrocatalytic Oxidation of Ascorbic Acid and Dopamine. *Electrochim. Acta* **2006**, *52* (2), 455–465.

(63) Hu, M.; Fritsch, I. Application of Electrochemical Redox Cycling: Toward Differentiation of Dopamine and Norepinephrine. *Anal. Chem.* **2016**, *88* (11), 5574–5578.

(64) Robinson, D. L.; Venton, B. J.; Heien, M. L. A. V; Wightman, R. M. Detecting Subsecond Dopamine Release with Fast-Scan Cyclic Voltammetry in Vivo. *Clin. Chem.* **2003**, *49* (10), 1763–1773.

(65) Pajski, M. L.; Venton, B. J. Adenosine Release Evoked by Short Electrical Stimulations in Striatal Brain Slices Is Primarily Activity Dependent. *ACS Chem. Neurosci.* **2010**, *1* (12), 775–787.

(66) Lee, S. T.; Venton, B. J. Regional Variations of Spontaneous, Transient Adenosine Release in Brain Slices. *ACS Chem. Neurosci.* **2018**, *9* (3), 505–513.

(67) Weese, M. E.; Krevh, R. A.; Li, Y.; Alvarez, N. T.; Ross, A. E. Defect Sites Modulate Fouling Resistance on Carbon-Nanotube Fiber Electrodes. *ACS Sens.* **2019**, *4*, 1001–1007.

(68) Güell, A. G.; Meadows, K. E.; Unwin, P. R.; MacPherson, J. V. Trace Voltammetric Detection of Serotonin at Carbon Electrodes: Comparison of Glassy Carbon, Boron Doped Diamond and Carbon Nanotube Network Electrodes. *Phys. Chem. Chem. Phys.* **2010**, *12*

(34), 10108–10114.

(69) Liu, X.; Xiao, T.; Wu, F.; Shen, M.-Y.; Zhang, M.; Yu, H.; Mao, L. Ultrathin Cell-Membrane-Mimic Phosphorylcholine Polymer Film Coating Enables Large Improvements for In Vivo Electrochemical Detection. *Angew. Chem., Int. Ed.* **2017**, *56* (39), 11802–11806.

(70) Singh, Y. S.; Sawarynski, L. E.; Dabiri, P. D.; Choi, W. R.; Andrews, A. M. Head-to-Head Comparisons of Carbon Fiber Microelectrode Coatings for Sensitive and Selective Neurotransmitter Detection by Voltammetry. *Anal. Chem.* **2011**, *83* (17), 6658–6666.

(71) Wang, X.; Shen, X.; Gao, J.; Sun, F. Consecutive Deposition of Amorphous SiO2 Interlayer and Diamond Film on Graphite by Chemical Vapor Deposition. *Carbon* **2017**, *117*, 126–136.

(72) Antonin, O.; Schoeppner, R.; Gabureac, M.; Pethö, L.; Michler, J.; Raynaud, P.; Nelis, T. Nano Crystalline Diamond MicroWave Chemical Vapor Deposition Growth on Three Dimension Structured Silicon Substrates at Low Temperature. *Diam. Relat. Mater.* **2018**, *83* (November 2017), 67–74.

CHAPTER 5

Structural Similarity Image Analysis for Detection of Adenosine and Dopamine in Fast-Scan Cyclic Voltammetry Color Plots

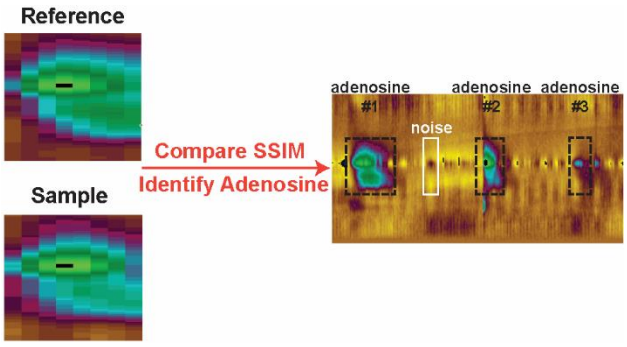

Chapter 5 was submitted and under reviewed with *Anal. Chem.* at the time of submission.

Abstract

Fast-scan cyclic voltammetry (FSCV) is widely used for *in vivo* detection of neurotransmitters, but data analysis for continuous FSCV is difficult because of the large amount of data and signal drift. Most data analysis has focused on dopamine, but other neurochemicals such as adenosine have cyclic voltammograms that are more complicated and change over time. FSCV of adenosine results in a primary oxidation and then a secondary oxidation peak that is slightly delayed and grows in over time. Here, we propose an image analysis-based algorithm to automate the identification and characterization of spontaneous, transient adenosine events from FSCV data. Structural similarity (SSIM) index was utilized to compare a sample FSCV color plot with known adenosine reference color plots, and the SSIM cutoff score was optimized to distinguish between adenosine and other signals. High-pass digital filtering was also applied to remove the background drift and lower the noise, which produced a better LOD. The SSIM algorithm detected more adenosine events than a previous algorithm based on current vs time traces, with 99.5 ± 0.6% precision, 95 ± 3% recall, and 97 ± 2% F_1 score (*n* = 15 experiments from three researchers). For selectivity, it successfully rejected signals from pH changes, histamine, and H_2O_2. This SSIM-based detection was generalized to detect dopamine, including simultaneous events with dopamine and adenosine. The combination of image analysis and signal processing improves the efficiency of automated analysis of FSCV data, using all the data to detect multiple analytes.

5.1 Introduction

Fast-scan cyclic voltammetry (FSCV)[1–3] has been adopted by neurochemists to monitor rapid dynamics of electroactive molecules *in vivo* such as dopamine,[4–7] serotonin,[8,9] adenosine,[10,11] and hydrogen peroxide (H_2O_2)[12,13] because of its fast temporal response.[4,14–18] FSCV also gives a unique cyclic voltammogram (CV) for each analyte and thus has better selectivity than other electrochemical techniques such as amperometry.[7,19] False color plots were invented to illustrate the Faradaic signals, noise, and signal drift in the FSCV current-potential-time data.[20] Yet, analyzing large datasets requires significant effort by humans and could be biased. Statistical techniques such as principal component regression (PCR) and partial least square regression (PLSR) have been used to discriminate neurotransmitter signals from the noise and pH shifts in FSCV data.[21–24] However, these techniques analyze a single CV and fail to accurately detect and quantify neurotransmitters which have CV shapes changing within the same event.[25] Using an alternative data analysis algorithm that uses the whole 3D data set will improve the accuracy and efficiency of the analysis.

Adenosine is a neuromodulator that regulates cell signaling, blood flow, sleep, and neurotransmission.[10,11,26,27] FSCV has revealed the rapid dynamics of adenosine release *in vivo*, including a spontaneous mode of adenosine events that are random and hard to predict.[10,14,28,29] Adenosine is difficult to detect because it undergoes at least two oxidation steps and results in two Faradaic peaks that grow on different time scales.[10,30] Thus, the CV shapes within the same adenosine event are different, and this complicates the PCR analysis.[14,25] In a previous study,[25] we proposed an automated algorithm (“Borman Method”) to detect adenosine events by using the temporal relationship between primary and secondary peak in current-time traces. The program differentiated adenosine from

other high-oxidation potential compounds such as H_2O_2 and histamine.[12,25,31] Nevertheless, using only two current-time traces to analyze the data ignores most of the data set and is susceptible to electrical noise and background drift in continuous measurements.[23,32,33] Therefore, data analysis using the full color plot would be more accurate.

An alternative solution for FSCV data analysis is to consider the 3D color plot as an image, and then apply an image processing technique to it. Because of differences in redox potential, redox kinetics, and mass transport properties, each neurotransmitter produces a unique “image” with different peak potential, peak width, and temporal characteristics in the FSCV color plot. Hence, detecting a neurotransmitter from the color plot data becomes a problem of image recognition.[34] One key image recognition method is the structural similarity (SSIM) index, developed based on the human visual system, which recognizes objects from the structural variation in a perceived view.[35] With the SSIM index, the similarity between a sample image and a reference image is calculated as a function of luminance, contrast, and structure.[35] It outperforms other measures such as mean squared error that compare the intensity difference pixel by pixel, as the latter does not consider the whole image structure and does not tolerate a slight shift in the image.[35,36] The SSIM index has been implemented to detect an object in many applications such as digit recognition,[36] mammograms,[37] electrocardiograms,[38] and mass spectrometry imaging.[34]

In this work, we implemented the SSIM image analysis (termed “SSIM Method”), to analyze FSCV data. We developed new software that uses the SSIM to detect transient adenosine events by comparing FSCV color plots between the sample data and reference events. A high-pass filter was applied to remove the background charging current and

background drift,[32] eliminating the need for background subtraction. The new software was tested by analyzing 15 datasets of spontaneous adenosine detection in rats and mice, and it resulted in 99.5 ± 0.6% precision, 95 ± 3% recall, and 97 ± 2% F_1 overall score. The SSIM index effectively rejected noise and other chemical interferents. Finally, the SSIM image analysis was generalized to detect dopamine, including dopamine events that occur simultaneously with adenosine events. The combination of image analysis and signal processing enhances high accuracy, precision, and efficiency for the automated analysis of FSCV data.

5.2 Experimental Section

5.2.1 Carbon-Fiber Microelectrodes and FSCV Instrumentation

Carbon-fiber microelectrodes (CFMEs) were prepared from T-650 carbon fibers (Cytec Engineering Materials, West Patterson, NJ) with 7-µm diameter. The fiber was insulated and sealed in a glass capillary[39] to leave an exposed fiber length of 100 µm. FSCV data were collected at a ChemClamp potentiostat (Dagan, Minneapolis, MN) using a two-electrode system, including CFME working electrode and Ag/AgCl reference electrode. The FSCV waveform was –0.4 V holding potential, +1.45 V switching potential, 400 v/s scan rate, and 10 Hz repetition rate. All data were collected with HDCV Analysis (Department of Chemistry, University of North Carolina at Chapel Hill).

5.2.2 Chemicals and In Vitro Experiments

Adenosine, dopamine, histamine, and adenosine triphosphate (ATP) were purchased from Acros Organics (Morris Plains, NJ), and H_2O_2 was purchased from Macron (Center Valley, PA). Stock solutions were prepared in 0.1 M $HClO_4$ to 10 mM

concentration. The final working solutions were prepared by diluting the stock solution in the phosphate-buffered saline (PBS) containing 131.25 mM NaCl, 3.00 mM KCl, 10.0 mM NaH_2PO_4, 1.2 mM $MgCl_2$, 2.0 mM Na_2SO_4, and 1.2 mM $CaCl_2$ with pH adjusted to 7.4. The buffer was also adjusted to pH 7.3 by HCl or pH 7.5 by NaOH to test the effect of pH change. *In vitro* experiments and electrode calibration were conducted with a flow cell connected to a syringe pump (Harvard Apparatus, Holliston, MA) and a six-port loop injector with an air actuator (VIVI Valco Instruments, Houston, TX).

5.2.3 Animal Methods

All animal experiments were approved by the University of Virginia Animal Care and Use Committee. Male Sprague-Dawley rats (Charles River Laboratories, Wilmington, MA) and male C57BL/6J mice (Jackson Laboratory, Bar Harbor, ME) were housed on a 12:12 h light/dark cycle with food and water provided *ad libitum*. All surgery was performed under isofluorane anesthesia and all effort to minimize animal suffering.

For rats and mice *in vivo* data, an animal was put in a stereotaxic frame, surgical areas were shaved and local anesthetized with bupivacaine (Sensorcaine, MPF, APP Pharmaceuticals, LLC; Schaumburg, IL), and the skull was drilled to place the electrodes in. *In vivo* rat data were measured in the caudate putamen (coordinates: ML +2.0, AP +1.2, DV –4.5 mm), basolateral amygdala (coordinates: ML +4.5, AP –2.8, DV –8.2 mm), hippocampus (coordinates: ML +2.0, AP –3.8, DV –2.5 mm), and prefrontal cortex (coordinates: ML +0.8, AP +2.7, DV –3.0 mm). *In vivo* mice data were measured in three different brain regions[40]: caudate putamen (coordinates: ML +1.5, AP +1.1, DV –3.0 mm), hippocampus (coordinates: ML +2.4, AP –2.5, DV –1.8 mm), and prefrontal cortex (coordinates: ML +0.2, AP +1.3, DV –1.5 mm). The animal was sacrificed by decapitation

after the experiment. For mice brain slice data, a mouse was anesthetized with isofluorane and decapitated immediately. The brain was removed within 2 min and placed in 0–5°C artificial cerebral spinal fluid (aCSF) for 2 min for recovery. 400-µm slices of the caudate-putamen were prepared using a vibratome (LeicaVT1000S, Bannockburn, IL) and transferred to oxygenated aCSF (95% O_2, 5% CO_2) to recover for 1 h before the measurement. aCSF (maintained at 35–37 °C) flowed over the brain slice using a perfusion pump (Watson-Marlo 205U, Wilmington, MA) at a rate of 2 mL/min for all experiments. CFME was inserted into the caudate-putamen region (coordinates: ML +2.0, AP +1.2, DV –4.5 mm) for 75 µm depth.

5.2.4 SSIM Calculation, Digital Filtering, and Program Implementation

SSIM calculation, digital filtering, and the SSIM Method software were implemented in MATLAB 2019b (MathWorks, Inc., Natick, MA). The SSIM index $\mathrm{SSIM}(\boldsymbol{x},\boldsymbol{y})$ is a product of similarity between image $\boldsymbol{x}$ and $\boldsymbol{y}$ in luminance (mean intensity) $l(\boldsymbol{x},\boldsymbol{y})$, contrast (standard deviation of intensity) $c(\boldsymbol{x},\boldsymbol{y})$, and structure (standardized intensity) $s(\boldsymbol{x},\boldsymbol{y})$. The mathematical definition of all three terms can be found in reference [35]. The overall SSIM index is (Eq. 5.1).

$$\mathrm{SSIM}(\boldsymbol{x},\boldsymbol{y}) = [l(\boldsymbol{x},\boldsymbol{y})]^{\alpha}[c(\boldsymbol{x},\boldsymbol{y})]^{\beta}[s(\boldsymbol{x},\boldsymbol{y})]^{\gamma} \quad \text{(Eq. 5.1)}$$

In this work, we used $\alpha = \beta = \gamma = 1$. SSIM indices were computed locally for each potential-time pixel to obtain an SSIM matrix. Then, the matrix was scalar multiplied with a weight matrix to emphasize specific FSCV color plot features. The sum of all elements in the product matrix was normalized get the final SSIM index, which ranges from 0 (no similarity) to 1 (identical image). Each transient reference and sample were normalized to its maximum current before the SSIM calculation. Digital filters were applied to the

FSCV color plot for data preprocessing with the following design parameters. A high-pass, second-order Butterworth filter[32] with the half-power frequency of 0.03 Hz (for background detrending) or 0.5 Hz (for noise calculation). A Savitzky-Golay filter[41] was used for smoothing had a window length of 15.

There were two versions of the SSIM Method (see "*Performance Evaluation: Internal Reference vs Standard Library*"). The "Internal Reference" version required the input of the start time of six transient adenosine references from a user and the primary peak potential to find the peak current was determined from the references. For this version, a user must go through data set that will be analyzed and find six transient adenosine references. To maximize coverage of the transient adenosine events, each of the six references should have varied size. In this article, two large (peak concentration > 0.25 µM), two medium (0.1–0.25 µM), and two small (< 0.1 µM) transient events were chosen for each analyzed data set. Then, the user will put the file number and start time (not the peak time) of the event into the software. Alternatively, the "Standard Library" version used 15 adenosine references built in the software, and the primary peak potential was determined from the first adenosine event in the data.

5.2.5 Performance Evaluation and Statistics

The SSIM Method was evaluated and optimized by the recall, precision, and F_1 score[42] based on the number of true positives (TP), false positives (FP), and false negatives (FN) benchmarked against the Borman Method[25] with secondary peak correction.[43] Precision is the ratio of the true events to the detected events, which may include the false positives, and is written as (Eq. 5.2),

$$\text{Precision} = \frac{\text{TP}}{\text{TP} + \text{FP}} \quad \text{(Eq. 5.2)}$$

Thus, high precision indicates low false positives. Recall is the ratio between the number of detected adenosine events to the number of actual events. This ratio is (Eq. 5.3).

$$\text{Recall} = \frac{\text{TP}}{\text{TP} + \text{FN}} \quad \text{(Eq. 5.3)}$$

High recall means low false negatives. F_1 score is the harmonic mean of recall and precision to combine both performance indices and is written as (Eq. 5.4).

$$F_1 = 2\frac{(\text{Recall})(\text{Precision})}{\text{Recall} + \text{Precision}} \quad \text{(Eq. 5.4)}$$

Adenosine transient events not picked by the Borman Method were manually checked by human to determine if they were truly adenosine.

All data are presented as the mean ± standard deviation (SD) for *n* number of measurements, except the adenosine event characteristics, which are presented as the mean ± standard error of the mean (SEM) computed from bootstrapping,[44] which was used to approximate the standard error of the mean (SEM) of data. The approximation is better than SD/$\sqrt{n}$, especially for the data that follows other distributions rather than the Gaussian distribution. The procedure for bootstrapping of a dataset with m samples are:

1) Perform 10,000 independent resampling. Each resampling consists of m samples drawn with replacement (i.e. each sample will be either chosen once or chosen twice or not chosen).
2) Calculate the mean of each resampling. Therefore, 10,000 means will be obtained.
3) Approximate the standard error of the mean by calculating the standard deviation of 10,000 means calculated in the Step 2).

Statistical analyses were performed in GraphPad 8 (GraphPad Software, La Jolla, CA), and significance was defined at $p < 0.05$.

5.3 Results and Discussion

5.3.1 FSCV of Adenosine

Adenosine undergoes a two-step irreversible oxidation in FSCV (a tertiary oxidation peak for adenosine is possible but rarely observed *in vivo)*.[10,45] Fig. 5.1 shows FSCV of an *in vivo* spontaneous, transient adenosine event measured in a mouse brain. In the very first CV (time point 1), adenosine oxidation gives a peak of 5 nA at +1.35 V vs Ag/AgCl on the backward scan.[10] One second later, at time point 2, the anodic peak current increased to 17 nA and a new anodic peak of 7 nA appeared at +1.2 V on the forward scan. Two seconds after the first CV (point 3), the primary peak has shrunk to 11 nA, and the secondary peak grown to 9 nA. The relationship between primary and secondary anodic peaks of adenosine is visualized by the false color plot (Fig. 5.1), which illustrates the secondary peak lags behind the primary peak about 0.1–0.3 s, and then stays elevated in current for longer. This time lag creates a rule to help experimenters manually identify the adenosine *in vivo* from the color plot,[11] but the identification of adenosine using a single CV is problematic because the CV shapes within the same transient event are not always the same.

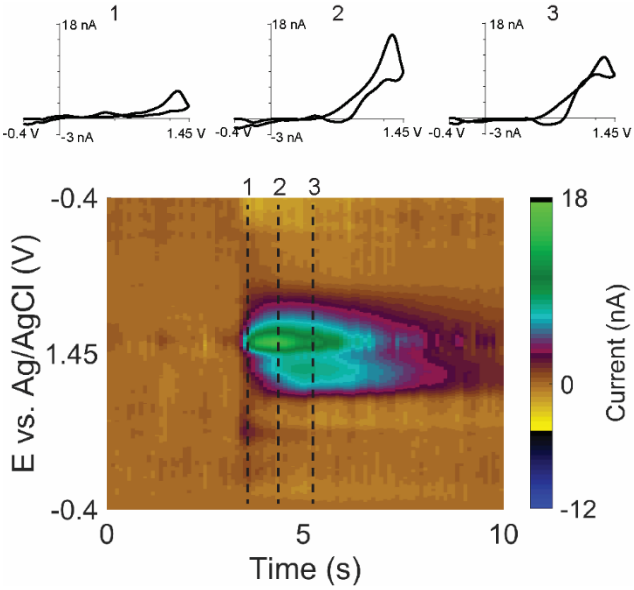

Fig. 5.1 FSCV of *in vivo* transient adenosine event. Top: CVs of adenosine at different time point after the transient started (1) 0.1 s, (2) 1.1 s, (3) 2.1 s. Bottom: Color plot showing the transient adenosine event.

5.3.2 SSIM Image Analysis for Adenosine

SSIM index is the key method for our new algorithm, termed "SSIM Method", to detect adenosine from the FSCV color plot data. SSIM index is calculated from the luminance, contrast, and structure similarity between a sample image and a reference image, with the highest index of 1 representing an identical image.[35] Hence, this image analysis approach requires standard adenosine references. A weight matrix was introduced to emphasize similarity of specific regions in an image,[35] and scalar multiplication between the matrix and the local SSIM index gave the overall SSIM index. A cutoff score was set to identify the image as adenosine (*vide infra*).[36]

Fig. 5.2 gives examples of adenosine reference events, the weight matrix, and example data for SSIM calculation. To examine adenosine, the normalized color plots for the references and samples were compared using a 1.8-s wide data from potential +0.7 to +1.45 to +0.7 V. This window contains both adenosine anodic peaks, but the amount

of data was reduced by half, which shortens the analysis time, which is proportional to the number of SSIM calculation. The reference event captures the start of the adenosine event because it is important to distinguish the temporal delay between primary and secondary anodic peaks, but the time window does not always include the end of the transient event, as clearance kinetics vary more. Adenosine events vary widely in concentration and duration,[14] so different reference events were chosen to span the range of concentrations and durations typically observed. Fig. 5.2A–C shows three normalized adenosine transient reference events with different peak currents: large (9 nA, Reference A, Fig. 5.2A), medium (5 nA, Reference B, Fig. 5.2B), and small (2 nA, Reference C, Fig. 5.2C). These three references have different lag times and peak durations, leading to different image structures. To improve the selectivity for adenosine, the weight matrix for SSIM calculation (Fig. 5.2D) has a weight of 1.5 in the primary peak region and weight of 6 in the secondary peak region. The weight for the secondary peak region is higher to prioritize picking events with the secondary peak and therefore rejecting noise or other neurochemicals that have a peak only at the primary anodic potential.

Fig. 5.2E–H shows four sample windows of data analyzed. For this example, the SSIM index for each sample was calculated compared to each adenosine reference (Fig. 5.2A–C). Sample 1 (Fig. 5.2E) is a large adenosine event (13 nA) with SSIM indices of 0.78, 0.49, and 0.20 for Reference A, B, and C, respectively. This adenosine has high peak current and wide peak width, similar to Reference A, so the SSIM score compared Reference A is the highest. Sample 2 (Fig. 5.2F) is a medium concentration event (4 nA), with lower peak current and duration and so the SSIM index is low for Reference A (0.18), but higher for Reference B (0.87), which has similar current and peak width, and also higher for Reference C (0.56) because of the similar peak shape. Sample 3 (Fig. 5.2G) is

a small adenosine event (0.6 nA) and is the most similar to Reference C which is also small (SSIM index = 0.59). These SSIM calculations demonstrate the need to compare to many adenosine reference events with varied peak currents and durations.

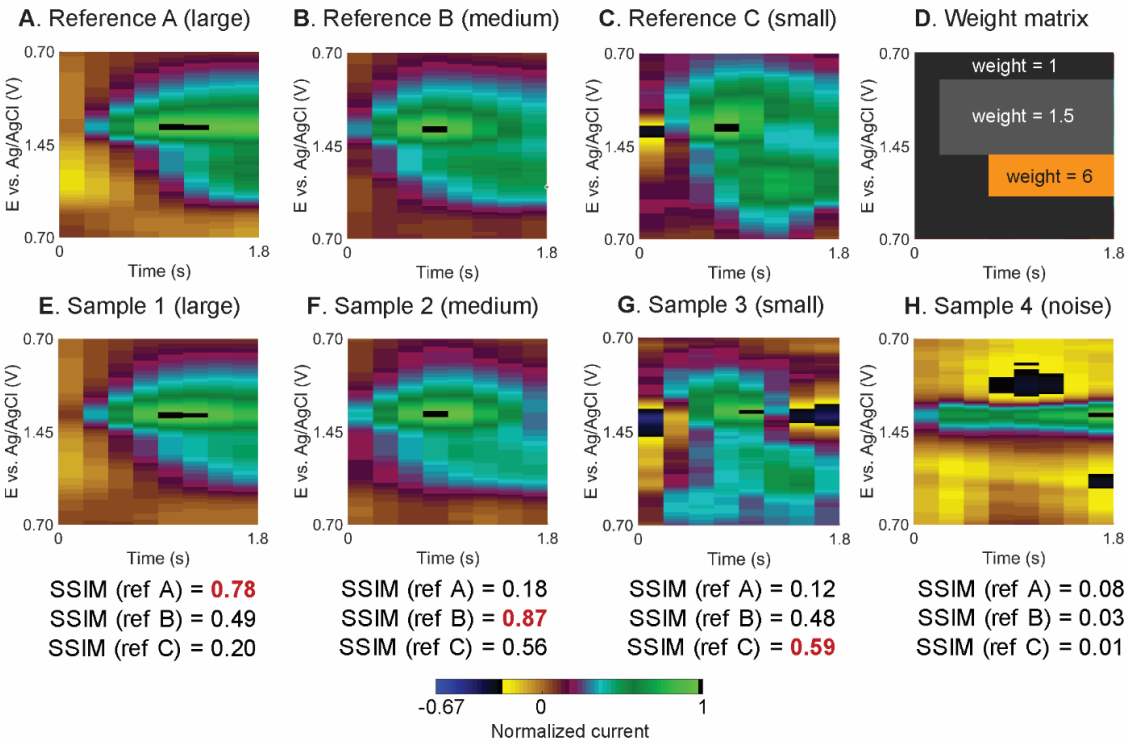

Fig. 5.2 SSIM calculation between *in vivo* adenosine transient references and sample data. All color plots are zoomed in to the potential of interests and normalized to its maximum current to show the range of signals. False color plots of adenosine references: (A) large (peak current = 9 nA), (B) medium (5 nA), and (C) small (2 nA) adenosine events. (D) Weight matrix emphasizes the secondary peak. False color plots of tested FSCV signal with their SSIM indices respected to the three references: (E) large (13 nA), (F) medium (4 nA), (G) small (0.6 nA) adenosine signals, and (H) noise at the switching potential.

There is frequent noise in FSCV color plots, particularly at the switching potential (where the background current is less stable)[46] which is near the peak oxidation for adenosine. Sample 4 (Fig. 5.2H) is a 1.5-nA noise event near the switching potential that gives a SSIM index much lower (0.08, 0.03, and 0.01, respectively) than for the adenosine events. Our previous algorithm struggled with noise near the switching potential, [25] if the

noise was broad and there was also noise at the secondary anodic peak potential. With SSIM, the overall structure is taken into account, and thus it is easier to reject an event as possible noise.

5.3.3 Digital Filtering for Background Drift Correction and Data Smoothing

One challenge for the analysis of FSCV continuous data is the background drift, which is caused by changes in pH, other ions, the electrode surface, or stability of the electronics.[23,32,33,47] Fig. 5.3A illustrates 3 min of unsubtracted FSCV data from an *in vivo* experiment. Traditionally, FSCV data are analyzed from background-subtracted color plot (Fig. 5.3B) to visualize current changes. However, some signals are concealed by the background drift. In Fig. 5.3B, from 40-s onward, there is a 4-5 nA background drift, which obscures small adenosine events that have lower peak currents (boxed in Fig. 5.3B). Our previous Borman algorithm used incremental background subtraction, subtracting the background every 10 s before scanning for adenosine events, but the method was cumbersome because the same trace needed to be analyzed multiple times.[25] Here, we adopted the method of DeWaele et al. to eliminate background drift using a high-pass Butterworth filter.[32] High-pass filtering removes low frequency background drift while keeping the higher frequency events due to rapid release of neurotransmitter. In addition, we added a smoothing filter, the Savitzy-Golay filter, to remove small current fluctuations that might be wrongly recognized as a peak.[41] The color plot in Fig. 5.3C has high pass and Savitzy-Golay filtering and the background (and drift) at all potentials was eliminated, producing cleaner data that can be directly analyzed. Fig. 5.3C reveals a small, 2 nA adenosine event that was hidden in the baseline drift before the filtering. An important point is that with high-pass filtering, no background subtraction is needed because the baseline background is a DC signal and thus is filtered out. Fig. 5.4A plots the current-

time trace of the data after high-pass and Savitzky-Golay filtering to illustrate the reduction in noise and baseline detrending. Therefore, data preprocessing by digital filtering eliminates the background drift and noise, allowing more adenosine events to be detected in the FSCV continuous data.

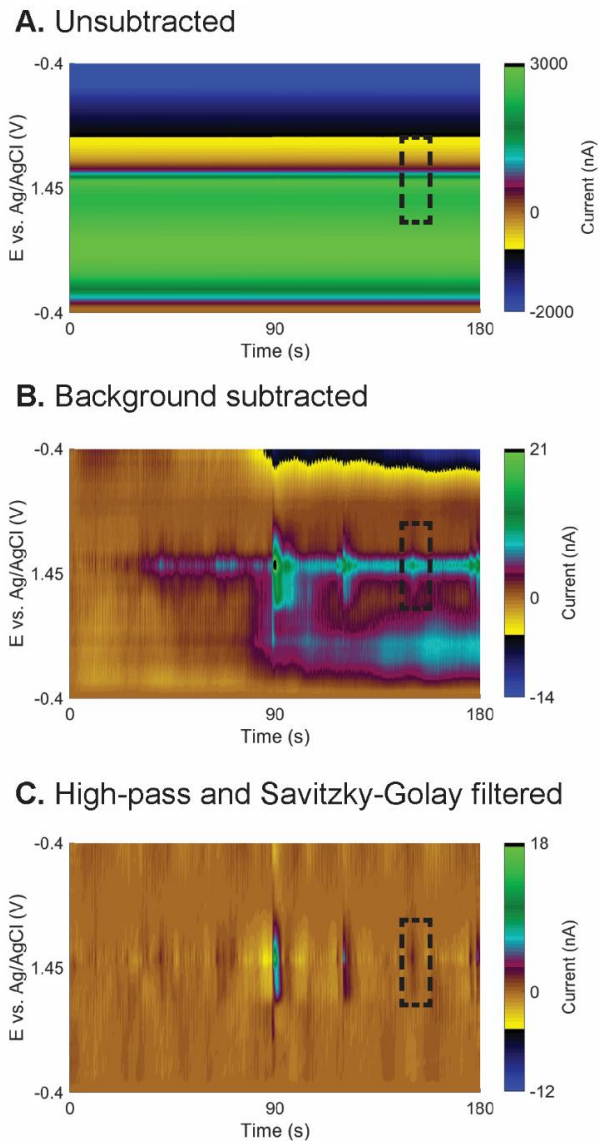

Fig. 5.3 Data preprocessing. 3-min color plots of (A) unsubtracted data, (B) background-subtracted data using t = 0 s as a background, and (C) data after high-pass (0.03 Hz) and Savitzky-Golay filtering. Dashed boxes indicate one small adenosine event hidden in the background drift but observed after filtering.

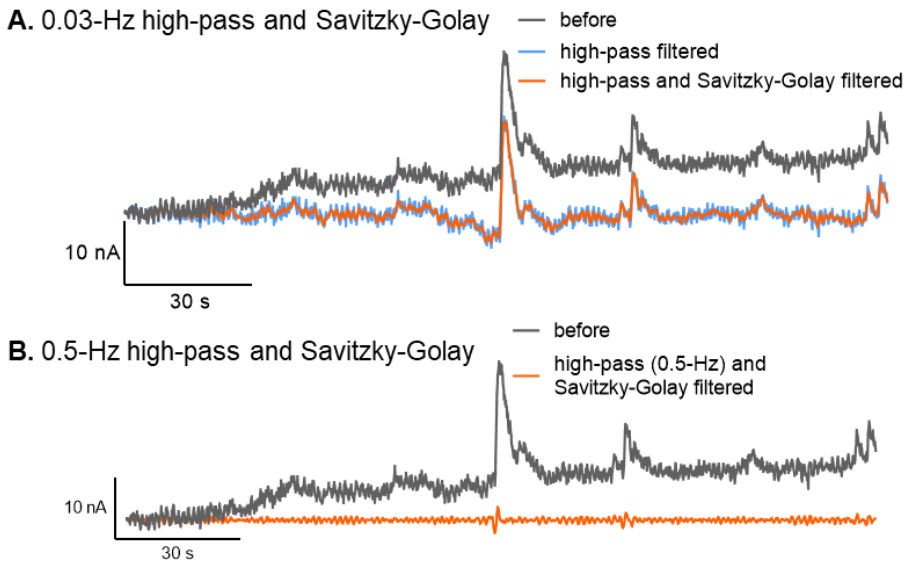

Fig. 5.4 Adenosine primary peak current-time trace from Fig. 5.3. (A) Data before, after high-pass filtering (0.03-Hz cutoff frequency) and Savitzky-Golay filtering for image analysis. (B) Data before and after high-pass filtering (0.5-Hz cutoff frequency) and Savitzky-Golay filtering for noise calculation. The noise trace has the same level as the noise in (A). In this data, S/N = 3 at current = 0.9 nA.

5.3.4 The SSIM Method Algorithm and Optimization

The new algorithm was tested by analyzing 15 data sets and comparing the results with the Borman method and validation by human users. Fig. 5.5A summarizes the software algorithm. For each 3 min color plot, the high-pass filter and Savitzky-Golay filter is applied to the data to correct the background drift and smooth the signal. Then, the data is cut into the potential range of +0.7 to +1.45 to +0.7 V, and the pixel resolution in both time and potential axes is decreased by half to speed up the analysis. The SSIM index of each time point is calculated for a 1.8-s window on the color plot to compare the structural similarity with each reference adenosine event, and the window is incrementally shifted by 0.2 s (Example of SSIM index-time trace from different adenosine references can be found in Fig. 5.6). After obtaining the SSIM index for all data points in the file, the program records seeding times that give the SSIM index higher than the cutoff.

Next, peak characterization is performed for each seeding time. The peak current and peak duration, defined as peak width at half-maximum, are determined at every seeding time from the primary peak current-time trace; the peak is confirmed if it has a S/N ≥ 3. The noise is one standard deviation of the current-time trace after being processed by the 0.5-Hz high-pass Butterworth filter and Savitzky-Golay filter (Fig. 5.4B). The output of the program is a table of adenosine peak positions (in time), peak concentrations, peak durations, and inter-event times in a spreadsheet file (Fig. 5.7).

The key parameter for the accuracy of the SSIM Method is the cutoff score for SSIM index, which helps balance between false negatives and false positives. To optimize the SSIM cutoff, six datasets were analyzed with different SSIM cutoffs ranging from 0.40 to 0.60, and compared with the Borman method.[25] The precision, recall, and F_1 scores were evaluated for each cutoff (Fig. 5.5B). A higher cutoff required a signal to be more similar to the references (high precision), but some noisy adenosine events were not identified (low recall). On the other hand, lower SSIM cutoff picked more events (high recall), but included broad peaks humans did not verify were adenosine (low precision). The combination of both precision and recall is an F_1 score, which was maximal at the SSIM cutoff of 0.50, giving 99.1 ± 0.6% precision, 96 ± 4% recall, and 98 ± 2% F_1 (n = 6). Hence, this cutoff was used for the rest of the program testing and validation.

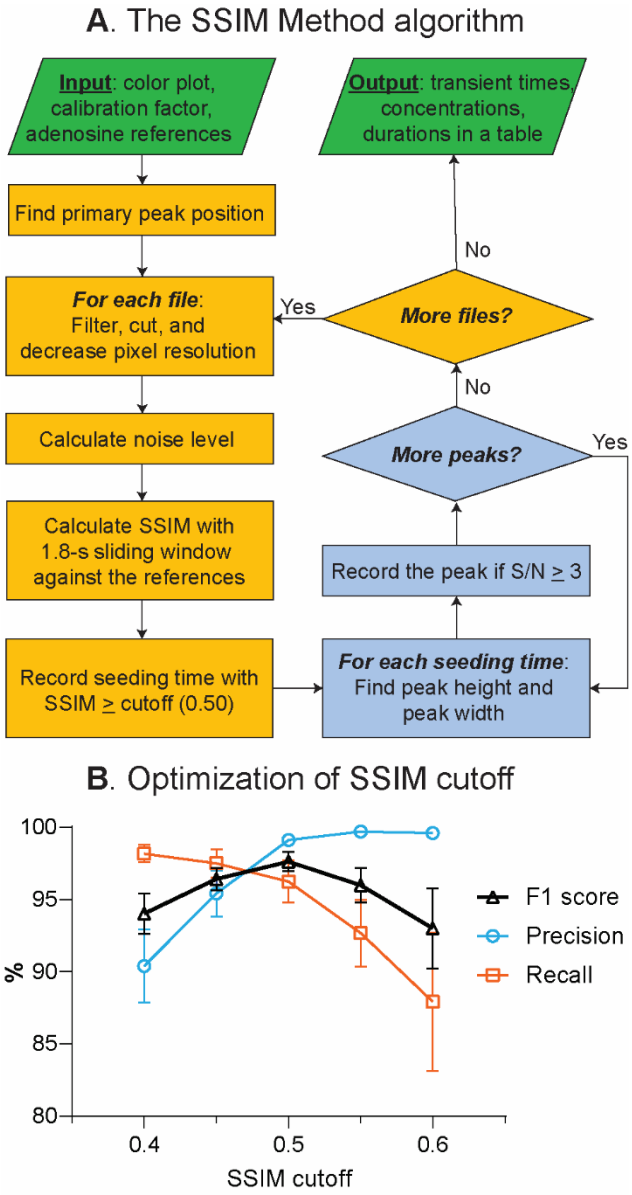

Fig. 5.5 SSIM Method. (A) Algorithm for the detection and characterization of transient adenosine events. (B) Optimization of SSIM cutoff from n = 6 experiments.

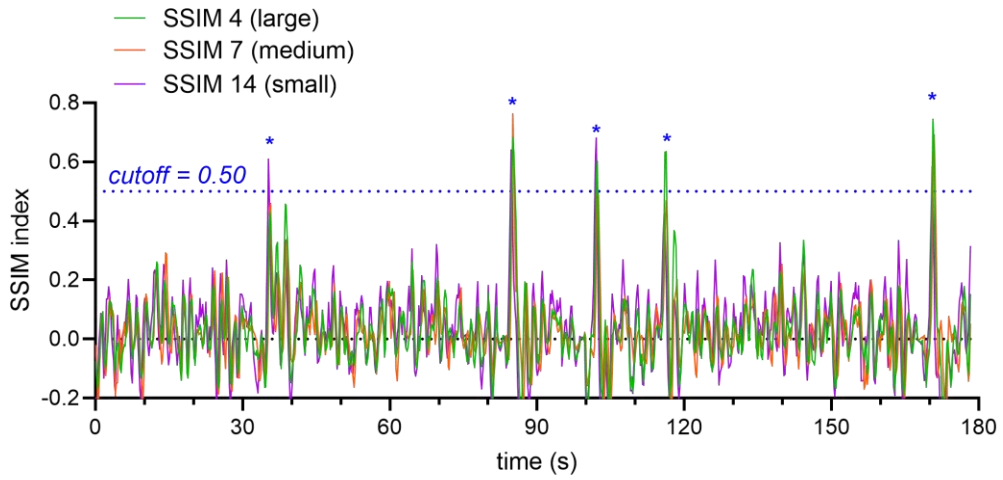

Fig. 5.6 Example of SSIM index-time trace of a 3-min FSCV data calculated with respect to three adenosine references with different size in the standard library (Fig. 5.9). Asterisks indicate the time position with SSIM ≥ 0.50.

File	Seed_s	SSIM	PeakTime_s	Curr_nA	Conc_uM	HalfWidth_s	Noise3_nA	PassSN	InterTime_s
1	82.1	0.63	**82.7**	1.55	**0.0516**	1.28	0.65	1	82.7
2	6.7	0.67	**7.2**	3.20	**0.1068**	1.26	0.66	1	104.5
3	92.9	0.65	**94.0**	2.16	**0.0721**	1.77	0.60	1	266.8
3	137.9	0.70	**138.5**	1.69	**0.0562**	0.68	0.60	1	44.5
4	133.5	0.73	**134.2**	3.47	**0.1158**	1.19	0.66	1	175.7
6	160.1	0.52	**160.9**	4.19	**0.1397**	1.12	0.65	1	386.7
7	37.3	0.76	**38.4**	10.84	**0.3613**	2.02	0.77	1	57.5
7	161.7	0.53	**162.8**	11.02	**0.3673**	1.35	0.77	1	124.4
7	174.3	0.57	**175.0**	2.05	**0.0684**	1.90	0.77	1	12.2
8	173.9	0.72	**175.2**	30.69	**1.0231**	3.03	0.84	1	180.2
10	23.3	0.64	**23.4**	1.15	**0.0382**	0.80	0.62	1	208.2
10	91.9	0.60	**93.0**	1.89	**0.0632**	1.08	0.62	1	69.6

Fig. 5.7 Example output spreadsheet from The SSIM Method. Each row is the characterization of each adenosine event with S/N ≥ 3. Each column is (from left to right): file number, seeding time (s), SSIM index, peak time (s), peak current (nA), peak concentration (μM), peak duration (s), cutoff peak current (S/N = 3), passing S/N?, and inter-event time (s).

5.3.5 Performance Evaluation: Internal Reference vs Standard Library

The SSIM Method was further tested with more datasets to assess the performance and robustness of the SSIM image analysis algorithm. Data from 15 *in vivo* experiments, 10 from rats and 5 from mice, collected by three different experimenters in

four different brain regions were analyzed by both the SSIM Method and Borman Method with secondary peak correction.[43] Positive events not picked by the Borman method were checked by human. The first version of the algorithm was termed “Internal Reference” because the user chooses six reference adenosine events from that animal (examples shown in Fig. 5.8). Because of the similarity in the experimental conditions, a signal in the analyzed data was required to match only one of the six references. Table 1 shows the precision, recall, and F_1 scores from the SSIM Method with internal references. The scores were 99.5 ± 0.6% precision, 95 ± 3% recall, and 97 ± 2% F_1 (n = 15). In other words, the software gave only 0.5% false positives and 5% false negatives. The scores were also better than the previous Borman method[25] because the SSIM analysis used all FSCV information from the color plot and the digital filtering corrected the background drift.

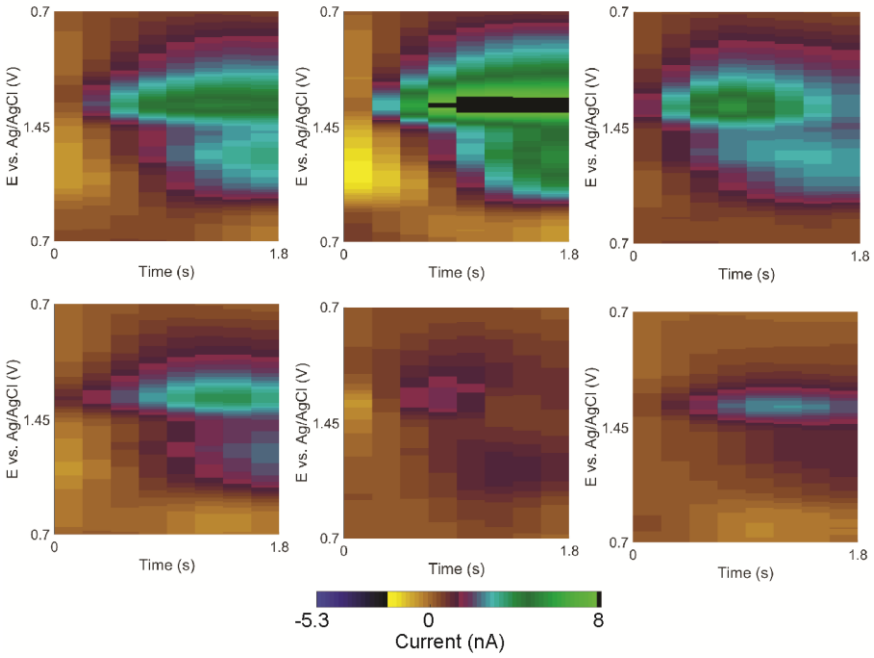

Fig. 5.8 Example of six internal adenosine references from one experiment. File number and start time (not peak time) of each reference were put by the user at the beginning of the program.

Table 5.1 Performance of the SSIM Method

Species	n	SSIM Method, internal reference			SSIM Method, standard library		
		Precision	Recall	F_1 score	Precision	Recall	F_1 score
Rats	10	99.3 ± 0.7	96 ± 3	**98 ± 1**	99 ± 2	95 ± 5	**97 ± 3**
Mice	5	99.9 ± 0.3	94 ± 4	**97 ± 2**	99.6 ± 0.7	89 ± 8	**94 ± 5**
Total	**15**	**99.5 ± 0.6**	**95 ± 3**	**97 ± 2**	**99 ± 1**	**94 ± 7**	**96 ± 4**

Values shown are mean ± SD.

Alternatively, the second version of the algorithm, called the "Standard Library," uses a library of adenosine events collected from different experiments. Here, the SSIM calculation is performed between the input data and a library of 15 adenosine events (Fig. 5.9) collected from 12 experiments in four brain regions (caudate-putamen, prefrontal cortex, hippocampus, basolateral amygdala). More references are needed for this approach because of the greater variation between experimental conditions. With more variation and references, a signal was required to match at least two of the 15 references in order to be identified as adenosine. The SSIM Method using the standard library also yielded high performance scores: 99 ± 1% precision, 94 ± 7% recall, and 96 ± 4 % F_1 (n = 15). The difference in performance between two methods were not significant (unpaired t-test, p = 0.347 for precision, p = 0.219 for recall, and p = 0.123 for F_1) and the library method is easier because it does not require the user to pick references from the data set. Moreover, the library was tested with data sets from FSCV detection of adenosine in brain slice tissue. Even though the shape of adenosine CVs from brain slice data (Fig. 5.10) is slightly different from the *in vivo* library data, the algorithm still performed well with 100% precision, 93% recall, and 96% F_1 (n = 52 events from two data sets). A library for brain slice data could also be made in the future.

One important feature of the SSIM Method is the short analysis time. Traditionally, the manual analysis of 4-hour experimental data took 10 to 18 h. The previous Borman

Method reduced the analysis time to 40 min.[25] In this newly proposed SSIM Method, the analysis time was only 20 min when using the Internal References method and 42 min when using the Standard Library method (longer because it compares the data to more references). Overall, the SSIM Method improved the accuracy and precision of finding adenosine events, while achieving reasonable analysis times.

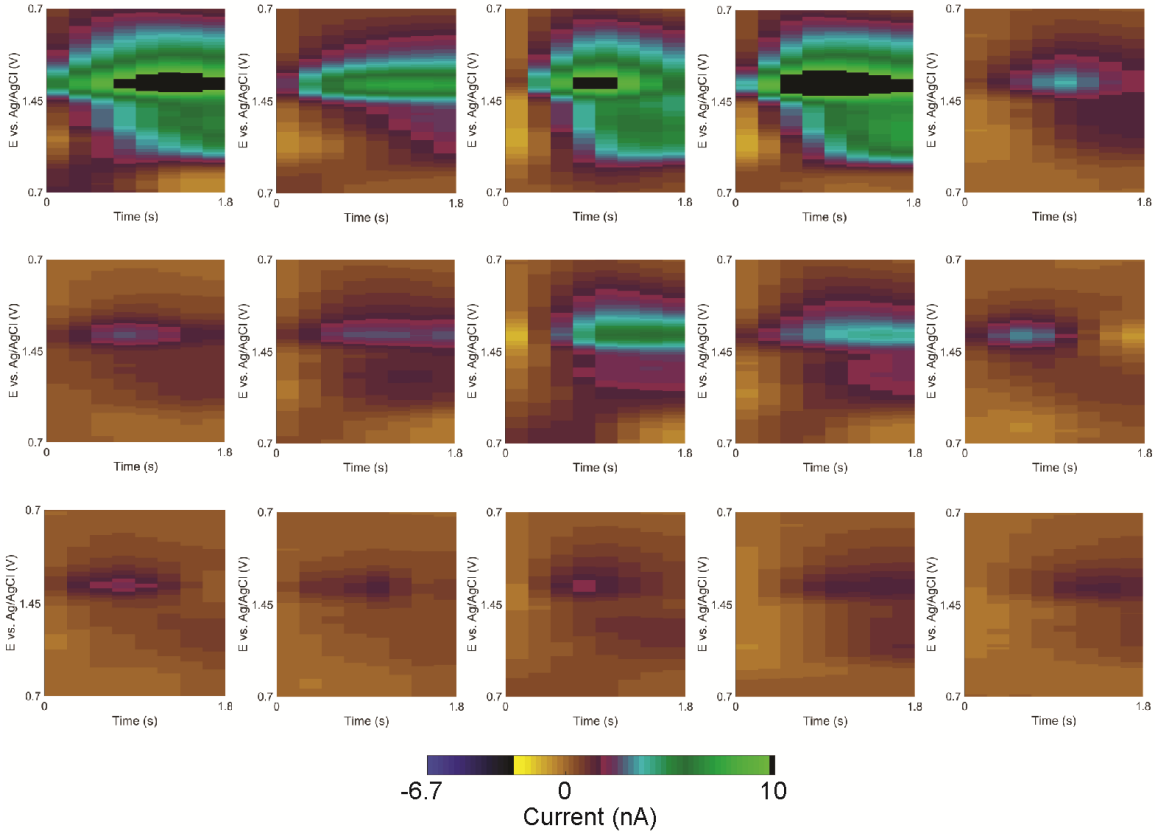

Fig. 5.9 Fifteen adenosine references for the standard library (4 caudate-putamen rats, 3 basolateral amygdala rats, 2 hippocampus rats, 2 prefrontal cortex rats, 2 caudate-putamen mice, and 2 hippocampus mice).

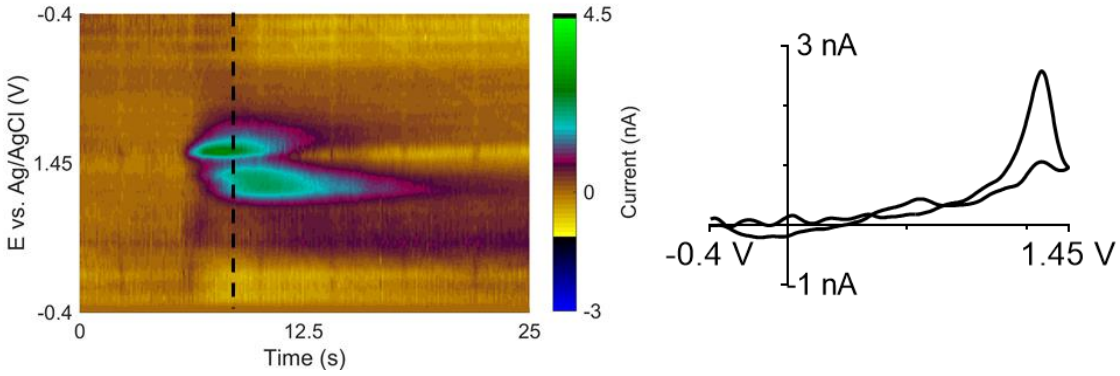

Fig. 5.10 Example data from adenosine in brain slice tissue. CV of adenosine (from dashed time point) illustrated more separation between primary and secondary anodic peaks than the CV from *in vivo* data. This event has the highest SSIM index = 0.81 (compared to the standard library Fig. 5.9).

5.3.6 Performance Evaluation: Adenosine Event Characteristics

Adenosine event characteristics were also compared from the SSIM Method and Borman Method with secondary peak correction.[43] Table 5.2 shows the pooled total of the adenosine events found in the 10 rat datasets (3 caudate-putamen, 3 basolateral amygdala, 2 hippocampus, and 2 prefrontal cortex) and 5 mice datasets (2 caudate-putamen, 2 hippocampus, and 1 prefrontal cortex. Results for the separate datasets can be found in Table 5.3). The Borman method identified 1,470 events while the SSIM Method identified 2,826 events for the internal reference version and 2,494 for the standard library method. There was a significant main effect of the algorithm on the number of events (one-way ANOVA, $p < 0.0001$, $n = 15$), and the number of events from the SSIM Method was significantly higher than the Borman Method (Bonferroni post-test, $p < 0.0001$ for both internal references and standard library methods). Nevertheless, the numbers of events between two methods of the SSIM Method were not significantly different ($p = 0.126$), illustrating that both approaches can be used interchangeably without affecting the data analysis. More events were identified by the SSIM Method because

digital filtering allowed identification adenosine events hidden by the background drift and image analysis took advantage of the unique image of adenosine to identify it from other signals and noise.

Table 5.2 Results from the SSIM Method using internal references and standard library, compared to the Borman Method with secondary peak correction (Separate results for each experiment in Table 5.3).

Species	n	Method	Number of events	Peak concentration (μM)	Peak duration (s)	Inter-event time (s)
Rats	10	Borman	870	0.146 ± 0.005	1.7 ± 0.1	78.5 ± 4.9
		SSIM, internal reference	1,807	0.102 ± 0.003	1.4 ± 0.1	39.2 ± 1.3
		SSIM, standard library	1,627	0.106 ± 0.003	1.4 ± 0.1	43.3 ± 1.4
Mice	5	Borman	600	0.085 ± 0.003	1.6 ± 0.1	53.6 ± 2.7
		SSIM, internal reference	1,019	0.067 ± 0.002	1.4 ± 0.1	31.6 ± 1.3
		SSIM, standard library	867	0.069 ± 0.003	1.4 ± 0.1	37.1 ± 1.6

Values shown are mean ± SEM.
SEM = one standard deviation of the bootstrapped mean, resampled 10,000 times.

Table 5.3 Separated result for each experiment.

Experiment	Borman method with secondary peak correction				SSIM with internal references				SSIM with standard library			
	number of transients	peak concentration (μM)	peak duration (s)	inter-event time (s)	number of transients	peak concentration (μM)	peak duration (s)	inter-event time (s)	number of transients	peak concentration (μM)	peak duration (s)	inter-event time (s)
R1	29	0.151 ± 0.012	2.4 ± 0.2	218.8 ± 40.1	73	0.122 ± 0.009	1.0 ± 0.1	99.6 ± 11.5	84	0.103 ± 0.007	1.0 ± 0.1	86.4 ± 8.5
R2	15	0.139 ± 0.005	2.5 ± 0.3	428.1 ± 124.0	78	0.081 ± 0.013	1.2 ± 0.1	84.2 ± 10.4	59	0.072 ± 0.011	1.2 ± 0.1	112.0 ± 15.0
R3	37	0.178 ± 0.010	1.7 ± 0.1	181.5 ± 37.9	85	0.146 ± 0.008	1.0 ± 0.1	84.8 ± 8.9	124	0.132 ± 0.006	1.0 ± 0.1	57.9 ± 4.4
R4	45	0.130 ± 0.016	1.7 ± 0.1	160.9 ± 25.8	123	0.087 ± 0.009	1.2 ± 0.1	58.6 ± 8.2	117	0.088 ± 0.009	1.2 ± 0.1	61.6 ± 8.3
R5	15	0.067 ± 0.005	1.9 ± 0.2	474.6 ± 102.2	67	0.048 ± 0.002	1.0 ± 0.1	103.4 ± 10.2	59	0.047 ± 0.002	1.0 ± 0.1	115.8 ± 14.2
R6	87	0.112 ± 0.012	2.0 ± 0.1	78.5 ± 8.3	201	0.072 ± 0.007	1.5 ± 0.1	35.3 ± 2.5	128	0.092 ± 0.009	1.6 ± 0.1	53.6 ± 5.0
R7	91	0.127 ± 0.019	1.8 ± 0.1	77.1 ± 9.8	218	0.075 ± 0.008	1.4 ± 0.1	32.7 ± 1.9	250	0.064 ± 0.007	1.4 ± 0.1	28.6 ± 1.4
R8	119	0.119 ± 0.011	1.2 ± 0.1	60.0 ± 5.0	252	0.092 ± 0.007	1.3 ± 0.1	28.4 ± 1.6	158	0.116 ± 0.010	1.4 ± 0.1	45.4 ± 3.2
R9	155	0.140 ± 0.009	1.5 ± 0.1	46.3 ± 3.1	307	0.100 ± 0.005	1.2 ± 0.1	23.4 ± 0.9	262	0.105 ± 0.006	1.2 ± 0.1	27.3 ± 1.4
R10	277	0.182 ± 0.011	1.9 ± 0.1	25.9 ± 1.5	403	0.144 ± 0.008	1.6 ± 0.1	17.9 ± 0.08	386	0.145 ± 0.008	1.6 ± 0.1	18.6 ± 0.7
M1	105	0.119 ± 0.013	1.6 ± 0.1	34.4 ± 3.0	151	0.110 ± 0.011	1.4 ± 0.1	23.9 ± 1.3	149	0.111 ± 0.011	1.5 ± 0.1	24.2 ± 1.5
M2	114	0.074 ± 0.003	1.5 ± 0.1	63.4 ± 5.0	174	0.060 ± 0.003	1.3 ± 0.1	41.4 ± 2.9	120	0.063 ± 0.004	1.3 ± 0.1	60.2 ± 5.2
M3	40	0.098 ± 0.005	1.5 ± 0.1	175.8 ± 24.1	63	0.094 ± 0.006	1.2 ± 0.1	113.2 ± 13.3	65	0.076 ± 0.005	1.2 ± 0.1	108.7 ± 13.2
M4	107	0.070 ± 0.003	1.6 ± 0.1	67.0 ± 5.4	259	0.044 ± 0.002	1.3 ± 0.1	27.7 ± 1.4	193	0.046 ± 0.003	1.3 ± 0.1	37.0 ± 2.2
M5	234	0.081 ± 0.005	1.6 ± 0.1	30.8 ± 1.7	372	0.064 ± 0.003	1.5 ± 0.1	19.3 ± 0.8	340	0.065 ± 0.004	1.5 ± 0.1	21.1 ± 0.9

Values shown are mean ± SEM.
SEM = one standard deviation of the bootstrapped mean, resampled for 10,000 times. R = rat, M = mice.

Table 5.2 also shows the average peak characteristics from both methods. The average peak concentration, peak duration, and inter-event time from the SSIM Method were lower than the Borman Method. Statistical comparisons are best done on the distributions (Fig. 5.11 for rats, Fig. 5.12 for similar data on mice) and the peak concentration distribution between the Borman and SSIM Methods were significantly different (K-S test, $p < 0.0001$ for both internal reference and standard library). The LOD for the Borman method is 40 nM (Fig. 5.11A),[25] but the SSIM Method can pick events down to 15 nM (see example in Fig. 5.13). Thus, the lower LOD shifted the histograms and means to lower concentrations. The concentration distribution between the internal reference and standard library methods of SSIM Method was not significantly different ($p = 0.305$). Similarly, the peak durations were also significantly different between the Borman and SSIM Methods (Fig. 5.11BEH and Fig. 5.12BEH, $p < 0.0001$ for both rats and mice datasets), but not between two versions of the SSIM Method ($p = 0.624$ for rats datasets and $p = 0.934$ for mice datasets). Smaller concentration peaks typically have smaller durations, so the duration distribution shifts left for the SSIM method. For the inter-event time (Fig. 5.11CFI and Fig. 5.12CFI), the SSIM Method identified more events, so the inter-event times were shorter than those from the Borman Method ($p < 0.0001$). The SSIM Method with internal references identified slightly more adenosine events than with the standard library, so the distribution between them was significantly different ($p < 0.05$). SSIM Method is better at identifying smaller concentration events and will reveal more events because the peak concentration can be lower than 40 nM, as in a brain slice tissue, where the LOD of adenosine detection was set to be 10 nM.[29]

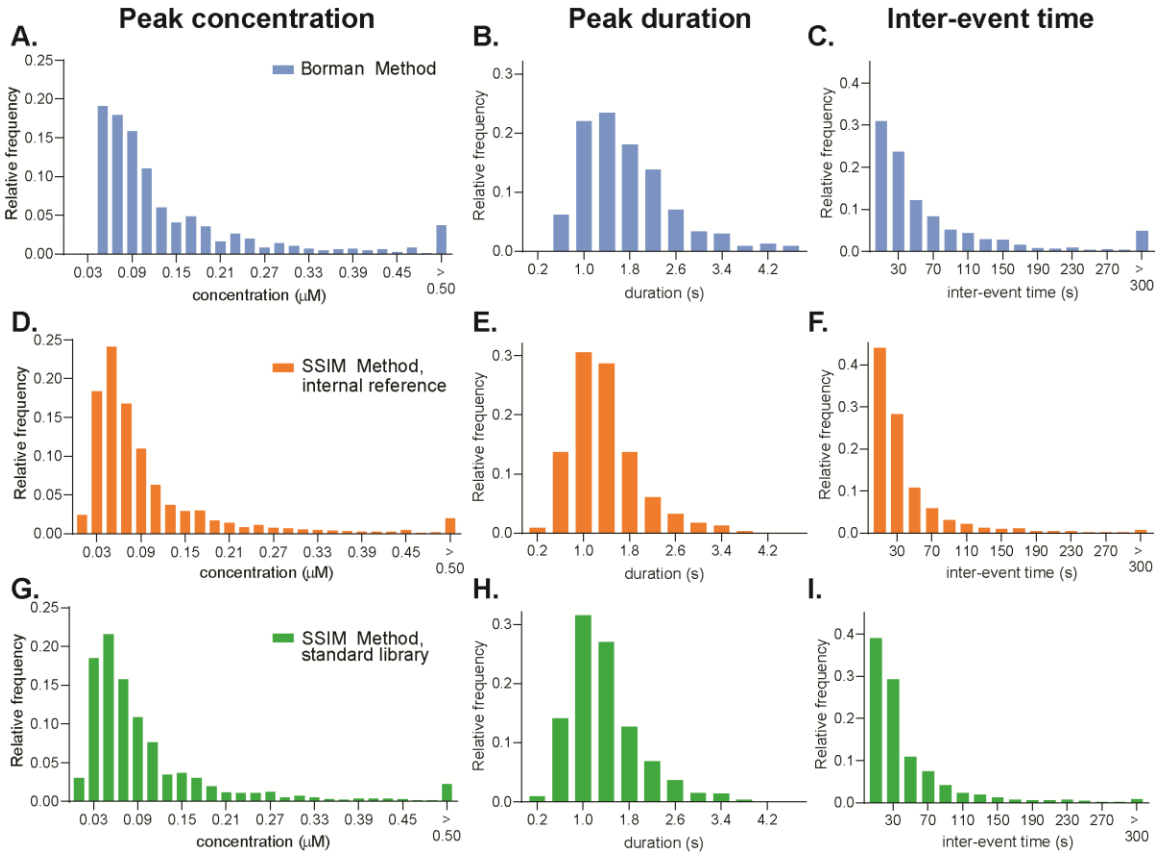

Fig. 5.11 Comparison of the adenosine characteristics between the Borman and SSIM Methods. Histogram of adenosine characteristics from ten, 2-hour rat datasets. (A, D, G) peak concentration (bin width = 0.020 μM), (B, E, H) peak duration (bin width = 0.4 s) and (C, F, I) inter-event time (bin width = 20 s). (A, B, C) Borman Method with secondary peak correction (870 events), (D, E, F) SSIM Method with internal references (1,807 events), and (G, H, I) SSIM Method using standard library (1,627 events).

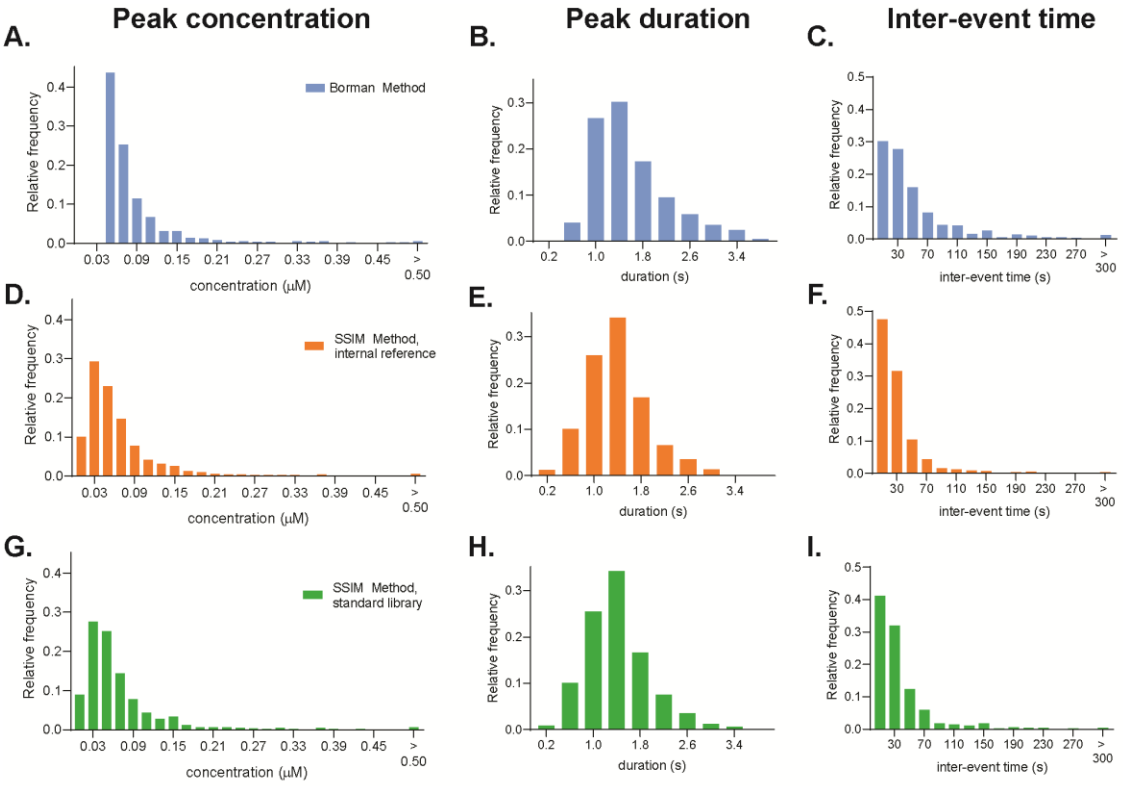

Fig. 5.12 Comparison of the adenosine characteristics between the Borman and the SSIM Methods in mice. Histogram of adenosine transient characteristics from five, 2-hour mouse datasets. (A, D, G) peak concentration (bin width = 0.020 µM), (B, E, H) peak duration (bin width = 0.4 s) and (C, F, I) inter-event time (bin width = 20 s). (A, B, C) Borman Method with secondary peak correction (600 events), (D, E, F) SSIM Method using internal adenosine references (1,019 events), and (G, H, I) SSIM Method using standard library (867 events).

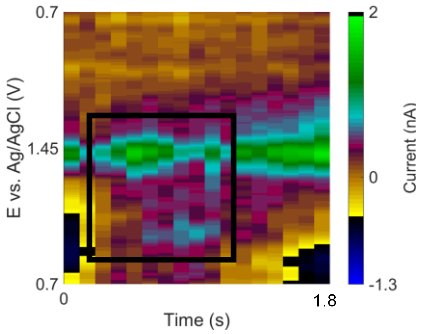

Fig. 5.13 An adenosine event with peak concentration of 15 nM (peak current = 0.7 nA).

5.3.7 Testing Chemical Selectivity In Vitro

The SSIM image analysis was also tested for its robustness with other electroactive neurotransmitters and pH shifts. Fig. 5.14 shows example *in vitro* FSCV color plot of 1 µM adenosine, compared with other high-oxidation potential compounds, including 50 µM H_2O_2, 1 µM histamine, and 1 µM ATP. H_2O_2 is a reactive oxygen species important for signal transduction and has an oxidation potential of +1.2 V on the backward scan (Fig. 5.14B),[12] but its SSIM index was low (0.14 ± 0.05, n = 15) because there is no secondary anodic peak. Histamine, a molecule which is important in immune systems and regulates sleep, also has an anodic peak at +1.2 V on the backward scan but with extra secondary, fouling, and adsorption peaks (Fig. 5.14C).[31] These extra features altered the image and considerably decreased the index (SSIM = 0.11 ± 0.05, n = 15). On the other hand, ATP has the same redox moiety and undergoes the same oxidation mechanism as adenosine,[30,48] so its color plot (Fig. 5.14D) was more similar to that of adenosine (Fig. 6A) and the score was moderate (SSIM = 0.52 ± 0.16). Nevertheless, given that the measured SSIM of adenosine *in vivo* (0.50 cutoff) is less than measured *in vitro* (lowest 0.80, Fig. 5.15) by 0.30, the SSIM index of ATP *in vivo* is also likely lower than the *in vitro* value and would not pass the cutoff. The SSIM calculation was also performed with the signal from a pH shift (Fig. 5.14E–F), as changing the pH and ionic environment on the electrode surface alters the background CV.[23,33] SSIM scores were low for both acidic shift to pH 7.3 (Fig. 5.14E, SSIM = 0.08 ± 0.04) and basic shift to pH 7.5 (Fig. 5.14F, SSIM = 0.08 ± 0.04) because of the different image structure. In contrast, the SSIM of adenosine with pH change or with lower concentration were all higher than 0.70 (Fig. 5.15). This experiment shows that the SSIM image analysis successfully detects adenosine in a slightly different environment and rejects other electroactive

species with different FSCV signals. Future studies may investigate the optimization of the weight matrix for SSIM calculation to better distinguish the electroactive neurotransmitters with similar structure.

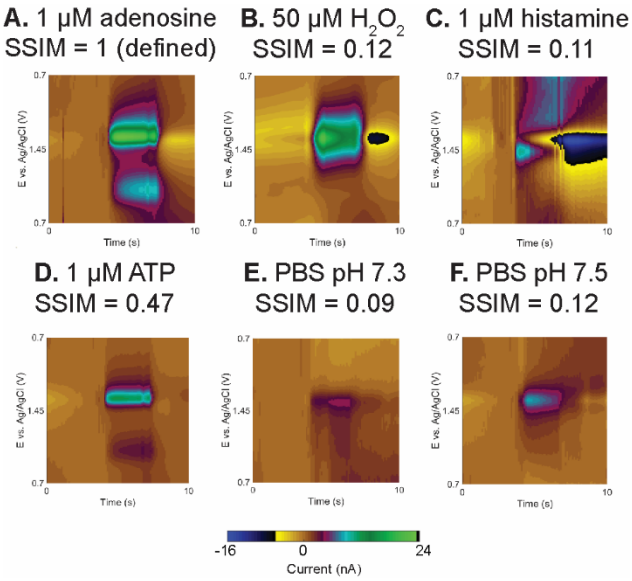

Fig. 5.14 SSIM index of possible interferents. The analyzed portion of the color plot, from +0.7 to +1.45 V, with SSIM index for (A) 1 µM adenosine, (B) 50 µM H_2O_2, (C) 1 µM histamine, (D) 1 µM ATP, (E) PBS pH 7.3, and (F) PBS pH 7.5. Each solution was injected for 3 s followed by PBS pH 7.4 washing. All solutions were prepared in PBS pH 7.4 buffer except indicated. Each color plot was normalized, smoothed, and high pass filtered before SSIM calculation.

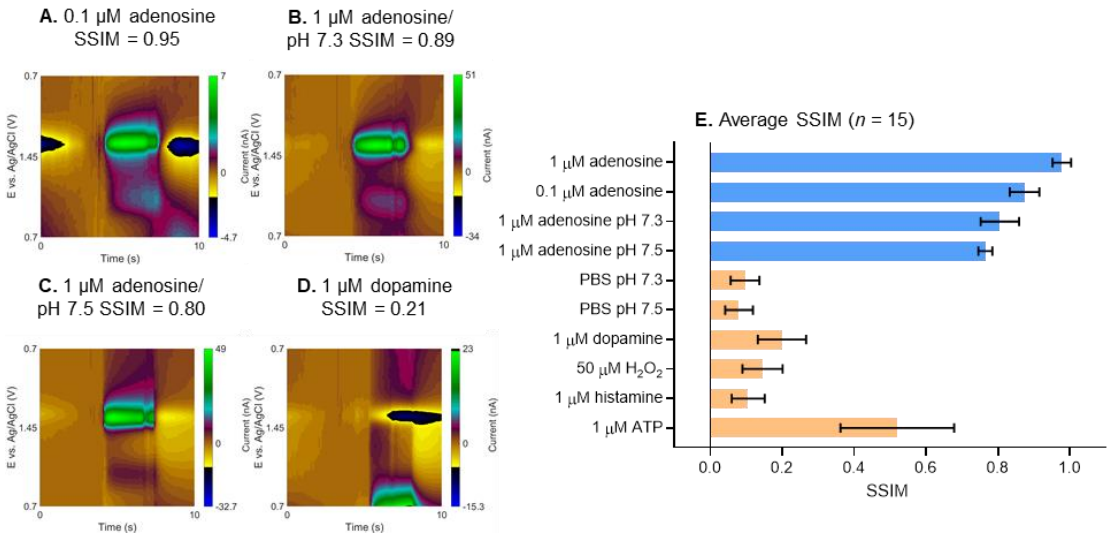

Fig. 5.15 SSIM index for *in vitro* adenosine and dopamine. Color plot with SSIM score of (A) 0.1 µM adenosine, (B) 1 µM adenosine in PBS pH 7.3, and (C) 1 µM adenosine in PBS pH 7.5. (D) 1 µM dopamine. The SSIM indices were calculated using Fig. 5.14A as the reference. All solutions were prepared in PBS pH 7.4 buffer except indicated. Each color plot was normalized, smoothed, and high pass filtered before SSIM calculation. (E) Average SSIM index for each compound (*n* = 15 measurements from 5 electrodes).

5.3.8 Generalization of SSIM Image Analysis: Co-Detection of Adenosine and Dopamine

To examine the adaptability to detect other neurochemicals, the SSIM algorithm was modified to detect dopamine, specifically detection of spontaneous co-release of adenosine and dopamine in the caudate-putamen (Example full color plot data are in Fig. 5.16). Adenosine acts a neuromodulator of dopamine,[11,49–51] so understanding co-release is important to understand adenosine neuromodulation. Co-detection of dopamine and adenosine was performed by simply running the algorithm twice, the first round using adenosine references for adenosine detection and the second round using dopamine references for dopamine detection, since the redox reactions occur at different potentials. Fig. 5.17 shows example reference images of dopamine and adenosine (Fig. 5.17A-B) and a weight matrix for detecting dopamine (Fig. 5.17C). The dopamine weight matrix has a value of one near the oxidation and reduction peaks and zero in the middle of the

color plot to ignore the existence of adenosine. The SSIM calculation was performed with the events in Fig. 5.17D–H with a SSIM cutoff score was 0.50. Samples 5, 6, and 7 (Fig. 5.17D–F) have both dopamine and adenosine events with different dopamine concentrations (90, 50, and 95 nM, respectively). The SSIM indices for both samples are higher than 0.50 compared with one of the references. On the other hand, Sample 8 and 9 (Fig. 5.17G-H) are adenosine events without dopamine, and they have low SSIM scores and thus are rejected by the software as dopamine. Nevertheless, all samples (Fig. 5.17D–H) passed the SSIM cutoff for adenosine detection using the standard library in Fig. 5.9 and the adenosine weight matrix (Fig. 5.2C), illustrating that the presence of dopamine did not interfere the adenosine recognition. Future work can customize the analysis for other neurochemicals, but the SSIM image analysis is versatile for automated recognition of two neurochemicals from FSCV color plots.

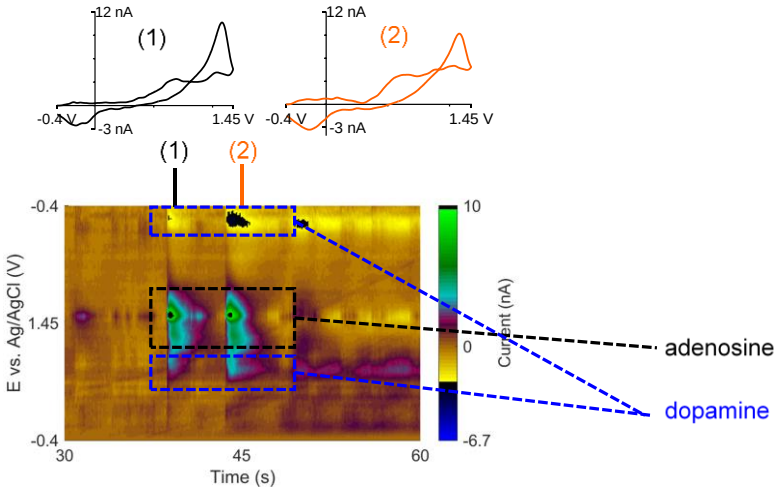

Fig. 5.16 Spontaneous co-releases of adenosine and dopamine in a rat caudate-putamen. CVs (1) and (2) contain the two anodic peaks of adenosine and one anodic and one cathodic peak of dopamine.

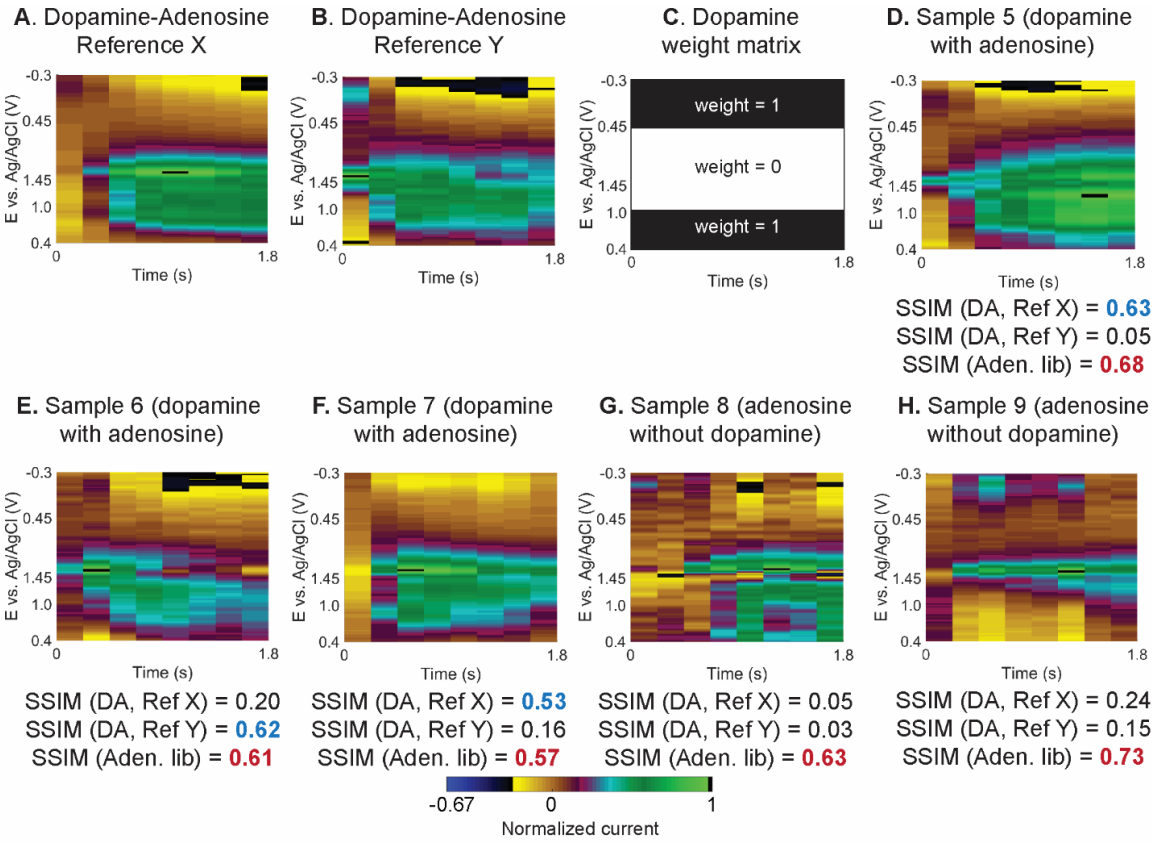

Fig. 5.17 Detection of spontaneous dopamine events that were co-released with adenosine. (A-B) False color plot of two references X and Y with adenosine and dopamine present. (C) Weight matrix for dopamine that ignores adenosine signal from the calculation. (D-F) False color plots of events with dopamine and adenosine, and (G-H) adenosine without dopamine. Reported SSIM indices are for two dopamine references (DA, Ref X and Y) and the adenosine standard library (Aden. Lib). The peak CVs of all data can be found in Fig. 5.18.

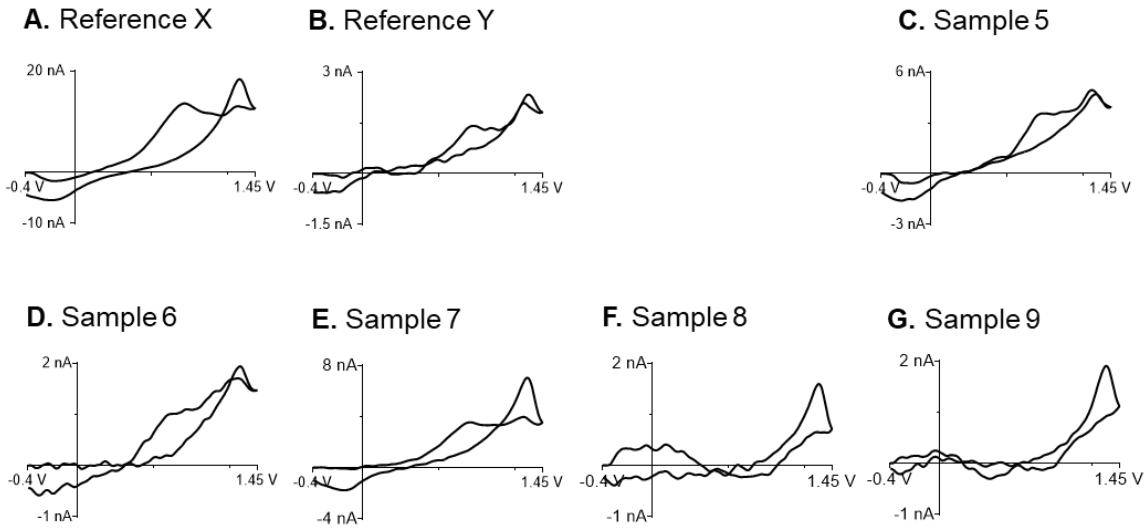

Fig. 5.18 Peak CVs from dopamine-adenosine co-release data in Fig. 5.17 (A) Reference X, (B) Reference Y, (C) Sample 5, (D) Sample 6, (E) Sample 7, (F) Sample 8, and (G) Sample 9. All CVs except (F) and (G) has both adenosine and dopamine features.

5.4 Conclusions

An automated algorithm based on SSIM index image analysis was designed to detect and characterize transient adenosine events from an FSCV color plot. The algorithm compared the image structure of sample data with adenosine references, either internally selected from the same experiment or externally built as a standard library. The program was tested with data from multiple researchers, in both mice and rats, and in different brain regions. Combined with digital filtering to remove background drift, the program identified more adenosine events than the previous algorithm, especially smaller events. The new algorithm also reduced analysis time and had better performance, less than 1% false positive and 5% false negative, because the whole current-potential-time data for adenosine was utilized instead of a single current-time trace. The algorithm was robust and rejected signals from pH shift and other chemical interferents. Finally, the

program was modified to detect dopamine, including dopamine and adenosine co-release. In summary, the SSIM image analysis is a robust technique to classify electrochemical signal from different neurotransmitters and will improve the consistency between researchers and laboratories.

5.5 References

(1) Armstrong-James, M.; Millar, J.; Kruk, L. Quantification of Noradrenaline Iontophoresis. *Nature* **1980**, *288*, 181–183.

(2) Venton, B. J.; Cao, Q. Fundamentals of Fast-Scan Cyclic Voltammetry for Dopamine Detection. *Analyst* **2020**, *145*, 1158–1168.

(3) Puthongkham, P.; Venton, B. J. Recent Advances in Fast-Scan Cyclic Voltammetry. *Analyst* **2020**, *145*, 1087–1102.

(4) Venton, B. J.; Wightman, R. M. Psychoanalytical Electrochemistry: Dopamine and Behavior. *Anal. Chem.* **2003**, *75* (19), 414A-421A.

(5) Johnson, J. A.; Wightman, R. M. Cyclic Voltammetric Measurements of Neurotransmitters. *Electrochem. Soc. Interface* **2018**, *26*, 53–57.

(6) Willuhn, I.; Burgeno, L. M.; Groblewski, P. A.; Phillips, P. E. M. Excessive Cocaine Use Results from Decreased Phasic Dopamine Signaling in the Striatum. *Nat. Neurosci.* **2014**, *17* (5), 704–709.

(7) Robinson, D. L.; Hermans, A.; Seipel, A. T.; Wightman, R. M. Monitoring Rapid Chemical Communication in the Brain. *Chem. Rev.* **2008**, *108*, 2554–2584.

(8) Jackson, B. P.; Dietz, S. M.; Wightman, R. M. Fast-Scan Cyclic Voltammetry of 5-Hydroxytryptamine. *Anal. Chem.* **1995**, *67* (6), 1115–1120.

(9) Hashemi, P.; Dankoski, E. C.; Petrovic, J.; Keithley, R. B.; Wightman, R. M. Voltammetric Detection of 5-Hydroxytryptamine Release in the Rat Brain. *Anal. Chem.* **2009**, *81* (22), 9462–9471.

(10) Swamy, B. E. K.; Venton, B. J. Subsecond Detection of Physiological Adenosine Concentrations Using Fast-Scan Cyclic Voltammetry. *Anal. Chem.* **2007**, *79* (2), 744–750.

(11) Nguyen, M. D.; Venton, B. J. Fast-Scan Cyclic Voltammetry for the Characterization of Rapid Adenosine Release. *Comput. Struct. Biotechnol. J.* **2015**, *13*, 47–54.

(12) Sanford, A. L.; Morton, S. W.; Whitehouse, K. L.; Oara, H. M.; Lugo-Morales, L. Z.; Roberts, J. G.; Sombers, L. A. Voltammetric Detection of Hydrogen Peroxide at Carbon Fiber Microelectrodes. *Anal. Chem.* **2010**, *82* (12), 5205–5210.

(13) Spanos, M.; Gras-Najjar, J.; Letchworth, J. M.; Sanford, A. L.; Toups, J. V.; Sombers, L. A. Quantitation of Hydrogen Peroxide Fluctuations and Their Modulation of Dopamine Dynamics in the Rat Dorsal Striatum Using Fast-Scan Cyclic Voltammetry. *ACS Chem. Neurosci.* **2013**, *4* (5), 782–789.

(14) Nguyen, M. D.; Lee, S. T.; Ross, A. E.; Ryals, M.; Choudhry, V. I.; Venton, B. J. Characterization of Spontaneous, Transient Adenosine Release in the Caudate-Putamen and Prefrontal Cortex. *PLoS One* **2014**, *9* (1), e87165.

(15) Dankoski, E. C.; Mark Wightman, R. Monitoring Serotonin Signaling on a Subsecond Time Scale. *Front. Integr. Neurosci.* **2013**, *7* (MAY), 1–13.

(16) Roberts, J. G.; Sombers, L. A. Fast-Scan Cyclic Voltammetry: Chemical Sensing in the Brain and Beyond. *Anal. Chem.* **2018**, *90* (1), 490–504.

(17) Ganesana, M.; Lee, S. T.; Wang, Y.; Venton, B. J. Analytical Techniques in Neuroscience: Recent Advances in Imaging, Separation, and Electrochemical Methods. *Anal. Chem.* **2017**, *89* (1), 314–341.

(18) Hersey, M.; Berger, S. N.; Holmes, J.; West, A.; Hashemi, P. Recent Developments in Carbon Sensors for At-Source Electroanalysis. *Anal. Chem.* **2019**, *91* (1), 27–43.

(19) Kile, B. M.; Walsh, P. L.; McElligott, Z. A.; Bucher, E. S.; Guillot, T. S.; Salahpour, A.; Caron, M. G.; Wightman, R. M. Optimizing the Temporal Resolution of Fast-Scan Cyclic Voltammetry. *ACS Chem. Neurosci.* **2012**, *3* (4), 285–292.

(20) Michael, D.; Travis, E. R.; Wightman, R. M. Color Images for Fast-Scan CV Measurements in Biological Systems. *Anal. Chem.* **1998**, *70* (17), 586A-592A.

(21) Heien, M. L. A. V.; Johnson, M. A.; Wightman, R. M. Resolving Neurotransmitters Detected by Fast-Scan Cyclic Voltammetry. *Anal. Chem.* **2004**, *76* (19), 5697–5704.

(22) Keithley, R. B.; Heien, M. L. A. V.; Wightman, R. M. Multivariate Concentration Determination Using Principal Component Regression with Residual Analysis. *TrAC, Trends Anal. Chem.* **2009**, *28* (9), 1127–1136.

(23) Meunier, C. J.; McCarty, G. S.; Sombers, L. A. Drift Subtraction for FSCV Using Double-Waveform Partial-Least-Squares Regression. *Anal. Chem.* **2019**, *91*, 7319–7327.

(24) Bucher, E. S.; Brooks, K.; Verber, M. D.; Keithley, R. B.; Owesson-White, C.; Carroll, S.; Takmakov, P.; McKinney, C. J.; Wightman, R. M. Flexible Software Platform for Fast-Scan Cyclic Voltammetry Data Acquisition and Analysis. *Anal. Chem.* **2013**, *85* (21), 10344–10353.

(25) Borman, R. P.; Wang, Y.; Nguyen, M. D.; Ganesana, M.; Lee, S. T.; Venton, B. J. Automated Algorithm for Detection of Transient Adenosine Release. *ACS Chem. Neurosci.* **2017**, *8* (2), 386–393.

(26) Cechova, S.; Venton, B. J. Transient Adenosine Efflux in the Rat Caudate-Putamen. *J. Neurochem.* **2008**, *105* (4), 1253–1263.

(27) Burnstock, G. Purinergic Signaling in the Cardiovascular System. *Circ. Res.* **2017**, *120* (1), 207–228.

(28) Ganesana, M.; Venton, B. J. Early Changes in Transient Adenosine during Cerebral Ischemia and Reperfusion Injury. *PLoS One* **2018**, *13* (5), e0196932.

(29) Lee, S. T.; Venton, B. J. Regional Variations of Spontaneous, Transient Adenosine Release in Brain Slices. *ACS Chem. Neurosci.* **2018**, *9* (3), 505–513.

(30) Ross, A. E.; Venton, B. J. Sawhorse Waveform Voltammetry for Selective Detection of Adenosine, ATP, and Hydrogen Peroxide. *Anal. Chem.* **2014**, *86* (15), 7486–7493.

(31) Puthongkham, P.; Lee, S. T.; Venton, B. J. Mechanism of Histamine Oxidation and Electropolymerization at Carbon Electrodes. *Anal. Chem.* **2019**, *91*, 8366–8373.

(32) DeWaele, M.; Oh, Y.; Park, C.; Kang, Y. M.; Shin, H.; Blaha, C.; Bennet, K. E.; Kim, I. Y.; Lee, K. H.; Jang, D. P. Baseline Drift Detrending Techniques for Fast Scan Cyclic Voltammetry. *Analyst* **2017**, *142*, 4317–4321.

(33) Johnson, J. A.; Hobbs, C. N.; Wightman, R. M. Removal of Differential Capacitive Interferences in Fast-Scan Cyclic Voltammetry. *Anal. Chem.* **2017**, *89* (11), 6166–6174.

(34) Ekelöf, M.; Garrard, K. P.; Judd, R.; Rosen, E. P.; Xie, D. Y.; Kashuba, A. D. M.; Muddiman, D. C. Evaluation of Digital Image Recognition Methods for Mass Spectrometry Imaging Data Analysis. *J. Am. Soc. Mass Spectrom.* **2018**, *29* (12), 2467–2470.

(35) Wang, Z.; Bovik, A. C.; Sheikh, H. R.; Simoncelli, E. P. Image Quality Assessment: From Error Visibility to Structural Similarity. *IEEE Trans. Image Process.* **2004**, *13* (4), 600–612.

(36) Rehman, A.; Gao, Y.; Wang, J.; Wang, Z. Image Classification Based on Complex Wavelet Structural Similarity. *Signal Process. Image Commun.* **2013**, *28* (8), 984–992.

(37) Casti, P.; Mencattini, A.; Salmeri, M.; Rangayyan, R. M. Analysis of Structural Similarity in Mammograms for Detection of Bilateral Asymmetry. *IEEE Trans. Med. Imaging* **2015**, *34* (2), 662–671.

(38) Shahriari, Y.; Fidler, R.; Pelter, M. M.; Bai, Y.; Villaroman, A.; Hu, X. Electrocardiogram Signal Quality Assessment Based on Structural Image Similarity Metric. *IEEE Trans. Biomed. Eng.* **2018**, *65* (4), 748–753.

(39) Huffman, M. L.; Venton, B. J. Electrochemical Properties of Different Carbon-Fiber Microelectrodes Using Fast-Scan Cyclic Voltammetry. *Electroanalysis* **2008**, *20* (22), 2422–2428.

(40) Wang, Y.; Venton, B. J. Comparison of Spontaneous and Mechanically-Stimulated Adenosine Release in Mice. *Neurochem. Int.* **2019**, *124* (November 2018), 46–50.

(41) Savitzky, A.; Golay, M. J. E. Smoothing and Differentiation of Data by Simplified Least Squares Procedures. *Anal. Chem.* **1964**, *36* (8), 1627–1639.

(42) Huang, Y. J.; Powers, R.; Montelione, G. T. Protein NMR Recall, Precision, and F-Measure Scores (RPF Scores): Structure Quality Assessment Measures Based on Information Retrieval Statistics. *J. Am. Chem. Soc.* **2005**, *127* (6), 1665–1674.

(43) Borgus, J. R.; Puthongkham, P.; Venton, B. J. Complex Sex and Estrous Cycle Differences in Spontaneous Transient Adenosine. *J. Neurochem.* **2020**.

(44) Efron, B.; Tibshirani, R. J. *An Introduction to the Bootstrap*, 1st ed.; Chapman & Hall, Inc.: New York, 1993.

(45) Dryhurst, G.; Elving, P. J. Electrochemical Oxidation of Adenine: Reaction Products and Mechanisms. *J. Electrochem. Soc.* **1968**, *115* (10), 1014.

(46) Michael, D. J.; Joseph, J. D.; Kilpatrick, M. R.; Travis, E. R.; Wightman, R. M. Improving Data Acquisition for Fast-Scan Cyclic Voltammetry. *Anal. Chem.* **1999**, *71* (18), 3941–3947.

(47) Takmakov, P.; Zachek, M. K.; Keithley, R. B.; Walsh, P. L.; Donley, C.; McCarty, G. S.; Wightman, R. M. Carbon Microelectrodes with a Renewable Surface. *Anal. Chem.* **2010**, *82* (5), 2020–2028.

(48) Xu, Y.; Venton, B. J. Microelectrode Sensing of Adenosine/Adenosine-5'-Triphosphate with Fast-Scan Cyclic Voltammetry. *Electroanalysis* **2010**, *22* (11), 1167–1174.

(49) Pajski, M. L.; Venton, B. J. Adenosine Release Evoked by Short Electrical Stimulations in Striatal Brain Slices Is Primarily Activity Dependent. *ACS Chem. Neurosci.* **2010**, *1* (12), 775–787.

(50) Ross, A. E.; Venton, B. J. Adenosine Transiently Modulates Stimulated Dopamine Release in the Caudate-Putamen via A1 Receptors. *J. Neurochem.* **2015**, *132* (1), 51–60.

(51) Quarta, D.; Borycz, J.; Solinas, M.; Patkar, K.; Hockemeyer, J.; Ciruela, F.; Lluis, C.; Franco, R.; Woods, A. S.; Goldberg, S. R.; et al. Adenosine Receptor-Mediated Modulation of Dopamine Release in the Nucleus Accumbens Depends on Glutamate Neurotransmission and N-Methyl-D-Aspartate Receptor Stimulation. *J. Neurochem.* **2004**, *91* (4), 873–880.

CHAPTER 6

Conclusions and Future Directions

Parts of Chapter 6 were reprinted and modified with permission from *Anal. Chem.* **2019,** *91,* 4618-4624, Copyright 2019 American Chemical Society, and *Analyst* **2020,** *145,* 1087-1102 published by The Royal Society of Chemistry.

6.1 Contribution of the Dissertation to the Field

My dissertation mainly focused on investigating three independent approaches to improve real-time electrochemical detection of neurotransmitters with FSCV. First, the redox mechanism of histamine and its oxidation potential were determined to propose a better FSCV method for its detection. Second, CNHs and NDs were incorporated on CFMEs to improve their sensitivity, selectivity, and antifouling properties for the detection of catecholamines. Third, structural similarity image analysis was combined with signal processing techniques to devise a new software that automated the analysis of FSCV data with improved sensitivity and selectivity. This chapter will summarize the overall findings of my work and discuss their contributions to the FSCV and electrochemistry field, concluding with the future directions.

6.1.1 Knowing Mechanism of Histamine Oxidation Improves Its FSCV Detection

The lack of fundamental studies on histamine redox mechanism led to contradiction in the proposed histamine oxidation potentials in FSCV. Chapter 2 resolved the conflict between the previous works on the detection of histamine using FSCV, by establishing its redox mechanism and identifying the oxidation potential of histamine as 1.1 V vs Ag/AgCl. This information supported the Wightman and Lee group interpretation on the histamine anodic peak appearing after 1.1 V.[1,2] On the other hand, the proposed mechanism contradicted with the work by Hashemi's group, which interpreted the 0.3 V peak to be the faradaic peak,[3] which our data suggests may be an adsorption peak. Although their experimental design validated the use of adsorption peak, the analytical performance for histamine detection is better if the faradaic peak at 1.2 V on the backward scan is utilized instead. In addition, Chapter 2 showed that histamine oxidation fouls the

electrode due to the adsorption of electropolymerization product on the electrode surface. The electrode fouling decreased the faradaic current in continuous measurements of histamine. To improve the histamine detection, Nafion coating[4] was incorporated to decrease the polymer adsorption and limit the histamine fouling at CFME. Therefore, a better understanding of histamine oxidation mechanism and FSCV response greatly helped in choosing the waveform and improve the analytical performance for histamine FSCV detection. Knowledge of histamine electrochemistry will also facilitate the discrimination of the FSCV signal from high-oxidation potential species such as adenosine and H_2O_2.[5,6] Better FSCV methods for histamine detection will encourage the neurochemistry field to conduct more studies in histamine rapid neurotransmission such as its role in *Drosophila* visual processing[7] and its relationship with serotonin.[8]

For the electrochemistry field in general, the analytical techniques from this study can be used to determine a redox potential and mechanism of any electroactive species. The field has used amperometry and CV to determine the oxidation or reduction potential for the species to optimize the required potential and waveform for analytical measurement.[9] Also, this work showed that FSCV is a suitable electrochemical technique to study continuous electrochemical phenomena such as electrode fouling, in addition to its common neurochemical applications. Moreover, XPS has proven to be a versatile technique to analyze the electrode surface after the redox process and complement the data to confirm the redox mechanism. Thus, the combination of electrochemical and surface techniques helps the field reveal the mechanistic insight of electrode reactions.

6.1.2 Carbon Nanohorns and Nanodiamonds Improve the Detection of Catecholamines

CFME has been the standard FSCV working electrode *in vivo* due to their small size, excellent biocompatibility, and favorable electrochemical properties toward neurotransmitter redox reaction.[10] However, sensitivity becomes an issue when detecting low concentration of neurotransmitter releases (< 10 nM).[11] Long-term implantation of the electrode is also challenging because of the sensitivity degradation from electrochemical fouling and biofouling.[12] Chapters 3 and 4 presented CNHs and NDs-modified CFMEs to improve the sensitivity, limit of detection, and antifouling properties of the CFMEs. CNHs and NDs increased the adsorption of dopamine on the CFME, in addition to the surface area expansion. Therefore, both CNH- and ND-modified CFMEs improved the limit of detection of dopamine from > 10 nM at CFME to 3–6 nM at the modified electrodes. CNHs and NDs also enhanced the signal from other cationic neurotransmitters such as epinephrine, norepinephrine, and serotonin. Moreover, the surface hydrophilicity of both CNHs and NDs alleviated electrochemical fouling from serotonin and 5-HIAA oxidation and biofouling from proteins and biomolecules adsorption. The improved antifouling properties preserved the sensitivity of FSCV detection during the course of long experiment, such as long-term behavior study.[13] Therefore, CNHs and NDs improved sensitivity, selectivity, and antifouling properties of CFMEs and will ease the chronic FSCV measurements for studying long-term neurotransmission *in vivo*.[13]

One important advantage of the work in Chapters 3 and 4 is that CNH/CFMEs and ND/CFMEs were prepared by simple methods, electrodeposition and drop casting, respectively. No expensive cleanroom or special instrumentation was required to prepare these modified electrodes because the nanomaterials are already in the appropriate form to modify the CFME surface. Thus, the modified electrodes can be prepared in any

laboratory. Nevertheless, these simple methods are necessary to fabricate the electrodes because the direct fabrication technology is still unavailable for CNHs and NDs, unlike CNTs and graphene,[11,14] Future technology can explore their direct synthesis to control their coverage on CFMEs or conductive substrates.

These two chapters also provided fundamental insights on electrochemical properties of CNHs and NDs, which have been less explored than graphene and CNTs. Electrochemical performance of the sensors was discussed by considering morphology, adsorption, and electrocatalytic properties of carbon nanomaterials, in addition to the surface area expansion. For CNHs, their cone shape enhanced the electric field at the tip, and the dahlia-like aggregation increases their porosity; both phenomena enhanced dopamine adsorption from the plain CFME. The surface oxide groups of CNHs could be increased by oxidative etching in NaOH to increase the adsorption. In the future, similar oxidation could be performed for chemical functionalization of CNHs in the selective sensors or adsorbent.[15] For NDs, both size and surface functional group affected their adsorption and electrochemical properties. ND-COOH adsorbed more dopamine and exhibited better electrocatalytic properties than ND-H because of the negative charge from surface oxides and the increased density of electronic states from the presence of C=O and C=C groups. Size of NDs also affected their aggregation on the CFME surface and the overall electrochemical properties. Moreover, the sp^3-hybridized carbons of NDs decreased electrode fouling, similar to other diamond-based electrode materials such as boron-doped diamond.[16] Their antifouling properties could be use in other electrochemical devices such as rechargeable batteries to prevent short circuiting.[17] Thus, these two chapters explored the properties of CNHs and NDs that will expand their applications in electrochemistry and other areas.

6.1.3 The SSIM Method Enhances Accuracy, Precision, and Consistency in Automated Data Analysis

Automated analysis of FSCV data is essential to reduce the labor from manually analyzing the large amount of the data and to ensure the consistency between experimenters. However, automated analysis of adenosine FSCV is difficult because of adenosine cyclic voltammogram shape changing within the same transient event[5] such that classic multivariate techniques like PCR fails to pick up the adenosine transients. Chapter 5 proposed an alternative method to solve the problem by utilizing SSIM image analysis algorithm to find a signal of adenosine from an FSCV color plot. SSIM identified the adenosine signal from its unique structure in a color plot, not just from an individual voltammogram or current-time trace, thus it used all the electrochemical information. Moreover, digital filtering was applied to eliminate the background drift and noise to improve the limit of detection in order to recognize small transient events. Therefore, the SSIM Method improved the adenosine FSCV data analysis with < 1% false positives and < 5% false negatives, better than the previous method that used only current-time trace.[18] Chapter 5 also demonstrated the versatility of the SSIM algorithm by generalizing to analyze dopamine, in addition to adenosine, and demonstrated good selectivity. Ultimately, the SSIM image analysis will ensure the consistency between experimenters and laboratories and encourage studies on rapid signaling of adenosine and other neurotransmitters.

The SSIM Method from Chapter 5 is the first application of an image processing algorithm in analyzing electrochemical data. The algorithm could be applied to analyze any data from other electrochemical and analytical techniques that can be represented as an image. The SSIM algorithm has also been shown to find the chemical signal by

considering the unique pattern or structure from the compound, such as in excitation-emission matrix fluorescence spectroscopy.[19] Moreover, it was combined with chemical imaging techniques such as fluorescence and mass spectrometry imaging[20] to find a physical structure from a chemical image. Thus, SSIM algorithm is a potential data analysis algorithm for analytical chemistry field to enhance automated data analysis.

Finally, the three approaches for FSCV method development presented in this dissertation are independent, thus they can be combined to improve analytical performance for neurotransmitter detection. For example, with the knowledge of histamine oxidation mechanism and fouling, new FSCV waveform could be developed to eliminate the fouling while preserving the sensitivity and selectivity. ND-modified CFME could be used to further improve the sensitivity and limit the electrode fouling, and the SSIM Method can be improved to analyze the histamine FSCV data. Overall, developing better FSCV method will help us acquire more accurate picture of rapid signaling of neurotransmitters and neuromodulators.

6.2 Future Directions

6.2.1 Micro/Nanostructured Carbon Electrodes for Improving Temporal Resolution

This dissertation has proposed methods to improve sensitivity, selectivity, and antifouling properties of CFMEs but did not talk about temporal resolution. At CFME, using the higher repetition frequency decreases the signal because of the less adsorption time. To enhance the sensitivity at higher frequency, new electrode materials have been identified from their surface structures that act as thin layer cells and promote momentary trapping of the analyte. Carbon nanotube yarns, produced from direct spinning of a single CNT thread,[21] have high sensitivity due to a large specific surface area and fast electron

transfer kinetics.[22] The Venton group discovered that the dopamine anodic current at carbon nanotube yarn microelectrode (CNTYME) was frequency-independent.[23] By using CNTYMEs, the temporal resolution were improved without decreasing sensitivity, up to a repetition frequency of 500 Hz, 50-times better temporal resolution. The surface roughness of CNTYMEs was higher than CFMEs (1910 ± 190 nm vs 420 ± 30 nm),[24] and was the same order of magnitude as the diffusion distance of dopamine in one dopamine waveform. This could mainly because the dopamine-o-quinone is trapped in rough CNTYME surface like a thin-layer cell. Increased surface roughness increases capacitance, but the beneficial effects of the trapping effect are greater than the increase in noise from the capacitance, as the cyclic voltammogram of dopamine is more reversible at CNTYME and redox amplification greatly enhanced Faradaic currents. Therefore, carbon nanomaterials with crevices that have micrometer roughness allow better temporal resolution with enhanced sensitivity.

A completely different geometry of electrode has been formed that works on the same thin-layer cell trapping principle. With the collaboration of Mirkin's group, our group reported a cavity CNPE, which was prepared by chemical vapor deposition (CVD) of carbon in the pulled quartz capillary.[25,26] The CVD parameters were optimized to yield the few hundred nanometers diameter cavity geometry at the tip (Fig. 6.1A). When a negative holding potential was applied to the electrode, the cationic dopamine was trapped in the cavity, so the thin-layer effect that allow the redox cycling was observed and led to its frequency-independent properties (Fig. 6.1B). Despite being a nanoelectrode, the sensitivity is sufficient to detect micromolar dopamine because the cavity preconcentrated dopamine and the enhanced electric field increased dopamine adsorption. The cavity CNPE was also robust enough to detect dopamine exogenously in rat brain slice tissue.

However, the CNPEs are only amorphous carbon, and the surface may be improved with treatments that increase the number of edge planes and surface oxides. Interestingly, the thin-layer effect also revealed the secondary anodic peak of catecholamines, in addition to the frequency-independent response. The cavity CNPE exhibited the secondary oxidation peak of dopamine (Fig. 6.1C), and the peak was greatly amplified with epinephrine (Fig. 6.1D), which the cyclization prior to the secondary oxidation is more feasible.[27] Future work can examine and utilize the thin-layer effect of CNTYME and cavity CNPE to achieve better selectivity among catecholamines from the cyclic voltammogram shape differentiation.

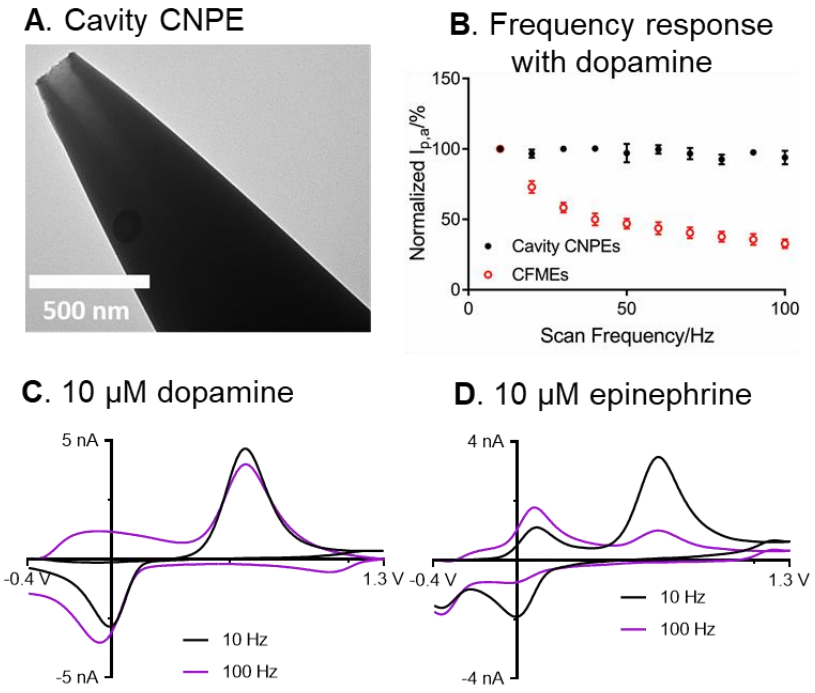

Fig. 6.1 FSCV at Cavity CNPE. (A) SEM image shows cavity depth of 500 nm and orifice diameter of 200 nm. (B) FSCV of 10 μM dopamine showed frequency independence of the cavity CNPE compared to CFME. Reprinted from [25]. Copyright 2019 American Chemical Society. CVs collected from 10-Hz and 100-Hz repetition frequency of (C) 10 μM dopamine and (D) 10 μM epinephrine.

6.2.2 Nanostructured Electrodes for Improving Spatial Resolution

FSCV has been traditionally performed with microelectrodes, but new biological questions will require smaller electrodes such as nanoelectrodes. For example, researchers are examining the role of discrete brain regions in *Drosophila*[28–30] and zebrafish embryo[31] for neurotransmission. *Drosophila* have a mushroom body that controls many sensory processes; these bodies have discrete regions smaller than 10 µm in width,[28] so a CFME of 7 µm is too large to monitor in these different regions. Another motivation for using smaller electrodes is electrochemical measurements at synapses, which are typically 100 nm gaps between neurons.[32] Several possible approaches to fabricate a free-standing nanoelectrode for neurotransmitter detection have been investigated. Conical carbon-fiber nanoelectrodes produced from flame-etched carbon fibers had tip diameter and shaft length in nanometer ranges, and were useful for monitoring individual vesicular exocytosis at a single synapse of superior cervical ganglion by amperometry.[33] Similar electrodes were placed in PC12 cells to analyze the intracellular vesicle content for cytometry.[34]

Recent technology allows bottom-up fabrication of electrodes with customizable geometry and surface structure in nanoscale. Our group reported a novel 3D-printed, free-standing microelectrode prepared by direct laser writing on photopolymer on a metal wire and rapid thermal processing pyrolysis and demonstrated that the final electrode had a diameter of 30-µm with <1-µm spiked features.[35] 3D printing and lithography are still being optimized and could be used in the future for smaller electrodes with nanometer features. While nanoelectrodes can be used in FSCV, their tiny surface area demands further sensitivity enhancements for successful biological measurements in smaller regions.

6.2.3 Machine Learning for Improving Data Analysis

FSCV data from *in vivo* experiments are usually complex. Electrochemical signals from different neurotransmitters may be similar, such as the CV shape of catecholamines.[27] Also, relating the change or pattern in neurotransmitter concentrations to the specific behavior is challenging because of the complicated nervous system.[32] Traditionally, simple mathematical methods such as PCA have been used to differentiate and recognize these similar and complex FSCV signals. Currently, machine learning is an emerging tool to perform such data analysis and has been widely implemented in every aspect with the available data. A machine learning algorithm builds a mathematical model (i.e. to automatically optimize a set of regression parameters) from the training set to perform a task without being specified the rule.[36] Thus, it is more promising than conventional simple regression or PCA because it can find the inherent structure or pattern in the data, develop the "rule" from the training set, and automatically improve the rule based on further training. Machine learning has been used in analytical chemistry to develop an electronic nose[37] and to predict an optimized material for specific applications.[38]

There have been some applications of machine learning in the FSCV field. A closed-loop deep-brain stimulation was developed by using an artificial neural network, an algorithm that mimics complex neuron wiring, to predict stimulation parameters to maintain the targeted dopamine concentration from the collected FSCV data.[39] Dopamine and serotonin concentrations were estimated from their derivative CVs via multivariate linear regression algorithm to investigate their roles in reward-based decision making used by humans.[40,41] There are still many unexplored opportunities to implement machine learning in FSCV, but a large set of FSCV data are required because more training data sets help

establish better rules and thus better algorithm performance.[36] Standardized FSCV data could be collected in databases to reduce the discrepancy of the data between different research groups. However, the current hodgepodge of file formats from the mostly home written software code does not currently support databasing FSCV data. Thus, consistency in data formatting and better machine learning algorithms will facilitate collaborations between the research groups and also to unravel the unanswered questions in neuroscience.

6.3 Final Remarks

In conclusion, my dissertation developed novel microelectrodes and methods to improve FSCV detection of neurotransmitters. Investigation of redox mechanism provided the fundamental insights to optimize the detection method. Development of nanomaterial microelectrodes revealed the electrochemical properties of nanomaterials and enhanced the microelectrode properties for neurotransmitter detection. Combination of image analysis and signal processing utilized all electrochemical information from FSCV data to automate the data analysis. New technology in micro/nanoelectrode fabrication will promote fundamental studies in electrochemistry, and machine learning will become a versatile tool for efficiently analyzing electrochemical data. The knowledge and methods from my dissertation will expand the application of FSCV in neurochemical research. Better methods for real-time detection of neurotransmitters will lead to the understanding of our brain chemistry to devise a treatment for neurodegenerative diseases.

6.4 References

(1) Pihel, K.; Hsieh, S.; Jorgenson, J. W.; Wightman, R. M. Electrochemical Detection of Histamine and 5-Hydroxytryptamine at Isolated Mast Cells. *Anal. Chem.* **1995**, *67* (24), 4514–4521.

(2) Chang, S. Y.; Jay, T.; Muñoz, J.; Kim, I.; Lee, K. H. Wireless Fast-Scan Cyclic Voltammetry Measurement of Histamine Using WINCS - A Proof-of-Principle Study. *Analyst* **2012**, *137* (9), 2158–2165.

(3) Samaranayake, S.; Abdalla, A.; Robke, R.; Wood, K. M.; Zeqja, A.; Hashemi, P. In Vivo Histamine Voltammetry in the Mouse Premammillary Nucleus. *Analyst* **2015**, *140* (11), 3759–3765.

(4) Hashemi, P.; Dankoski, E. C.; Petrovic, J.; Keithley, R. B.; Wightman, R. M. Voltammetric Detection of 5-Hydroxytryptamine Release in the Rat Brain. *Anal. Chem.* **2009**, *81* (22), 9462–9471.

(5) Swamy, B. E. K.; Venton, B. J. Subsecond Detection of Physiological Adenosine Concentrations Using Fast-Scan Cyclic Voltammetry. *Anal. Chem.* **2007**, *79* (2), 744–750.

(6) Sanford, A. L.; Morton, S. W.; Whitehouse, K. L.; Oara, H. M.; Lugo-Morales, L. Z.; Roberts, J. G.; Sombers, L. A. Voltammetric Detection of Hydrogen Peroxide at Carbon Fiber Microelectrodes. *Anal. Chem.* **2010**, *82* (12), 5205–5210.

(7) Denno, M. E.; Privman, E.; Borman, R. P.; Wolin, D. C.; Venton, B. J. Quantification of Histamine and Carcinine in Drosophila Melanogaster Tissues. *ACS Chem. Neurosci.* **2016**, *7* (3), 407–414.

(8) Travis, E. R.; Wang, Y. M.; Michael, D. J.; Caron, M. G.; Wightman, R. M. Differential Quantal Release of Histamine and 5-Hydroxytryptamine from Mast Cells of Vesicular Monoamine Transporter 2 Knockout Mice. *Proc. Natl. Acad. Sci. U. S. A.* **2000**, *97* (1), 162–167.

(9) Bard, A. J.; Faulkner, L. R. *Electrochemical Methods: Fundamentals and Applications*, 2nd ed.; John Wiley and Sons: New York, 2001.

(10) Huffman, M. L.; Venton, B. J. Carbon-Fiber Microelectrodes for in Vivo Applications. *Analyst* **2009**, *134*, 18–24.

(11) Yang, C.; Jacobs, C. B.; Nguyen, M. D.; Ganesana, M.; Zestos, A. G.; Ivanov, I. N.; Puretzky, A. A.; Rouleau, C. M.; Geohegan, D. B.; Venton, B. J. Carbon Nanotubes Grown on Metal Microelectrodes for the Detection of Dopamine. *Anal. Chem.* **2016**, *88*, 645–652.

(12) Yang, C.; Wang, Y.; Jacobs, C. B.; Ivanov, I.; Venton, B. J. O2 Plasma Etching and Anti-Static Gun Surface Modifications for CNT Yarn Microelectrode Improve Sensitivity and Anti-Fouling Properties. *Anal. Chem.* **2017**, 5605–5611.

(13) Rodeberg, N. T.; Sandberg, S. G.; Johnson, J. A.; Phillips, P. E. M.; Wightman, R. M. Hitchhiker's Guide to Voltammetry: Acute and Chronic Electrodes for in Vivo Fast-Scan Cyclic Voltammetry. *ACS Chem. Neurosci.* **2017**, *8*, 221–234.

(14) Wu, T.; Alharbi, A.; Kiani, R.; Shahrjerdi, D. Quantitative Principles for Precise Engineering of Sensitivity in Graphene Electrochemical Sensors. *Adv. Mater.* **2018**, *1805752*, 1–12.

(15) Liu, F.; Xiang, G.; Yuan, R.; Chen, X.; Luo, F.; Jiang, D.; Huang, S.; Li, Y.; Pu, X. Procalcitonin Sensitive Detection Based on Graphene-Gold Nanocomposite Film Sensor Platform and Single-Walled Carbon Nanohorns/Hollow Pt Chains Complex as Signal Tags. *Biosens. Bioelectron.* **2014**, *60*, 210–217.

(16) Granger, M. C.; Witek, M.; Xu, J.; Wang, J.; Hupert, M.; Hanks, A.; Koppang, M. D.; Butler, J. E.; Lucazeau, G.; Mermoux, M.; et al. Standard Electrochemical Behavior of High-Quality,

Boron-Doped Polycrystalline Diamond Thin-Film Electrodes. *Anal. Chem.* **2000**, *72* (16), 3793–3804.

(17) Cheng, X.-B.; Zhao, M.-Q.; Chen, C.; Pentecost, A.; Maleski, K.; Mathis, T.; Zhang, X.-Q.; Zhang, Q.; Jiang, J.; Gogotsi, Y. Nanodiamonds Suppress the Growth of Lithium Dendrites. *Nat. Commun.* **2017**, *8* (1), 336.

(18) Borman, R. P.; Wang, Y.; Nguyen, M. D.; Ganesana, M.; Lee, S. T.; Venton, B. J. Automated Algorithm for Detection of Transient Adenosine Release. *ACS Chem. Neurosci.* **2017**, *8* (2), 386–393.

(19) Yu, S.; Xiao, X. Recovery of Excitation-Emission Fluorescence Spectroscopy Based on Structural Similarity. *Chemom. Intell. Lab. Syst.* **2016**, *156*, 54–61.

(20) Ekelöf, M.; Garrard, K. P.; Judd, R.; Rosen, E. P.; Xie, D. Y.; Kashuba, A. D. M.; Muddiman, D. C. Evaluation of Digital Image Recognition Methods for Mass Spectrometry Imaging Data Analysis. *J. Am. Soc. Mass Spectrom.* **2018**, *29* (12), 2467–2470.

(21) Li, W.; Jayasinghe, C.; Shanov, V.; Schulz, M. Spinning Carbon Nanotube Nanothread under a Scanning Electron Microscope. *Materials (Basel).* **2011**, *4* (9), 1519–1527.

(22) Schmidt, A. C.; Wang, X.; Zhu, Y.; Sombers, L. A. Carbon Nanotube Yarn Electrodes for Enhanced Detection of Neurotransmitter Dynamics in Live Brain Tissue. *ACS Nano* **2013**, *7* (9), 7864–7873.

(23) Jacobs, C. B.; Ivanov, I. N.; Nguyen, M. D.; Zestos, A. G.; Venton, B. J. High Temporal Resolution Measurements of Dopamine with Carbon Nanotube Yarn Microelectrodes. *Anal. Chem.* **2014**, *86*, 5721–5727.

(24) Yang, C.; Trikantzopoulos, E.; Nguyen, M. D.; Jacobs, C. B.; Wang, Y.; Mahjouri-Samani, M.; Ivanov, I. N.; Venton, B. J. Laser Treated Carbon Nanotube Yarn Microelectrodes for Rapid and Sensitive Detection of Dopamine in Vivo. *ACS Sens.* **2016**, *1*, 508–515.

(25) Yang, C.; Hu, K.; Wang, D.; Zubi, Y.; Lee, S. T.; Puthongkham, P.; Mirkin, M. V.; Venton, B. J. Cavity Carbon-Nanopipette Electrodes for Dopamine Detection. *Anal. Chem.* **2019**, *91*, 4618–4624.

(26) Yu, Y.; Mirkin, M. V; Gao, Y.; Mashtalir, O.; Friedman, G.; Gogotsi, Y. Carbon Pipette-Based Electrochemical Nanosampler. *Anal. Chem.* **2014**, *86*, 3365–3372.

(27) Baur, J. E.; Kristensen, E. W.; May, L. J.; Wiedemann, D. J.; Wightman, R. M. Fast-Scan Voltammetry of Biogenic Amines. *Anal. Chem.* **1988**, *60* (13), 1268–1272.

(28) Shin, M.; Copeland, J. M.; Venton, B. J. Drosophila as a Model System for Neurotransmitter Measurements. *ACS Chem. Neurosci.* **2018**, *9* (8), 1872–1883.

(29) Borue, X.; Cooper, S.; Hirsh, J.; Condron, B.; Venton, B. J. Quantitative Evaluation of Serotonin Release and Clearance in Drosophila. *J. Neurosci. Methods* **2009**, *179* (2), 300–308.

(30) Vickrey, T. L.; Condron, B.; Venton, B. J. Detection of Endogenous Dopamine Changes in Drosophila Melanogaster Using Fast-Scan Cyclic Voltammetry. *Anal. Chem.* **2009**, *81* (22), 9306–9313.

(31) Shin, M.; Field, T. M.; Stucky, C. S.; Furgurson, M. N.; Johnson, M. A. Ex Vivo Measurement of Electrically Evoked Dopamine Release in Zebrafish Whole Brain. *ACS Chem. Neurosci.* **2017**, *8* (9), 1880–1888.

(32) Shin, M.; Wang, Y.; Borgus, J. R.; Venton, B. J. Electrochemistry at the Synapse. *Annu. Rev. Anal. Chem.* **2019**, *12* (1), 297–321.

(33) Li, Y.-T.; Zhang, S.-H.; Wang, L.; Xiao, R.-R.; Liu, W.; Zhang, X.-W.; Zhou, Z.; Amatore, C.; Huang, W.-H. Nanoelectrode for Amperometric Monitoring of Individual Vesicular

Exocytosis inside Single Synapses. *Angew. Chem., Int. Ed.* **2014**, *53* (46), 12456–12460.

(34) Li, X.; Majdi, S.; Dunevall, J.; Fathali, H.; Ewing, A. G. Quantitative Measurement of Transmitters in Individual Vesicles in the Cytoplasm of Single Cells with Nanotip Electrodes. *Angew. Chem., Int. Ed.* **2015**, *54* (41), 11978–11982.

(35) Yang, C.; Cao, Q.; Puthongkham, P.; Lee, S. T.; Ganesana, M.; Lavrik, N. V; Venton, B. J. 3D-Printed Carbon Electrodes for Neurotransmitter Detection. *Angew. Chem., Int. Ed.* **2018**, *57*, 14255–14259.

(36) Butler, K. T.; Davies, D. W.; Cartwright, H.; Isayev, O.; Walsh, A. Machine Learning for Molecular and Materials Science. *Nature* **2018**, *559* (7715), 547–555.

(37) Liu, H.; Li, Q.; Yan, B.; Zhang, L.; Gu, Y. Bionic Electronic Nose Based on MOS Sensors Array and Machine Learning Algorithms Used for Wine Properties Detection. *Sensors (Basel).* **2019**, *19*, 45.

(38) Deringer, V. L.; Merlet, C.; Hu, Y.; Lee, T. H.; Kattirtzi, J. A.; Pecher, O.; Csányi, G.; Elliott, S. R.; Grey, C. P. Towards an Atomistic Understanding of Disordered Carbon Electrode Materials. *Chem. Commun.* **2018**, *54*, 5988–5991.

(39) Grahn, P. J.; Mallory, G. W.; Khurram, O. U.; Berry, B. M.; Hachmann, J. T.; Bieber, A. J.; Bennet, K. E.; Min, H. K.; Chang, S. Y.; Lee, K. H.; et al. A Neurochemical Closed-Loop Controller for Deep Brain Stimulation: Toward Individualized Smart Neuromodulation Therapies. *Front. Neurosci.* **2014**, *8* (8 JUN), 1–11.

(40) Moran, R. J.; Kishida, K. T.; Lohrenz, T.; Saez, I.; Laxton, A. W.; Witcher, M. R.; Tatter, S. B.; Ellis, T. L.; Phillips, P. E.; Dayan, P.; et al. The Protective Action Encoding of Serotonin Transients in the Human Brain. *Neuropsychopharmacology* **2018**, *43*, 1425–1435.

(41) Kishida, K. T.; Saez, I.; Lohrenz, T.; Witcher, M. R.; Laxton, A. W.; Tatter, S. B.; White, J. P.; Ellis, T. L.; Phillips, P. E. M.; Montague, P. R. Subsecond Dopamine Fluctuations in Human Striatum Encode Superposed Error Signals about Actual and Counterfactual Reward. *Proc. Natl. Acad. Sci. U. S. A.* **2016**, *113* (1), 200–205.

APPENDIX

A.1 User Manual for "The SSIM Method" for FSCV Adenosine Data Analysis

The SSIM Method was developed in MATLAB 2019b. Make sure that your MATLAB also has the "Signal Processing Toolbox," which can be added when you installed MATLAB. The software can be downloaded from https://github.com/maxchem6/imgADanalysis. Please download the whole folder, then extract it to have every file in the same folder.

To analyze the adenosine FSCV data…

1. Open HDCV Analysis, then open .hdcv data file. Click "Export Options" and check only "Color Plot Write." Click Done.

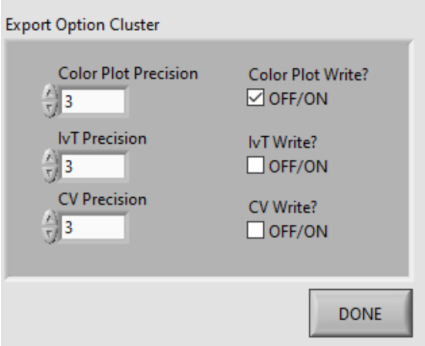

2. Uncheck "Background subtracted." Put file number (1, 2, …) in "suffix" box. Then click "Export."

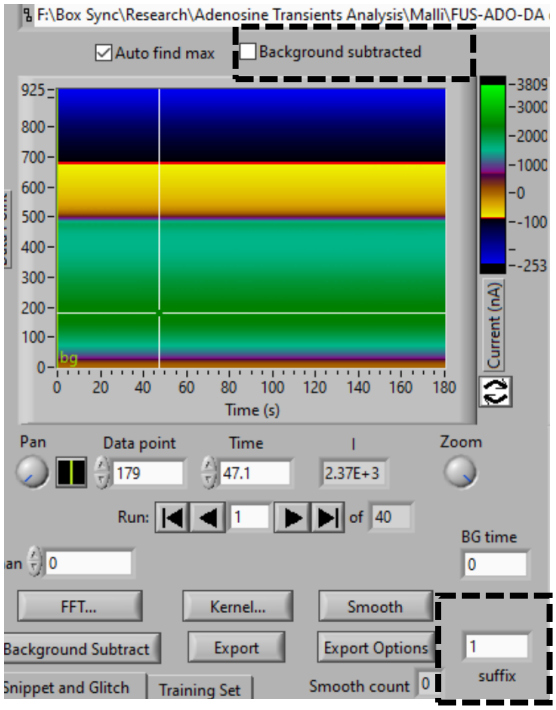

3. Open MATLAB. Click “Browse for folder” icon, and choose the program folder.

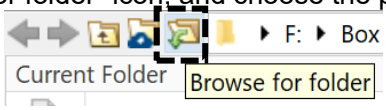

4. For adenosine data, double-click “imageFSCVAnalysis.m” and run.

5. In the Command Window, the program will ask if you want to build you own reference (“internal references”) or use the “standard library.”
   - For “internal reference,” type 1 and Enter. Then, put the file number and rise time (not peak time!) for six transient adenosine events from your data. (i.e. you have to quickly go through your data before using the program) Wide range of concentration and duration is recommended: two large (> 0.25 µM), two medium (0.1-0.25 µM), and two small (< 0.1 µM) transient events.
   - For “standard library,” type 2 and Enter.

6. Type the calibration factor (peak current for 1 uM adenosine) and Enter.

7. Choose the FSCV .hdcv Color files that you exported. They do not have to be in the same folder as the program, but the file number (suffix) must be in the correct order. Click “Open.”

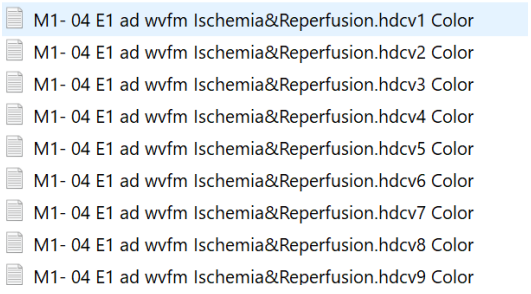

8. The program should analyze the data now. It takes 5-7 min per 1 h of experiment (20 3-min files).

9. Once finished, the program will save the analysis result in the Excel file named “adenosineResult_YYYY-MM-DD_HHRR.xlsx” in the program folder.

10. To read the Excel file, open it from Windows folder directly, or Right-click in the MATLAB and choose “Open Outside MATLAB.”

File	Seed_s	SSIM	PeakTime_s	Curr_nA	Conc_uM	HalfWidth_s	Noise3_nA	PassSN	InterTime_s
1	82.1	0.632591966	82.7	1.547586531	0.051586218	1.280772929	0.65447738	1	82.7
2	6.7	0.668964949	7.2	3.204680983	0.106822699	1.264166879	0.659310528	1	104.5
3	92.9	0.646278721	94	2.163939384	0.072131313	1.768712233	0.600552293	1	266.8
3	137.9	0.704180864	138.5	1.686710291	0.056223676	0.679213616	0.600552293	1	44.5
4	133.5	0.729573787	134.2	3.474531339	0.115817711	1.192998001	0.656324034	1	175.7
6	160.1	0.522474481	160.9	4.192193938	0.139739798	1.122563041	0.652724363	1	386.7

Columns: A. file number, B. seeding time (s), C. SSIM index, D. peak time (s), E. current (nA), F. concentration (uM), G. peak duration (s), H. S/N=3 level (nA), I. Pass S/N?, and J. inter-event time (s). May need only column F, G, and J for your experiment.

A.2 List of Publications from this Dissertation

1. **Puthongkham, P.**; Yang, C.; Venton, B. J. Carbon Nanohorn-Modified Carbon Fiber Microelectrodes for Dopamine Detection. *Electroanalysis* **2018**, *30,* 1073-1081.

2. **Puthongkham, P.**; Lee. S. T.; Venton, B. J. Mechanism of Histamine Oxidation and Electropolymerization at Carbon Electrodes. *Anal. Chem.* **2019,** *91,* 8366-8373.

3. **Puthongkham, P.**; Venton, B. J. Nanodiamond Coating Improves the Sensitivity and Antifouling Properties of Carbon-Fiber Microelectrodes. *ACS Sens.* **2019,** *4,* 2403-2411.

4. Cao, Q.*; **Puthongkham, P.***; Venton, B. J. Review: New Insights into Optimizing Chemical and 3D Surface Structures of Carbon Electrodes for Neurotransmitter Detection. *Anal. Methods* **2019**, *11,* 247-261. (*equal contribution)

5. **Puthongkham, P.**; Venton, B. J. Recent Advances in Fast-Scan Cyclic Voltammetry. *Analyst* **2020,** *145,* 1087-1102.

6. **Puthongkham, P.**; Rocha, J.; Wang, Y.; Ganesana, M.; Borgus, J. R.; Gahlmann, A.; Venton, B. J. Structural Similarity Image Analysis for Detection of Adenosine and Dopamine in Fast-Scan Cyclic Voltammetry Color Plots. (under preparation).